

Southwest Indian Ocean Risk Assessment Financing Initiative (SWIO-RAFI):

Component 1 - Hazard

FINAL Report Submitted to the World Bank

June 1st, 2016

Copyright

2016 AIR Worldwide Corporation. All rights reserved.

Trademarks

AIR Worldwide is a registered trademark in the European Union.

Confidentiality

AIR invests substantial resources in the development of its models, modeling methodologies and databases. This document contains proprietary and confidential information and is intended for the exclusive use of AIR clients who are subject to the restrictions of the confidentiality provisions set forth in license and other nondisclosure agreements.

Contact Information

If you have any questions regarding this document, contact:

AIR Worldwide Corporation
388 Market Street, Suite 750
San Francisco, CA 94111
USA
Tel: (415) 912-3111
Fax: (415) 912-3112



Table of Contents

Executive Summary	1
1 Introduction	2
1.1 Limitations.....	3
2 Hazard Catalogs and Analysis	4
2.1 Tropical Cyclone	4
2.1.1 Wind	6
2.1.2 Precipitation Hazard and Flooding	9
2.1.3 Storm Surge Flooding.....	11
2.1.4 Tropical Cyclone Consequence Summary	13
2.2 Non-Tropical Cyclone Flood.....	13
2.2.1 Non-Tropical Cyclone Consequence Summary	16
2.3 Earthquake.....	16
2.3.1 Ground Shaking	18
2.3.2 Tsunami.....	20
2.3.3 Earthquake Consequence Summary	21
2.4 Landslide (Comoros).....	21
2.5 Summary and Data Limitations.....	23
3 Hazard Profiles	25
3.1 Comoros.....	27
3.2 Madagascar	28
3.3 Mauritius	29
3.4 Seychelles.....	30
3.5 Zanzibar	31
3.6 Marquee Events	32

4	Appendix A – Detailed Model Documentation	38
4.1	Tropical Cyclone	38
4.1.1	Event Generation	38
4.1.2	Stochastic Catalog Summary Statistics.....	44
4.1.3	Local Intensity Calculation	50
4.1.4	Storm Surge Flooding.....	61
4.1.5	References	65
4.2	Non-Tropical Cyclone Flooding.....	67
4.2.1	Generation of Stochastic Catalog for Non-Tropical Cyclone Rainfall.....	69
4.2.2	Non-Tropical Cyclone Induced Precipitation	71
4.2.3	Non-Tropical Cyclone Flooding.....	73
4.2.4	Precipitation Hazard Analysis	74
4.3	Earthquake.....	94
4.3.1	Earthquakes in the Southwest Indian Ocean	94
4.3.2	Local Intensity Calculation	120
4.3.3	Tsunamis in the Southwest Indian Ocean	129
4.3.4	References	137
4.4	Landslide	139
4.4.1	Introduction	139
4.4.2	Landslide Susceptibility	139
4.4.3	Brief Summary of Methodologies	140
4.4.4	Data Sources	141
4.4.5	Assumptions and Limitations of Methodology and Data	146
4.4.6	Discussion and Results.....	147
4.4.7	Conclusion	149

4.4.8	References	151
5	Appendix B – Consequence Database	154
5.1	Consequence Database for Tropical Cyclones and Flooding	154
5.1.1	Data Sources	154
5.1.2	Explanation of Database Data and Data Fields.....	155
5.1.3	Discussion of Significant Events	157
5.1.4	Database Statistics.....	161
5.1.5	Database Statistics of Tropical Cyclones.....	164
5.1.6	Database Statistics of Floods.....	167
5.1.7	Database Statistics of Landslides	169
5.2	Consequence Database for Earthquakes and Tsunami	169
5.2.1	Data Sources	169
5.2.2	Explanation of Database Data and Data Fields.....	170
5.2.3	Discussion of Significant Events	172
5.2.4	Database Statistics.....	174
5.2.5	Database Statistics of Landslides	177
5.3	References.....	178
	About AIR Worldwide Corporation.....	180



Table of Figures

Figure 1: Domain of the AIR Tropical Cyclone Model for the Southwest Indian Ocean Basin	4
Figure 2: Storm tracks by Saffir-Simpson category for the 65 year historical record (left) and a randomly selected 65 year period in the stochastic catalog (right).....	5
Figure 3: Comparison of Historical and Simulated Annual Count Probabilities for Tropical Cyclones in the Model Domain.....	6
Figure 4: Comparison of Historical and Simulated Seasonal Frequency at Genesis for Tropical Cyclones in the Model Domain.....	6
Figure 5: Comparison of modeled and reported tropical cyclone wind speed (1-minute sustained at 10m) for Madagascar (left) and Mauritius (right).....	8
Figure 6: Comparison of modeled wind footprints with station recordings (1-minute sustained at 10m) for tropical cyclones Hollanda (Mauritius, 1994) and Giovanna (Madagascar, 2012)	8
Figure 7: Comparison of cumulative TRMM and modeled precipitation for tropical cyclones between 1998 and 2014 (left). Comparison of GSOD rain gauge measurements and modeled precipitation for tropical cyclones between 1979 and 2015 (right).....	10
Figure 8: Precipitation footprint for tropical cyclone Giovanna (2012) based on TRMM (left) and AIR modeled (right)	10
Figure 9: Modeled storm surge footprints for tropical cyclones Giovanna (2012, left) and Hellen (2014, right) in Madagascar	12
Figure 10: Comparison of Modeled Storm Surge Heights from GDACS and AIR models.....	12
Figure 11: Illustration of results from NTC rainfall climatology construction: TRMM rainfall induced from Cyclone Eline (left) and the corresponding NTC rainfall (right)	14
Figure 12: Comparison of historical average annual TRMM precipitation with the selected TRMM grid point for Comoros. Blue bars show the average annual precipitation across all years (1998-2013) and green bars shows the selected TRMM station. The red line shows the error percentage for each year.	15
Figure 13. Domain of the AIR Earthquake Model for the Southwest Indian Ocean Region.....	17
Figure 14. Historical (left) vs. Stochastic (right) 114 year Catalogs of Earthquake Events. (<i>Note: The Mid-Indian ridge is only partially modeled (e.g., Zone 26) due to its remoteness relative to populated islands, resulting in the discrepancy between the historical and simulated event distributions on the right-hand side of each image</i>)	18

Figure 15. Modeled vs. Historical Frequency-Magnitude Distributions in the Southwest Indian Ocean (left) and Modeled vs. Historical Depth Distributions in the Southwest Indian Ocean (right) 18

Figure 16. AIR (left) vs. USGS (right) Modeled Ground Motion, the 1991 Madagascar Earthquake 19

Figure 17: Comparison between the modeled Seychelles tsunami map (left) and 2004 tsunami inundation by UNDP (right) for the island of Mahé 20

Figure 18: Landslide susceptibility zonation for Comoros by island with historical landslides shown in black (90 m x 90 m resolution) 22

Figure A.1. Domain of the AIR Typhoon Model for the SWIO Basin 39

Figure A.2. Annual Probability of Simulated Tropical Cyclone Landfalls – Madagascar 40

Figure A.3. Distribution of Historical Events by Month for the Model Domain 41

Figure A.4. Historical Storm Genesis Locations (left) and Smoothed Historical Genesis Locations (right) 41

Figure A.5. Simulated Storm Probability by Intensity Category at Landfall – Madagascar 43

Figure A.6. Comparison of Historical and Simulated Seasonal Frequency at Genesis for Tropical Cyclones in the Model Domain..... 45

Figure A.7. Comparison of Historical and Simulated Annual Count Probabilities for Tropical Cyclones in the Model Domain 45

Figure A.8. Comparison of Historical and Simulated Landfall Frequency – Madagascar 46

Figure A.9. Comparison of Historical and Simulated Landfall Frequency – Mauritius..... 46

Figure A.10. Comparison of Historical and Simulated Landfall Frequency – Comoros 46

Figure A.11. Comparison of Historical and Simulated Landfall Frequency – Seychelles 47

Figure A.12. Comparison of Historical (left) and Modeled Storm Tracks (right) for a 65-Year Period 47

Figure A.13. Comparison of Historical and Simulated Intensity at Landfall – Madagascar..... 48

Figure A.14. Comparison of Historical and Simulated Intensity at Landfall – Mauritius..... 49

Figure A.15. Storm Track Density based on Historical (left) and Simulated Events (right) 49

Figure A.16. The Relationship between Central Pressure and Wind Speed 51

Figure A.17. Effects of Topography on Wind 53



Figure A.18. Terrain Effects on Wind Velocity Profiles (adapted from Cook)..... 54

Figure A.19. Example of AIR friction factors used in the Southwest Indian basin model for Madagascar 55

Figure A.20. Example of AIR gust factors used in the Southwest Indian basin model for Madagascar 56

Figure A.21. Modeled Average Precipitation Rates by Storm Intensity 58

Figure A.22. Representation of Overland Flow Routing (Rojas et al. 2003) 61

Figure A.23: Illustration of storm surge (Source: <http://www.nhc.noaa.gov/surge/>)..... 62

Figure A.24: Maximum surge recorded for different tropical cyclones in the U.S. 62

Figure A.25: Spatial distribution of H_s for different V_{tm} and V_{max} 63

Figure A.26: Comparison of Modeled Storm Surge Heights from GDACS and AIR models..... 64

Figure A.27. Illustration of results from NTC rainfall climatology construction at two time steps: 2-17-03Z (top) and 2-17-15Z (bottom). Total TRMM rainfall, including that from Cyclone Eline (left), and the corresponding NTC related rainfall (right) 68

Figure A.28. Tropical cyclone activity in the SWIO basin for 2000 (a) and the resulting total TRMM rainfall (b), NTC rainfall (c), tropical cyclone rainfall (d), and percent contribution of tropical cyclone rainfall (e) 69

Figure A.29. Composition of precipitation events for the 7-5-days clause. Blue bars are daily NTC rainfall, red dash box represent the cumulative rainfall during the storm period, solid magenta box represent the time from the beginning of the previous peak event to the next peak event and green solid box represents the duration from the previous peak to the beginning of the next storm 73

Figure A.30: Ratio of monthly weather station rain gauge measurements to TRMM data for weather stations in Madagascar and Mauritius. 74

Figure A.31. TRMM grid points covering the main island of Comoros. The highlighted point in cyan represents the selected TRMM grid cell 74

Figure A.32. Comparison of historical average annual TRMM precipitation with the selected TRMM grid point. Blue bars show the average annual precipitation of across all years (1998-2013) and green bars shows the selected TRMM station. Red line shows the error percentage for each year..... 75

Figure A.33. Comparison of daily statistical properties from historical TRMM precipitation and 10,000 years of stochastic simulations for the selected TRMM point..... 76

Figure A.34. Frequency distribution of stochastically generated and historical areal annual precipitation across Comoros 76



Figure A.35. Comparison between Consequence Database and TRMM-based NTC Precipitation Event Occurrence by Year for Comoros 77

Figure A.36. Hydro-climatology based zonal representation of TRMM grid points within Madagascar. The highlighted points in cyan represent the selected TRMM grid cells. 78

Figure A.37. Comparison of historical average annual TRMM precipitation with the selected TRMM grid point. Blue bars show the average annual precipitation of across all years (1998-2013) and green bars shows the selected TRMM station for each zone; (a) zone 1, (b) zone 2, (c) zone 3, (d) zone 4, and (e) zone 5. Red line shows the error percentage for each year. 79

Figure A.38. Comparison of NTC TRMM precipitation with observed historical rain gauge data for the NTC period from May to October. Blue bars show the NTC TRMM precipitation of across all years (1998-2013) and green bars shows the observed precipitation; (a) comparison of total annual precipitation for the historical period from 1998-2013, and (b) Comparison of mean monthly precipitation for the same historical period. 80

Figure A.39. Comparison of daily statistical properties from historical TRMM precipitation and 10,000 years of stochastic simulations for each zone number 81

Figure A.40. Frequency distribution of stochastically generated and historical areal annual precipitation across Madagascar 82

Figure A.41. Comparison between Consequence Database and TRMM-based NTC Precipitation Event Occurrence by Year for Madagascar 83

Figure A.42. Comparison between the NTC Precipitation Event Occurrence Frequency of the NTC TRMM Data (left) and that of the Stochastic Catalog (right)..... 83

Figure A.43. TRMM grid points covering main islands of Mauritius. The highlighted point in cyan represents the selected TRMM grid cell. 84

Figure A.44. Comparison of historical average annual TRMM precipitation with the selected TRMM grid point. Blue bars show the average annual precipitation of across all years (1998-2013) and green bars shows the selected TRMM station. Red line shows the error percentage for each year..... 84

Figure A.45. Comparison of daily statistical properties from historical TRMM precipitation and 10,000 years of stochastic simulations for the selected TRMM point. 85

Figure A.46. Frequency distribution of stochastically generated and historical areal annual precipitation across Mauritius 85

Figure A.47. Comparison between Consequence Database and TRMM-based NTC Precipitation Event Occurrence by Year for Mauritius..... 86

Figure A.48. TRMM grid points covering the inner islands of Seychelles. The highlighted point in cyan represents the selected TRMM grid cell. 87

Figure A.49. Comparison of historical average annual TRMM precipitation with the selected TRMM grid point. Blue bars show the average annual precipitation of across all years (1998-2013) and green bars shows the selected TRMM station. Red line shows the error percentage for each year..... 87

Figure A.50. Comparison of daily statistical properties from historical TRMM precipitation and 10,000 years of stochastic simulations for the selected TRMM point. 88

Figure A.51. Frequency distribution of stochastically generated and historical areal annual precipitation across Seychelles..... 88

Figure A.52. Comparison between Consequence Database and TRMM-based NTC Precipitation Event Occurrence by Year for Seychelles 89

Figure A.53. TRMM grid points covering main islands of Zanzibar. The highlighted point in cyan represents the selected TRMM grid cell. 90

Figure A.54. Comparison of historical average annual TRMM precipitation with the selected TRMM grid point. Blue bars show the average annual precipitation of across all years (1998-2013) and green bars shows the selected TRMM station. Red line shows the error percentage for each year..... 90

Figure A.55. Comparison of daily statistical properties from historical TRMM precipitation and 10,000 years of stochastic simulations for the selected TRMM point. 91

Figure A.56. Frequency distribution of stochastically generated and historical areal annual precipitation across Zanzibar 91

Figure A.57. Comparison between Consequence Database and TRMM-based NTC Precipitation Event Occurrence by Year for Zanzibar 92

Figure A.58. The Earth’s Layers at a Subduction Zone 95

Figure A.59. Completeness of Auxiliary and Historical Record Data, Based on Earthquake Source Dimension 99

Figure A.60. Sample Gutenberg-Richter Distribution 100

Figure A.61. Tectonic plates in the Sub-Saharan and Southwest Indian Ocean Regions (source: Horner-Johnson et al., 2007) 101

Figure A.62. Marquee earthquake events in the Southwest Indian Ocean region 103

Figure A.63. Model Domain for the AIR Earthquake Model for Sub Sahara and Southwest Indian Ocean 104



Figure A.64. Historical Seismicity by Magnitude 105

Figure A.65. Faults in the Sub-Sahara and Southwest Indian Ocean regions 106

Figure A.66. Modeled Seismic Source Zones in the Sub-Sahara and Southwest Indian Ocean regions 108

Figure A.67. Seismic Source Zones 8 (right) and 23 (left) in the Southwest Indian Ocean region 109

Figure A.68. Schematic of the Procedure Utilized to Model Seismic Moment Rate..... 110

Figure A.69. GPS Velocity Observations from Sub-Saharan Africa Geodetic Strain Rate Model 1.0 (*Stamps et al, 2015*) and Calculated Annual Moment Rates in the Southwest Indian Ocean region 111

Figure A.70. Schematic representation of A) the spatial distribution of historical earthquakes in the model domain; and B) the spatial distribution of smoothed gridded seismicity 113

Figure A.71. Depths redistribution in the Southwest Indian Ocean for in-land (left) and ocean (right) earthquakes using the EHB (1998) catalog..... 114

Figure A.72. 10,000 year time-independent stochastic catalog in the Southwest Indian Ocean region..... 115

Figure A.73. Focal Depth..... 116

Figure A.74. Modeled vs. Historical Frequency-Magnitude Distributions in the Southwest Indian Ocean 118

Figure A.75. Modeled vs. Historical Magnitude Distributions in the Southwest Indian Ocean 118

Figure A.76. Historical (left) vs. Stochastic (right) 114 year Catalogs of Earthquake Events (*Note: The Mid-Indian ridge is only partially modeled (e.g., Zone 26) due to its remoteness relative to populated islands, resulting in the discrepancy between the historical and simulated event distributions on the right-hand side of each image*) 119

Figure A.77. Modeled vs. Historical Cumulative Depth Probability Distributions 120

Figure A.78. Modeled vs. Historical Depth Distributions in the Southwest Indian Ocean..... 120

Figure A.79. NEHRP Classification Soil Map in the Southwest Indian Ocean Region..... 123

Figure A.80. Comoros: peak horizontal ground acceleration at the 100-year mean return period. 126

Figure A.81. Madagascar (left) and Mauritius (right) peak horizontal ground acceleration at the 100-year mean return period. 126

Figure A.82. Seychelles (left) and Zanzibar (right) peak horizontal ground acceleration at the 100-year mean return period. 127

Figure A.83. AIR (left) vs. USGS (right) Modeled Ground Motion, the 1985 Madagascar Earthquake 128



Figure A.84. AIR (left) vs. USGS (right) Modeled Ground Motion, the 1991 Madagascar Earthquake 128

Figure A.85. An illustration of the mechanism of tsunami genesis at subduction zones (source: Wikipedia)... 129

Figure A.86. An example of a pre-computed tsunami simulated on the Sunda fault in the ComMIT interface 130

Figure A.87. Tectonic setting of the SWIO Region (source: IRIS, Google)..... 131

Figure A.88. Tsunami risk zones for Zanzibar 133

Figure A.89. Selected tsunami risk zones for Madagascar..... 134

Figure A.90. Comparison between the modeled Seychelles tsunami map (left) and 2004 tsunami inundation by UNDP (right) for the island of Mahé 135

Figure A.91 Land use map of the Comoros archipelago (Island of Grand Comore, Anjouan, and Moheli) developed under the project for Community Involvement Sustainable Development (ECDD) from high resolution satellite images (UNDP Comoros 2014)..... 143

Figure A.92 Map of 0.5 km MODIS-based Global Land Cover Climatology from the USGS Land Cover Institute 144

Figure A.93 SRTM 90 meter resolution data (Shuttle Radar Topography Mission, SRTM GL)) 144

Figure A.94 Grand Comore island soil descriptions. White spaces denote areas of no listed information and coincide with the locations of the two shield volcanoes of La Grille and Mount Karthala. (UNDP Comoros 2014) 145

Figure A.95 Anjouan island soil descriptions (UNDP Comoros 2014) 145

Figure A.96 Data from the Harmonized World Soil Database (FAO et al. 2012)..... 146

Figure A.97 Locations of previous landslides for the Union of Comoros are indicated in brown (Abdoulkarim and Soule 2011)..... 146

Figure A.98 Landslide susceptibility zonation for Comoros by island with historical landslides shown in black (90 m x 90 m resolution) 148

Figure A.99 Affected site ~2 kilometers from the town of Ouallah 1 in Moheli (Source: Mansourou, 2014)..... 149

Figure B.1 Tropical cyclone Giovanna (2012) and storm track on the right. [Source: (left) Giovanna Feb 13 2012 0630Z by NASA image by Jeff Schmaltz, LANCE/EOSDIS MODIS Rapid Response Team at NASA GSFC; (right) Giovanna 2012 track by Keith Edkins - Created using Wikipedia:WikiProject Tropical cyclones/Tracks] 157

Figure B.2 (left) Flooding of Vouvouni Village, April 2012 and (right) Destroyed road and bridge at Hambou, Grande Comore, April 2012 (Source for both photos: DGSC)..... 158

Figure B.3 Tropical cyclone Ivan (2008) and storm track on the right. [Source: (left) Ivan 16 Feb 2008 0645Z by NASA image courtesy, LANCE/EOSDIS MODIS Land Rapid Response Team, at NASA GSFC; (right) Ivan 2008 track – Created using Wikipedia:WikiProject Tropical cyclones/Tracks]..... 159

Figure B.4 Tropical cyclone Indlala (2007) [Source: (left) Indlala March 15 2007 by NASA image by Jeff Schmaltz, LANCE/EOSDIS MODIS Rapid Response Team at NASA GSFC; (right) Indlala 2007 track - Created using Wikipedia:WikiProject Tropical cyclones/Tracks] 159

Figure B.5 Tropical cyclone Gafilo (2004) and storm track on the right. [Source: (left) Gafilo 2004-03-06 0655Z by NASA image courtesy, Jeff Schmaltz, LANCE/EOSDIS MODIS Land Rapid Response Team, at NASA GSFC; (right) Gafilo 2004 track - Created using Wikipedia:WikiProject Tropical cyclones/Tracks]..... 160

Figure B.6 Flooding in 2003, Madagascar. (Source: UNDP / Michel Matera) 161

Figure B.7 (left) Phreatic eruption of Mount Karthala on the afternoon of April 17, 2005 (Source: Daniel Hoffschir, Global Volcanism Program), and (right) Lava lake formed in Chahalé crater of Mount Karthala (Source: Hamid Soulé, Karthala Volcano Observatory)..... 172

Figure B.8 The remains of a road swept away by the tsunami (photo taken from repaired section). (Source: M. de Vries, UNEP)..... 173

Figure B.9 Landslide on Anjouan, Comoros, induced by moderate earthquake and tropical cyclone Hellen (Source: Walter D. Mooney, USGS)..... 174

Figure B.10 Landslide on Moheli, Comoros, induced by moderate earthquake and tropical cyclone Hellen (Source: Mansourou, 2014)..... 174

List of Tables

Table 1: Number of recorded tropical cyclone events for each SWIO island nation, by decade. Events considered to be “catastrophic” are provided in parentheses.....	13
Table 2: Number of recorded non-tropical cyclone flooding events for each SWIO island nation, by decade. Events considered to be “catastrophic” are provided in parentheses.....	16
Table 3: Number of significant earthquake events for each SWIO island nation, by decade. Events considered to be “catastrophic” are provided in parentheses.	21
Table 4: Provided hazard intensity measures and units for each data- and shape-file output.....	25
Table 5: Selected marquee historical events organized by peril	26
Table A.1. Comparison of Historical and Simulated Values at Landfall – Madagascar.....	48
Table A.2. Comparison of areal annual precipitation for 10,000 years across Comoros compared to the historical time period	77
Table A.3. Comparison of cross-correlation statistics of the selected TRMM grid cells in each zone for the historical time period between 1998 and 2013.....	81
Table A.4. Comparison of areal annual precipitation for 10,000 years across Madagascar compared to the historical time period	82
Table A.5: Comparison of areal annual precipitation for 10,000 years across Mauritius compared to the historical time period.....	86
Table A.6: Comparison of areal annual precipitation for 10,000 years across Seychelles compared to the historical time period	89
Table A.7: Comparison of areal annual precipitation for 10,000 years across Zanzibar compared to the historical time period	92
Table A.8. Marquee earthquakes events.....	103
Table A.9. Modeled Seismic Source Zones in the Southwest Indian Ocean region	108
Table A.10. NEHRP Soil Classifications and average shear-wave velocities	123
Table A.11 Comparison of proportions of areas within high, medium, and low landslide susceptibility for islands and landslides.....	148

Table B.1 Summary for Comoros, Madagascar, Mauritius, Seychelles, and Zanzibar by decade of consequence database for tropical cyclones, floods, and related secondary hazards. Economic losses are not trended..... 162

Table B.2 Summary for Comoros by decade of consequence database for tropical cyclones, floods, and related secondary hazards. Economic losses are not trended. 163

Table B.3 Summary for Madagascar by decade of consequence database for tropical cyclones, floods, and related secondary hazards. Economic losses are not trended. 163

Table B.4 Summary for Mauritius by decade of consequence database for tropical cyclones, floods, and related secondary hazards. Economic losses are not trended. 163

Table B.5 Summary for Seychelles by decade of consequence database for tropical cyclones, floods, and related secondary hazards. Economic losses are not trended. 164

Table B.6 Summary for Zanzibar by decade of consequence database for tropical cyclones, floods, and related secondary hazards. Economic losses are not trended. 164

Table B.7 Summary for Comoros, Madagascar, Mauritius, Seychelles, and Zanzibar by decade of consequence database for tropical cyclones. Economic losses are not trended. 165

Table B.8 Summary for Comoros by decade of consequence database for tropical cyclones. Economic losses are not trended. 165

Table B.9 Summary for Madagascar by decade of consequence database for tropical cyclones. Economic losses are not trended..... 166

Table B.10 Summary for Mauritius by decade of consequence database for tropical cyclones. Economic losses are not trended..... 166

Table B.11 Summary for Seychelles by decade of consequence database for tropical cyclones. Economic losses are not trended..... 166

Table B.12 Summary for Comoros, Madagascar, Mauritius, Seychelles, and Zanzibar by decade of consequence database for non-cyclone precipitation and flooding. Economic losses are not trended. 167

Table B.13 Summary for Comoros by decade of consequence database for non-cyclone precipitation and flooding. Economic losses are not trended. 167

Table B.14 Summary for Madagascar by decade of consequence database for non-cyclone precipitation and flooding. Economic losses are not trended. 168

Table B.15 Summary for Mauritius by decade of consequence database for non-cyclone precipitation and flooding. Economic losses are not trended. 168



Table B.16 Summary for Seychelles by decade of consequence database for non-cyclone precipitation and flooding. Economic losses are not trended. 168

Table B.17 Summary for Zanzibar by decade of consequence database for non-cyclone precipitation and flooding. Economic losses are not trended. 169

Table B.18 Summary for Comoros, Madagascar, Mauritius, Seychelles, and Zanzibar by decade of consequence database for earthquakes, tsunami, and volcanic eruptions. Economic losses are not trended. 176

Executive Summary

The South West Indian Ocean Risk Assessment and Financing Initiative (SWIO RAFI) was established at the request of the Indian Ocean Commission (IOC) on behalf of Comoros, Madagascar, Mauritius, Seychelles, and Zanzibar. The goal of SWIO RAFI is to improve the resiliency and capacity of the island states through the creation of disaster risk financing strategies. A key component of this effort involves the quantification of site-specific risk from the perils of floods, earthquakes, and tropical cyclones as well as their secondary hazards of storm surge and tsunamis.

The present report details project Component 1, which comprises the development of regional hazard intensity profiles for each of the considered perils. The two primary components of the hazard profiles are (1) a catalog of events (e.g., tropical cyclones, earthquakes) and associated event parameters (e.g., Central Pressure, Moment Magnitude), and (2) intensity calculations that translate event parameters into spatially distributed hazard intensities (e.g., wind speeds, ground shaking).

Historical databases of events are inherently limited due to the relatively short timeline of human recordings; therefore, probabilistic, or stochastic, catalogs are simulated using statistics derived from the historical catalog, in order to develop a more reliable assessment of the events expected in any given year. For the SWIO region, 10,000 simulated years of tropical cyclone and earthquake events are generated and compiled into a stochastic catalog. Each event in the historical and stochastic catalogs is evaluated using regionally appropriate hazard intensity calculations that estimate the event's extent and severity. The resulting spatially distributed hazard intensities are primary inputs to the loss calculation, which evaluates the economic impact of each event and is considered in Component 4 of the project.

In this report, modeled expected hazard intensity profiles at mean return periods of 25, 50, 100, 250, 500, and 1,000 years are presented for each considered island nation and peril. Additionally, selected historical event intensity footprints are presented and compared to reported intensities. Return period hazard intensities are calculated on a 30 arc-second (approximately 1km) grid. Hazard maps and associated data files are the primary outputs of Component 1 and are provided as a digital addendum to this report. A summary of each hazard model is provided in the main body of this report and detailed technical model documentation and a historical event consequence database are provided in Appendices A and B, respectively.

1 Introduction

Hazard catalogs and intensity calculation modules are integral components of all AIR models. Each modeled peril requires a reliable historical catalog of events that includes all past recorded natural catastrophes, whether or not these events affected human populations or incurred economic losses. Statistics for fundamental parameters of the historical events are extracted and used to simulate a longer, but statistically consistent, catalog of stochastic events. These catalogs serve as the primary inputs to hazard intensity calculations, which allow AIR to evaluate the severity of both historical and simulated events. For the SWIO basin, AIR developed comprehensive historical and stochastic catalogs and intensity calculation modules for tropical cyclone and earthquake events. As per the ToR provided by the World Bank, Component 1 comprises the following three main objectives for each considered SWIO island nation:

- Create a set of GIS-compatible hazard layers for tropical cyclone, storm surge, flood, earthquakes, and tsunamis. The hazard layers should define the regions susceptible to events with return periods ranging from 25 to 1,000 years.
- Create a set of GIS-compatible hazard layers representing the areas affected by historical tropical cyclone, storm surge, flood, earthquake, and tsunami events.
- Make hazard information accessible using open-source GIS software, such as QGIS, and DRM tools such as InaSAFE.

The general approach adopted for achieving these objectives consists of (1) the collection of regional event information on prior tropical cyclones, earthquakes, floods, and their associated secondary perils, (2) the development of simulated events using parametric models that are informed by statistics derived from the historical record, (3) the collection of regional datasets that describe the physical properties (e.g., land-use, land-cover, geology) of the modeled domain, (4) the development of parametric models that calculate the spatial distribution of hazard intensities from historical and stochastic events, and (5) the calculation of spatially distributed hazard intensity mean return periods.

The stochastic catalogs of tropical cyclone events are used to calculate mean return period maps for wind, precipitation induced flooding, and storm surge. Similarly, stochastic catalogs for non-tropical cyclone (NTC) precipitation are used to calculate mean return period flood maps. Stochastic catalogs of earthquake events are used to calculate ground shaking severity, while maximum tsunami extents are calculated using a hybrid-qualitative model.

The sections presented herein provide an overview of the general hazard development framework applied for the SWIO region. A detailed technical discussion of the individual considerations and methodologies applied for each of the SWIO island nations and for each peril is provided in Appendix A. The final outputs of Component 1 are geospatial databases of hazard intensities for each modeled peril on a 30 arc-second

(approximately 1km) grid. The hazard intensities and associated metadata are provided as a digital addendum to this report.

1.1 Limitations

The hazard catalogs and intensity calculation modules summarized in this report are intended for use by the governments of the SWIO island nations and the World Bank to assist their understanding of the risk from natural catastrophes. Proper application of this information requires recognition and understanding of the limitations of both the scope and methodology of the entire study.

The scope of services performed during this assessment may not adequately address the needs of other users, and any re-use of (or failure to use) this report or the findings, conclusions, or recommendations presented herein are at the sole risk of the user. Our conclusions and recommendations are based on our professional opinion, engineering experience and judgment, analyses conducted during the course of the study, information and data available in the literature and those provided by the World Bank and various local agencies, and are derived in accordance with current standards of professional practice.

2 Hazard Catalogs and Analysis

The following section overviews the development of the historical and stochastic event catalogs and the local intensity calculations for each hazard considered in the SWIO region. Detailed model documentation for each peril, including the parametric statistics and distributions used in the development of the stochastic catalogs and hazard modules, is provided in Appendix A. The impacts of significant historical natural catastrophes in the SWIO region and their relative prevalence in each country are also summarized. A structured consequence database of reported impacts, in terms of event counts, event severity, casualties, and economic losses, from each investigated natural catastrophe is described further in Appendix B and provided as a digital addendum to this report.

2.1 Tropical Cyclone

Tropical cyclones (TC) are the most frequent catastrophic hazard in the SWIO region and have been responsible for significant historical economic losses and casualties, particularly in the island nations of Madagascar and Mauritius. In terms of tropical cyclone formation, the Southwest Indian basin is one of the most active areas in the world. Not only are tropical cyclones more frequent in this ocean basin, but they are also more intense than in other parts of the world. On average, 13 tropical cyclones with wind speeds exceeding 63 km/h form here each year. The SWIO cyclone season begins November 15 and ends April 30 of the following calendar year. Modeled frequency, meteorological data, and track information are analyzed in the geographical domain depicted in Figure 1.

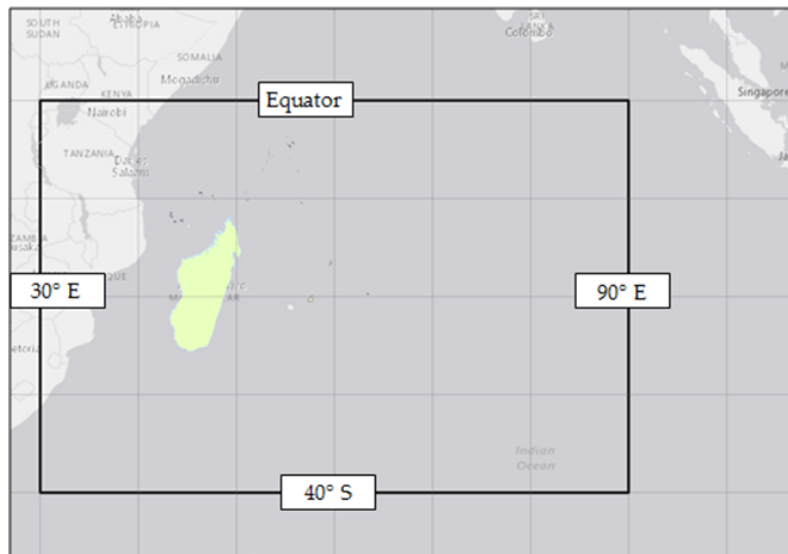


Figure 1: Domain of the AIR Tropical Cyclone Model for the Southwest Indian Ocean Basin

The historical record of tropical cyclones in the SWIO region, which is based on information from local meteorological agencies (e.g., RSMC La Reunion, Australian Bureau of Meteorology (BoM), Joint Typhoon Warning Center (JTWC)) includes 847 events that took place between the years 1950 and 2014 (Figure 2). Parametric statistics derived from the historical catalog, such as annual frequency, landfall frequency, seasonality, genesis location, forward speed, central pressure, and radius of maximum winds, serve as the basis for the stochastic catalog. Distributions and auto-regressive models are calibrated using these parameters and subsequently numerically sampled using Monte Carlo techniques to develop a catalog of simulated events that is statistically consistent with the historical record of events. For example, Figure 3 and Figure 4 present comparisons between the historical and stochastically generated probabilities of storm counts in the SWIO basin and the seasonality of storms throughout the year, respectively. A detailed discussion of these parameters, model distributions, and the validation of each parameter is provided in Appendix A.

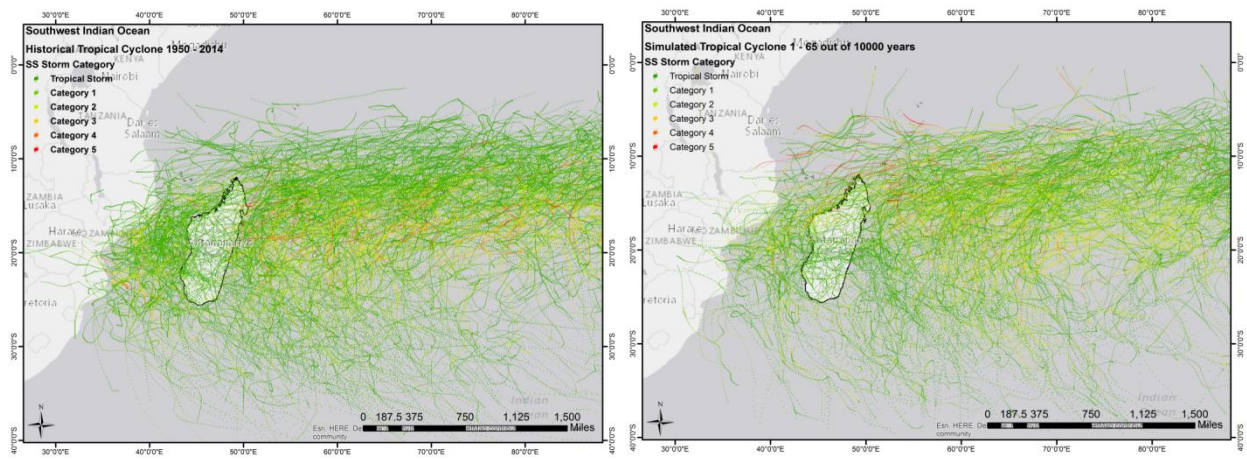


Figure 2: Storm tracks by Saffir-Simpson category for the 65 year historical record (left) and a randomly selected 65 year period in the stochastic catalog (right)

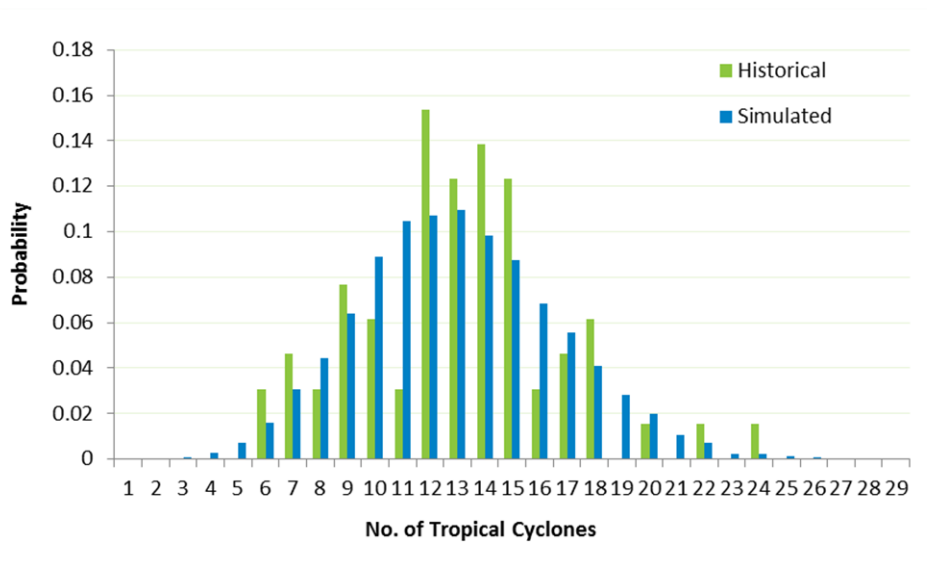


Figure 3: Comparison of Historical and Simulated Annual Count Probabilities for Tropical Cyclones in the Model Domain

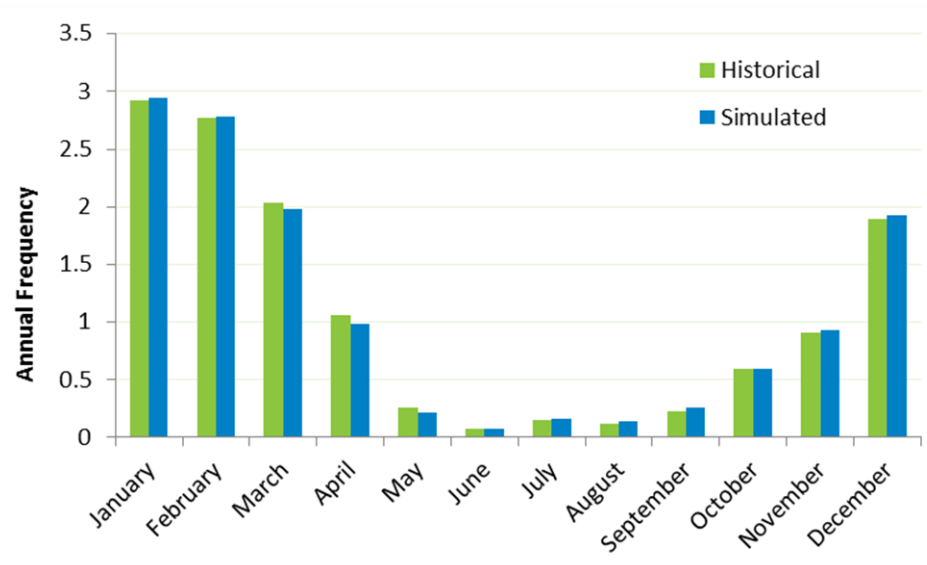


Figure 4: Comparison of Historical and Simulated Seasonal Frequency at Genesis for Tropical Cyclones in the Model Domain

2.1.1 Wind

High wind speeds, which are inversely related to the central pressure (Cp) of a storm, are a key contributor to damage from tropical cyclones. The Southwest Indian Ocean has some of warmest sea surface temperatures anywhere and has unique environmental pressure and storm size characteristics compared to other basins.



Among other parameters, it is particularly important to use a region-specific C_p -wind relationship to model the maximum wind speeds caused by storms in the SWIO region. The wind field intensity model employed in the SWIO model involves first computing the gradient wind as a function of central pressure and peripheral pressure. A gradient wind profile is then calculated, based on the work of Willoughby et al. (2006), and reduced to the surface via a gradient wind reduction factor. Additional storm factors, such as asymmetry and directionality, and topographical effects, such as surface friction and gust factors, are then applied to the wind profile in order to generate a realistic wind footprint for each increment along the path of a storm. The technical details of the SWIO wind intensity module are provided in Appendix A.

To validate the wind hazard calculation, modeled wind speeds are compared with weather station observations provided by local agencies (e.g., Direction Générale de la Météorologie (MDG), Mauritius Meteorological Services) or ancillary global agencies (e.g., NASA, NOAA). When available, return period wind speeds are also compared to hazard maps produced by government agencies for disaster risk management (DRM) or planning (DRP) purposes or for local building codes. Accurate wind speed weather station measurements during tropical cyclone conditions are often challenging to obtain due to power or instrument failure. In the SWIO region, wind speed recordings are both sparse and, when available, often report inconsistent or unrealistic wind speeds, when compared to global agencies. Tropical cyclone wind speeds were compared for Mauritius and Madagascar using local agency data and NOAA Global Summary of Day (GSOD) readings from automated weather stations. The comparison between modeled and recorded wind speeds is presented in Figure 5, which indicates that, despite significant spatial variability, there is reasonable correlation between modeled and measured wind speeds. A comparison between modeled and reported wind speeds is also illustrated in Figure 6 for tropical cyclone Hollanda (1994) in Mauritius and tropical cyclone Giovanna (2012) in Madagascar. Reliable wind speed data for each country is expected to improve the calibration of the wind model.

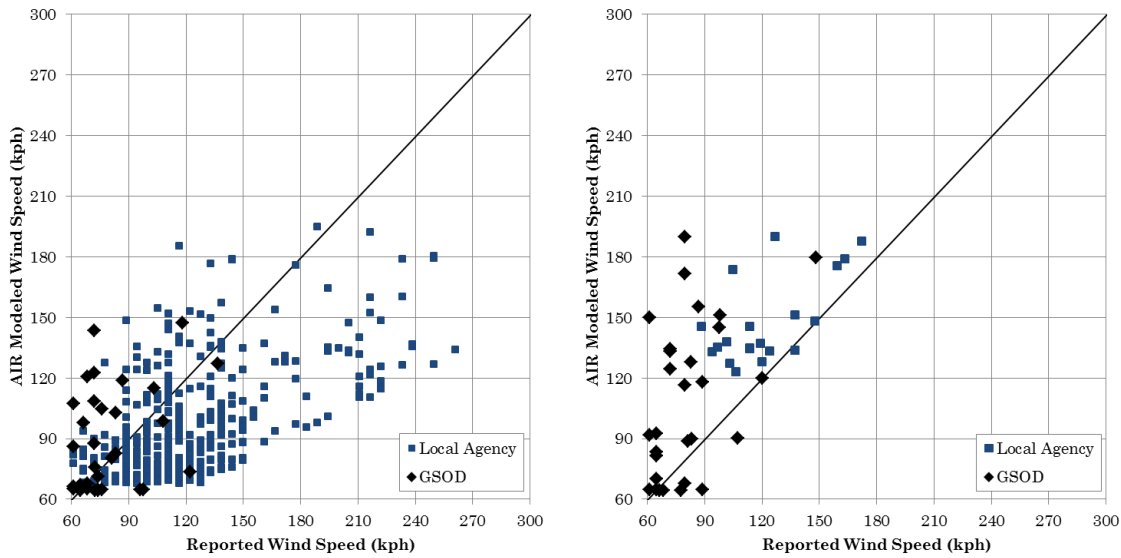


Figure 5: Comparison of modeled and reported tropical cyclone wind speed (1-minute sustained at 10m) for Madagascar (left) and Mauritius (right)

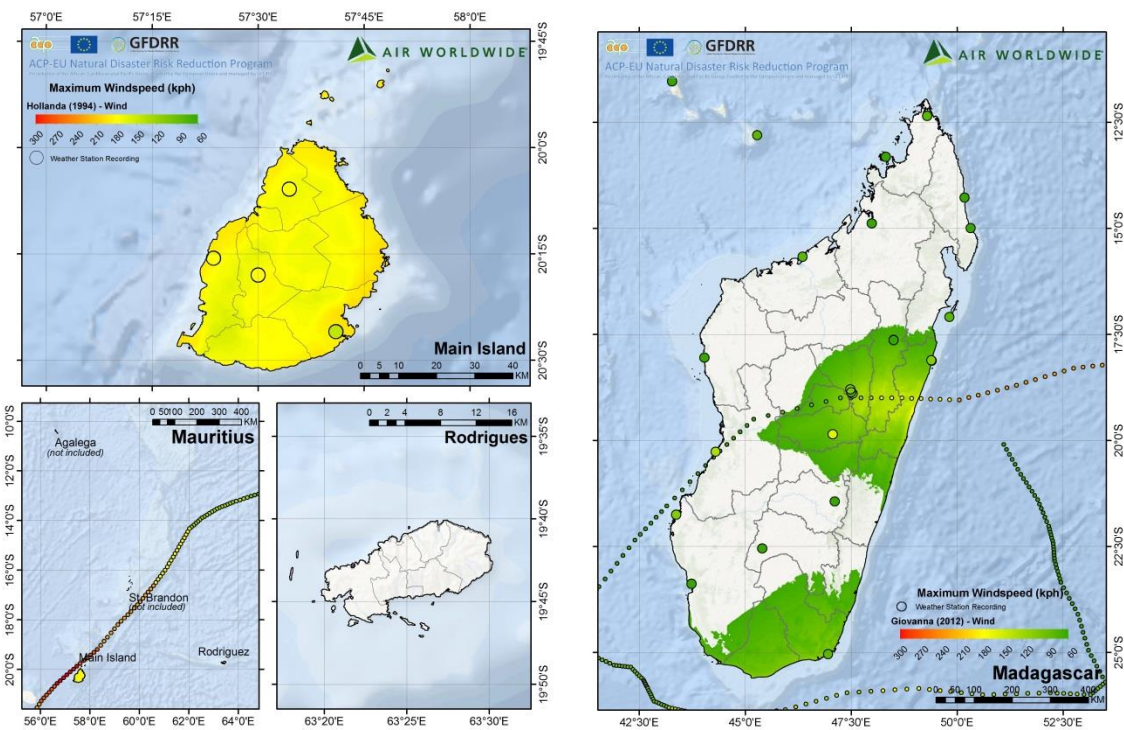


Figure 6: Comparison of modeled wind footprints with station recordings (1-minute sustained at 10m) for tropical cyclones Hollanda (Mauritius, 1994) and Giovanna (Madagascar, 2012)

2.1.2 Precipitation Hazard and Flooding

The precipitation flood component of the model relies on a parametric precipitation model that leverages high-quality precipitation data from tropical cyclones. One of the highest quality precipitation data sources is the Tropical Rainfall Measuring Mission (TRMM), which is conducted jointly by the National Aeronautics and Space Administration (NASA) and the Japan Aerospace Exploration Agency (JAXA). TRMM is available from 1998 through 2014 at a three-hourly time interval and $0.25^\circ \times 0.25^\circ$ resolution. TRMM data is extensively validated and widely used, making it ideal for developing and calibrating a parametric precipitation model.

The parametric precipitation model has two key parameters: the maximum precipitation rate (P_{max}) and outer radius of precipitation (R_{outer}). P_{max} is the average precipitation rate (i.e., mm/hr) and R_{outer} is the maximum distance from the center of the storm where the average precipitation rate is ≥ 1 mm/hr. P_{max} and R_{outer} are derived from TRMM data collected within the basin domain and modeled using normal and Weibull distributions, respectively.

While the precipitation module identifies where rain is likely to fall—which helps to identify where flood risk exists—a separate module is used to determine the spatial distribution of runoff and maximum flood depth. Precipitation-induced flooding is modeled dynamically, based on the two-dimensional rainfall runoff CASC2D-SED (CASCade 2 Dimensional SEDiment) model developed at Colorado State University (Rojas et al., 2003). The maximum flood depth is calculated based on hourly precipitation routed through the model. The required input data for this model are elevation, soil and a land/sea mask. This model is based on the shallow water equations (i.e., Saint Venant equations) derived from conservation of mass, energy, and momentum. Shallow water equations are generally appropriate for modeling runoff or pluvial flooding, where the horizontal length scale is much greater than the vertical.

Validating the precipitation and flooding models requires reliable spatial and temporal recording of rainfall and flood depths during tropical cyclone events. As noted for the wind peril, weather stations often fail under tropical cyclone conditions due to power loss or other equipment malfunction. For precipitation, the additional issue of wind driven rain can lead to large discrepancies between actual and gauge-measured precipitation. Lastly, precipitation patterns are highly uncertain, particularly with respect to tropical cyclone tracks, thus a parametric model is not expected to completely capture the full extent of tropical cyclone induced rainfall. As no reliable historical flood measurements were available during the course of this investigation, the precipitation model has been validated against TRMM satellite data and GSOD station measurements. Comparisons between modeled and measured cumulative precipitation for several tropical cyclone events are shown in Figure 7. As expected, the model performs well relative to TRMM, which was used for initial model calibration, however the model also performs well when compared to GSOD station precipitation measurements, which provides an independent evaluation. This comparison is further illustrated in Figure 8 for tropical cyclone Giovanna (2012) in Madagascar, where TRMM and GSOD weather station measurements compare favorably with the modeled precipitation footprint.

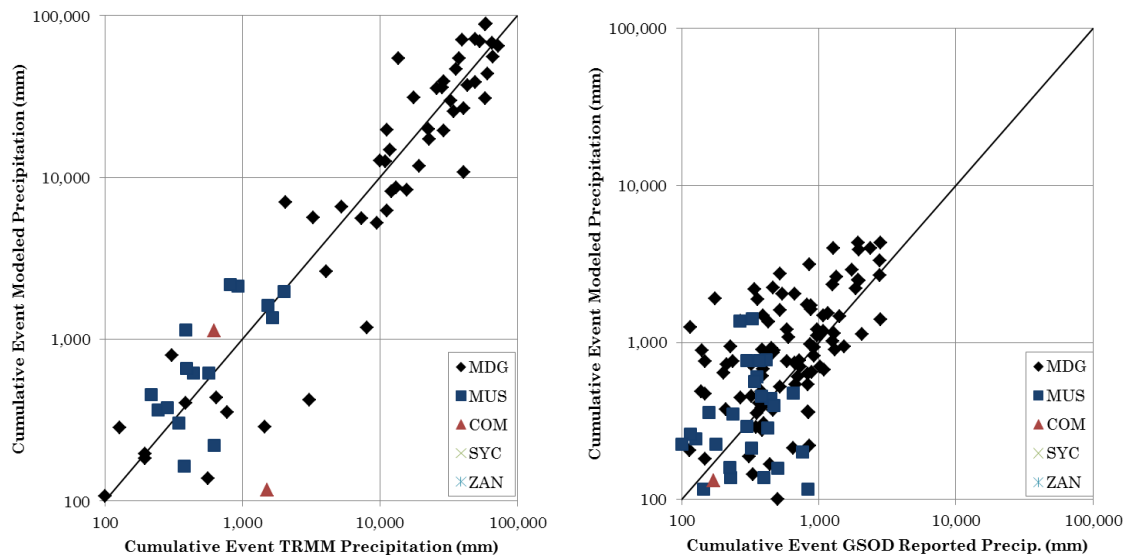


Figure 7: Comparison of cumulative TRMM and modeled precipitation for tropical cyclones between 1998 and 2014 (left). Comparison of GSOD rain gauge measurements and modeled precipitation for tropical cyclones between 1979 and 2015 (right).

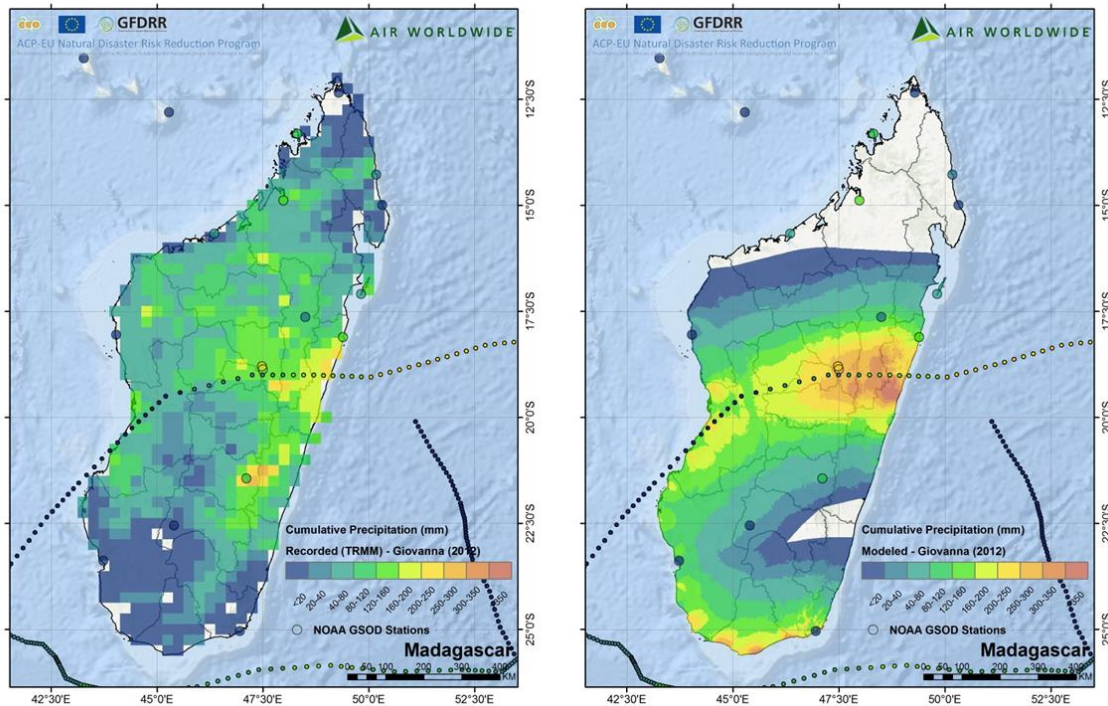


Figure 8: Precipitation footprint for tropical cyclone Giovanna (2012) based on TRMM (left) and AIR modeled (right)

2.1.3 Storm Surge Flooding

Tropical cyclone-induced surge is an abnormal rise in sea level accompanying intense storms. During intense storms, the wind circulation around the eye of the storm blows against the ocean surface and produces vertical circulation in the ocean. As the storm moves towards the coast, the ocean becomes shallower, and, as a result, the vertical circulation of ocean water is pushed inland. The surge height is the difference between the observed level of the sea surface and the level that would have occurred in the absence of the storm (i.e., mean sea level). Daily tidal fluctuations are not considered in the storm surge calculation.

The storm surge model adopted in this study is based on a parametric model proposed by Young (1998, 2007). The storm surge model relies on the primary meteorological variables of a tropical cyclone, including central pressure (C_p), forward wind speed (V_{fm}), maximum wind velocity (V_{max}), and radius of maximum wind (R_{max}). The modeled storm surge height is generally more sensitive to changes in the meteorological variables of V_{fm} and V_{max} than to C_p . Other quantities that are considered are the wind profile, the location of the site with respect to the storm track, angle of approach to the coast, and the elevation. Using Young's approach, the model first computes a significant wave height (H_s), which is defined as the average wave height of the highest third of the waves. For a given storm, the spatially distributed storm surge footprint can be estimated using V_{max} , V_{fm} , and the computed H_s . The spatial distribution of H_s incorporates the effects of water depth by applying techniques developed by Liu (1996). Similar to the wind field, the profile of the storm surge field is not symmetrical around the storm track. The highest surge usually occurs near the radius of maximum winds, or where the strongest winds occur. Since wind direction is approximately parallel to the storm direction, in the Southern Hemisphere, the surge will be higher to the left of the tropical cyclone track than to the right, while the opposite holds for storm surge in the Northern Hemisphere. An example of the modeled storm surge inundation footprint for tropical cyclones Giovanna (2012) and Hellen (2014) in Madagascar is presented in Figure 9.

Since measured storm surge values are not available in the SWIO region, validation is instead performed by comparing the AIR model estimates with the model estimates provided by the Global Disaster Alert and Coordinate System (GDACS). GDACS modeled results for three historical storms in Madagascar, Giovanna (2012), Haruna (2013), and Hellen (2014), are used for validation. Figure 10 shows the comparison between modeled storm surge heights between the GDACS and AIR models for the three historical storms. While the GDACS and AIR models apply different storm surge calculation methodologies, the estimated surge heights compare reasonably well despite some expected differences between the two models.

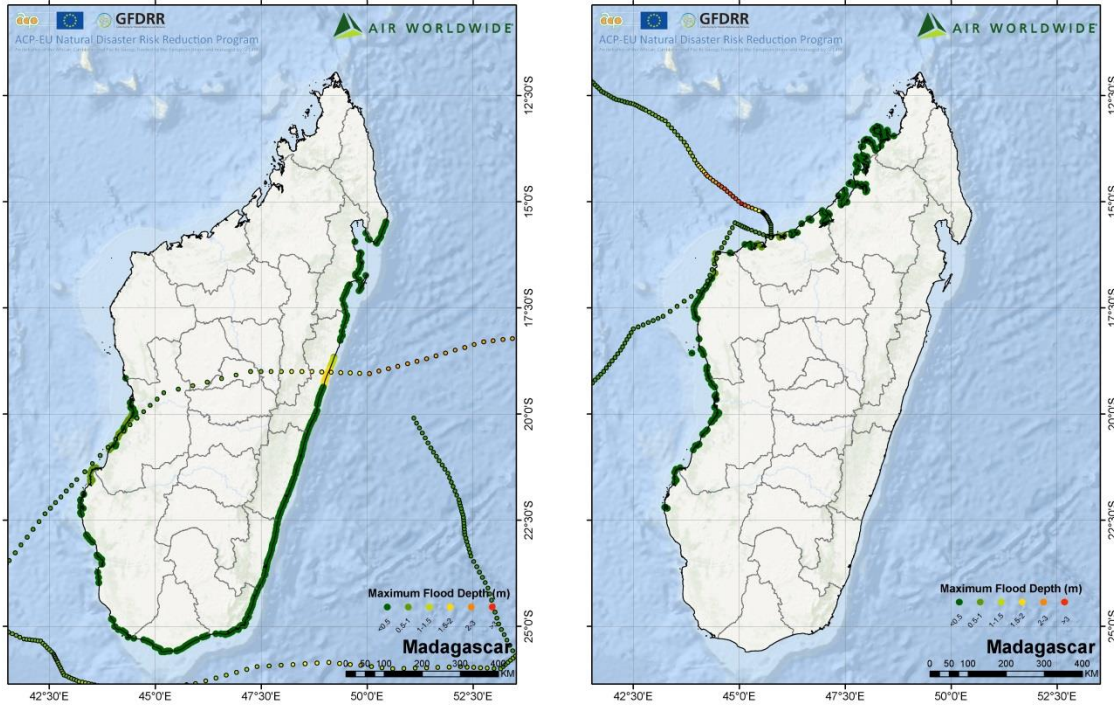


Figure 9: Modeled storm surge footprints for tropical cyclones Giovanna (2012, left) and Hellen (2014, right) in Madagascar

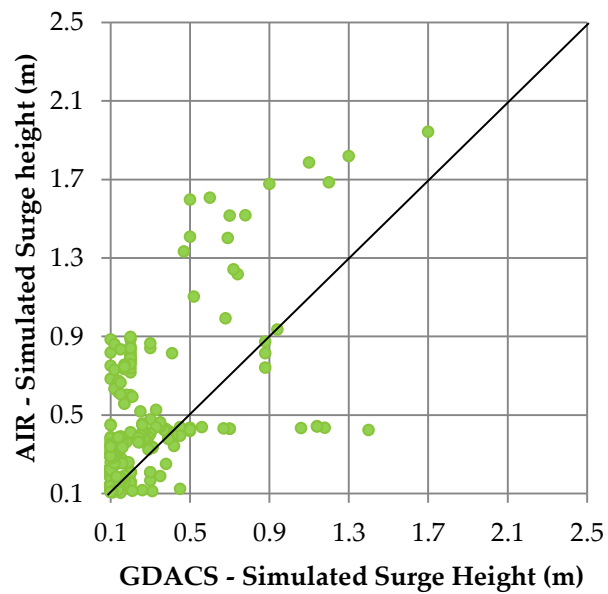


Figure 10: Comparison of Modeled Storm Surge Heights from GDACS and AIR models

2.1.4 Tropical Cyclone Consequence Summary

While the historical record includes nearly 850 tropical cyclone events, many of these storms are bypassing or cause little damage. Events are documented in the consequence database when they impact a population center or cause physical damage. These documented events are then further classified as “catastrophic” if they are reported with ≥10,000 people affected, at least \$10M USD in losses, or ≥10 deaths. The tropical cyclone consequence database contains information gathered from publically available sources about the impacts of 104 events, which constitutes approximately 82% of the reported catastrophic event entries for all tropical cyclone and non-tropical cyclone perils in the region. The distribution of total events and catastrophic events (demarcated with parentheses) are provided in Table 1. Between 1950 and 2015, Madagascar has the highest tropical cyclone event count at 59, of which 48 entries are considered catastrophic events. During this same time period, Mauritius, Comoros, and Seychelles experienced 19, 7, and 1 catastrophic event(s), respectively. Zanzibar does not have historical observations on the direct impact from tropical cyclones within the consequence database. Additional discussion on the impacts of historical tropical cyclones in the SWIO region is provided in Appendix B.

Table 1: Number of recorded tropical cyclone events for each SWIO island nation, by decade. Events considered to be “catastrophic” are provided in parentheses.

<i>Decade</i>	<i>Comoros</i>	<i>Madagascar</i>	<i>Mauritius</i>	<i>Seychelles</i>	<i>Zanzibar</i>
1950-1959	1 (1)	0 (0)	0 (0)	0 (0)	0 (0)
1960-1969	0 (0)	2 (2)	6 (3)	0 (0)	0 (0)
1970-1979	0 (0)	6 (6)	4 (3)	0 (0)	0 (0)
1980-1989	5 (4)	7 (6)	11 (6)	0 (0)	0 (0)
1990-1999	1 (1)	9 (8)	5 (3)	1 (0)	0 (0)
2000-2009	1 (0)	26 (17)	4 (3)	3 (1)	0 (0)
2010-2015	1 (1)	9 (9)	1 (1)	0 (0)	0 (0)
Total	9 (7)	59 (48)	31 (19)	4 (1)	0 (0)

2.2 Non-Tropical Cyclone Flooding

Regular precipitation, or non-tropical cyclone (NTC) rainfall, induced flood events are significant throughout the SWIO region. Characterizing NTC hazard is particularly important for characterizing the flooding risk in countries that are rarely subjected to tropical cyclones, such as Zanzibar, Comoros, and Seychelles. In order to generate a stochastic catalog of non-tropical cyclone rainfall, climatology of non-tropical cyclone rainfall must first be constructed. The same TRMM dataset used for the tropical cyclone precipitation model is also used to derive statistics regarding NTC precipitation. For NTC, TRMM measurements from the years of 1998 through 2013 are compared with the historical catalog of TC events and rainfall within a radius of 500km of the central track of each storm is removed from the NTC data. The selected exclusion zone of 500km is based on research

of the median outer radius of Indian Ocean basin tropical storms (Chavas and Emanuel, 2010) and, while a static measurement, compares favorably and prevents overlap with the median R_{outer} parameter used for the TC precipitation model (i.e., precipitation is not double-counted). An example of the resulting non-tropical cyclone dataset is provided in Figure 11, which illustrates the removal of rainfall caused by tropical cyclone Eline (2000) as it makes landfall in Madagascar.

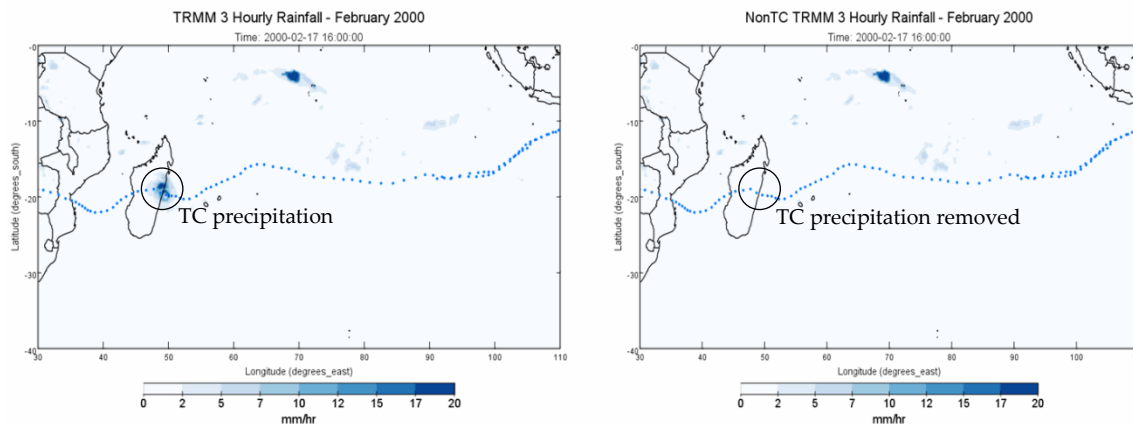


Figure 11: Illustration of results from NTC rainfall climatology construction: TRMM rainfall induced from Cyclone Eline (left) and the corresponding NTC rainfall (right)

A more comprehensive treatment of the climatology can be implemented using general circulation models and regional climate models as carried out by AIR for various other regions of the world; however, the project scope and timeline necessitated a scientifically sound but less complicated approach using a stochastic weather generator with input from TRMM data.

A stochastic catalog of daily NTC rainfall for 10,000 simulated independent years was developed based on the NTC rainfall climatology derived from the TRMM data discussed above. In general, stochastic weather generators use the statistics of weather station rainfall to construct synthetic, but physically meaningful, time-series of rainfall at a site that preserves the basic statistics of the station. In the present investigation, a stochastic weather generator (WGEN) is employed to construct synthetic precipitation data for each country in the SWIO region. WGEN uses a first-order Markov chain with two states, wet or dry, to determine the occurrence of precipitation, and a two-parameter gamma distribution to model the precipitation amount in a day. WGEN has been widely used in various studies in different climatic conditions and has repeatedly been found to have excellent success in replicating the climatic rainfall statistics. WGEN does not consider spatial correlation, therefore the appropriate selection of weather generation “stations” is critical for generating realistic rainfall patterns. For each country, the selection of a “station” is accomplished by identifying the TRMM grid location that best matches (i.e., minimizes the error) the average accumulated TRMM precipitation for all grid points in an independent precipitation zone. With the exception of Madagascar, the island nations in the SWIO region are small relative to the resolution of the TRMM data and only have one precipitation zone;

therefore Comoros, Mauritius, Seychelles, and Zanzibar are assigned a single precipitation generation point per country that represents the average precipitation statistics of the entire island nation. While this methodology does not consider micro-climates within individual islands, it has been successfully applied in other regions with small islands (e.g., Philippines) and demonstrated to adequately simulate regional weather patterns. Figure 12 illustrates the selection of the WGEN point in Comoros, which minimizes the error between the station precipitation and the average TRMM precipitation for all points in the Comoros.

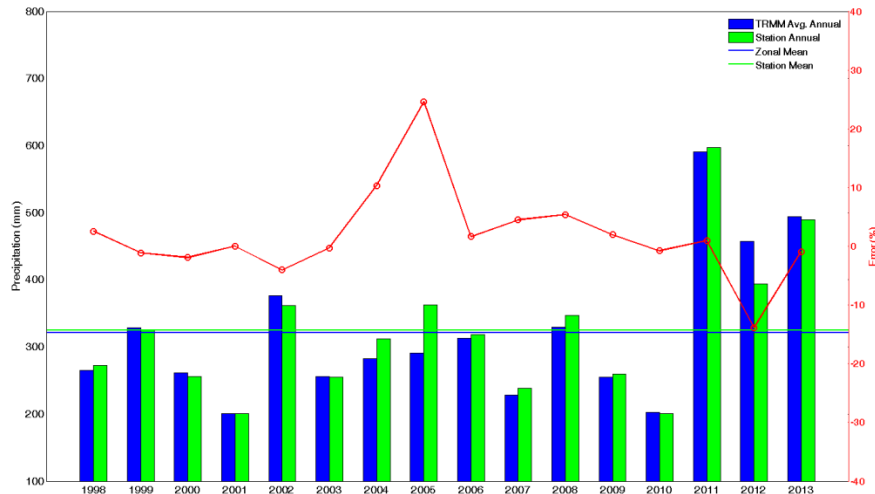


Figure 12: Comparison of historical average annual TRMM precipitation with the selected TRMM grid point for Comoros. Blue bars show the average annual precipitation across all years (1998-2013) and green bars shows the selected TRMM station. The red line shows the error percentage for each year.

A flooding event caused by NTC precipitation is not only a function of daily cumulative precipitation, but also of the duration of rainfall and both natural (e.g., infiltration, run-off) and manmade (e.g., dams, channels) flood mitigation measures. Therefore, in addition to daily precipitation a unique event definition is calibrated for each country using past reports of significant NTC flooding and subsequently applied to determine whether a spatiotemporal precipitation pattern is likely to cause flooding. In the present investigation, a “7-5-days clause” is introduced to determine the occurrence of an NTC precipitation event — a seven-day minimum total rainfall threshold and a five-day inter-storm period. For brevity, the NTC modeling methodology and event definitions are elaborated further in Appendix A

TC and NTC precipitation-induced flooding are modeled using the CASC2D-SED methodology overviewed previously and discussed in detail in Appendix A. For NTC, event precipitation is assumed to fall uniformly over the entire independent precipitation region for the duration of the event. The CASC2D model then dynamically distributes the precipitation throughout the affected region and calculates flood depths.

2.2.1 Non-Tropical Cyclone Flooding Consequence Summary

The non-tropical cyclone flood consequence database contains information gathered from publically available sources about the impacts of 67 events. The distribution of total events and catastrophic events (demarcated with parentheses) are provided in Table 2. Between 1970 and 2015, Mauritius and Seychelles have the highest non-tropical cyclone flooding event count at 20 and 22, respectively, of which 9 entries in Mauritius and 1 entry in Seychelles are considered catastrophic events. During this same time period, Madagascar, Comoros, and Zanzibar experienced 9, 2, and 2 catastrophic event(s), respectively. Additional discussion on the impacts of historical non-tropical cyclones in the SWIO region is provided in Appendix B.

Table 2: Number of recorded non-tropical cyclone flooding events for each SWIO island nation, by decade. Events considered to be “catastrophic” are provided in parentheses.

<i>Timespan</i>	<i>Comoros</i>	<i>Madagascar</i>	<i>Mauritius</i>	<i>Seychelles</i>	<i>Zanzibar</i>
1970-1979	1 (0)	0 (0)	0 (0)	0 (0)	0 (0)
1980-1989	1 (1)	1 (1)	0 (0)	0 (0)	0 (0)
1990-1999	0 (0)	1 (1)	3 (0)	2 (0)	0 (0)
2000-2009	3 (0)	10 (5)	11 (2)	14 (0)	2 (1)
2010-2015	2 (1)	2 (2)	6 (2)	6 (1)	2 (1)
Total	7 (2)	14 (9)	20 (4)	22 (1)	4 (2)

2.3 Earthquake

Earthquakes (EQ) represent a frequent natural catastrophe in the SWIO region, but the major seismic sources in the region are remote from any of the island nations in the region. As a consequence, no or low historical economic losses and casualties have been reported in the five nations considered in this study, of which Comoros, Madagascar and Zanzibar are the riskiest. In terms of earthquake formation, the Southwest Indian Ocean region is located between two highly seismic active zones, namely the Mid-Indian ridge and the East-African rift system, which separate the Somalian tectonic plate of the Nubian and Indian plates. Earthquakes in this region are frequent but usually of low to moderate magnitude. On average, 10 earthquakes of an average moment magnitude of ≥ 5.3 occur each year. Modeled frequency and historical data are analyzed in the geographical domain depicted in Figure 13.

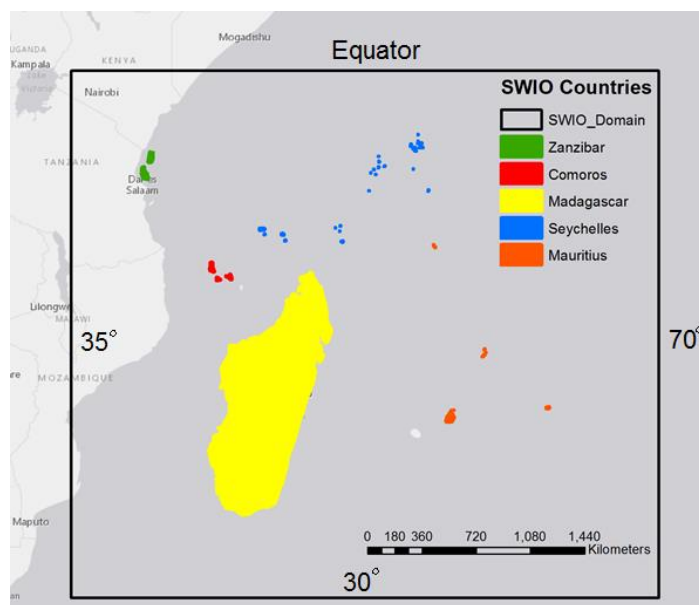


Figure 13. Domain of the AIR Earthquake Model for the Southwest Indian Ocean Region

The historical record of earthquakes in the SWIO region, which is based on information from various local and regional historical earthquake catalogs (e.g., Global Earthquake Magnitude (GEM) Historical Earthquake Catalogue, International Seismic Centre (ISC) EHB Bulletin, Incorporated Research Institutions for Seismology (IRIS) Earthquake Catalog, United States Geological Survey (USGS)), includes 1,228 events of moment magnitude 5 or greater that occurred between the years 1901 and 2014 (Figure 14). Parametric statistics derived from the historical catalog, such as magnitude-frequency and depth distributions, as well as slip rates and geometries of known faults in the region serve as the basis for the stochastic catalog. A combination of the parameter distributions and fault geometry for known crustal faults are the inputs for the Monte Carlo simulation techniques used to develop a catalog of simulated events that is statistically consistent with the historical record of events. For example, Figure 14 presents a comparison between the historical catalog (left) and 114 randomly selected years of stochastically generated earthquake events (right), respectively. In addition, Figure 15 compares the historic and stochastic earthquake frequency-magnitude and depth distributions in the SWIO region, which provides a reasonable parametric validation of the stochastic event generation results. A detailed discussion of these parameters, model distributions, and the validation of each parameter is provided in Appendix A.

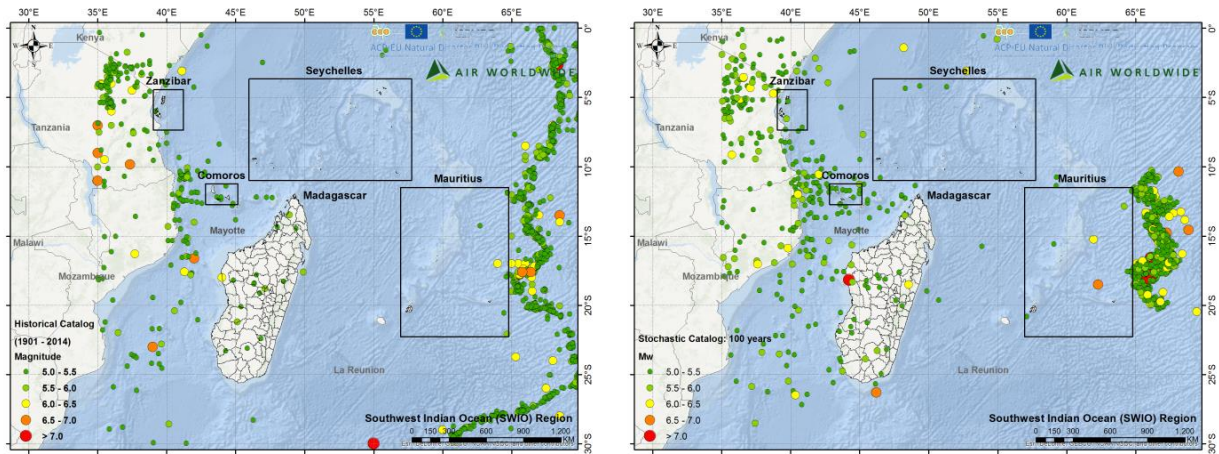


Figure 14. Historical (left) vs. Stochastic (right) 114 year Catalogs of Earthquake Events¹

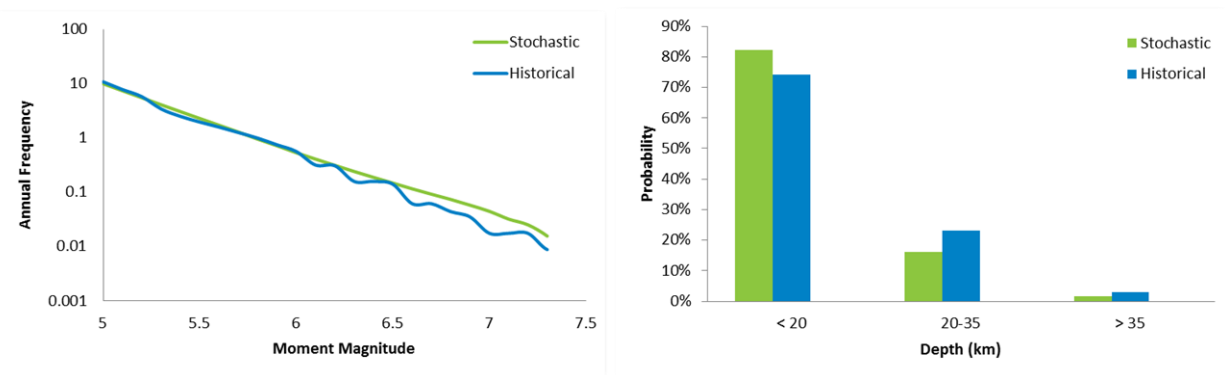


Figure 15. Modeled vs. Historical Frequency-Magnitude Distributions in the Southwest Indian Ocean (left) and Modeled vs. Historical Depth Distributions in the Southwest Indian Ocean (right)

2.3.1 Ground Shaking

The ground motion intensity that an earthquake generate in a region depends on the location of the rupture with respect to the site, the dynamic characteristics of the rupture, the traveling path of the waves from the source to the site, and the soil conditions at the site. The standard methodology for estimating ground motion intensities is predicated on empirical data extracted from recordings of past earthquakes with similar characteristics and supplemented by analytical simulations where data is scarce (e.g., ground motion generated by large earthquakes at short distance from the rupture). Unlike in the Western United States or Japan, where recordings from past earthquakes are plentiful, ground motion time histories are very rare in the SWIO region.

¹ The Mid-Indian ridge is only partially modeled (e.g., Zone 26) due to its remoteness relative to populated islands, resulting in the discrepancy between the historical and simulated event distributions on the right-hand side of each image

Therefore, the ground motions in the SWIO earthquake model are calculated under the generally tenable assumption that the attenuation of seismic waves in different regions of the world with the same tectonic setting is very similar. In the absence of regional data, the present investigation leverages ground motion prediction equations (GMPEs) developed using data from other parts of the world.. Additional information about GMPEs and details of the ground motion intensity module used in the SWIO hazard model are provided in Appendix A. Two intensity measures are used in the SWIO region to characterize the severity of earthquake ground shaking at a specified location, namely the peak ground acceleration (PGA) and the Modified Mercalli Intensity (MMI). PGA is the maximum absolute acceleration recorded during an earthquake at a location. MMI on the other hand is the perceived severity of an earthquake and is based on human judgement and the observed post-event damage. Well-known relationships are available for translating between PGA and MMI.

The SWIO region has minimal strong motion data resulting from the low seismicity and scarcity of instrumentation in the region, therefore the validation of the ground motion intensity calculation is performed by comparing to other agency’s modeled intensities in the region, such as those reported by the United States Geological Survey (USGS). Due to the low historical seismicity in the SWIO region, there are similarly few modeled intensities, which further complicates model validation. Thus, intensity validation is performed for the few significant events for which the USGS has also modeled regional intensities. This comparison is illustrated for one event in Figure 16, which contrasts the modeled ground motion intensity calculated by the AIR (left) and the USGS (right) models for the 1991 earthquakes in Madagascar. The ground-motion intensity shown is expressed as the peak ground acceleration (PGA) and validates well in terms of both intensity and spatial distribution.

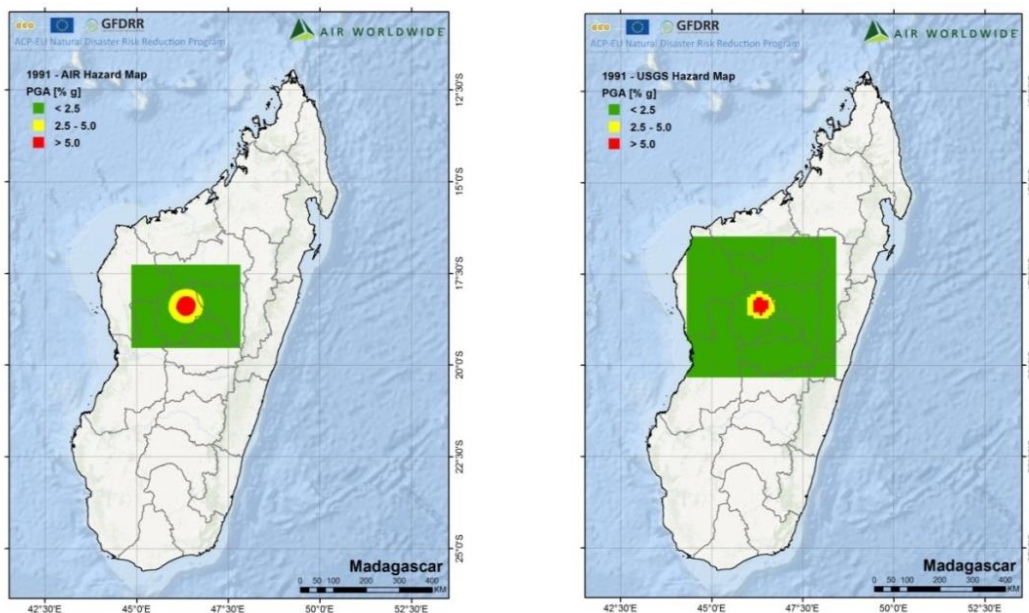


Figure 16. AIR (left) vs. USGS (right) Modeled Ground Motion, the 1991 Madagascar Earthquake

2.3.2 Tsunami

There have been no recorded instances of large tsunamis resulting from earthquakes in the SWIO region. This is because tsunamis are usually the result of high-magnitude subduction zone earthquakes, and the SWIO region does not experience many high magnitude earthquakes or contain any major subduction zones. However, the entire region is at risk of tsunamis generated by subduction zones elsewhere in the Indian Ocean, which are capable of traveling across the ocean (tele-tsunamis). Models of theoretical events from the AIR Southeast Asia Earthquake catalog were implemented in the ComMIT modeling platform, developed by NOAA, to produce “worst-case” tele-tsunami risk maps for each of the major SWIO islands. The tsunami risk maps do not show inundation depth or likelihood of tsunami inundation; they are instead intended to identify regions that are geographically susceptible to tele-tsunamis. Additional details of the tsunami modeling procedure are provided in Appendix A.

The only historical tele-tsunami event to affect the SWIO region in recent history was the 2004 Indian Ocean tsunami. Instrumentation in the region was not widespread at the time of this event, and many of the inundation measurements in the SWIO were inferred in damage surveys. The tsunami maps generated in this investigation were informed by recordings from this event, but also identify regions that could be at high risk from possible future events. For example, in Figure 17 additional tsunami-susceptible regions are identified in the comparison between the modeled inundation extents and those reported by the United Nations Development Program (UNDP) for the Seychelles island of Mahé following the 2004 event.

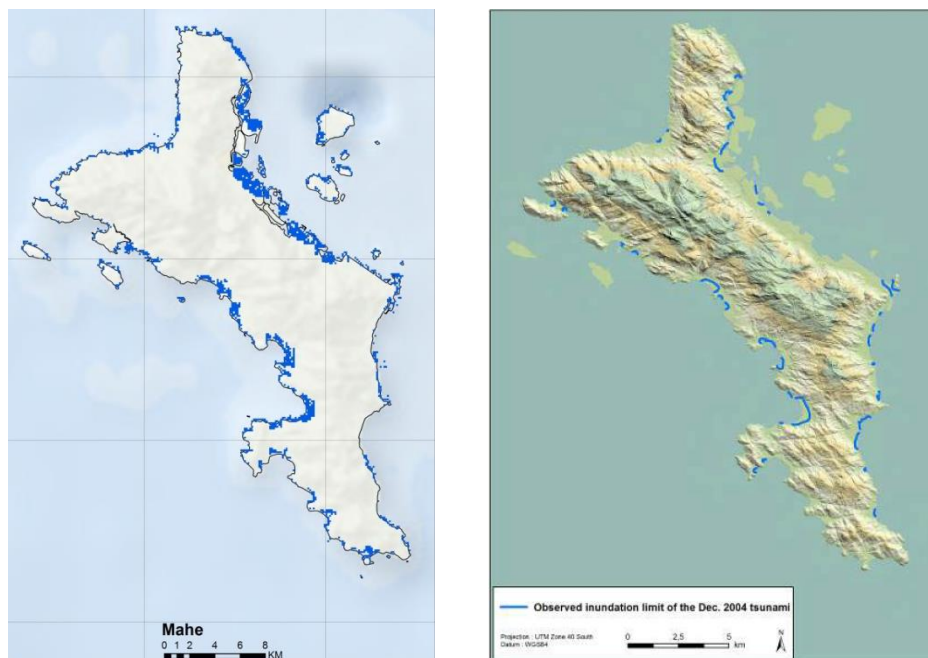


Figure 17: Comparison between the modeled Seychelles tsunami map (left) and 2004 tsunami inundation by UNDP (right) for the island of Mahé

2.3.3 Earthquake Consequence Summary

The earthquake and tsunami consequence database contains information gathered from publically available sources about the impacts of 22 events. The distribution of total events and catastrophic events (demarcated with parentheses) are provided in Table 3. Between 1883 and 2015, Comoros is the only country to experience significant ground shaking intensity, with minor events recorded in Madagascar and Mauritius. The most significant event to impact the SWIO region was the 2004 tsunami, which affected all 5 considered countries to some extent. As noted previously, the SWIO region has limited seismicity, which is reflected in the absence of significant earthquake related events in the consequence database. Additional discussion on the impacts of historical earthquakes and tsunamis in the SWIO region is provided in Appendix B.

Table 3: Number of significant earthquake events for each SWIO island nation, by decade. Events considered to be “catastrophic” are provided in parentheses.

<i>Decade</i>	<i>Comoros</i>	<i>Madagascar</i>	<i>Mauritius</i>	<i>Seychelles</i>	<i>Zanzibar</i>
Pre-1900	1 (0)	0 (0)	1 (0)	1 (0)	0 (0)
1900-1909	1 (1)	0 (0)	1 (0)	0 (0)	0 (0)
1910-1919	0 (0)	0 (0)	1 (0)	0 (0)	0 (0)
1920-1929	0 (0)	0 (0)	0 (0)	0 (0)	0 (0)
1930-1939	0 (0)	0 (0)	0 (0)	0 (0)	0 (0)
1940-1949	0 (0)	0 (0)	0 (0)	1 (0)	0 (0)
1950-1959	0 (0)	0 (0)	0 (0)	0 (0)	0 (0)
1960-1969	0 (0)	0 (0)	0 (0)	0 (0)	0 (0)
1970-1979	1 (1)	0 (0)	0 (0)	0 (0)	0 (0)
1980-1989	0 (0)	0 (0)	0 (0)	1 (0)	0 (0)
1991-1999	1 (0)	0 (0)	3 (0)	0 (0)	0 (0)
2000-2009	4 (2)	1 (0)	4 (0)	3 (1)	1 (0)
2010-2015	1 (0)	0 (0)	2 (0)	2 (0)	0 (0)
Total	9 (4)	1 (0)	12 (0)	8 (1)	1 (0)

2.4 Landslide (Comoros)

Per the ToR, landslide susceptibility has been analyzed for the island nation of Comoros and provided as a separate report (i.e., Component 3). As landslide constitutes a hazard, the previous analysis is summarized herein and the detailed technical documentation is provided in Appendix A for completeness. In the present investigation, landslide susceptibility zones for Comoros are developed by correlating landslide-inducing factors and areas where historical landslides have been recorded. In general, the basic causes of slope instability are well known from case-studies of specific failures. These landslide-inducing factors include geomorphological, hydraulic, hydrological, and anthropogenic characteristics.

The landslide susceptibility analysis method selected for the present investigation is the frequency ratio approach (Lepore et al. 2011). This method is preconditioned on historical landslide information, such as their

location, slope, and total landslide area. Each landslide-inducing factor in a historical landslide area is considered and is evaluated individually. Each factor is then reclassified into a series of bins (e.g., slope of ground surface into increments of 5° bins) as determined by engineering judgement.

The parameters used in the analysis are 1) slope aspect, 2) slope, 3) curvature, 4) elevation, 5) distance to roads, 6) land cover, 7) 500-year return period peak ground acceleration, 8) 100-year return period accumulated rainfall from tropical cyclone precipitation, and 9) 100-year return period flood depth from non-tropical cyclone precipitation. The resulting landslide hazard map for Comoros is presented in Figure 18 and captures >80% of historical landslides in the “high” and “medium” susceptibility zones.

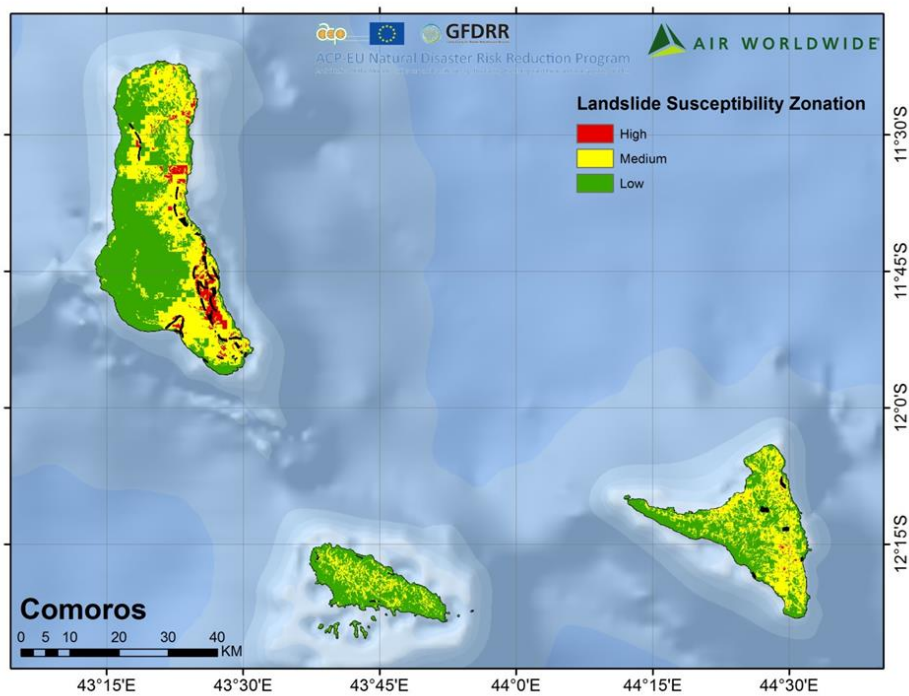


Figure 18: Landslide susceptibility zonation for Comoros by island with historical landslides shown in black (90 m x 90 m resolution)

2.5 Summary and Data Limitations

The previous sections provided a broad overview of each modeled peril for the SWIO RAFI project. Comprehensive model documentation for each model is also provided in Appendix A.

The SWIO hazard catalogs and intensity models have been developed for the purposes of a portfolio-based country-wide risk assessment to the natural hazards of tropical cyclones, earthquakes, and floods, with the specific intent to estimate economic losses from damage resulting from disaster events. The hazard models do not necessarily represent truth or fact of the actual regional hazards, but are rather an interpretation based on available data, statistical techniques, state-of-the-art catastrophe modeling methodologies, and engineering judgment.

Data limitations, in terms of its existence, accessibility, accuracy, and precision, significantly complicated the development of the SWIO hazard catalogs and intensity models. Several “data gaps” were identified during the development of these models and additional data in these categories is expected to be the most useful for improving the development of any future regional catastrophe models. The “data gaps” include:

- Meteorological data: Historical recordings for weather events, including both weather stations and regional weather data, are generally poor in the SWIO region. For example, historical recordings of tropical cyclones often omit critical parameters, such as central pressure or complete storm tracks, complicating the development of parametric statistics. Weather station data for wind and precipitation, when available, was found to be unreliable and oftentimes apparently in error, particularly when compared to reference data from international public agencies. Other impacts from meteorological events, such as recorded flood depths and storm surge inundation footprints, were not provided by local agencies and are unavailable from public sources. As a result, the model intensity validation performed for wind, precipitation, flood, and storm surge is largely anecdotal and relies heavily on the limited publically available datasets.
- Seismological data: Seismological data in the region is generally sparse and of poor quality. Event parameters for historical earthquake events and data on active geological faults, such as fault geometry, rupture mechanism, slip rate and characteristic magnitudes, were collected from various historical earthquake catalogs maintained by international public agencies and published research. Historical recordings, including shaking intensity recordings and GPS data for earthquake events are ostensibly absent in the SWIO region. As a result, the model intensity validation is a difficult process, and was based on the model intensity calculated by international agencies for a limited number of available historical events.
- Geological data: Particularly for the landslide assessment of Comoros, a more complete and precise inventory of historical landslide events (e.g., location, extent, date) is expected to improve the frequency ratio method results. Detailed geological maps, soil characterizations, or soil boring profiles are also expected to improve the results of this analysis.

- Storm surge: In order to develop a robust storm surge model, validating the modeled results with the measured data is critical. Presently, reliable measured storm surge values are unavailable in the SWIO region to validate the modeled results. Measured storm surge values across multiple locations would aid in identifying storm surge prone regions and assessing the impact of storm surge.
- Physical properties: The data used to calibrate the physical properties for each island (e.g., land-use, land-cover, soil type, etc...) provided by local agencies were variable between islands and, instead, consistent, global satellite-based datasets were used throughout the region. The use of this lower resolution data reduces the precision of the model, particularly for small islands that are often smaller than the resolution of the satellite based measurement.
- Event Impacts: The consequence database, which catalogs the reported impacts from all natural catastrophe events in the region, was limited to the events reported by local agencies and in the public record. Additionally, available information about the resultant damage and economic loss incurred following natural catastrophes is exceedingly limited in this region. The resolution of the database could be improved if data is separated by lower administrative regions, such as damaged houses or losses per province or municipality. While detailed information is available for selected historical events from the DesInventar database, certain statistics, such as the counts of damaged or destroyed houses, often appear low in comparison to reported countrywide impacts.

3 Hazard Profiles

Hazard intensity profiles are produced for tropical cyclone (TC) wind, TC precipitation flood, TC storm surge flood, non-tropical cyclone (NTC) precipitation flood, and earthquake (EQ) ground shaking for stochastic mean return periods of 25, 50, 100, 250, 500, and 1,000 years. The mean return period (MRP) provides only one average perspective of the hazard intensity for each peril and significant uncertainty exists at each MRP. The hazard profiles consist of the maximum modeled intensity at each respective recurrence interval on a 30-arc second (approximately 1km) resolution grid. Additionally, a non-probabilistic EQ tsunami inundation extent footprint is produced for all countries on a 3 arc-second grid (approximately 90m) and a landslide susceptibility layer is produced for Comoros only, also on a 3-arc second grid. Hazard intensity footprints for selected “marquee events” for the TC and EQ perils are also presented and discussed further in Appendix A and Appendix B.

The hazard intensity profiles presented in the following sections are intended to illustrate a single consistent (i.e., uniform scale) view of the data- and GIS shape-files provided in the digital addendum to this report. A high-resolution version of each map is also provided in the digital addendum. The sample hazard intensity maps presented herein correspond to the 100-year mean return period (equivalently the 1% annual exceedance probability) for each modeled peril. Additional views can be created using the provided data- and shape-files, according to the requirements of the end user. The hazard intensity measures provided for each peril, as required by the ToR, are listed in Table 4 below. Selected marquee historical events are summarized in Table 5.

The hazard intensity profiles are generated as intermediate model outputs and the results are intended for use within the context of a natural catastrophe risk assessment (i.e., Component 4). The hazard outputs are nonetheless useful for identifying regions of heightened risk or, in combination with building exposure footprints (i.e., Component 2), for performing spatial aggregations of value at risk.

Table 4: Provided hazard intensity measures and units for each data- and shape-file output

<i>Sub-Peril</i>	<i>Tropical Cyclone (TC)</i>	<i>Non-Tropical Cyclone (NTC)</i>	<i>Earthquake (EQ)</i>	<i>Landslide (LS)</i>
Wind (W)	1-min sustained (kph)*; 10-min sustained (kph); 3-sec gust (kph)	-	-	-
Precipitation Flood (F)	mm	mm	-	-
Storm Surge Flood (SS)	mm	-	-	-
Shake (S)	-	-	PGA, MMI	-
Tsunami (TS)	-	-	m [†]	-
Susceptibility Index (SI)	-	-	-	SI [°]

*1-min. sustained wind speeds are presented in the report, 10-min. sustained and 3-sec. gust are provided in the data files

[†]Inundation extent only, no associated flood depths are provided

[°]Susceptibility Index (SI) is unitless

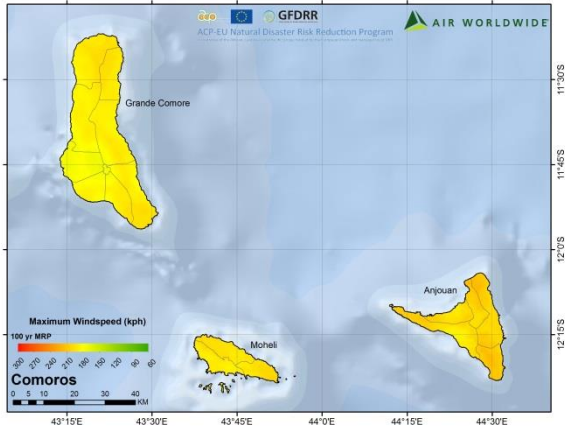


Table 5: Selected marquee historical events organized by peril

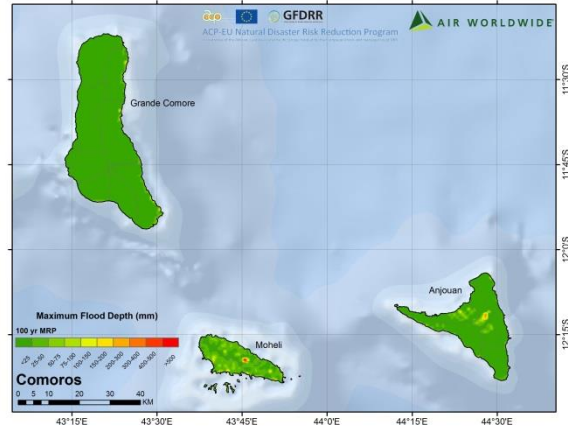
<i>Peril</i>	<i>Sub-Peril</i>	<i>Affected Country</i>	<i>Event Year</i>	<i>Event Name</i>	<i>AIR EventID</i>
TC	Wind, Flood, Storm Surge	Madagascar	1994	Geralda	590
TC	Wind, Flood, Storm Surge	Madagascar	2000	Eline	674
TC	Wind, Flood, Storm Surge	Madagascar	2004	Gafilo	729
TC	Wind, Flood, Storm Surge	Madagascar	2007	Indlala	763
TC	Wind, Flood, Storm Surge	Madagascar	2008	Ivan	775
TC	Wind, Flood, Storm Surge	Madagascar	2012	Giovanna	821
TC	Wind, Flood, Storm Surge	Madagascar	2013	Haruna	834
TC	Wind, Flood, Storm Surge	Madagascar	2014	Hellen	846
TC	Wind, Flood, Storm Surge	Mauritius	1989	Firinga	517
TC	Wind, Flood, Storm Surge	Mauritius	1994	Hollanda	591
TC	Wind, Flood, Storm Surge	Mauritius	1999	Davina	665
TC	Wind, Flood, Storm Surge	Mauritius	2002	Dina	697
EQ	Shake	Comoros	1985	M6.3	6858
EQ	Shake	Madagascar	1985	M5.5	7078
EQ	Shake	Madagascar	1991	M5.5	8783

3.1 Comoros

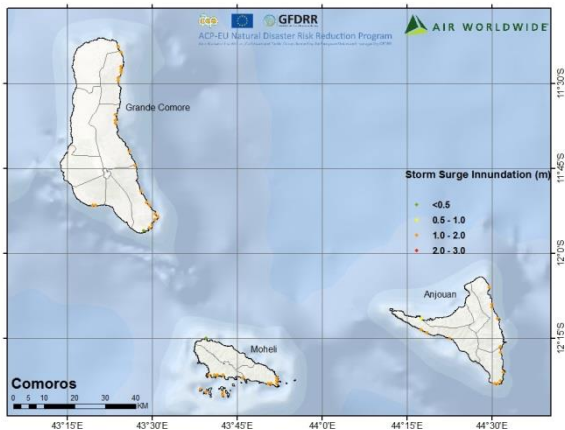
TC: Wind (100yr RP)



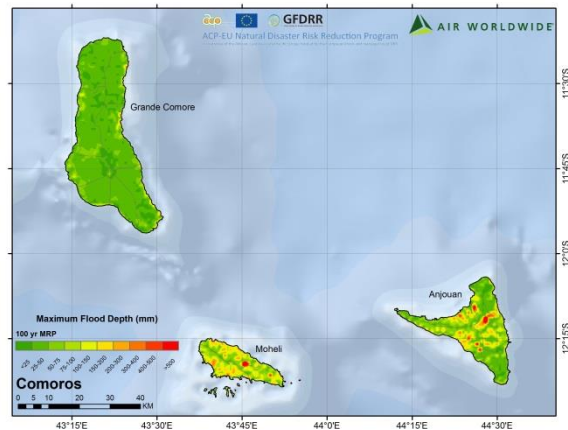
TC: Flooding (100yr RP)



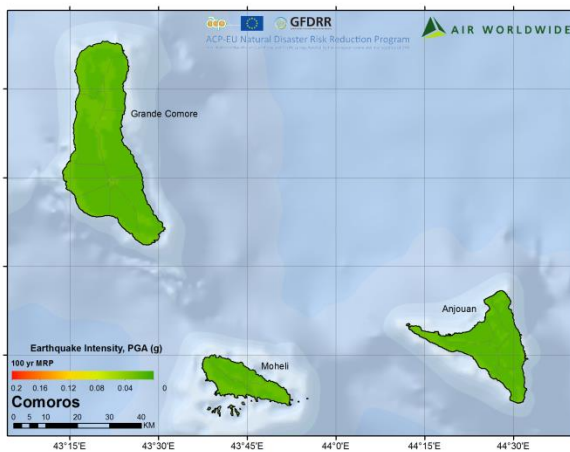
TC: Storm Surge (100yr RP)



NTC: Flood (100 yr RP)



EQ: Ground Shaking (100yr RP)

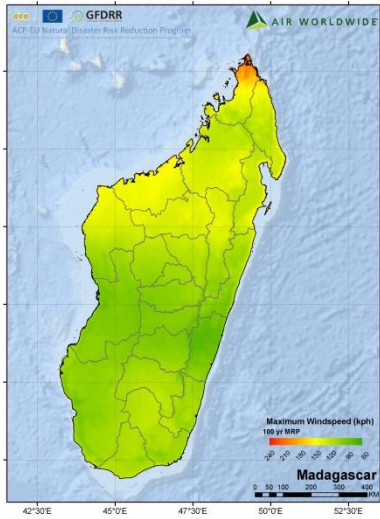


EQ: Tsunami Run-up

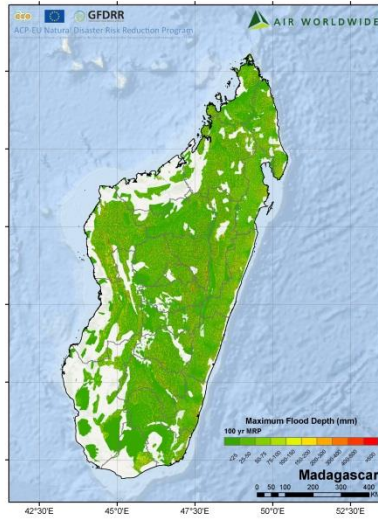


3.2 Madagascar

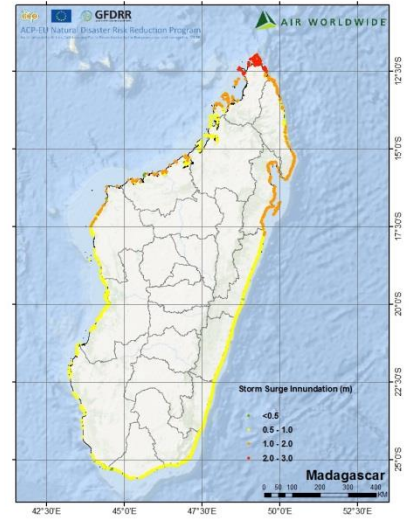
TC: Wind (100yr RP)



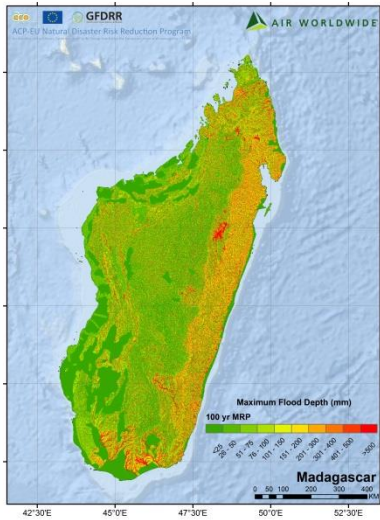
TC: Flooding (100yr RP)



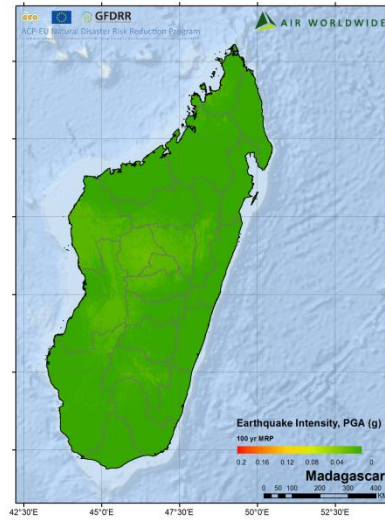
TC: Storm Surge (100yr RP)



NTC: Flood (100 yr RP)



EQ: Ground Shaking (100yr RP)

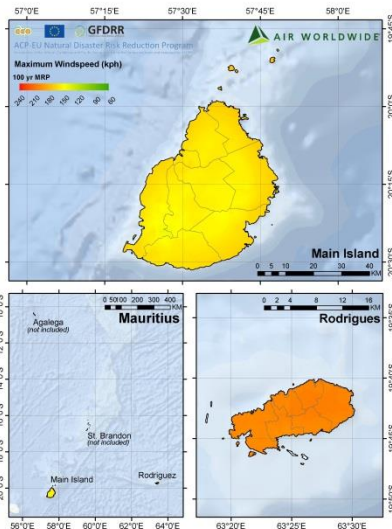


EQ: Tsunami Run-up

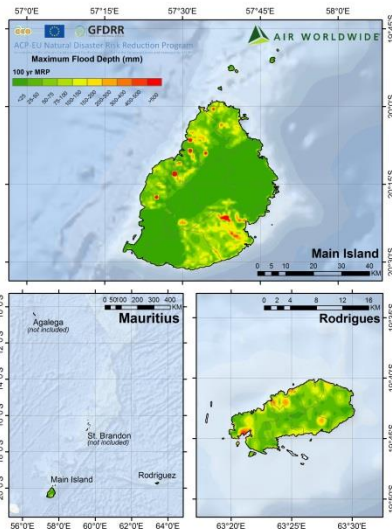


3.3 Mauritius

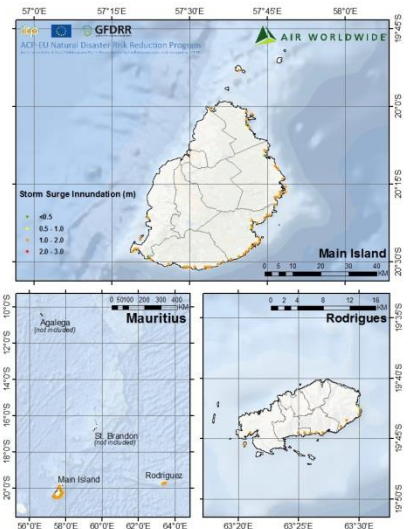
TC: Wind (100yr RP)



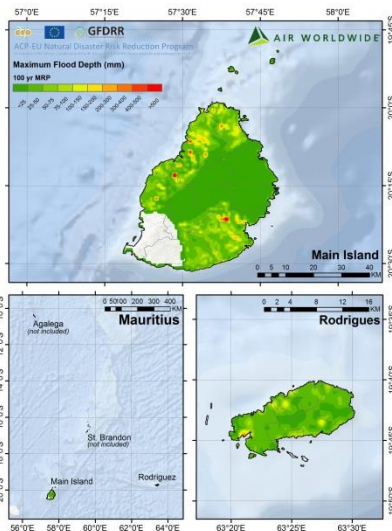
TC: Flooding (100yr RP)



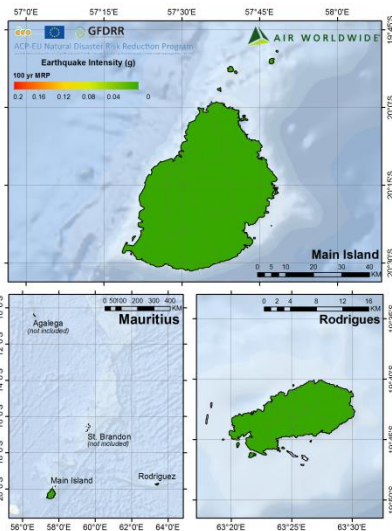
TC: Storm Surge (100yr RP)



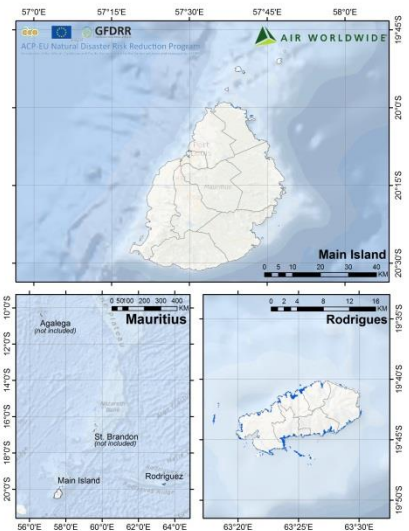
NTC: Flood (100 yr RP)



EQ: Ground Shaking (100yr RP)

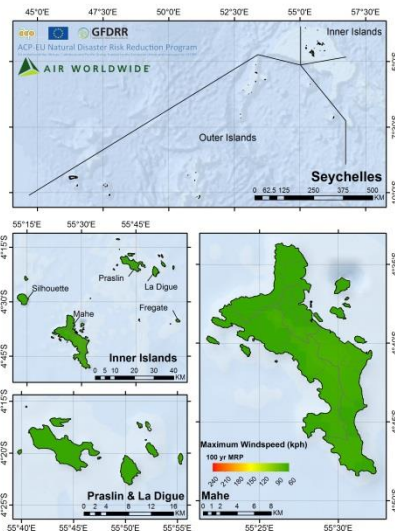


EQ: Tsunami Run-up

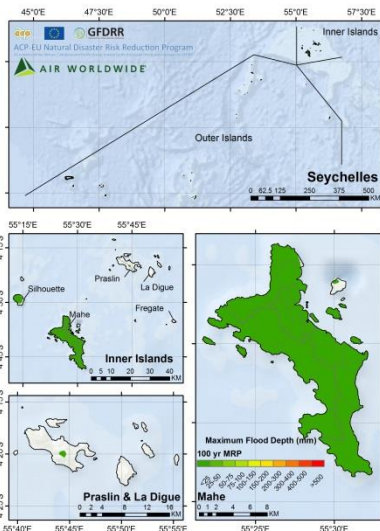


3.4 Seychelles

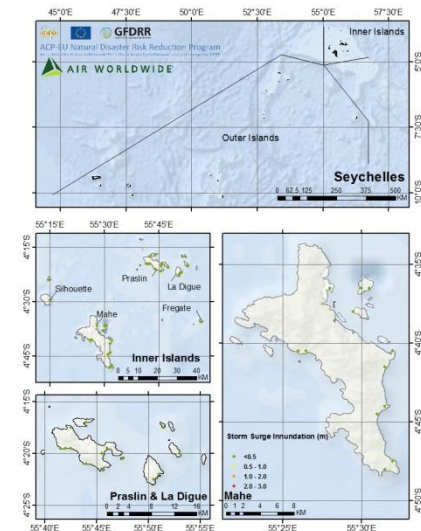
TC: Wind (100yr RP)



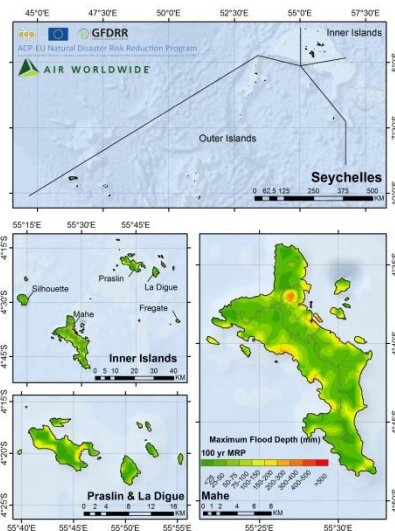
TC: Flooding (100yr RP)



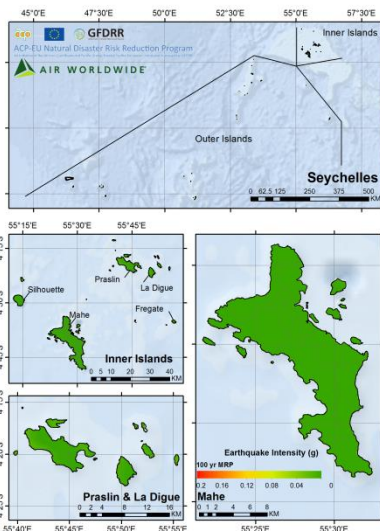
TC: Storm Surge (100yr RP)



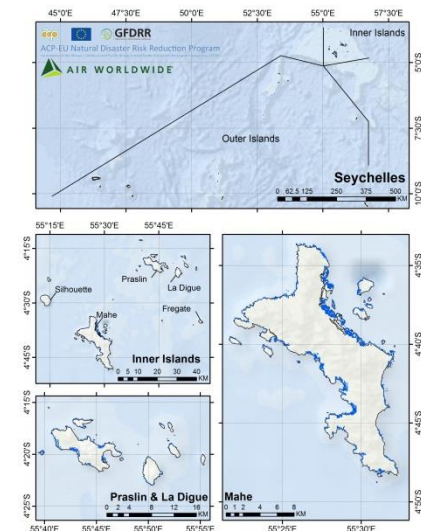
NTC: Flood (100 yr RP)



EQ: Ground Shaking (100yr RP)

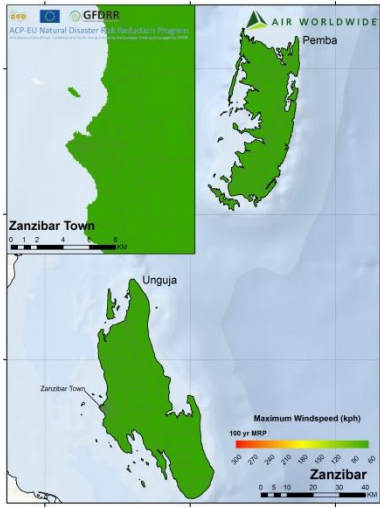


EQ: Tsunami Run-up

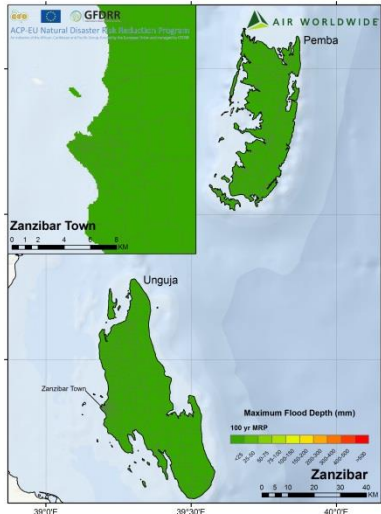


3.5 Zanzibar

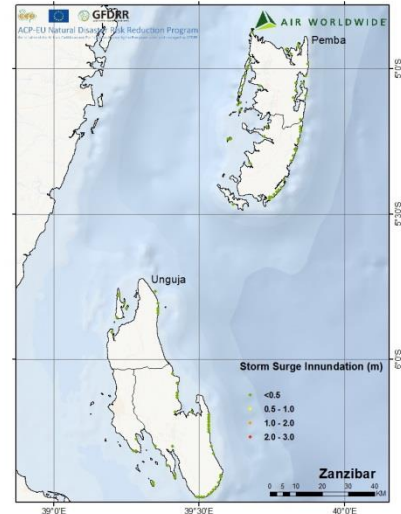
TC: Wind (100yr RP)



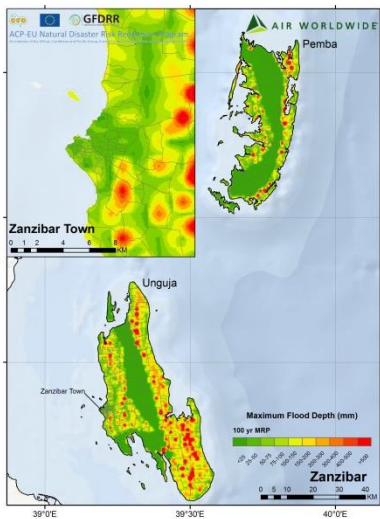
TC: Flooding (100yr RP)



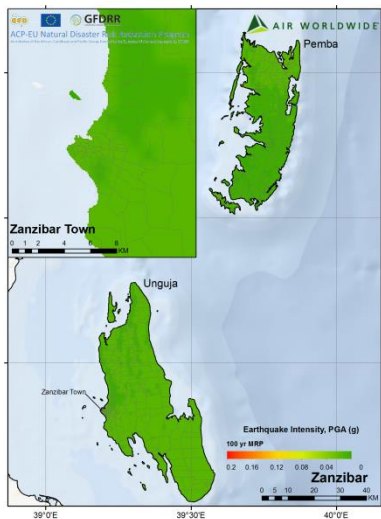
TC: Storm Surge (100yr RP)



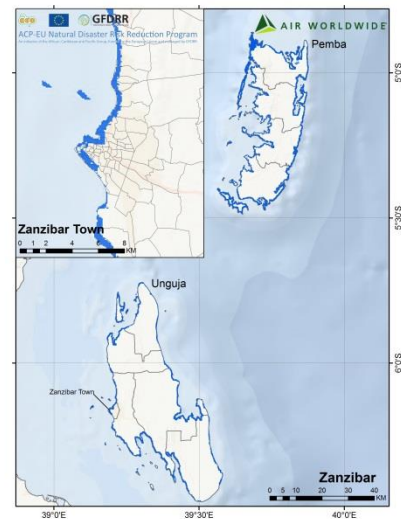
NTC: Flood (100 yr RP)



EQ: Ground Shaking (100yr RP)



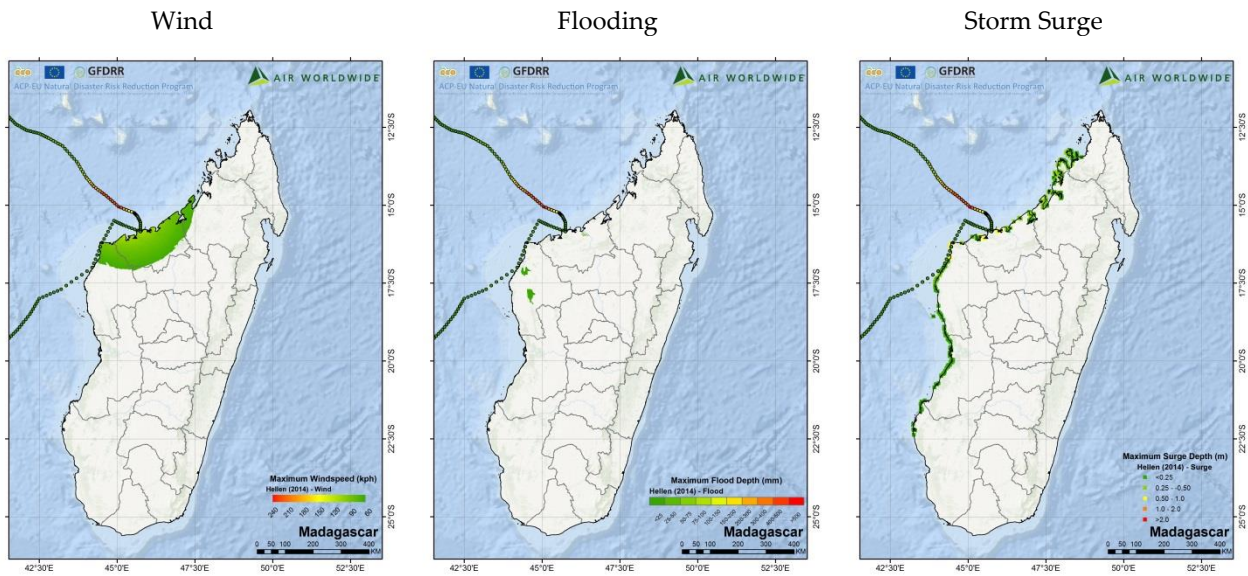
EQ: Tsunami Run-up



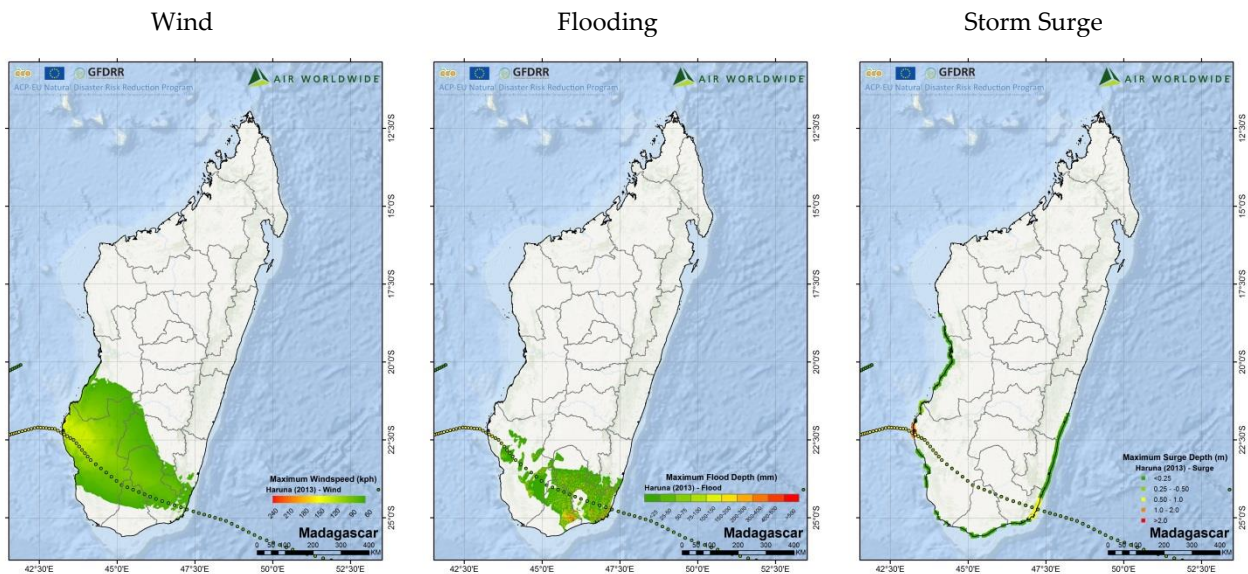
3.6 Marquee Events

Hazard footprints for historically significant or “marquee” events are provided herein. The considered hazard sub-perils include wind, precipitation flooding, and storm surge flooding. High resolution maps for each event are also provided as a digital addendum to this report.

Madagascar - Tropical Cyclone Hellen (2014)

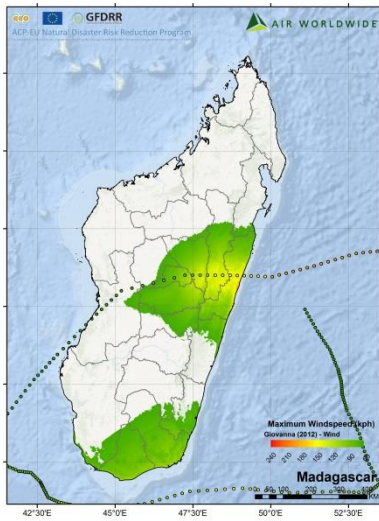


Madagascar - Tropical Haruna (2013)

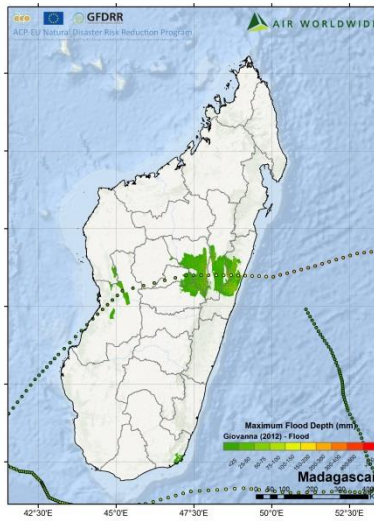


Madagascar - Tropical Cyclone Giovanna (2012)

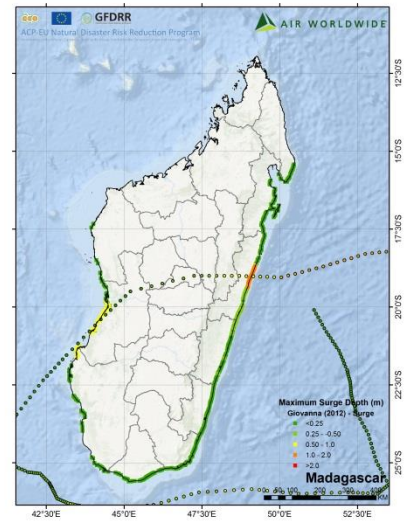
Wind



Flooding

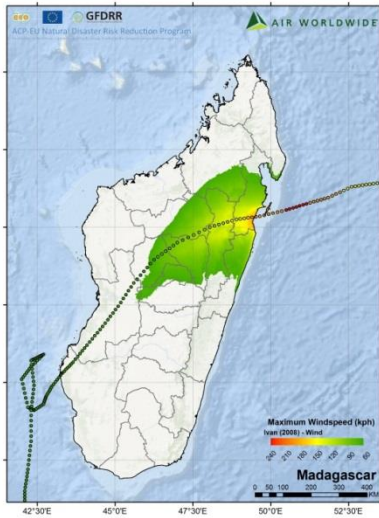


Storm Surge

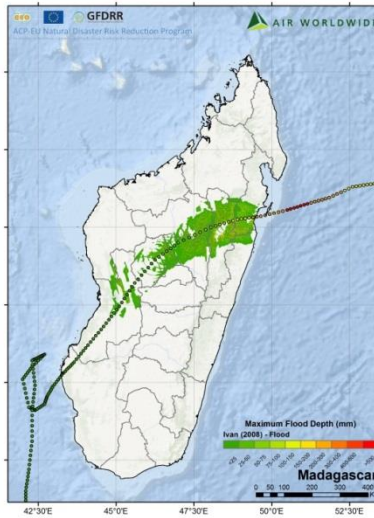


Madagascar - Tropical Cyclone Ivan (2008)

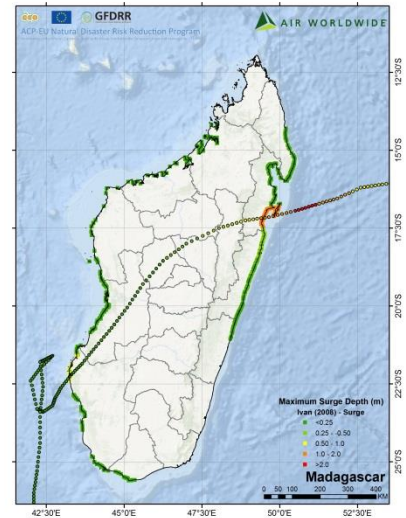
Wind



Flooding

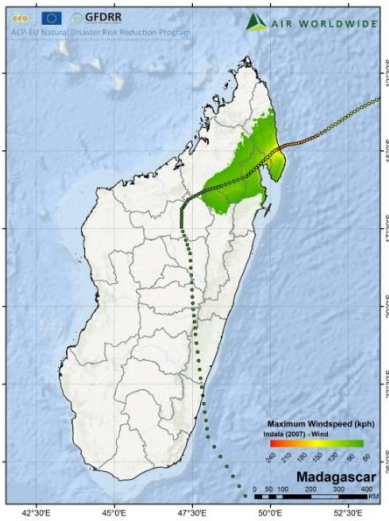


Storm Surge

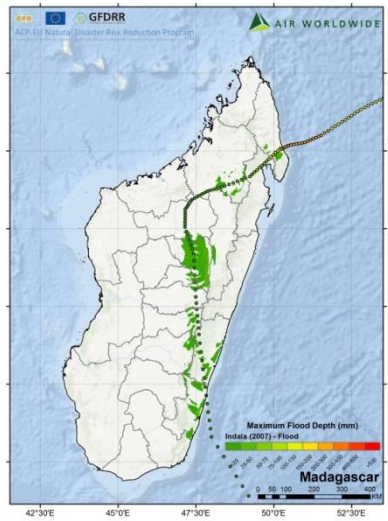


Madagascar - Tropical Cyclone Indlala (2007)

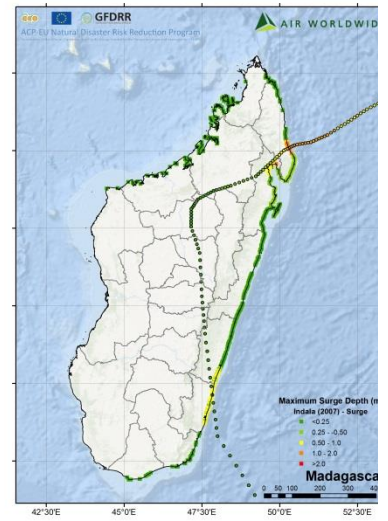
Wind



Flooding

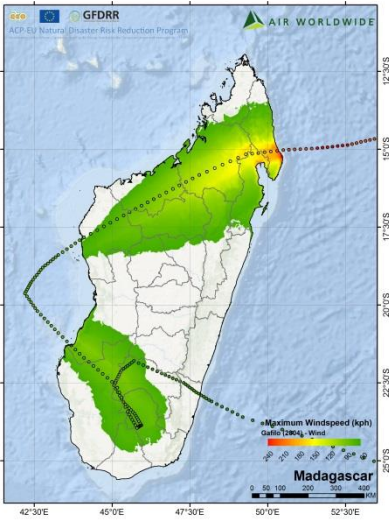


Storm Surge

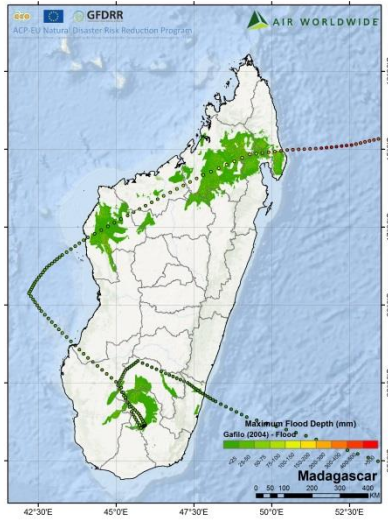


Madagascar - Tropical Cyclone Gafilo (2004)

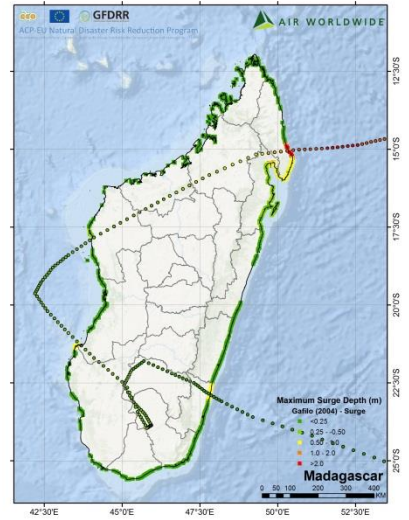
Wind



Flooding

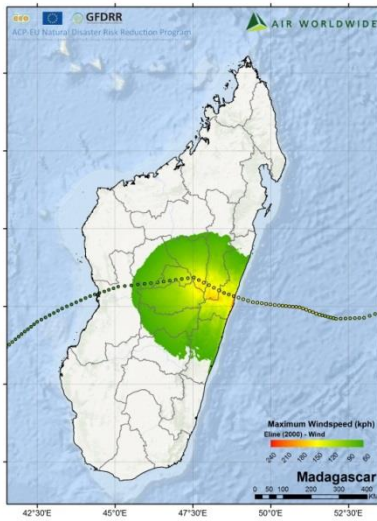


Storm Surge

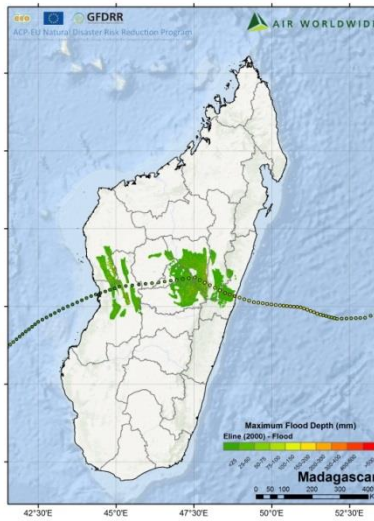


Madagascar - Tropical Cyclone Eline (2000)

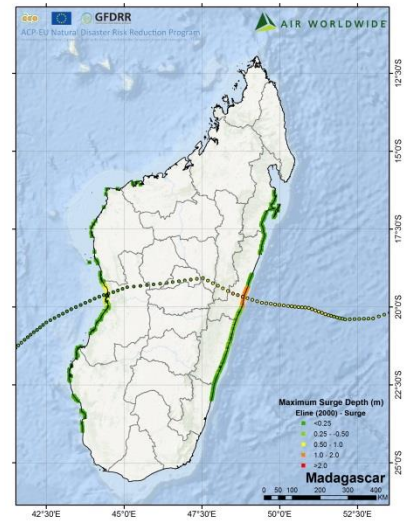
Wind



Flooding

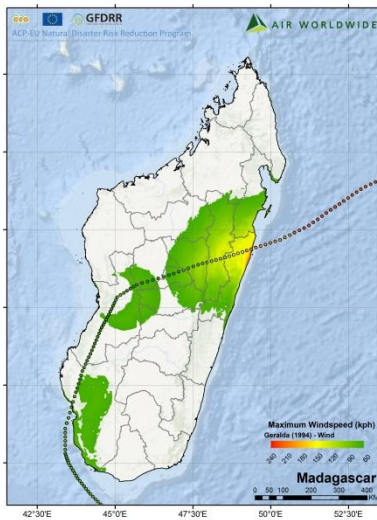


Storm Surge

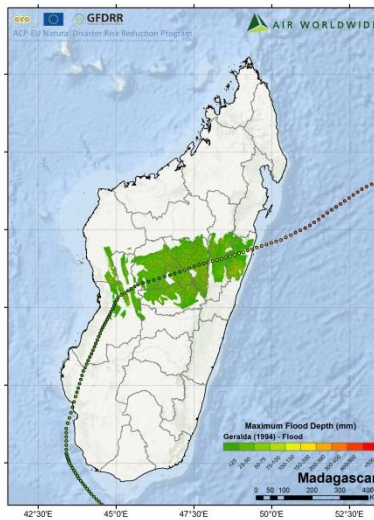


Madagascar - Tropical Cyclone Geralda (1994)

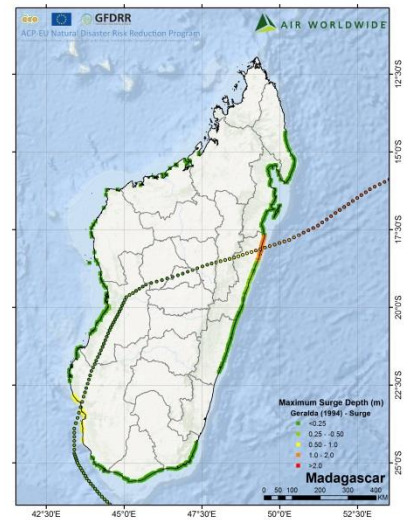
Wind



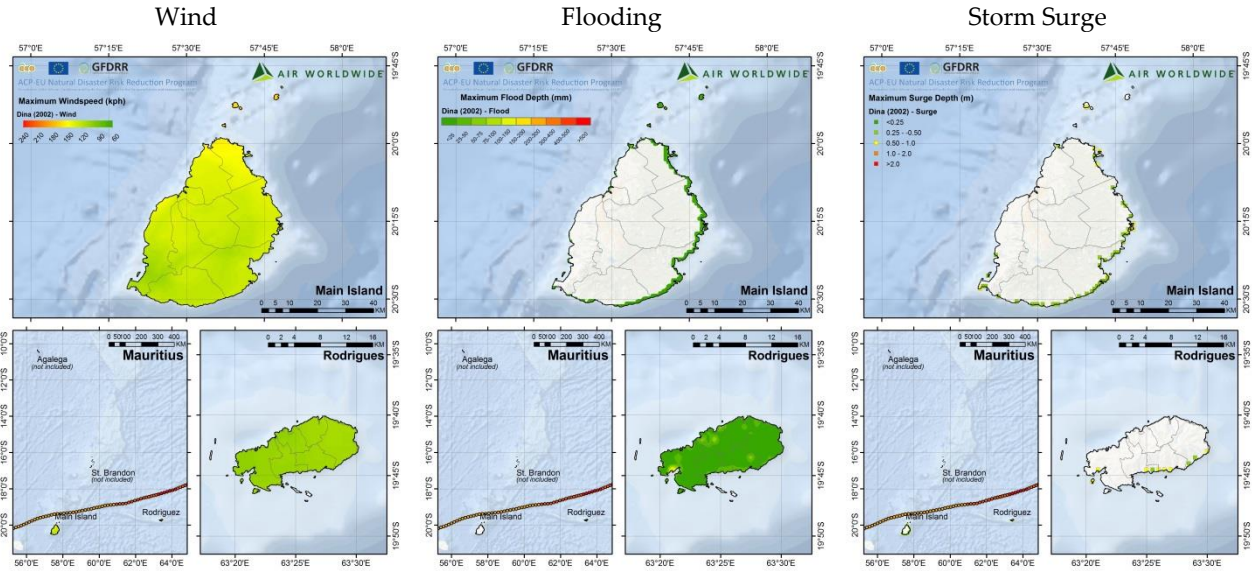
Flooding



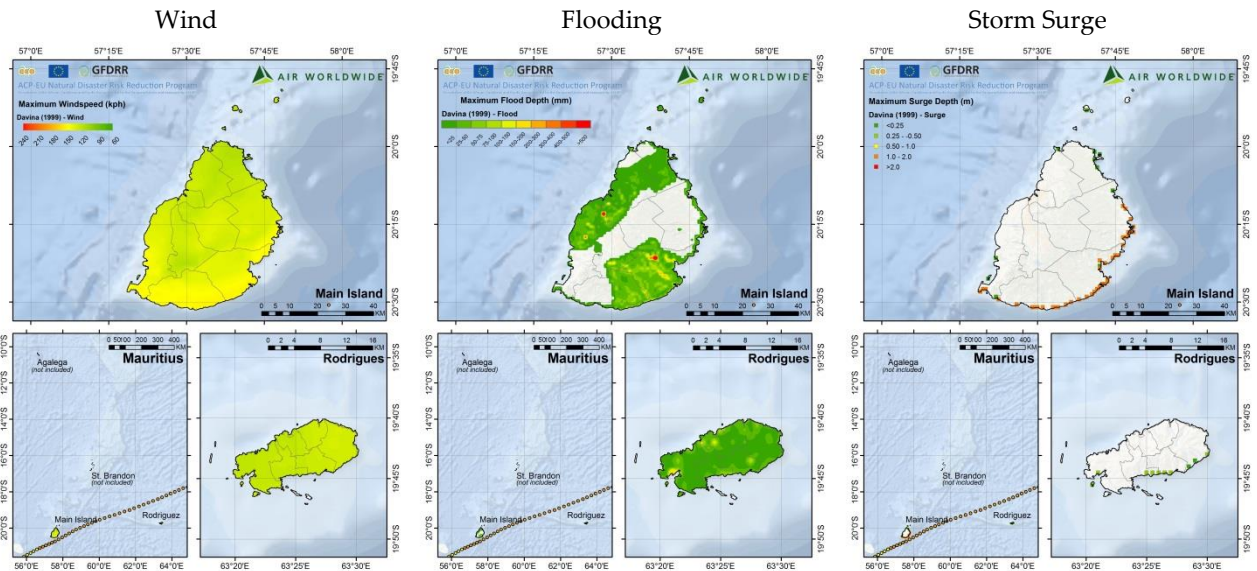
Storm Surge



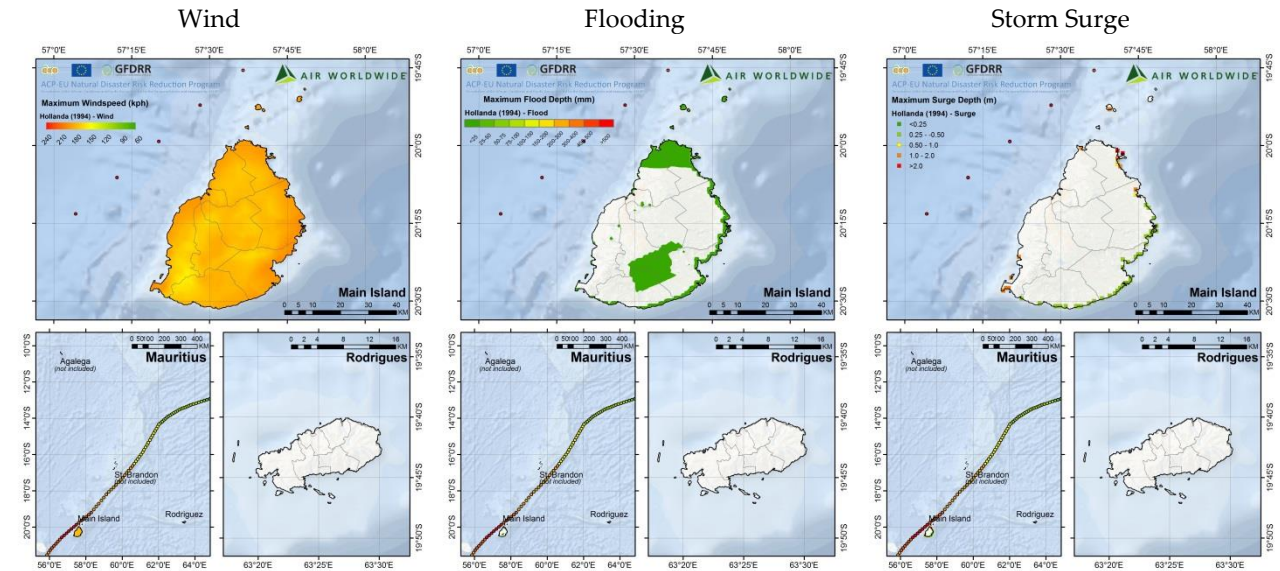
Mauritius - Tropical Cyclone Dina (2002)



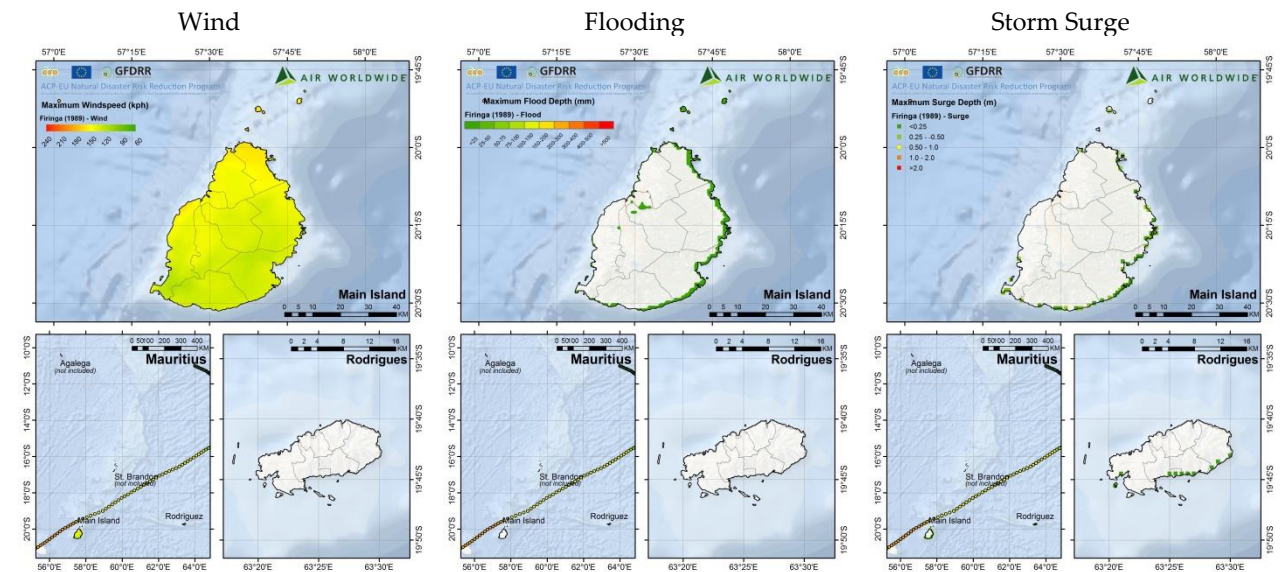
Mauritius - Tropical Cyclone Davina (1999)



Mauritius - Tropical Cyclone Hollanda (1994)



Mauritius - Tropical Cyclone Firinga (1989)



4 Appendix A – Detailed Model Documentation

Appendix A is provided as a technical supplement to the model overview presented in the main body of the report. Detailed descriptions of the data, methodology, and validation applied for the tropical cyclone, non-tropical cyclone, earthquake, and landslide models are provided in the following sections.

4.1 Tropical Cyclone

The tropical cyclone hazard model was developed for the perils of wind, precipitation flooding, and storm surge flooding the Southwest Indian Ocean region. A general description of the technical details of the tropical cyclone model, with a focus on the Southwest Indian Ocean region, is provided in this section. The section is structured in three major parts: (1) description of events and event generation techniques, (2) stochastic simulation of events, and (3) the local intensity calculation module.

4.1.1 Event Generation

The AIR tropical cyclone modeling team has collected data on 847 historical tropical cyclones that took place in the South Indian Ocean between the years 1950 and 2014. AIR relies on information from agencies that gather original data on historical tropical cyclones in the form of barograph traces from land stations and ships, actual wind records from weather service stations, aircraft reconnaissance flight data, radar data, precipitation data and other pressure and wind reports.

The stochastic catalog for the model is based on historical data from IBTrACs that collects and maintains data from a variety of sources; the primary sources for the SWIO region include:

- RSMC La Reunion
- Australian Bureau of Meteorology (BoM)
- Joint Typhoon Warning Center (JTWC)

The historical cyclone catalog, on which the model's stochastic catalog is based, was constructed by blending track information from the above agencies. All potentially damaging historical cyclones that have affected Southwest Indian Ocean countries were identified, including those that did not make landfall on the mainland.

Many parameters are used to generate stochastic tropical cyclone events, including the date and location of genesis. The storm's location, forward speed and direction, central pressure, radius of maximum winds (RMW), and the precipitation rate are all extracted from the IBTrACS database at 6-hour intervals and interpolated to 1-hour intervals for the duration of the storm. Additional parameters are recorded for

landfalling storms, namely the landfall hour, the landfall location (e.g., approximate latitude and longitude), the segment of the coast where landfall occurred, the track angle, and the central pressure.

When assessing tropical cyclone losses, the main environmental parameters used are wind speed and flood depth. Wind speed is computed using the storm’s size, location, forward speed, direction, regional terrain, and land-use-land-cover (LULC), while flood depth is computed using satellite-based precipitation measurements and a pluvial runoff model, as discussed further herein.

Model Domain

Because the model accounts for precipitation-induced flooding as well as wind and surge damage, the domain over which tropical cyclone-related hazards and losses are modeled needs to be considerably larger than it would be if only wind and surge damage were modeled. The precipitation footprint of tropical cyclones can extend over hundreds of square kilometers; thus even weak storms several hundred kilometers offshore can cause flood damage on land. The tropical cyclone model domain is shown in Figure A.1.

Furthermore, local flooding is often caused by precipitation that occurs upstream, so the flood damage footprint may be considerably larger than the wind, surge, or precipitation footprints. In addition, to account for the fact that it may take several days for peak flood levels to travel along a river network, the tropical cyclone’s track, intensity, and size must be accurately modeled for several days after the storm makes landfall (or its closest bypass).

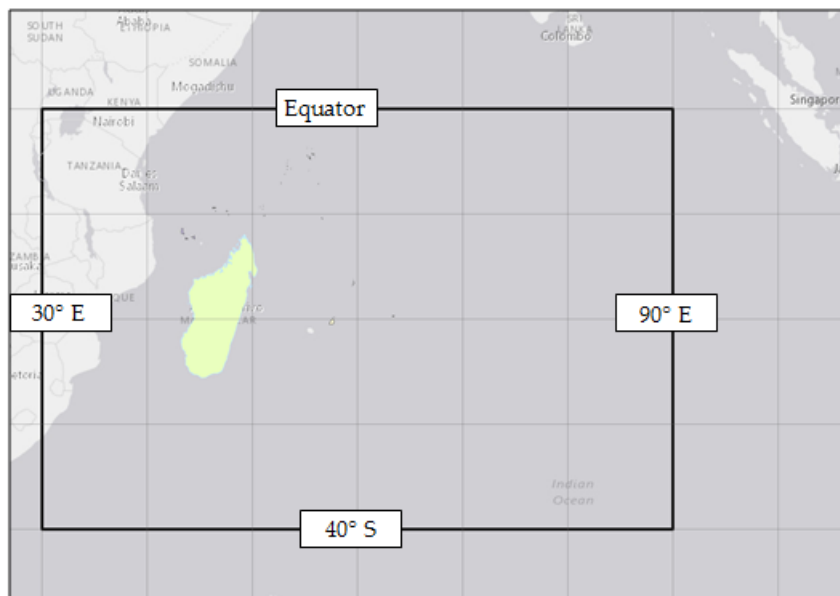


Figure A.1. Domain of the AIR Typhoon Model for the SWIO Basin

Annual Storm Frequency and Location

In the SWIO region, the cyclone season begins November 15 and ends April 30 of the following calendar year. Modeled frequency, meteorological data, and track information are analyzed in the geographical domain depicted above in Figure A.1.

In terms of tropical cyclone formation, the Southwest Indian basin is one of the most active areas in the world. On average, 13 tropical cyclones with wind speeds exceeding 63 km/h form here each year. Statistical goodness-of-fit tests reveal that the annual frequency of tropical cyclone formation in the model domain is best represented by a Poisson distribution. Figure A.2 shows the annual probability of tropical cyclone landfalls from the stochastic catalog for the Madagascar.

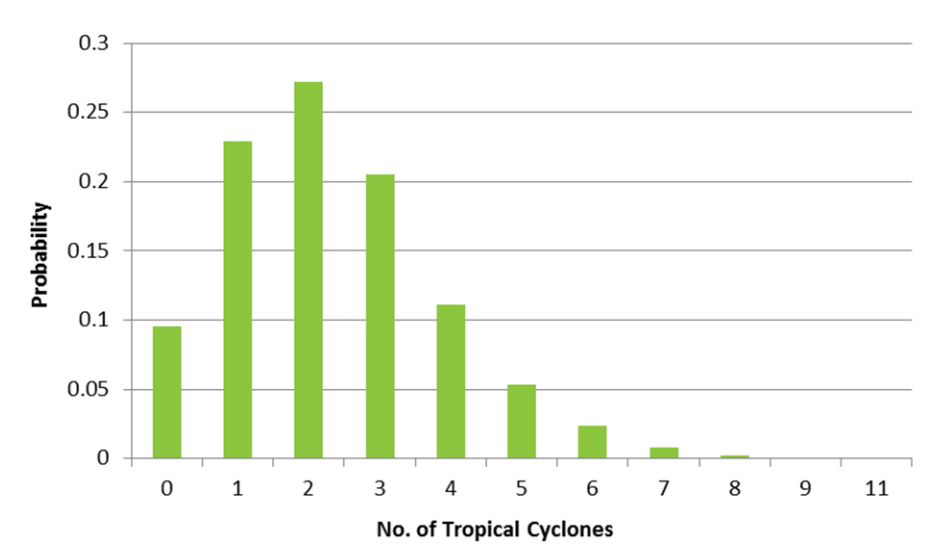


Figure A.2. Annual Probability of Simulated Tropical Cyclone Landfalls – Madagascar

Late fall and early winter are the most active times for tropical cyclones formation, and there is a clear seasonal cycle that peaks in January. The Southwest Indian basin is unique in that tropical cyclone formation has been observed in all months of the year. Figure A.3 shows the distribution of historical tropical cyclones by month, at genesis, in the model domain.

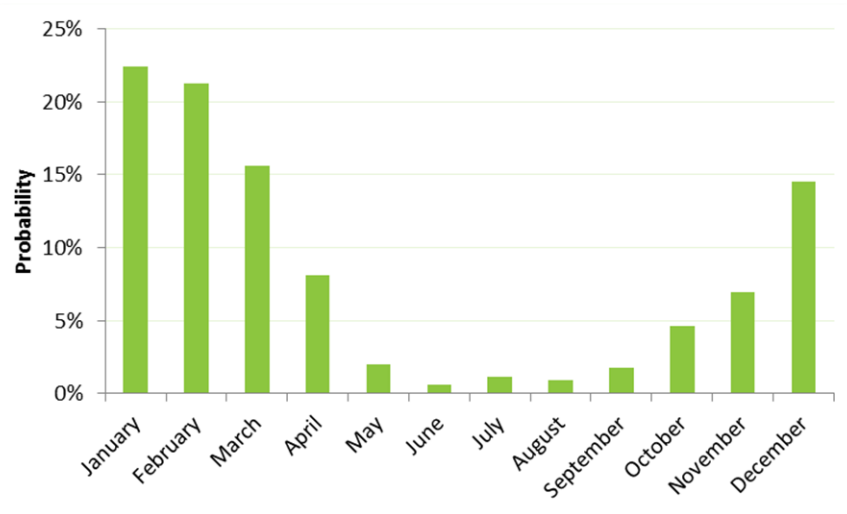


Figure A.3. Distribution of Historical Events by Month for the Model Domain

Storm Genesis Location

For each simulated storm, a corresponding historical storm is drawn at random from the set of all historical storms for the period 1950–2014. All genesis aspects, such as date of the simulated storm, starting location, track angle, forward speed, and central pressure are determined by stochastically perturbing the corresponding variables for the historical storm that was drawn. The perturbation is achieved by adding Gaussian “noise” to each historical value. Future evolution of the stochastic storm is then determined using autoregressive time series models as described in the sections that follow. The result is a “smoothed” area of storm genesis locations, as shown in Figure A.4.

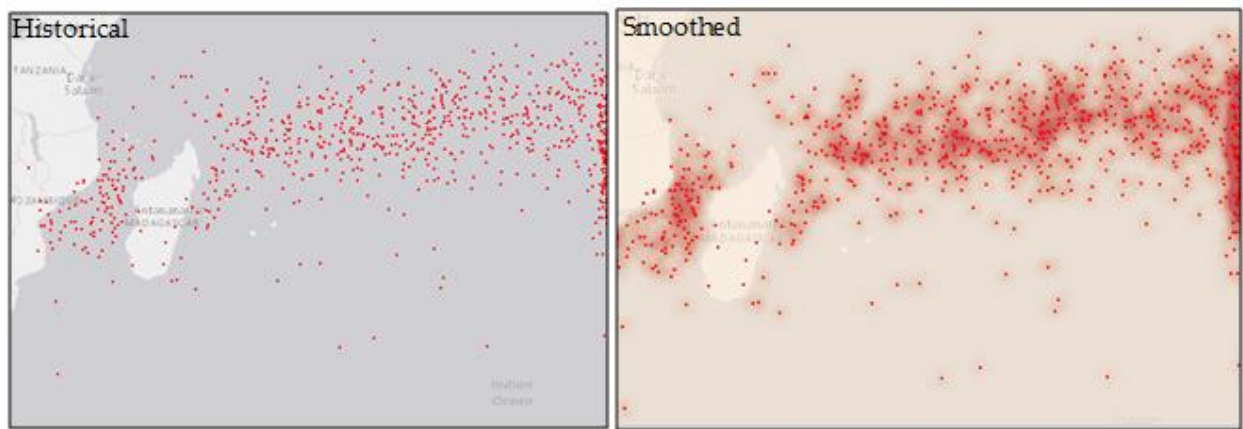


Figure A.4. Historical Storm Genesis Locations (left) and Smoothed Historical Genesis Locations (right)

Storm Track Generation

Track direction at any given point in time is a function of the direction of the storm at the previous time step. The dependence from one time period to the next can be measured by computing the auto-correlation function for historical storms. An analysis of the historical storm tracks indicates that a random-walk model represents the dependence on this variable quite well. That is, the storm direction at the next step equals the current storm direction plus a random perturbation drawn from a probability distribution that is allowed to vary spatially over the model domain. The simulation is implemented using six-hour time steps and conditional probability distributions estimated for $1.25^\circ \times 1.25^\circ$ grid cells using the historical data available for each grid cell.

The advantage of this probabilistic approach to storm track generation is that the tracks of simulated tropical cyclones resemble the curving and recurving tracks that are historically observed. Furthermore, the fact that they are fully probabilistic means that any possible storm track can be generated, not just historical tracks.

Multiple Landfalling Storms

A single tropical cyclone can make several landfalls or bypasses. In the AIR model, a “bypassing” storm is defined as one that does not make landfall but that passes sufficiently close to land to bring either tropical storm force (or higher) winds and/or flooding. Since the AIR model follows each simulated storm from the time of its inception until it dissipates, multiple landfalls and bypassing tropical cyclones are part of the simulation. The simulated frequency of multiple landfalls and bypassing storms is consistent with the historical frequency of these storms.

Forward Speed, Central Pressure, Radius of Maximum Winds

For each simulated storm, forward speed, central pressure and radius of maximum winds are also allowed to vary along the storm track.

Forward Speed

Forward, or translational, speed is the rate at which a cyclone moves from point to point along its track; this parameter contributes to overall wind speed as well as duration. In general, the lower the latitude of a cyclone, the faster the forward speed. Forward speed varies along the storm path, and the values observed at each time step are again correlated with the values observed at previous time steps.

An analysis of the auto-correlation function for historical storms shows that the dependence in forward speed can be represented by a first-order autoregressive model:

$$FS_t = \alpha_0 + \alpha_1 FS_{t-1} + \varepsilon_t$$



where F_{s_t} is the forward speed at time t , α_0 and α_1 are parameters estimated from the historical data, and ε_t is a noise or disturbance term. To capture the spatial variation in forward speed, the model domain is divided into 10° latitude bands, with the parameters α_0 and α_1 computed for each latitude band.

The combination of the simulated forward speed and storm direction determines the location of each simulated storm at successive time steps. This methodology yields smooth transitions in forward speed as the storm latitude changes.

Central Pressure

Central pressure is the primary determinant of tropical cyclone wind intensity. To develop a procedure for simulating central pressure along the storm path, AIR performed a time-series analysis of all historical storms to determine the dependence structure present in the data between consecutive six-hour time intervals. This dependence was measured by computing the auto-correlation function for each storm. The pattern of the computed auto-correlation function indicates that the dependence over time can best be described using a second-order auto-regressive model. According to this model, the central pressure Cp_t at time t can be represented as:

$$Cp_t = \alpha_0 + \alpha_1 Cp_{t-1} + \alpha_2 Cp_{t-2} + \varepsilon_t$$

where Cp_t and Cp_{t-2} are the central pressures at time $t-1$ and $t-2$, the parameters α_0 , α_1 , and α_2 are constants estimated from the data, and ε_t is a random disturbance term.

To capture the spatial variation in the coefficients, the parameters were estimated for each $2.5^\circ \times 2.5^\circ$ grid cell in the model domain. Figure A.5 shows the modeled distribution, by intensity, of tropical cyclones that make landfall in the Madagascar.

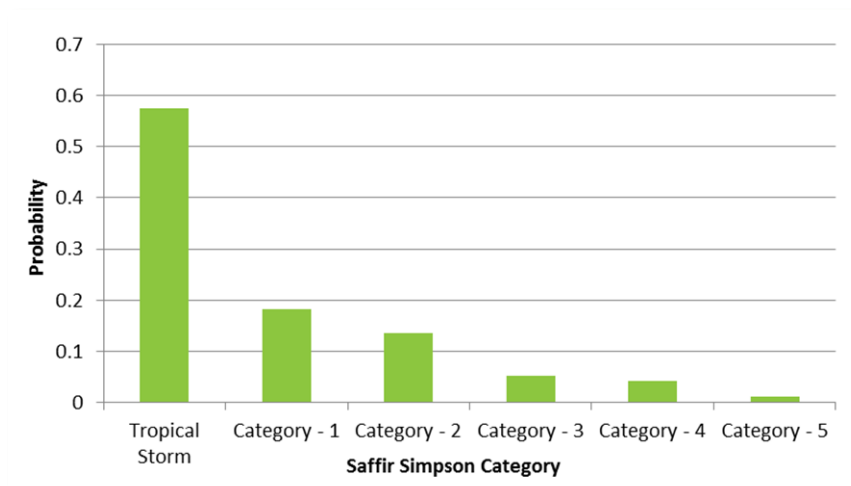


Figure A.5. Simulated Storm Probability by Intensity Category at Landfall – Madagascar

Radius of Maximum Winds

The radius of maximum winds (R_{max}) is the distance from the storm's center, or eye, to where the strongest winds are found. On average, the radius of maximum winds tends to be larger at latitudes farther from the equator and smaller for more intense storms. These relationships are explicitly accounted for in the model. While a smaller radius of maximum winds can correspond to greater storm intensity, it does not necessarily follow that losses will be greater. This is because a smaller radius usually results in a smaller affected area.

In the AIR Tropical Cyclone Model for Southwest Indian basin, R_{max} is calculated by a regression relationship dependent on central pressure and latitude:

$$R_{max_t} = \beta_0 + \beta_1(Cp_{wt} - Cp_t) + \beta_2\phi_t + \varepsilon_t$$

where Cp_{wt} and Cp_t are peripheral and central pressure, respectively, and ϕ_t is the storm latitude, all at time t . The disturbance term ε at time t is a linear function of the disturbance at the previous time $t-1$, and a normally distributed perturbation η :

$$\varepsilon_t = \alpha\varepsilon_{t-1} + \eta$$

4.1.2 Stochastic Catalog Summary Statistics

The AIR tropical cyclone model for the Southwest Indian basin contains more than 129,000 simulated events in the model domain, as defined previously. A total of 23,152 storms make landfall in Madagascar and 3,366 make landfall in Mauritius. The maximum number of landfalling events in a single year is 11 and 4 in the Madagascar and Mauritius, respectively.

Validating Stochastic Event Generation

AIR catastrophe models are extensively validated. Every component of the model is carefully verified against data obtained on historical events. This section provides a few exhibits illustrating the results of the validation process.

Validating Frequency

The annual frequency of tropical cyclone occurrence in the model domain is represented by a Poisson distribution. Figure A.6 shows a comparison between simulated and historical seasonality at genesis, while Figure A.7 compares simulated and historical annual count probabilities.

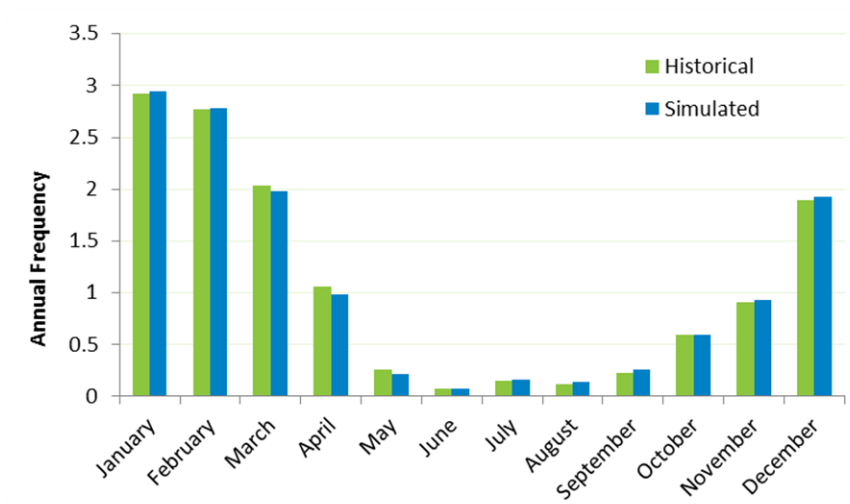


Figure A.6. Comparison of Historical and Simulated Seasonal Frequency at Genesis for Tropical Cyclones in the Model Domain

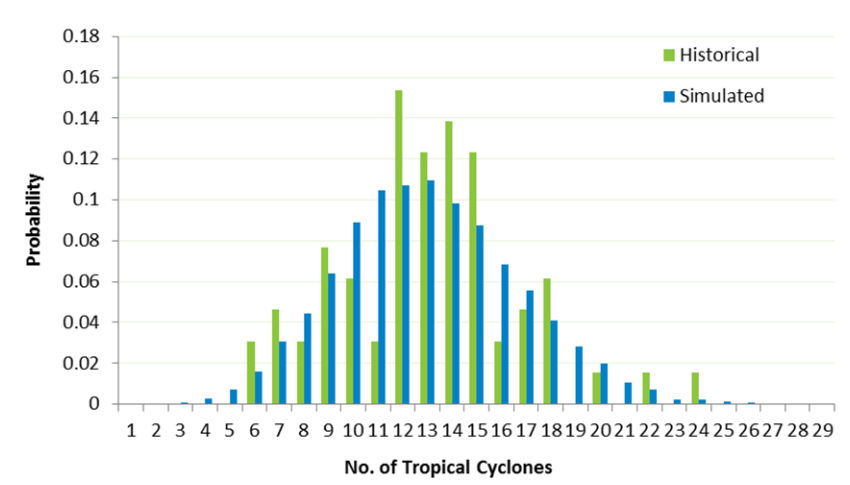


Figure A.7. Comparison of Historical and Simulated Annual Count Probabilities for Tropical Cyclones in the Model Domain

Figures A.8 through A.11 compare simulated and historical probabilities of landfalling tropical cyclones in Madagascar, Mauritius, Comoros, and Seychelles. Zanzibar is not represented due to the low number of historical tropical cyclone events in the island nation.

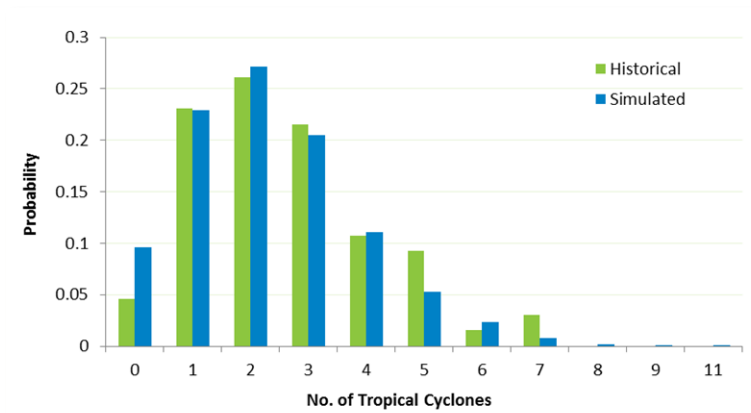


Figure A.8. Comparison of Historical and Simulated Landfall Frequency – Madagascar

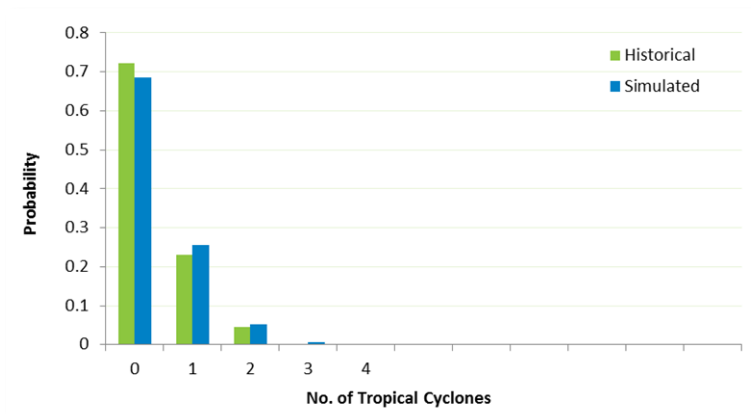


Figure A.9. Comparison of Historical and Simulated Landfall Frequency – Mauritius

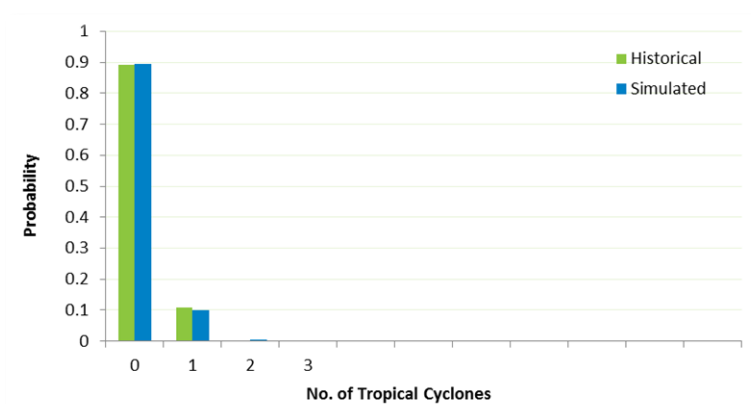


Figure A.10. Comparison of Historical and Simulated Landfall Frequency – Comoros

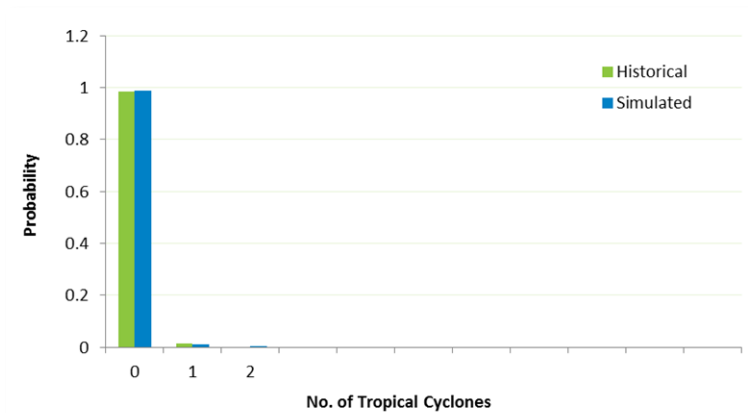


Figure A.11. Comparison of Historical and Simulated Landfall Frequency – Seychelles

Validating Storm Tracks

Tropical cyclones are steered by the surrounding mid- and upper-level environmental flow, which often changes seasonally in the Southwest Indian basin. In general, storms tend to move from east to west in the Southern Hemisphere tropics and begin recurving to the south and eventually the southeast as they move poleward.

Figure A.12 compares the historical catalog (1950–2014) and a randomly selected 65 year period of stochastically generated storm tracks under different intensity categories in the Southwest Indian basin. The modeled tracks illustrate the wide variety of directions that tropical cyclones affecting Southwest Indian Ocean Islands can follow, and demonstrate a reasonable agreement to the historical data.

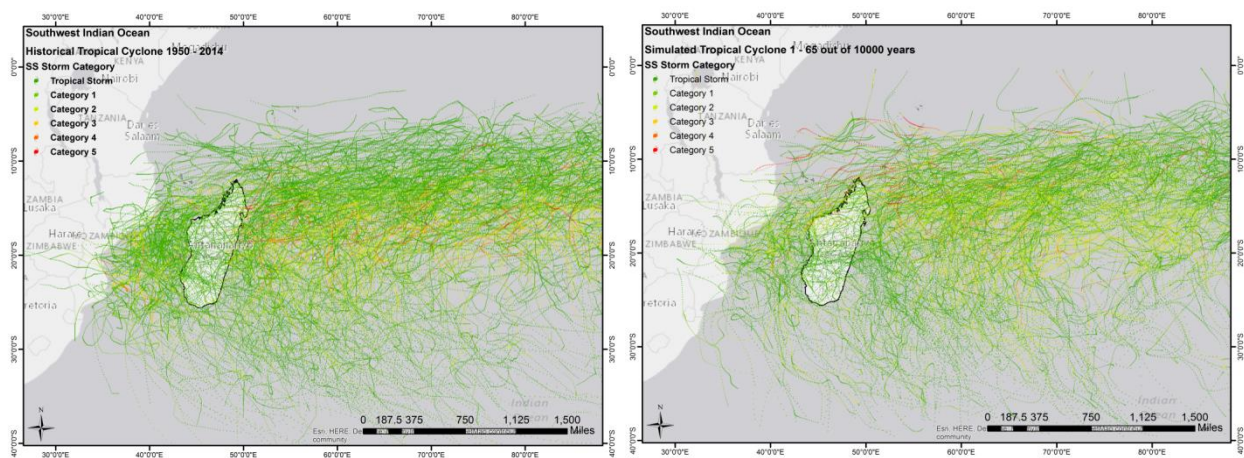


Figure A.12. Comparison of Historical (left) and Modeled Storm Tracks (right) for a 65-Year Period

Validating Meteorological Parameters at Landfall

Table A.1 compares the average landfalling central pressure, radius of maximum winds, and forward speed of the modeled and historical events. The comparison demonstrates that there are no obvious biases in any of the modeled parameters.

Table A.1. Comparison of Historical and Simulated Values at Landfall – Madagascar

<i>Model Variable</i>	<i>Average of Historical Catalog (1950-2014)</i>	<i>Average of Stochastic Catalog (10,000 years)</i>
Central Pressure	990 mb	990 mb
Radius of Max Winds	54 km	56 km
Forward Speed	17 km/h	19 km/h

Validating Landfall Frequency

Figure A.13 and Figure A.14 show a comparison between historical and simulated tropical cyclone intensity at landfall for Madagascar and the Mauritius, respectively.

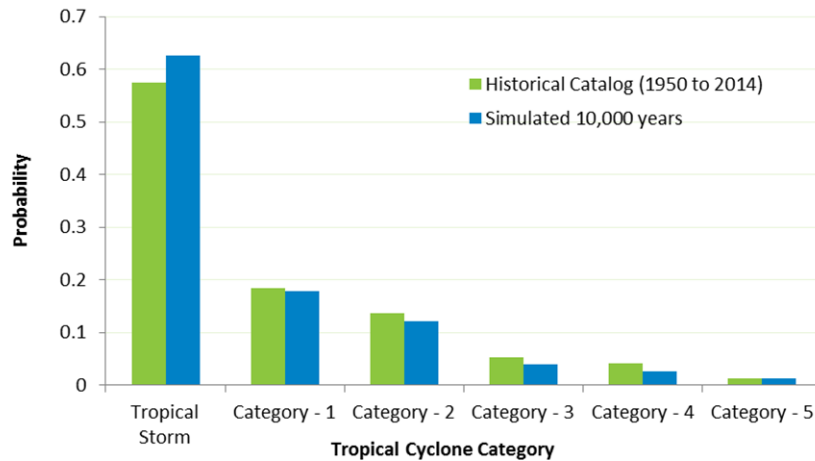


Figure A.13. Comparison of Historical and Simulated Intensity at Landfall – Madagascar

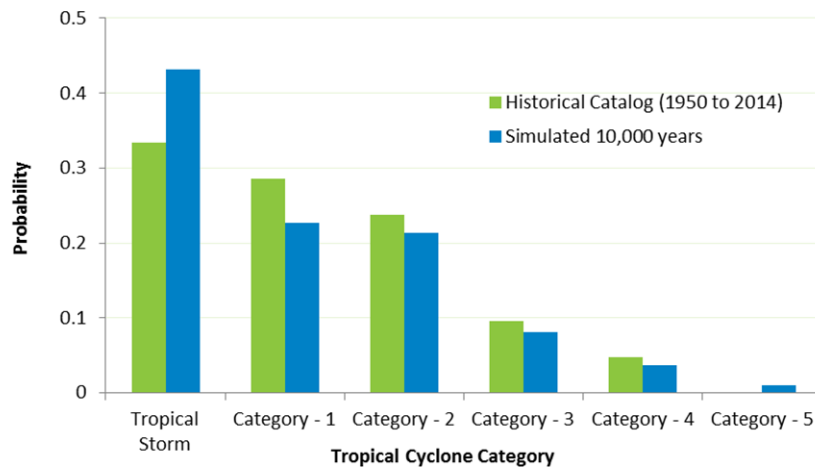


Figure A.14. Comparison of Historical and Simulated Intensity at Landfall – Mauritius

Validating Storm Density

All storms generated for the stochastic catalog are used to validate the number of storms that affect the model domain. To determine the storm density across the region, the number of storms whose track passes through each $2.5^\circ \times 2.5^\circ$ grid cell was determined for the historical data, and compared to the same number from the stochastic catalog. The annual storm track density for historical storms is compared to the density for stochastic storms in Figure A.15, which demonstrates good agreement and a similar spatial distribution of storm frequency.

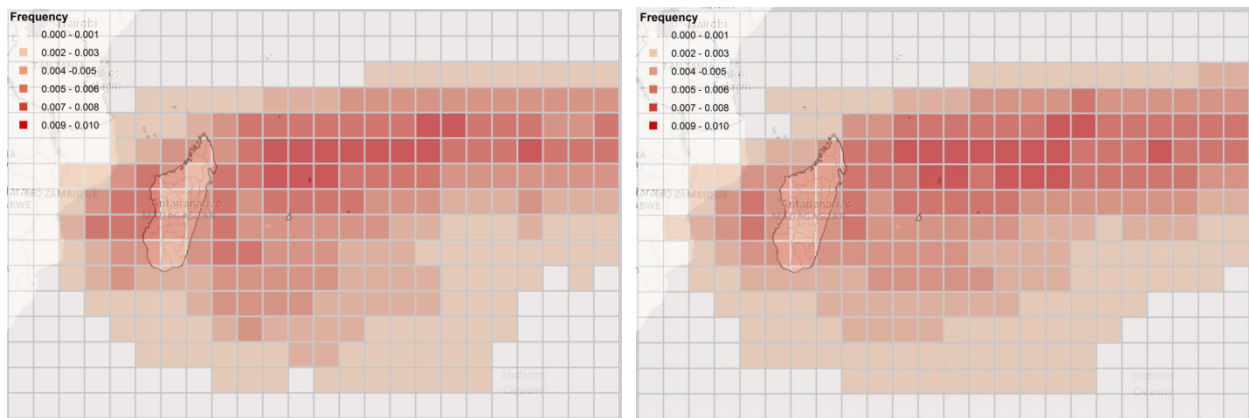


Figure A.15. Storm Track Density based on Historical (left) and Simulated Events (right)

4.1.3 Local Intensity Calculation

The intensity measures used in the AIR tropical cyclone model for SWIO island nations are:

- 10-meter, 1-minute sustained winds
- Flood depth (accumulated runoff) in millimeters

The derivation and implementation of these intensity parameters in the model are described below.

Modeling Local Wind Intensity

The generation of the local wind field involves first computing the gradient wind² as a function of central pressure and peripheral pressure. A gradient wind profile is applied, based on the work of Willoughby et al. (2006), and reduced to the surface via a gradient wind reduction factor. Asymmetry and topographical effects are added and friction and gust factors are applied.

The Relationship between Central Pressure and Wind Speed

The maximum gradient wind speed, V_{gr_max} (in meters per second), is calculated from a C_p -wind relationship that was derived using best track data specific to the Southwest Indian Ocean basin. A constant gradient wind reduction factor (GWRF) of 0.90 is used for all historical and stochastic events. The data, which was obtained from International Best Track Archive for Climate Stewardship (IBTrACS), covers the time period between 1950 and 2014. The piecewise C_p -wind relationships are as follows:

$$\begin{aligned}
 V_{gr_max} &= (\alpha_1(P_{env} - P_c)^2 + \alpha_2(P_{env} - P_c) + \alpha_3)/GWRF & (P_{env} - P_c) < 60 \\
 &= (\alpha_4(P_{env} - P_c) + \alpha_5)/GWRF & (P_{env} - P_c) \geq 60
 \end{aligned}$$

Figure A.16 compares the best track data from the IBTrACS with the relationship used in the AIR Cyclone Model for Southwest Indian countries, showing good agreement.

²Gradient wind is the flight-level wind, or the wind at the top of the planetary boundary layer, which is the point at which the earth's surface no longer imparts any effect on the wind. That is, gradient wind is the large-scale wind field balanced between the pressure gradient force and the Coriolis and centrifugal forces, in the absence of friction effects.

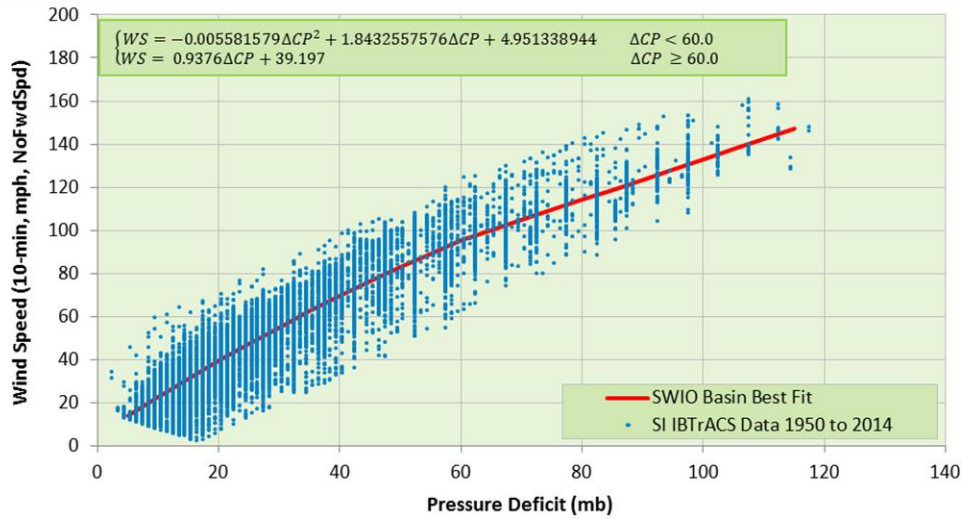


Figure A.16. The Relationship between Central Pressure and Wind Speed

Peripheral Pressure

The peripheral, or environmental, pressure (P_{env}) is the sea level pressure at the last closed isobar of the tropical cyclone circulation. Because the radius to the outer closed isobar typically ranges between 500 and 1000 km, another definition is the azimuthally-averaged sea level pressure at a fixed distance from the storm center. Scientists at AIR analyzed the NCEP-NCAR Reanalysis Project (NNRP) 2.5° global dataset (1981-2010) and calculated the azimuthally-averaged sea level pressure. An average of those values for all points within 10° of area of interest resulted in a peripheral pressure value of 1012.50 mb.

Gradient Wind Profile

The gradient wind profile, which is empirically derived and based on the work of Willoughby et al. (2006), is defined by three equations: one for the region inside of the eyewall, one for the eyewall region, and one for the region outside of the eyewall. The formulation uses two adjustable parameters (X_1 , X_2 in the equations below), to define the rate of decay of winds from the eyewall outward. This provides a high degree of flexibility to better match the observed rapid wind decay rate near the eyewall (X_2) and the more moderate decay farther away from the eyewall (X_1). The result is a gradient wind profile that compares well with observational data.

The gradient wind profile incorporated in the AIR model is as follows:

$$V_{gr}(r, R_{max}, \theta, V_{gr_max}) = V_{gr_inner} = V_{gr_max} \left(\frac{r}{R_{max}} \right)^n \quad (0 \leq r \leq R_1)$$

$$V_{gr}(r, R_{max}, \theta, V_{gr_max}) = V_{gr_inner}(1 - w) + V_{gr_outer}(w) \quad (R_1 \leq r \leq R_2)$$

$$V_{gr}(r, R_{max}, \theta, V_{gr_max}) = V_{gr_outer}$$

$$= V_{gr_max} \left[(1 - A) \cdot \exp\left(-\frac{r - R_{max}}{X_1}\right) + A \cdot \exp\left(-\frac{r - R_{max}}{X_2}\right) \right] \quad (R_2 \leq r)$$

where

- V_{gr} = gradient wind speed of a stationary tropical cyclone
- V_{gr_max} = maximum gradient wind speed of a stationary tropical cyclone
- V_{gr_inner} = gradient wind speed of a stationary tropical cyclone inside R_{max}
- V_{gr_outer} = gradient wind speed of a stationary tropical cyclone outside R_{max}
- r = distance from storm center
- R_{max} = radius of maximum winds
- θ = latitude
- w = ramp function for smooth transition from inner to the outer profile
- R_1 = inner eyewall radius
- R_2 = outer eyewall radius
- A = parameter to proportion the two exponentials in the profile
- X_1, X_2 = decay length parameters
- n = exponent for the power-law dependence within the eye

X_2 is a fixed distance equal to 25 km, and w is a function of R_1 and R_2 . X_1 , N , and A are functions of V_{gr_max} , R_{max} , and θ as follows

$$X_1 = 287.6 - 1.942V_{gr_max} + 7.799\ln(R_{max}) + 1.1819\theta$$

$$N = 2.1340 + 0.0077V_{gr_max} - 0.4522\ln(R_{max}) - 0.0038\theta$$

$$A = 0.5913 + 0.0029V_{gr_max} - 0.1361\ln(R_{max}) - 0.0042\theta \quad (A \geq 0)$$

Asymmetry Effect

In the Southern Hemisphere, tropical cyclone winds rotate clockwise. The combined effects of tropical cyclone winds and forward motion (or translational speed) will produce higher wind speeds on the left-hand side of the storm. The model captures this via the term F_{asym} in the equation below (from NOAA Technical Report NWS-23). In doing so, the model accounts for the dynamic interaction of translational and rotational speeds, as well as the inflow angle.



$$F_{asym} = 1.5(T^{0.63})(T_0^{0.37})\cos(\beta)$$

Where T is the forward speed in knots, T_0 is the conversion from knots to kilometers per hour, and β is the angle between the track direction and the surface wind direction.

Topographical Effects

Wind speeds increase on the windward slopes of mountains, hills and escarpments because of amplification created by the change in elevation or topography. Such features restrict the passage of wind, causing a compression of the streamlines, or the areas through which wind must travel. As wind speed is inversely proportional to the spacing of streamlines, wind accelerates as it moves uphill (Figure A.17).

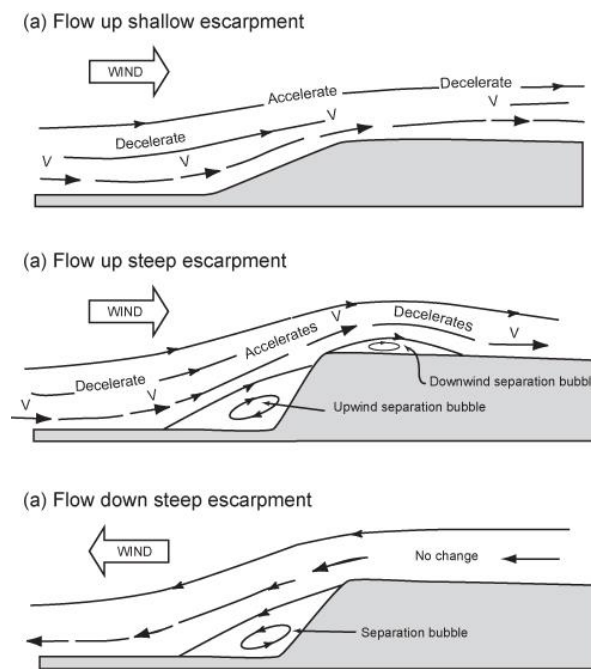


Figure A.17. Effects of Topography on Wind

The slope of the incline determines the degree of compression, so the amplification effect is accentuated on steeper hills. In addition, if the angle of incline is sharp, wind flow separates because momentum near the ground is insufficient to overcome the pressure gradient at the top. A turbulent "separation bubble" is established, which causes local vortices and high suction loads/stresses, increasing potential damage.

In the case of downhill winds, the leeward slope provides protection. If, however, the slope is sharp, a similar separation bubble manifests itself downwind and counteracts, to some degree, the protection provided by the hill or escarpment.

Using high-resolution topographic data, which is derived from elevation data, the AIR tropical cyclone for Southwest Indian Ocean island nations calculates gust, friction, and topographic values for each grid cell. The slope angle and distances between each cell centroid are computed and wind amplification and turbulence factors are assigned.

Surface Friction Effects on Wind Speeds

Differences in surface terrain on a smaller scale also affect wind speeds. Wind velocity profiles (Figure A.18) typically show higher wind speeds at higher elevations. Winds travel more slowly at ground level because of the horizontal drag force of the earth's surface, or surface friction. The addition of obstacles such as buildings will further reduce wind speed.

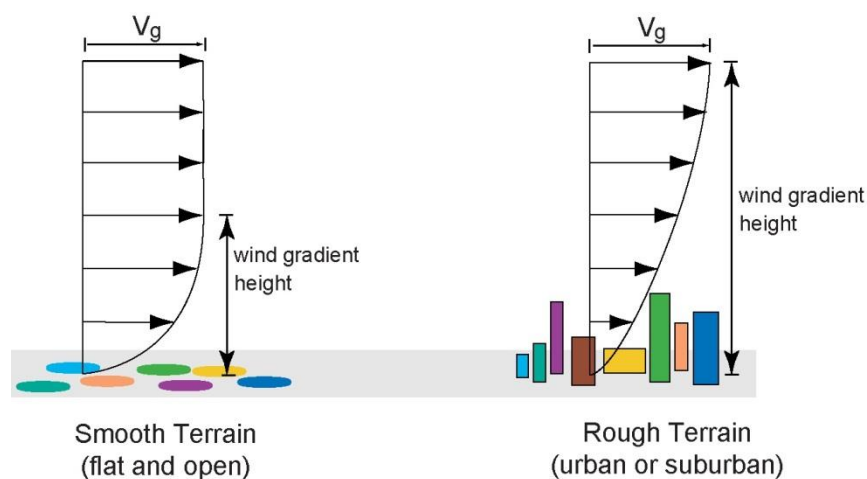


Figure A.18. Terrain Effects on Wind Velocity Profiles (adapted from Cook)

The gradient wind occurs 1-2 km above ground level and is therefore independent of the underlying surface conditions, except for the fact that storm intensity after landfall does account for the filling effect. Generation of the local wind field continues by modulating the gradient wind for elevation, sheltering, frictional, and gust effects. The model applies a friction coefficient at each location of interest to reflect estimates of surface roughness derived from digital land-use/land-cover (LULC) data. The LULC data used in the model is based on Global Land Cover Climatology information. The native resolution is 500 m and 1-km data was obtained by resampling. The dataset contains 17 classifications. A fetch length of 10 km was considered as the distance wind travels in a single direction over a relatively smooth surface before reaching a given location. The higher the fetch over water for example, the longer the wind will take to slow down upon reaching the shore. Thus, fetch affects wind speed at a given location.

In practice, wind has to blow over a certain distance before the planetary boundary layer (PBL)³ reaches equilibrium with the underlying surface. Downwind of a change in terrain roughness, such as the edge of an urban area, a new boundary layer begins to grow. Within this new layer the flow is not in equilibrium, and the wind profile adjusts.

To account for the boundary-layer adjustment, the friction factor is adjusted according to an effective roughness. The effective roughness is defined as the average surface roughness for an area extending from the location of interest outwards to a radius of 10 km—and is representative of the mean land surface acting on the wind field at that location.

The friction factors used for the AIR Tropical Cyclone Model for Madagascar are shown in Figure A.19. Note that the friction factors are much higher along the coastline.

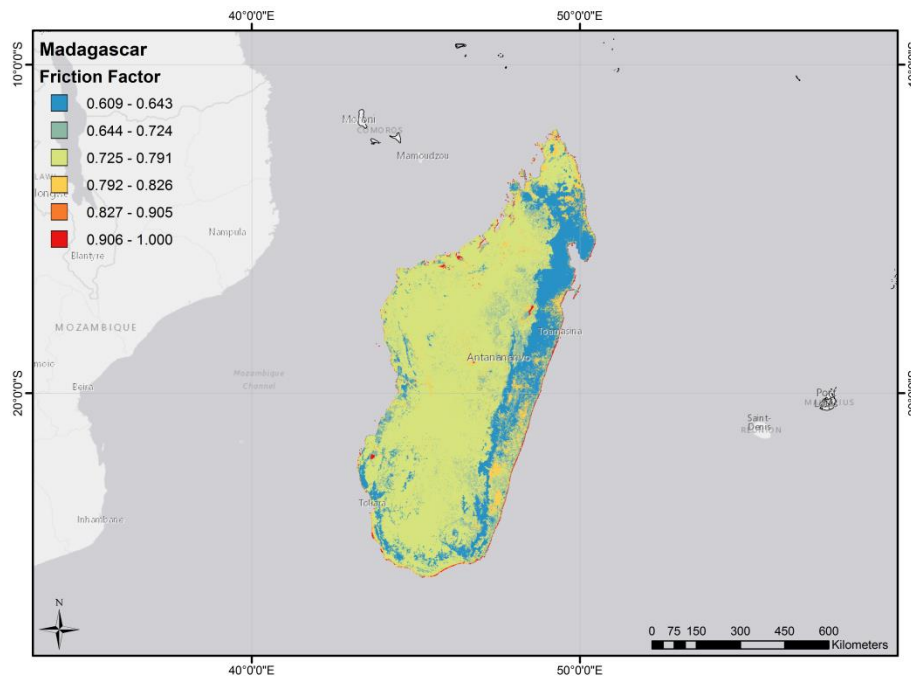


Figure A.19. Example of AIR friction factors used in the Southwest Indian basin model for Madagascar

Gust Effects on Surface Winds

Just as surface roughness exerts a frictional drag on the winds near the surface, so too can surface roughness enhance gustiness, which is a measure of how the wind speed near the surface varies as a function of time.

³ The lower layer of the atmosphere—extending vertically from the surface to between 300 and 600 meters— within which surface roughness has an effect on wind speeds. This height, beyond which surface roughness no longer affects wind speeds, is referred to as the gradient height.

Generally speaking, winds near the surface—even those in a tropical cyclone that is neither intensifying nor weakening—undergo oscillations that are the result of eddies of different sizes, which are generated from different land-use and land-cover and can cause temporary increases and decreases in wind speed.

The many eddies that exist at any given time result in different strengths and durations of gusts. These gusts range from extreme ones that last only seconds to weaker ones that can last for several minutes. Typically, very rough surfaces can increase the gustiness, while smooth surfaces tend to be associated with low levels of gustiness. Scientists at AIR have accounted for the gust effects on tropical cyclone winds not only across different types of surfaces, but also from different directions across those surfaces. The wind gust factors are shown in Figure A.20.

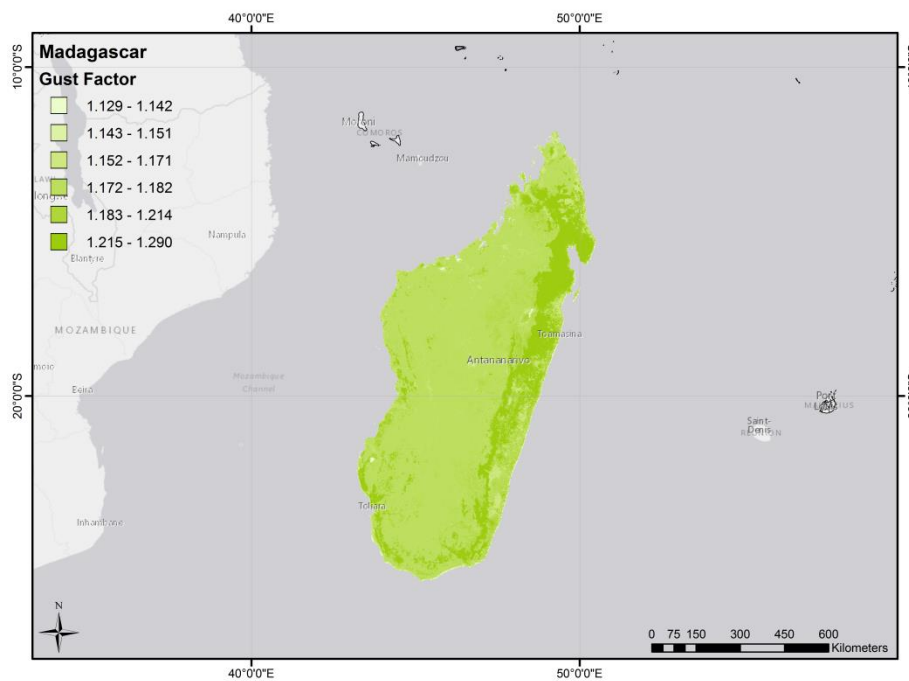


Figure A.20. Example of AIR gust factors used in the Southwest Indian basin model for Madagascar

Wind Field Directionality

The AIR model explicitly includes directional effects of surface roughness on locally estimated wind speeds. Rather than using a single friction factor that takes into account the average land surface surrounding a location, the wind-field model uses land use/land cover data to estimate the roughness in eight wind directions: north, northeast, east, southeast, south, southwest, west, and northwest.

A wind coming from the Indian Ocean will be relatively unobstructed. On the other hand, a wind from over land will undergo wind-reducing adjustments. In the AIR model, the influence of the maritime environment on

the wind transition is explicitly quantified, which yields a realistic wind field at a local level for the duration of the event.

Complete Specification of the Wind Field

As described above, once the relationship between central pressure and wind speed is established, many other aspects of the wind field are taken into consideration. The gradient wind profile is determined, and adjustments are made for asymmetry effects, surface friction, and topographical effects. A time profile of wind speeds is then developed and the effects of gusts are taken into account. The following expression takes all these variables into consideration, and can be used to calculate the wind velocity at a specific site.

$$V_{10m,1min}(lat,t,r,z0,\phi) = ff(z_0, \phi) \cdot Adj_{elev} \cdot Adj_{terrain} \cdot \{V_{gr_rMAX} (Cp(t,tLF)) \cdot Adj_{10m} \cdot Adj_{rad_decay} \cdot gf(z_0, \phi) + F_{asym}(\phi,r)\}$$

where:

$V_{10m,1min}$ = surface 10-m, 1-min wind speed

V_{gr_max} = maximum gradient wind speed at the radius of maximum winds

Adj_{elev} = adjustment factor for elevation

$Adj_{terrain}$ = adjustment factor for terrain

$ff(z_0, \phi)$ = friction factor for wind direction ϕ

$gf(z_0, \phi)$ = gust factor for wind direction ϕ

Adj_{10m} = adjustment factor to 10 meters (0.90)

Adj_{rad_decay} = adjustment for wind away from the radius of maximum winds

$F_{asym}(\phi,r)$ = effect of forward speed of motion

Modeling Precipitation-Induced Flooding

The flood component of the model relies on a parametric precipitation model that leverages high-quality precipitation data produced by tropical cyclones. One of the highest quality precipitation data sources is the Tropical Rainfall Measuring Mission (TRMM), which is conducted jointly by the National Aeronautics and Space Administration (NASA) and the Japan Aerospace Exploration Agency (JAXA). TRMM was launched in 1997 in an effort to provide reliable, high-quality precipitation data for storm prediction. TRMM makes use of five measurements using precipitation radar, TRMM microwave imagery, visible and infrared scanners, studies of clouds and the Earth's radiant energy system, and a lightning imaging sensor. TRMM is available at a three-hourly time interval and $0.25^\circ \times 0.25^\circ$ resolution. TRMM data is extensively validated and widely used, making it ideal for developing the parametric precipitation model.



Modeling Precipitation

The parametric precipitation model has two key parameters: the maximum precipitation rate (P_{max}) and outer radius of precipitation (R_{outer}). P_{max} is the maximum azimuthally-averaged precipitation rate, plus one standard deviation, evaluated within 250 km of the center, at concentric rings 25 km apart. One standard deviation conservatively accounts for any potential under sampling associated with the coarse temporal and spatial resolution. R_{outer} is the maximum distance from the center, also evaluated at 25-km concentric rings, where the average precipitation rate is 1 mm/hr. Values for each parameter are extracted from the TRMM data collected within the model domain.

The relationship between storm intensity and rainfall rate is derived from TRMM data using the Saffir-Simpson intensity categories subdivided into intensity bins. The results are consistent with previous studies (e.g., Lonfat et al., 2004, 2007) and demonstrate that the average rainfall rate increases with increasing storm intensity (Figure A.21) and decreases with increasing distance from the eyewall.

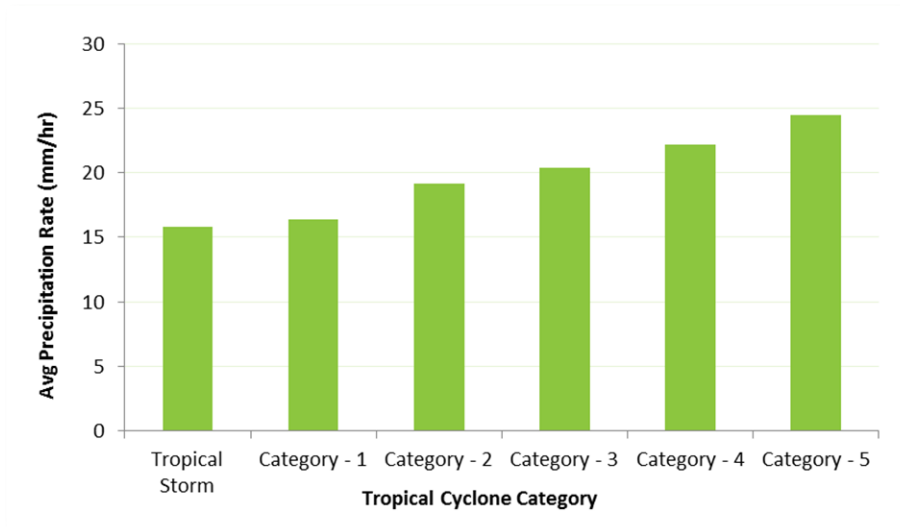


Figure A.21. Modeled Average Precipitation Rates by Storm Intensity

The lower and upper boundaries of P_{max} are 1 mm/hr and 100 mm/hr, respectively. R_{outer} is modeled using a Weibull distribution, with lower and upper bounds of 100 km and 750 km, respectively; R_{outer} is resampled if the drawn value falls outside of these bounds. Comparisons to TRMM data are favorable and demonstrate the reasonability of the distributions.

At each hourly time step, a circularly symmetric rainfall footprint is calculated based on P_{max} , R_{outer} , and the distance from center of the storm track. As the storm approaches landfall and after landfall, the precipitation

intensity changes due to several factors including filling, terrain, and coastal convergence, as shown in the equation:

$$P_{\text{hourly}} = P_{\text{base}} + P_{\text{coastal}} + P_{\text{topo}}$$

where P_{hourly} is the hourly precipitation at a given location, P_{base} is the base precipitation without any enhancements and is a function of P_{max} , R_{outer} , intensity, and distance from the center, P_{coastal} is the precipitation associated with coastal convergence, and P_{topo} is the precipitation contribution from topography. All precipitation amounts are provided in millimeters.

As tropical cyclones move inland and away from the warm ocean water, they weaken, or fill. As a result, precipitation decreases, and this decrease is captured by the stochastic relationship between intensity and peak rain rate.

Modeling the Flood Hazard

While the precipitation module identifies where rain is likely to fall—which helps to identify where the flood risk exists—a separate module is used to determine the spatial distribution of runoff and maximum flood depth.

Precipitation-induced flooding is modeled dynamically, based on the two-dimensional rainfall runoff CASC2D-SED (CASCade 2 Dimensional SEDiment) model developed at Colorado State University (Rojas et al., 2003). The maximum flood depth is calculated based on hourly precipitation routed through the model. The required input data for this model are elevation, soil and a land/sea mask.

This model is based on the shallow water equations (i.e., Saint Venant equations) derived from conservation of mass, energy, and momentum (i.e., primitive equations). Shallow water equations are generally appropriate for modeling runoff or pluvial flooding, where the horizontal length scale is much greater than the vertical. The generalized partial differential equations provided below are implemented in the model to calculate the continuity of mass and momentum of water.

Mass continuity:

$$e = \frac{\partial h}{\partial t} + \frac{\partial q_x}{\partial x} + \frac{\partial q_y}{\partial y}$$

Momentum:

$$x \text{ - direction } g \left(S_{0x} - S_{fx} - \frac{\partial h}{\partial x} \right) = \frac{\partial u}{\partial t} + u \frac{\partial u}{\partial x} + v \frac{\partial u}{\partial y}$$



$$y\text{-direction } g \left(S_{0y} - S_{fy} - \frac{\partial h}{\partial y} \right) = \frac{\partial v}{\partial t} + u \frac{\partial v}{\partial x} + v \frac{\partial v}{\partial y}$$

where

- e = rainfall excess (precipitation – interception – infiltration; m)
- g = gravitational acceleration (m/s²)
- h = surface depth (m)
- q_x, q_y = flow rates in the x and y directions (m/s)
- x, y = cell size (m)
- $S_0(x,y)$ = bed slopes in the x and y directions (dimensionless)
- $S_f(x,y)$ = friction slopes in the x and y directions (dimensionless)
- u, v = average velocities in the x and y directions (m/s).

Using these formulations, the model was built around an explicit centered finite-difference, diffusive wave scheme for overland flow routing. The diffusive wave method neglects momentum convection and lateral inflow (indicated by the right side of the momentum equations), and thereby assumes that water flow is driven mainly by gravity. The benefit in using such a method is the ability to account for backwater effects. A resistance law can be established from the mass continuity and momentum equations, assuming turbulent conditions, relating flow rate to depth and surface roughness, given as

$$q_{x,y} = \frac{\sqrt{S_{f(x,y)}}}{n} h^{5/3}$$

where n is the Manning coefficient (dimensionless) and is a measure of the relative frictional resistance to the flow of water.

The model explicitly accounts for spatially varying rainfall, infiltration, evaporation/vegetation interception, overland flow, and flow routing. Due to the grid resolution (30-arc second), channel flow and sediment transport are not included. As rain falls, the spatially varying hourly rainfall infiltrates the soil until saturation is reached. Once that occurs, ponding begins and overland flow commences.

Figure A.22 illustrates the model for overland flow routing. The numbers in the figure indicate the number of contributing cells for a few select grids and indicate the water flow as a function of slope.

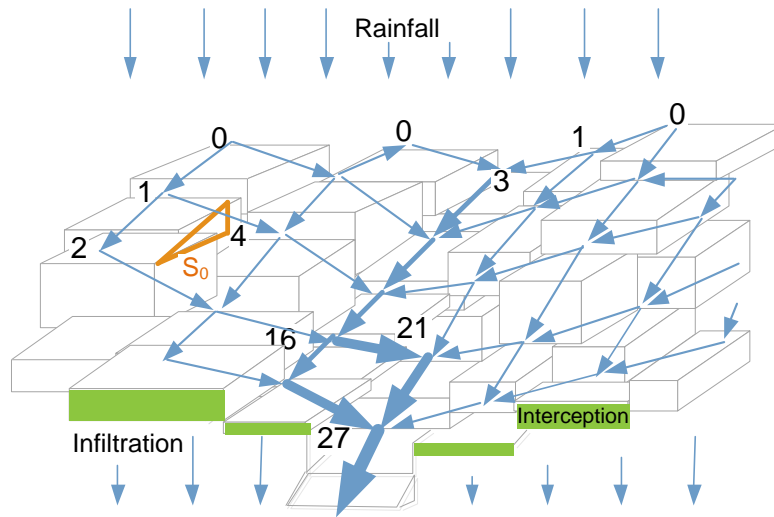


Figure A.22. Representation of Overland Flow Routing (Rojas et al. 2003)

Hourly rainfall is provided by the precipitation module while the infiltration rate and depth is calculated using the Green and Ampt (1911) infiltration model. Evaporation and vegetation interception is kept constant, at a conservative rate of 1 mm/hr, which is based on mean daily pan evaporation rates in the summer months of a tropical climate and average vegetation interception rates (Rutter et al., 1975 and 1977; Gash et al., 1995; Klingaman et al., 2007).

Overland flow is calculated from Manning’s equation (assuming turbulent conditions for the entire domain), while flow routing is based on the conservation of mass. In order to satisfy the Courant–Friedrichs–Lewy condition (Courant et al., 1967) and produce stable results, the flood module uses a 15-second time step. All initial and boundary conditions are set to zero for each cyclone event, therefore any initial soil saturation prior to the onset of a tropical cyclone event is not considered.

The modeled flood depth represents relative peak flood depth at a resolution of 30-arc seconds (approximately 1 km), which is a primary input to the loss calculation and can be used to identify regions of heightened flood risk.

4.1.4 Storm Surge Flooding

Tropical cyclone-induced surge is an abnormal rise in sea level accompanying intense storms. During intense storms, the wind circulation around the eye of the storm blows the ocean surface and produces vertical circulation in the ocean. As the storm moves towards the coast, the ocean becomes shallower, and as a result the vertical circulation of ocean water is pushed inland. The surge height is the difference between the observed level of the sea surface and the level that would have occurred in the absence of the storm (i.e., mean sea level). Daily tidal fluctuations are not considered in the storm surge calculation.

The storm surge phenomenon is illustrated in Figure A.23. Maximum storm surge observations recorded during several tropical cyclones that affected the U.S. since 1900 are presented in Figure A.24. The largest value of storm surge ever recorded worldwide was produced by Cyclone Mahina, which caused a 43 foot (13 meter) storm surge at Bathurst Bay, Australia in 1899.

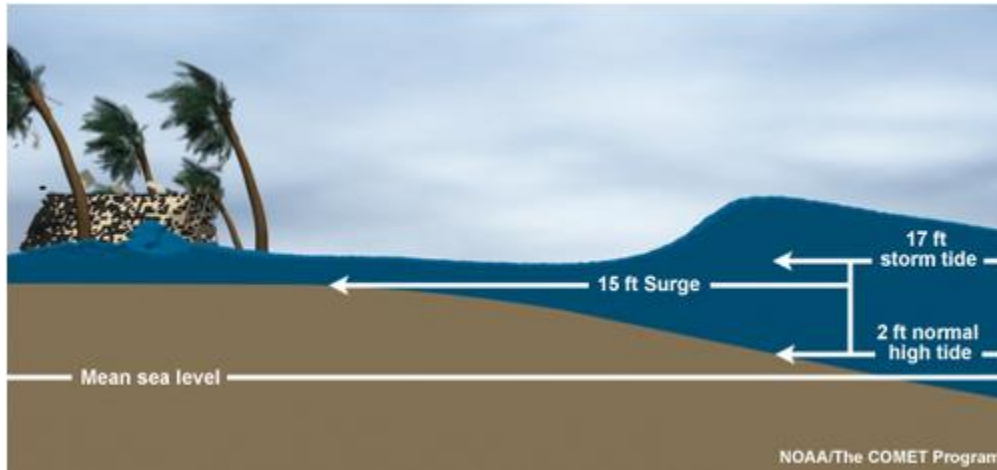


Figure A.23: Illustration of storm surge (Source: <http://www.nhc.noaa.gov/surge/>)

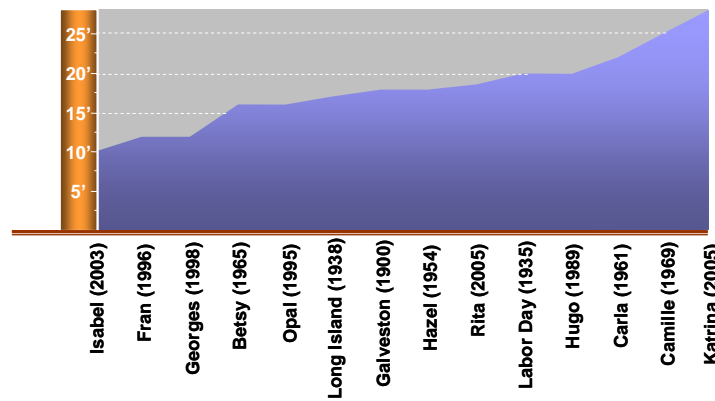


Figure A.24: Maximum surge recorded for different tropical cyclones in the U.S.

The storm surge model adopted in this study is based on a parametric model proposed by Young (1998, 2006). The storm surge model relies on the primary meteorological variables of a tropical cyclone, including central pressure (C_p), forward wind speed (V_{fm}), maximum wind velocity (V_{max}), and radius of maximum wind (R_{max}). Of these meteorological variables, C_p has the least impact on storm surge heights. Other quantities that are considered are the wind profile, the location of the site with respect to the storm track, angle of approach to the coast, and the elevation. Using Young's approach, the model first computes a significant wave height (H_s), which is defined as the average wave height of the highest third of the waves. Figure A.25 shows an example

of the dimensionless factors applied to estimate the spatial distribution of H_s as function of V_{max} and V_{fm} . For a given storm, the spatially distributed storm surge footprint can be estimated using V_{max}, V_{fm} , and the computed H_s . The spatial distribution of H_s , incorporated the effects of water depth by applying techniques developed by Liu (1996). In developing the storm surge model for the SWIO region, the storm surge is first calculated along a high-resolution coastline, and the resulting storm surge along the coastline is attenuated inland to the physical property locations that are up to 2km from the nearest coastline. The attenuation of the storm surge inland is largely dependent on terrain features and elevation profile. In this study, the rate of decay of storm surge is assumed to be 0.3m for every 1km (Nicholls et. al., 2007). Similar to the wind field, the profile of the storm surge field is not symmetrical around the storm track. The highest surge usually occurs near the radius of maximum winds, or where the strongest winds occur. Since wind direction is approximately parallel to the storm direction, in the Southern Hemisphere, the surge will be higher to the left of the tropical cyclone track than to the right, while the opposite holds for storm surge in the northern hemisphere.

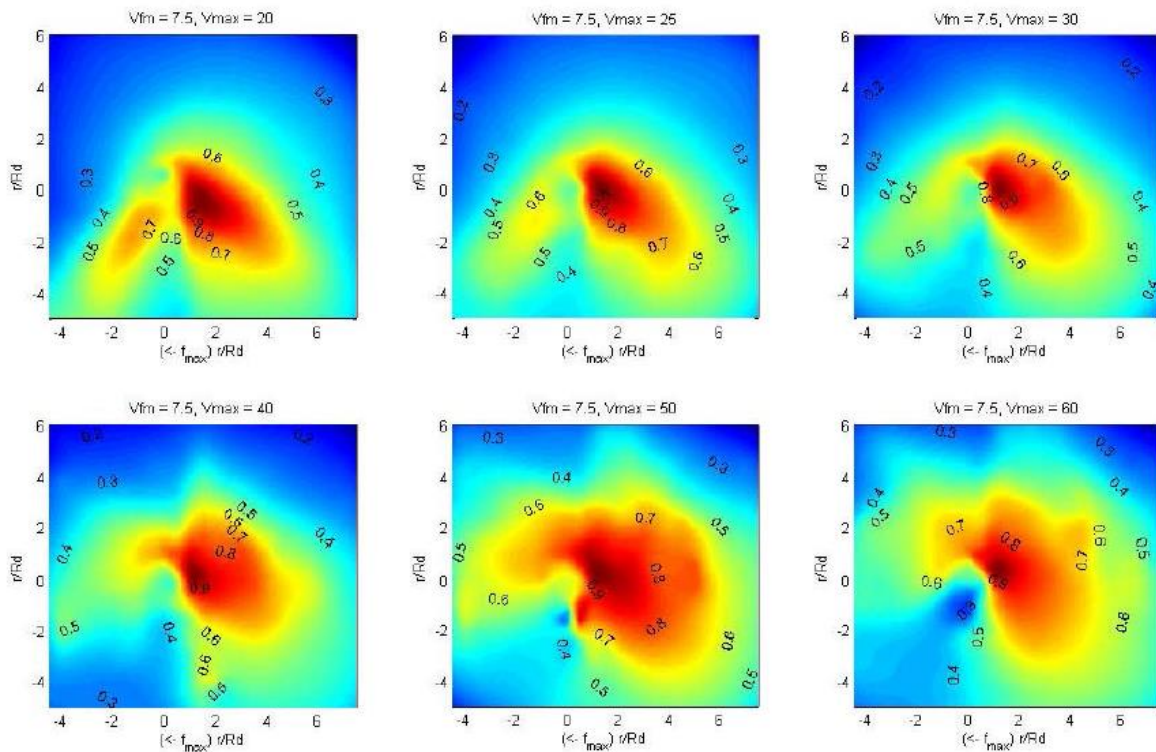


Figure A.25: Spatial distribution of H_s for different V_{fm} and V_{max}

Model Validation -

Since measured storm surge values are not available in the SWIO region, validation is instead performed by comparing the AIR model estimates with the model estimates provided by the Global Disaster Alert and

Coordinate System (GDACS). GDACS modeled results for three historical storms in Madagascar, Giovanna (2012), Haruna (2013), and Hellen (2014), are used for validation. Figure A.26 shows the comparison between modeled storm surge heights between GDACS and the AIR models for the three historical storms. The GDACS and AIR models apply different storm surge calculation methodologies, which leads to some expected differences between the two models. For example, the AIR storm surge model is primarily a function of the wind footprint, while GDACS uses a numerical hydrodynamic code to evaluate shallow water equations at the coastline (HyFlux2). Despite these differences, the estimated surge heights compare reasonably well between the two models.

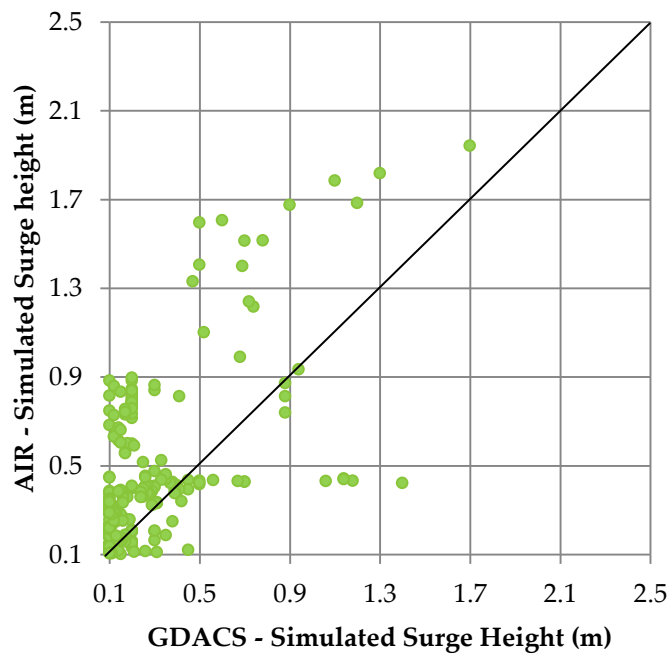


Figure A.26: Comparison of Modeled Storm Surge Heights from GDACS and AIR models

4.1.5 References

- American Society of Civil Engineers (ASCE), Minimum Design Loads for Buildings and Other Structures, ASCE-7, 650 pp.
- Courant R., K. Friedrichs, and H. Lewy, 1967, On the Partial Difference Equations of Mathematical Physics, IBM Journal, 215–234 originally in Mathematische Annalen 100, 32–74 (1928)
- Farr, T., P. Rosen, E. Caro, R. Crippen, R. Duren, S. Hensley, M. Kobrick, M. Paller, E. Rodriguez, L. Roth, D. Seal, S. Shaffer, J. Shimada, J. Umland, M. Werner, M. Oskin, D. Burbank, and D. Alsdorf, 2007, “The Shuttle Radar Topography Mission,” Reviews of Geophysics, 45, 1–33.
- Gash, J.H.C., C.R. Lloyd, and G. Lachaud 1995, “Estimating Sparse Forest Rainfall Interception with an Analytical Model,” Journal of Hydrology, 170, 79–86.
- Green, W. H., and G.A Ampt 1911, “Studies on Soil Physics – Part I. The Flow of Air and Water through Soils,” The Journal of Agricultural Science, 4, 1–24.
- Grimmond, C. S. B., and T. R. Oke 1999, “Aerodynamic Properties of Urban Areas Derived from Analysis of Surface Form,” Journal of Applied Meteorology, 38, 1262–1292
- Harper, B.A. 1999, “Numerical Modelling of Extreme Tropical Cyclone Winds,” Journal of Wind Engineering and Industrial Aerodynamics, 83, 35–47.
- Holland, G. J., 1980: An Analytic Model of the Wind and Pressure Profiles in Hurricanes. Monthly Weather Review, 108, 1212–1218.
- Holmes, J. 2007, Wind Loading on Structures, 2nd Edition, Spon Press, 392 pp.
- Kaplan, J., and M. DeMaria 1995, “A Simple Empirical Model for Predicting the Decay of Tropical Cyclone Winds after Landfall,” Journal of Applied Meteorology, 34, 2499–2512.
- Klingaman, N.P., D.F. Levia, and E.E. Frost, 2007: A Comparison of Three Canopy Interception Models for a Leafless Mixed Deciduous Forest Stand in the Eastern United States. Journal of Hydrometeorology, 8, 825–836.
- Kuleshov, Y., L. Qi, R. Fawcett, and D. Jones 2009, “On Developing a Tropical Cyclone Archive, Climatology and Seasonal Prediction for the South Indian and South Pacific Oceans,” National Climate Centre, Southeast Asian
- Lonfat M., F.D. Marks Jr., and S.S. Chen, 2004: Precipitation Distribution in Tropical Cyclones Using the Tropical Rainfall Measuring Mission (TRMM) Microwave Imager: A Global Perspective. Monthly Weather Review, 132, 1645–1660.

- Lonfat M., R. Rogers, T. Marchok, and F.D. Marks Jr. 2007, "A Parametric Model for Predicting Hurricane Rainfall," *Monthly Weather Review*, 135, 3086–3097.
- Mahendran, M. 1995, "Wind-Resistant Low-Rise Buildings in the Tropics," *ASCE Journal of Performance of Constructed Facilities*, 9, 330–346.
- National Geophysical Data Center, 2006, Bathymetry Data. Available at:
http://www.ngdc.noaa.gov/mgg/gdas/gd_designagrid.html
- Nicholls, M. 2007, Review of NT Cyclone Risks, Community Group for the Review of NT Cyclone Risks Inc., 79 pp.
- Oey, L.-Y 2005, "A Wetting and Drying Scheme for POM," *Ocean Modeling*, 9, 33–150.
- Oey, L.-Y 2006, "An OGCM with Movable Land-Sea Boundaries," *Ocean Modeling*, 13, 176–195.
- Rojas, R., P. Julien, and B. Johnson 2003, CASC2D-SED v. 1.0 Reference Manual, A 2-Dimensional Rainfall-Runoff and Sediment Model, Colorado State University, July 2003, 45 pp.
- Rutter, A.J., A.J. Morton, and P.C. Robbins 1975, "A Predictive Model of Rainfall Interception in Forests. II. Generalization of the Model and Comparison with Observations in some Coniferous and Hardwood Stands," *Journal of Applied Ecology*, 12, 367–380.
- Rutter, A.J. and A.J. Morton, 1977: A Predictive Model of Rainfall Interception in Forests: III. Sensitivity of the Model to Stand Parameters and Meteorological Variables. *Journal of Applied Ecology*, 14, 567–588.
- Simpson, J., C. Kummerow, W.K. Tao, and R.F. Adler 1996, "On the Tropical Rainfall Measuring Mission (TRMM)," *Meteorology and Atmospheric Physics*, 60, 19–36.
- Vickery, P. J. 2005, "Simple Empirical Models for Estimating the increase in the Central Pressure Of Tropical Cyclones after Landfall along the Coastline of the United States," *Journal of Applied Meteorology*, 44, 1807–1826.
- Willoughby, H. E., R. W. R. Darling and M. E. Rahn 2006, "Parametric Representation of the Primary Hurricane Vortex. Part II: A New Family of Sectionally Continuous Profiles," *Monthly Weather Review*, 134, 1102–1120.
- World Bank, World dataBank, World Development Indicators (WDI) & Global Development Finance (GDF), <http://databank.worldbank.org/ddp/home.do>

4.2 Non-Tropical Cyclone Flooding

Across the South-West Indian Ocean (SWIO) countries, non-tropical cyclone (NTC) precipitation induced flooding presents a significant regional hazard. As a result, it is sensible to account for these types of events when modeling the precipitation hazard for the SWIO countries. According to World Meteorological Organization (WMO), Southwest Indian (SI) basin is located from Africa to about 100 E (NOAA, 2015).

In order to generate a stochastic catalog of non-tropical cyclone rainfall, climatology of non-tropical cyclone rainfall must be constructed. Here, the Tropical Rainfall Measuring Mission (TRMM) multi satellite precipitation 3B42 v7 product is used (Huffman et al 2007). This continuous, gridded dataset relies on both satellite-based precipitation radar as well as total microwave imagery to derive three hourly measurements of rainfall at 0.25×0.25 degree spatial resolution from latitudes 50N to 50S. In this study, TRMM measurements from the years of 1998 through 2013 are used for analysis. A more comprehensive treatment of the climatology can be implemented using general circulation models and regional climate models as carried out by AIR for various other regions of the world; however, the project scope of work and timeline necessitated a simpler approach using a stochastic weather generator with input from TRMM data. This aspect can be further improved in future studies.

In order to isolate non-tropical cyclone induced rainfall, an approach that is common in the literature (e.g. Adler, 2000, Jiang and Zipser, 2010) is to define a radius around the track of tropical cyclones from which to remove precipitation. Research has shown that the median outer radius of Indian Ocean basin tropical storms is approximately 500km (Chavas and Emanuel, 2010). Therefore, using the IBTrACS data discussed previously for the tropical cyclone model, all rainfall within 500km of each tropical system's center location is removed from the TRMM dataset. To account for the temporal difference between IBTrACS (6-hr) and TRMM (3-hr) data, the IBTrACS data was linearly interpolated to pinpoint the storm's location at three-hour intervals (e.g., 03Z, 09Z, 15Z, 21Z).

An example of the resulting non-tropical cyclone dataset is shown below in Figure A.27. As seen, the methodology is able to successfully remove rainfall associated with tropical cyclone Eline (2000) as it makes landfall in Madagascar, while leaving the NTC rainfall found near northern Madagascar untouched. Also shown are the satisfactory results of using a linear interpolation for the three-hourly TRMM data at 03Z and 15Z.

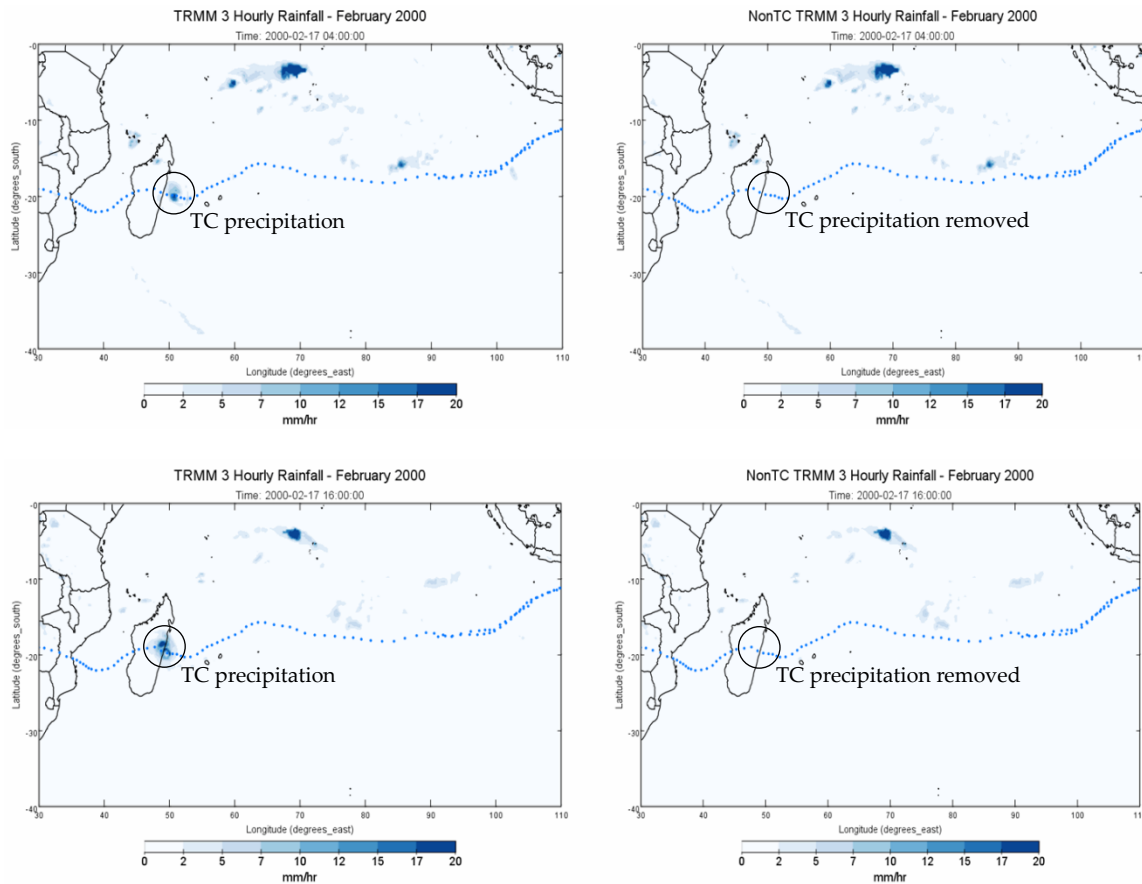


Figure A.27. Illustration of results from NTC rainfall climatology construction at two time steps: 2-17-03Z (top) and 2-17-15Z (bottom). Total TRMM rainfall, including that from Cyclone Eline (left), and the corresponding NTC related rainfall (right)

The results of the NTC TRMM rainfall climatology for a sample year are shown in Figure A.28. In 2000, an active tropical storm season setup across the eastern region of Madagascar. As shown, the methodology is able to pick up this dominant active region where nearly 250mm of rainfall during the year is caused by tropical activity. These results validate well with many studies that find 20-40% of the annual rainfall across this region can be attributed to tropical cyclone rainfall (Jiang and Zipser, 2010). Given the large total amount of rainfall in this region, nearly 200-400mm of annual rainfall remains non-tropical cyclone induced, particularly across the eastern region of Madagascar. Therefore, accounting for NTC rainfall-induced precipitation becomes necessary across the entire region.

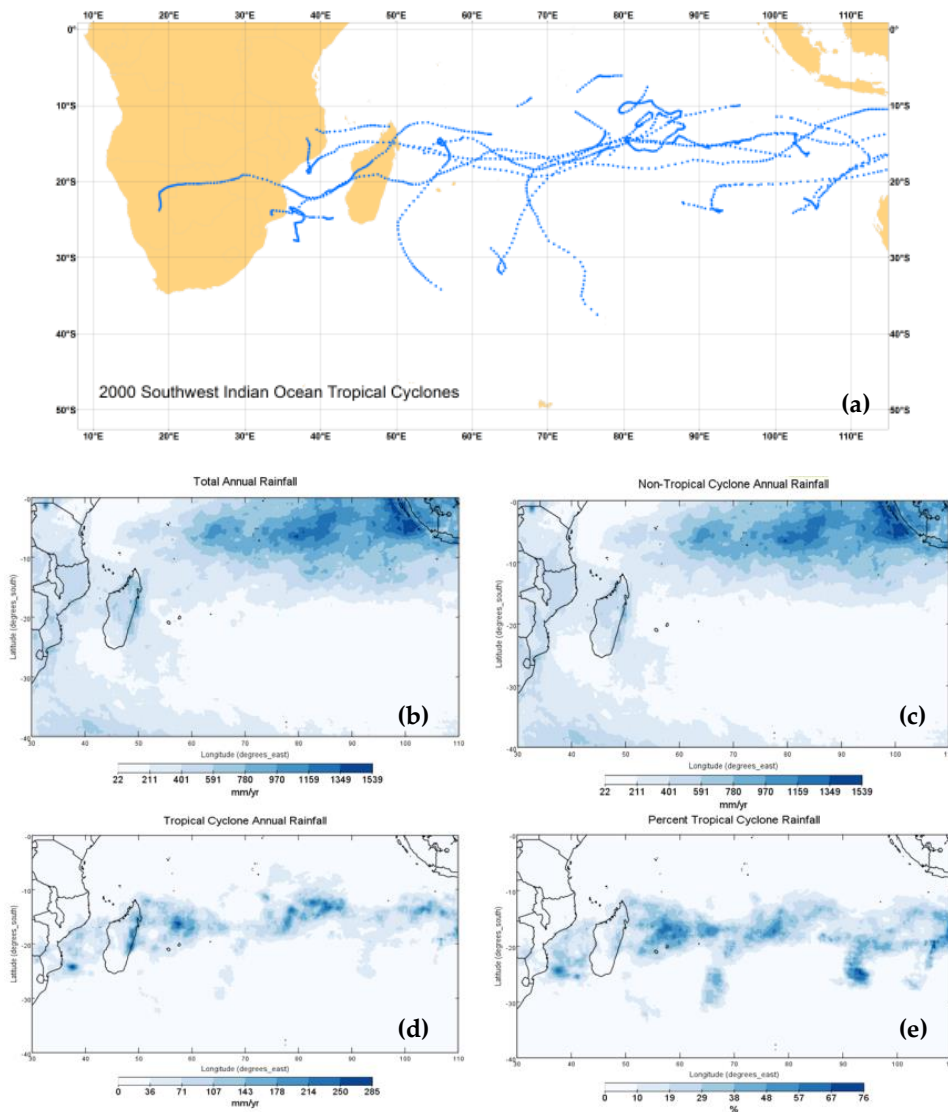


Figure A.28. Tropical cyclone activity in the SWIO basin for 2000 (a) and the resulting total TRMM rainfall (b), NTC rainfall (c), tropical cyclone rainfall (d), and percent contribution of tropical cyclone rainfall (e)

4.2.1 Generation of Stochastic Catalog for Non-Tropical Cyclone Rainfall

A stochastic catalog of daily NTC rainfall for 10,000 years was developed based on the NTC rainfall climatology derived from the TRMM data discussed above. To do this, a stochastic weather generator is employed to construct synthetic precipitation data for Madagascar, Zanzibar, Seychelles, Mauritius and Comoros. Here, the grid-cell point value from TRMM is treated as the station site data for input into the stochastic weather generator. In general, stochastic weather generators use the statistics of weather station

rainfall to construct synthetic, but physically meaningful, time-series of rainfall at a site that preserves the basic statistics of the station.

Space-Time Rainfall Generator

For this study, the development of the stochastic catalog begins with the generation of the space-time rainfall, which is the driving force in the flood simulation process. A computer simulation model for Weather GENERation (WGEN) is used to generate 3-hourly rainfall events.⁴ Rainfall simulation for an event-driven flood modeling has to satisfy the following requirements:

- Produce as yet unobserved, but realistic storm events over a long period of time (i.e., $\geq 10,000$ years) at a high spatial and temporal resolution and over the entire model domain
- Preserve rainfall occurrence and amount distributions at each location (e.g., rainfall accumulations)
- Preserve spatial and temporal dependencies in rainfall patterns (e.g., spatial distribution of areas that receive rain versus areas that do not)
- Preserve the seasonality of storm event occurrence and amount distributions

In order to meet the above requirements, the rainfall simulation process is split into event generation for hydrologic zones and preliminary hazard validation. These two processes are discussed in the next sections.

Hydro-Climatology based Event Generation

In hydrology, it is well known that rainfall fields are inherently heterogeneous, which means that the statistical moments of rainfall (e.g., the mean and the variance) change from one location to another. Statistical moments of long-term precipitation characteristics vary in different regions (climatic zones). Rainfall occurrence rates and amounts must be accurately simulated in order to account for the zonal variability of precipitation during stochastic rainfall event generation. A study by Smith and Schreiber (1973) states that a first-order Markov chain is more accurate than a Bernoulli model (i.e., sequential independence) for describing the occurrence of wet or dry time increments. For this study, a first-order Markov chain with only two states, wet or dry was used. A time increment is defined as wet if the total precipitation is greater than 0.2 mm. Let $P_i(W|W)$ be the probability of a wet time increment on time increment i given a wet time increment on time increment $i - 1$; let $P_i(W|D)$ be the probability of a wet time increment on time increment i given a dry time increment on time increment $i - 1$. Then:

$$P_i(D|W) = 1 - P_i(W|W) \tag{1}$$

⁴ The WGEN model is based on the procedure described by Richardson (1981). The precipitation component of WGEN is a Markov chain-gamma model. A first-order Markov chain with only two states, wet or dry transition probabilities, is used to generate the occurrence of wet or dry days. The transition probabilities are defined given $P_i(W|W)$, $P_i(W|D)$, and the wet or dry state on day $i - 1$. When a wet-day is generated, the two-parameter gamma distribution is used to generate the precipitation amount.

$$P_i(D|D) = 1 - P_i(W|D) \quad (2)$$

where $P_i(D|W)$ and $P_i(D|D)$ are the probabilities of a dry time increment given a wet time increment on time increment $i - 1$ and a dry time increment given a dry time increment on time increment $i - 1$, respectively. Therefore, transition probabilities are fully defined given $P_i(W|W)$, $P_i(W|D)$, and the wet or dry state on time increment $i - 1$.

Several probability density functions have been used to describe the distribution of rainfall amounts (Smith and Schreiber 1974; Woolhiser and Roldan 1982). Richardson (1982) has shown the two-parameter gamma distribution to be superior for describing precipitation amounts than the one-parameter exponential distribution. The density function of the two-parameter gamma distribution is given by:

$$f(p) = \frac{p^{\alpha-1}e^{-p/\beta}}{\beta^\alpha\Gamma(\alpha)}, p, \alpha, \beta > 0 \quad (3)$$

where $f(p)$ is the density function of precipitation amount (p), and α and β are the shape and scale parameters, respectively, e is the base of natural logarithm, and $\Gamma(\alpha)$ is the incomplete gamma function of α , and is given by:

$$\Gamma(\alpha) = \int_0^\infty p^{\alpha-1}e^{-p} dp \quad (4)$$

The values of $P_i(W|W)$, $P_i(W|D)$, α , and β vary continuously during the year for most locations. In WGEN, each of the four precipitation parameters are kept constant for a given month but are varied from month to month. WGEN has been widely used in various studies in different climatic conditions and was found to have excellent success in replicating the climatic rainfall statistics.

4.2.2 Non-Tropical Cyclone Induced Precipitation

In this section, the process of determining which NTC storms trigger a damaging precipitation event is explained using the stochastically generated NTC rainfall discussed previously.

To accommodate the nontrivial nature of NTC rainfall, a “7-5-days clause” is used to determine the occurrence of an NTC precipitation event — a seven-day minimum total rainfall threshold and a five-day inter-storm period. The clause reflects the observed duration of extreme precipitation events associated with monsoon-like weather systems, and precipitation threshold value can represent the tipping point of a damaging event occurring.

In the AIR model, the rules for constituting storm and precipitation events are as follows:



- An event starts when a storm occurs anywhere within the country if at least 5 days have passed after the peak of the rainfall from the previous event;
- An event ends if the inter-storm period, the time period between the peak rainfall from the last storm (ST_i) and the beginning of the next storm (ST_j), is at least 5 days;
- If the inter-storm period is less than 5 days, but the time from the beginning of ST_i is more than 7 days, then the end of the event and the beginning of a new one is set up at the point of minimum precipitation between ST_i and ST_j ;
- In contrast, if the inter-storm period is less than 5 days, and the time from the beginning of ST_i is also less than 7 days, then two (or more) events are considered to be a single event with multiple rainfall peaks. The end of such event is set up at the end of ST_j (or the very last event), implying that events can actually last longer than 7 days;
- The event is considered damaging if the cumulative rainfall during the storm period exceeds a threshold for each country;
- If two events occur within different start dates but overlap in their 7-day (or actual duration) coverage, then they are considered one event, regardless of spatial location.

Figure A.29 illustrates the event-composition process, using an example of two NTC precipitation events identified from precipitation series a station (Zone 3 and Zone 4) for Madagascar. The blue bars in the figure show the daily rainfall derived from the NTC TRMM data at the two zones. The box in solid green indicates when the concatenation of two storms is triggered according to the clause rules; that is, the duration from the previous peak to the beginning of the next storm is less than 5 days. The pink solid box indicates when the time from the beginning of previous peak event to the next peak event is more than 7 days. The red dash-line box encloses events identified based on the cumulative precipitation threshold value.

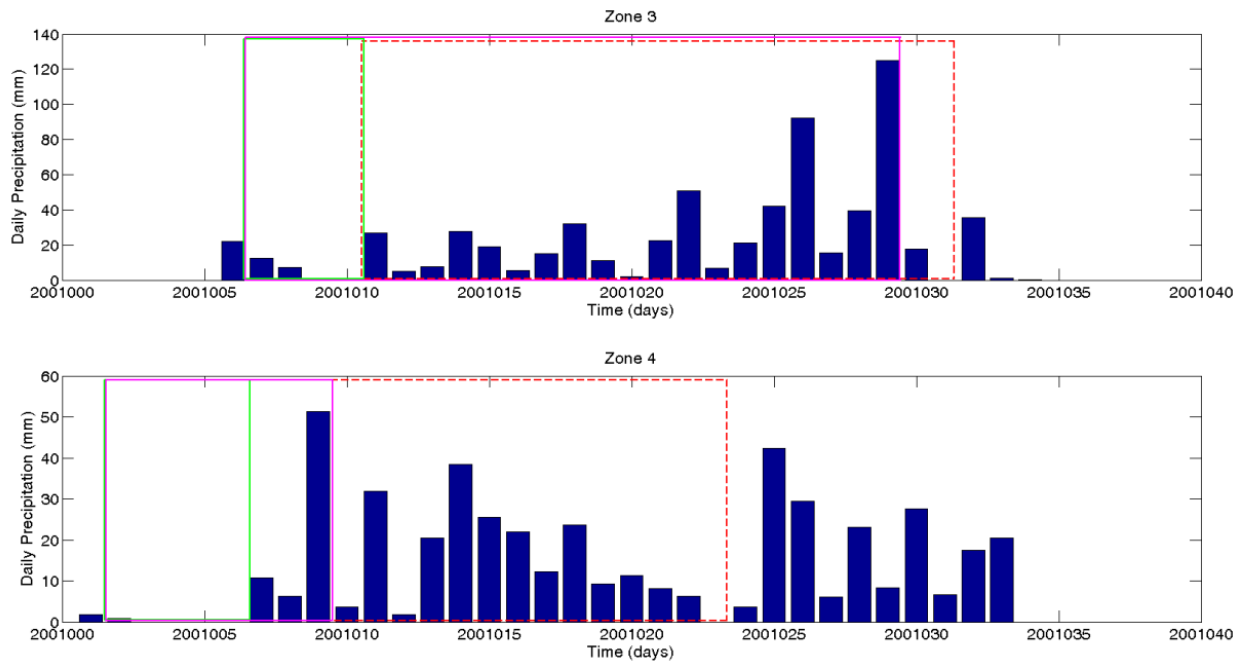


Figure A.29. Composition of precipitation events for the 7-5-days clause. Blue bars are daily NTC rainfall, red dash box represent the cumulative rainfall during the storm period, solid magenta box represent the time from the beginning of the previous peak event to the next peak event and green solid box represents the duration from the previous peak to the beginning of the next storm

4.2.3 Non-Tropical Cyclone Flooding

TC and NTC precipitation-induced flooding are modeled using the CASC2D-SED methodology overviewed previously and discussed in detail in “Tropical Cyclone” section of Appendix A. For NTC, event precipitation is assumed to fall uniformly over the entire independent precipitation region for the duration of the event. The CASC2D model then dynamically distributes the precipitation throughout the affected region and calculates flood depths.

Prior to calculating flood depths, a precipitation correction factor is applied to the TRMM 3-hr data to account for the uncertainties associated to TRMM multi-satellite precipitation estimates. The correction factor is calculated by comparing historical monthly rain gauge totals from multiple weather stations throughout the region to TRMM totals during the same time period. The monthly precipitation station data was provided by local meteorological agencies. Figure A.30 illustrates the ratio of mean monthly precipitation between station measurements and TRMM data for Madagascar and Mauritius. TRMM data in the region was found to be systematically lower than local gauge data, therefore the correction factor applied for all countries is >1.

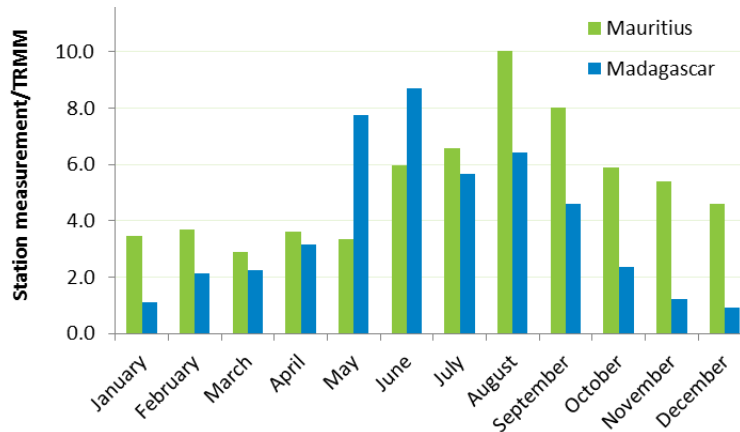


Figure A.30: Ratio of monthly weather station rain gauge measurements to TRMM data for weather stations in Madagascar and Mauritius.

4.2.4 Precipitation Hazard Analysis

The analysis of historical TRMM data and the generation of stochastic precipitation catalogs for each island nation in the SWIO region are presented in the following sections. Additionally, country specific event thresholds and precipitation statistics are discussed.

4.2.4.1 Comoros

Given the spatial extent and climatic variability of the SWIO region, and the relatively small land area of the Comoros islands, the climatic variability across the country of Comoros islands is considered minimal. Therefore, it is assumed that the variability of the climate is closely captured by a single TRMM grid node, which is used to represent the rainfall pattern and characteristics across the islands. The number of TRMM grid locations covering the main island of Comoros, Grande Comore, is shown in Figure A.31.

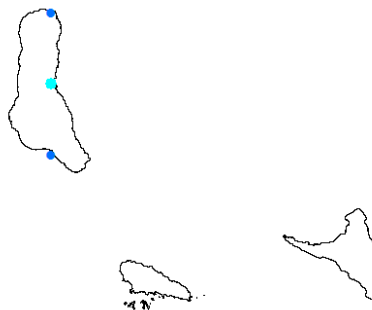


Figure A.31. TRMM grid points covering the main island of Comoros. The highlighted point in cyan represents the selected TRMM grid cell

Prior to the generation of stochastic precipitation, historical validation of precipitation modeling for the TRMM historical time period between 1998 and 2013 is performed for the selected TRMM point (Figure A.32). It is seen that the selected TRMM point represent long-term climatology and rainfall characteristics of Comoros with minimum error statistics across the period from 1998-2013. Stochastic generation of 10,000 years of daily precipitation is performed using WGEN for the selected TRMM grid cell location for Comoros.

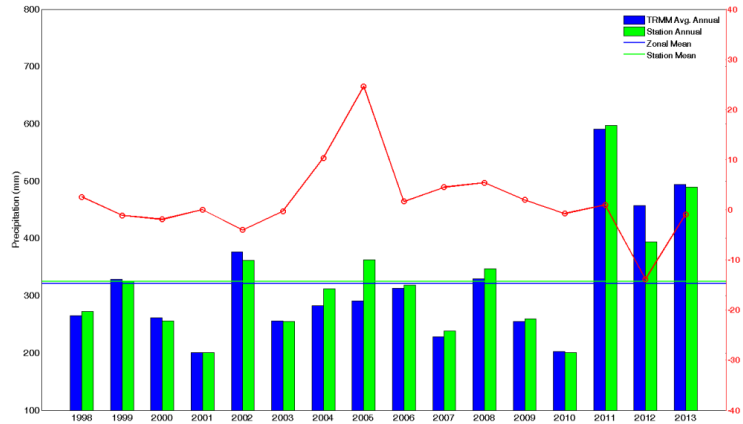


Figure A.32. Comparison of historical average annual TRMM precipitation with the selected TRMM grid point. Blue bars show the average annual precipitation of across all years (1998-2013) and green bars shows the selected TRMM station. Red line shows the error percentage for each year.

The statistical properties of daily precipitation, namely the mean, standard deviation, coefficient of variation of the historical (TRMM, 1998-2013) and stochastically generated (10,000 years) are compared in Figure A.33. The results demonstrate that the precipitation model preserves the statistical properties of the daily precipitation and seasonality of precipitation in Comoros. Daily mean precipitation amounts are well preserved (Figure A.33a) and the dispersion of daily precipitation amounts from the mean daily standard deviation is relatively preserved (Figure A.33b).

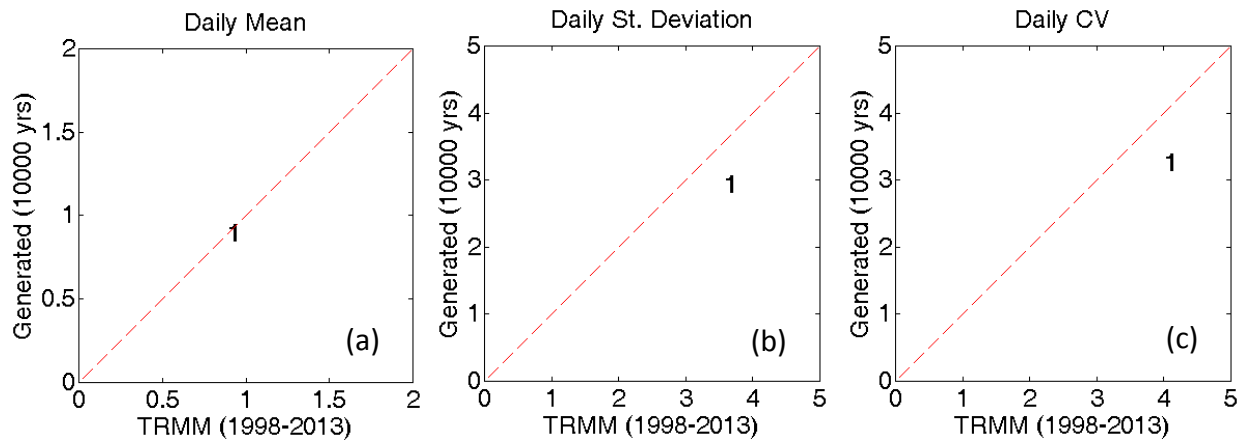


Figure A.33. Comparison of daily statistical properties from historical TRMM precipitation and 10,000 years of stochastic simulations for the selected TRMM point

WGEN-generated 10,000-year stochastic daily precipitation catalog is compared with the observed areal precipitation for Comoros in Figure A.34 and Table A.2. It is noted that the areal minimum mean and maximum precipitation from the stochastic simulation of 10,000 years differ slightly when compared to the TRMM historical period. This marginal difference is expected and is primarily attributed to the underestimated daily standard deviation and the relatively short duration of the historical catalog.

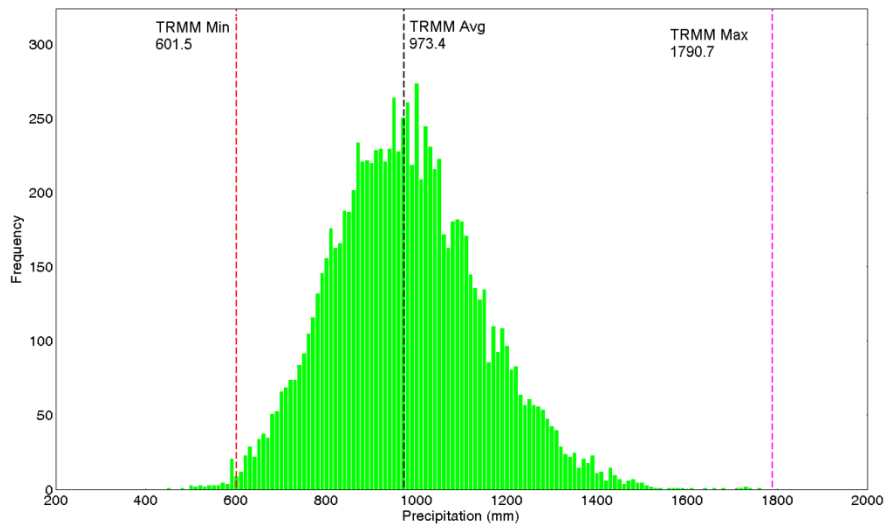


Figure A.34. Frequency distribution of stochastically generated and historical areal annual precipitation across Comoros

Table A.2. Comparison of areal annual precipitation for 10,000 years across Comoros compared to the historical time period

<i>Statistic</i>	<i>10,000 yrs Precipitation (mm)</i>	<i>TRMM (1998-2012) Precipitation (mm)</i>
Mean	979	973
Minimum	446	602
Maximum	1,757	1,791

The 7-5-days clause is applied to both the NTC TRMM data and the stochastic catalog for the Comoros. Note that some years; there is no recorded NTC related flood event in the consequence database. The annual frequency of NTC precipitation events based on the Consequence Database is plotted against that derived from the NTC TRMM data in Figure A.35, which shows that the inter-annual variation of both data bears high resemblance.

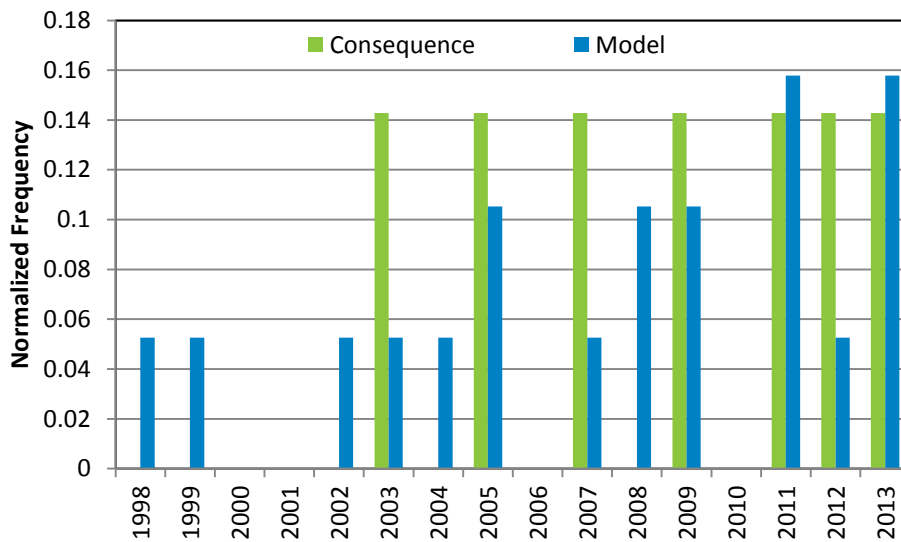


Figure A.35. Comparison between Consequence Database and TRMM-based NTC Precipitation Event Occurrence by Year for Comoros

4.2.4.2 Madagascar

Madagascar is divided into five hydro-climatological zones that reflect the hydro-climatology of the region⁵. The number of TRMM grid locations covering each hydro-climatological zones of the Madagascar is shown in Figure A.36. Out of these, five representative TRMM grid locations are selected for each of the hydrologic zones to generate the 10,000 year precipitation stochastic catalog. The TRMM grid locations with the minimum precipitation error in each zone are selected for catalog generation. The respective error values for this comparison are obtained by subtracting the mean annual precipitation at each grid location from the corresponding zonal mean annual precipitation for the historical period of TRMM measurements (1998 to 2013).

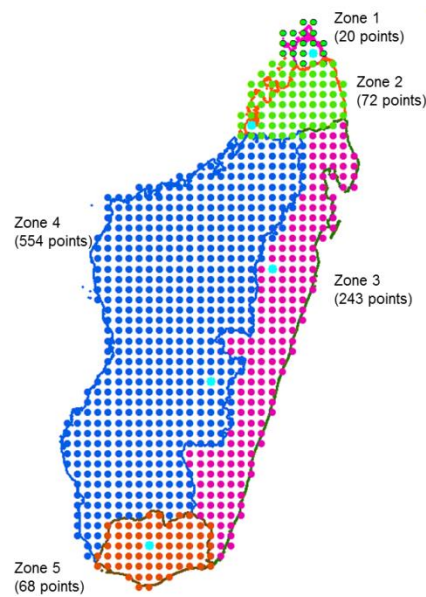


Figure A.36. Hydro-climatology based zonal representation of TRMM grid points within Madagascar. The highlighted points in cyan represent the selected TRMM grid cells.

Prior to the generation of stochastic precipitation, historical validation of precipitation modeling for the TRMM historical time period between 1998 and 2013 is performed for the selected TRMM points (Figure A.37). It is seen that each selected TRMM point represents the long-term climatology and rainfall characteristics of Madagascar with minimum error statistics across the period from 1998-2013. Stochastic generation of 10,000 years of daily precipitation is performed using WGEN for the selected TRMM grid cell location for each zone in Madagascar.

⁵ The report states that the Madagascar is divided into five hydro-climatological zones considering the relief: (i) slopes of the Ambre mountain, (ii) Tsaratanana slopes, (iii) east slopes running into the Indian ocean, (iv) western and north-western slopes whose waters run into the Mozambique channel, and (v) southern slope (Aldegheri, 1972).

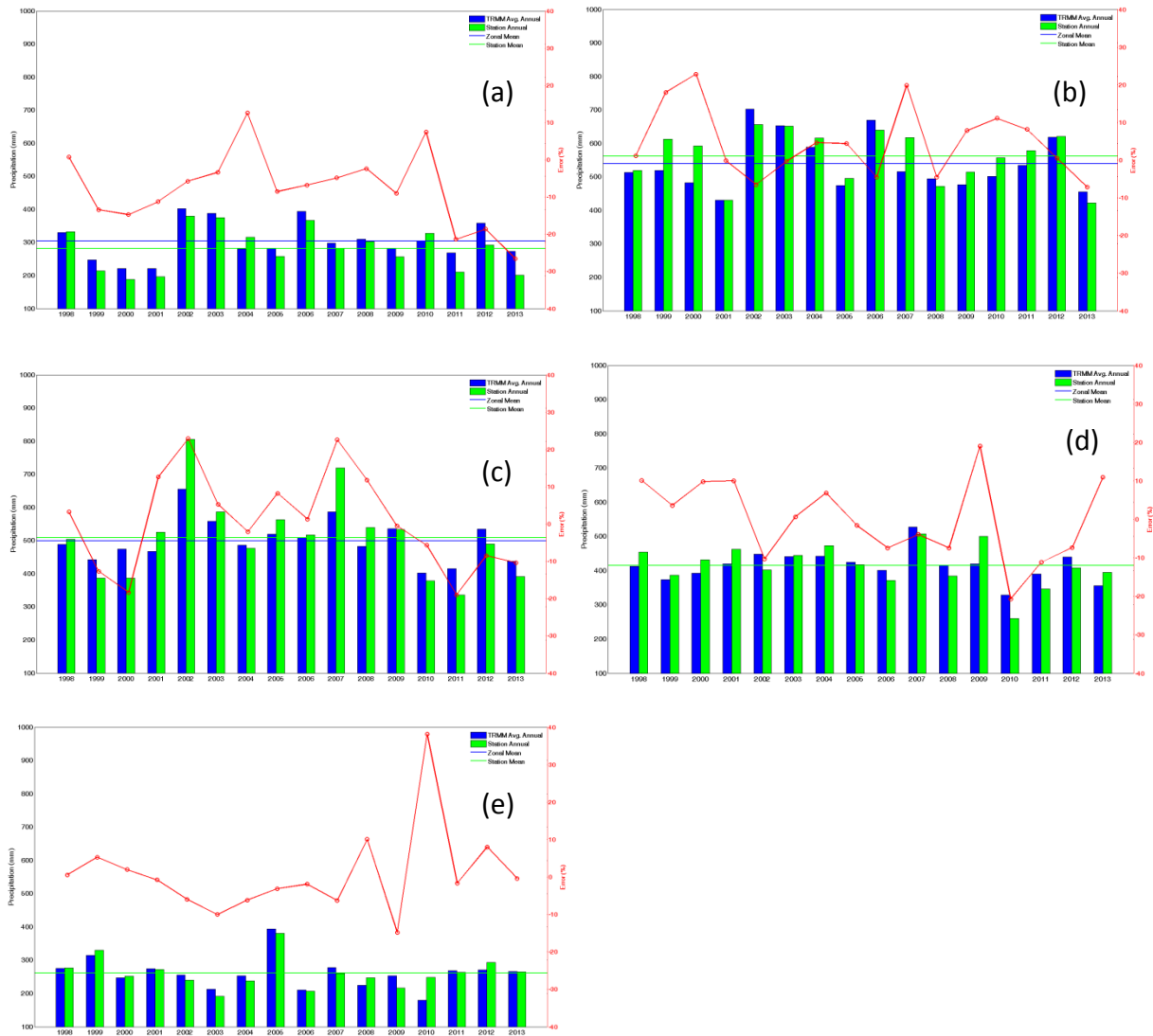


Figure A.37. Comparison of historical average annual TRMM precipitation with the selected TRMM grid point. Blue bars show the average annual precipitation of across all years (1998-2013) and green bars shows the selected TRMM station for each zone; (a) zone 1, (b) zone 2, (c) zone 3, (d) zone 4, and (e) zone 5. Red line shows the error percentage for each year.

In order to validate the TRMM derived NTC precipitation with observed precipitation during the NTC period (i.e., from May to October), a rainfall gauging station located at the airport of Anatananvario location is used. The effects of active tropical cyclone induced precipitation are minimized by omitting precipitation recorded during the period from November to April, which coincides with the tropical cyclone season. The results of this comparison are presented in Figure A.38 and demonstrate good agreement between gauge measurements and the satellite derived NTC precipitation used to calibrate the model.

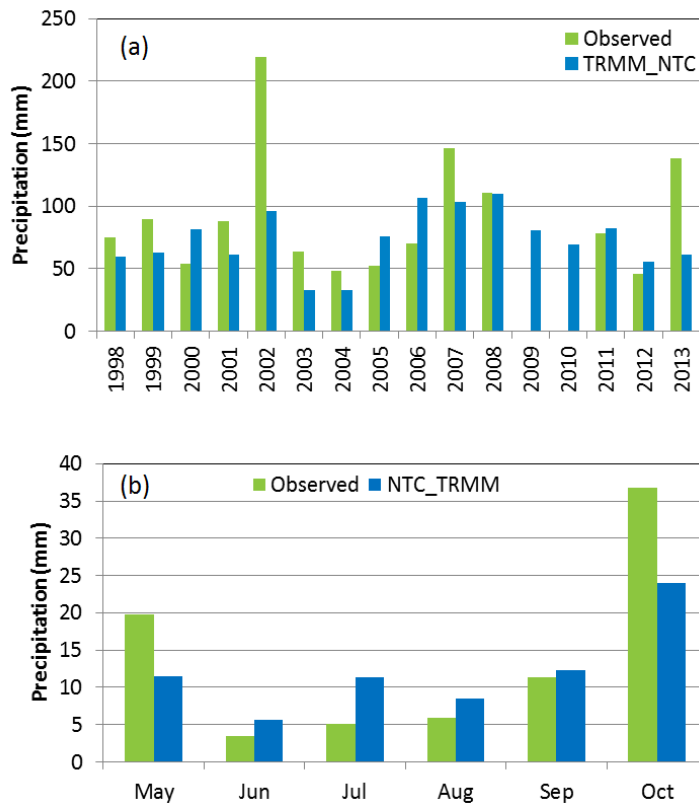


Figure A.38. Comparison of NTC TRMM precipitation with observed historical rain gauge data for the NTC period from May to October. Blue bars show the NTC TRMM precipitation of across all years (1998-2013) and green bars shows the observed precipitation; (a) comparison of total annual precipitation for the historical period from 1998-2013, and (b) Comparison of mean monthly precipitation for the same historical period.

Each hydrologic zone is assumed to have independent rainfall patterns and characteristics. This assumption is validated by performing a cross-correlation analysis for daily TRMM precipitation at the selected stations during the historical period between 1998 and 2013. As shown in Table A.3, the cross-correlations between each pair of hydrologic zones are relatively low, suggesting that the assumption of independence is reasonable.

Stochastic generation of 10,000 years of daily precipitation for the five hydrologic zones in Madagascar is performed using WGEN for the selected TRMM grid cell locations for each zone. Furthermore, a stochastic simulation of daily precipitation is performed in order to preserve the seasonality of precipitation occurrence.

The statistical properties of daily precipitation, such as the mean, standard deviation, coefficient of variation, and seasonality, of the historical (TRMM, 1998-2013) and stochastically generated (10,000 years) are compared in Figure A.39. The results reveal that the precipitation modeling preserves the statistical properties of the daily precipitation and seasonality of precipitation across all the hydrologic zones of the Madagascar. Daily mean

precipitation amounts are well preserved across the five hydrologic zones (Figure A.39a) and, as expected, the minimum and maximum mean daily precipitation values are observed in hydrologic zones 1 and 4, respectively. The dispersion of daily precipitation amounts from the mean daily standard deviation is also preserved (Figure A.39b).

Table A.3. Comparison of cross-correlation statistics of the selected TRMM grid cells in each zone for the historical time period between 1998 and 2013

Zone A	Zone B	Cross-correlation (ρ_{AB})
1	2	0.27
1	3	0.16
1	4	0.10
1	5	0.04
2	3	0.22
2	4	0.16
2	5	0.07
3	4	0.27
3	5	0.07
4	5	0.20

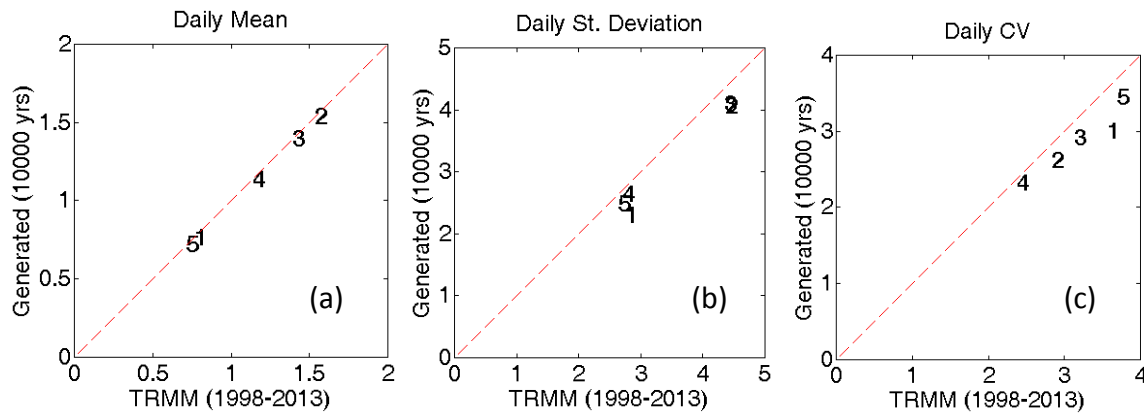


Figure A.39. Comparison of daily statistical properties from historical TRMM precipitation and 10,000 years of stochastic simulations for each zone number

WGEN-based stochastic simulation of precipitation for 10,000 years preserves the seasonality of precipitation event occurrence and amounts (Figure A.40). Monthly precipitation variability is also well-simulated across all hydrologic zones. Finally, the WGEN-generated 10,000-year stochastic daily precipitation catalog is compared with the observed areal precipitation for the country of Madagascar in Figure A.40 and Table A.4. As expected, the areal minimum and maximum precipitation from the stochastic simulation of 10,000 years are different

compared to the TRMM historical period due to the limited duration of the historical catalog (i.e., 16 years) and the unbounded gamma distribution applied to simulate precipitation rates.

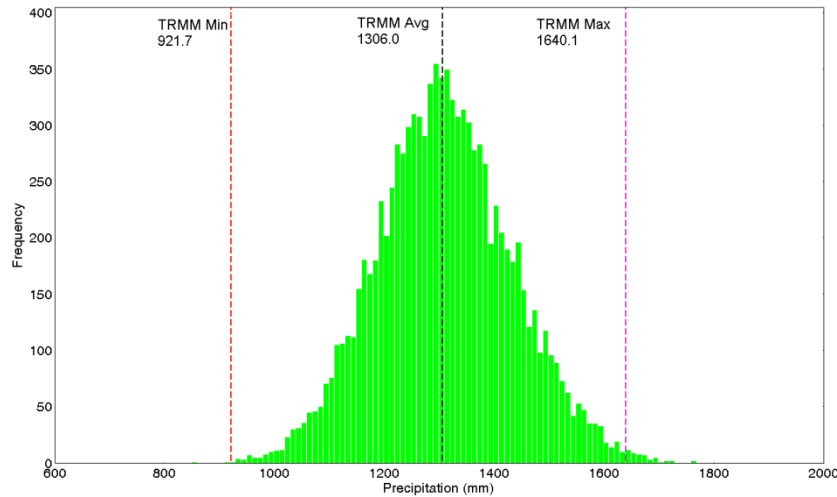


Figure A.40. Frequency distribution of stochastically generated and historical areal annual precipitation across Madagascar

Table A.4. Comparison of areal annual precipitation for 10,000 years across Madagascar compared to the historical time period

<i>Statistic</i>	<i>10,000 yrs Precipitation (mm)</i>	<i>TRMM (1998-2012) Precipitation (mm)</i>
Mean	1,310	1,306
Minimum	849	922
Maximum	1,764	1,640

The 7-5-days clause is applied to both the NTC TRMM data and the stochastic catalog for Madagascar. To examine if the identified NTC flood events exhibit a realistic frequency of occurrence, the Consequence Database presented in Appendix B, which consists of a list of significant loss-causing historical events, is compared to the event definition applied to the historical (TRMM) rainfall catalog. Multiple filters (e.g., no named storms and no tropical cyclone related annotations) are first used to identify the reported NTC precipitation events in the Consequence Database, and the total number of such events is derived for each year from 1998 to 2013. The annual frequency of NTC precipitation events based on the Consequence Database is plotted against that derived from the NTC TRMM data in Figure A.41, which shows that the inter-annual variation of both data bears reasonable resemblance.

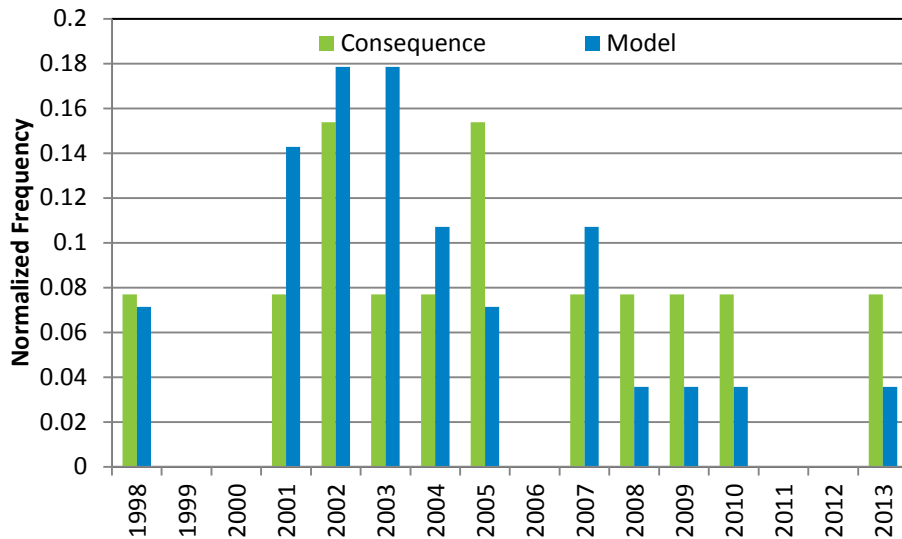


Figure A.41. Comparison between Consequence Database and TRMM-based NTC Precipitation Event Occurrence by Year for Madagascar

The spatial frequency of NTC precipitation event occurrences is further examined at the selected TRMM grid points across Madagascar. The total number of NTC event occurrences at each station is classified into three occurrence rates (e.g., high, middle, and low) based on the precipitation quartiles of the whole country, and the comparison of historical and stochastic occurrence rates are presented in Figure A.42. The results from this comparison indicate similar areas prone to NTC precipitation events in the historical and stochastic catalog, namely the eastern and northern parts of the country.

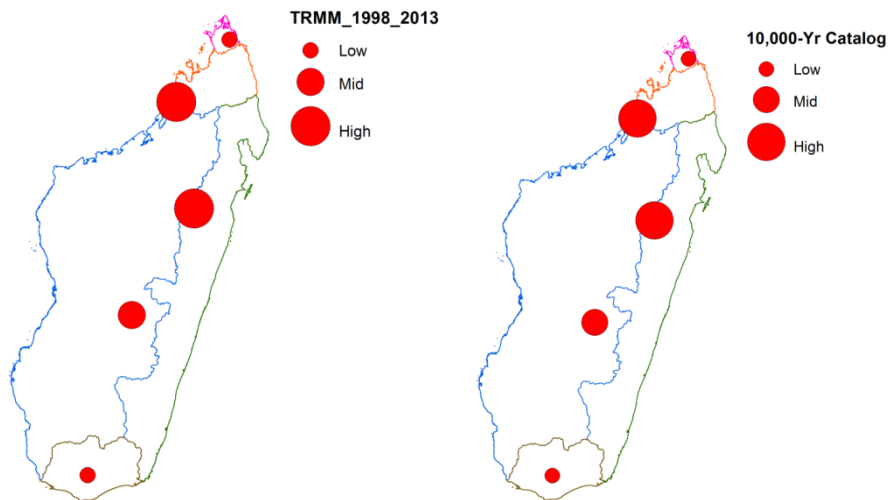


Figure A.42. Comparison between the NTC Precipitation Event Occurrence Frequency of the NTC TRMM Data (left) and that of the Stochastic Catalog (right)

4.2.4.3 Mauritius

Climatic variability across the main island of Mauritius is relatively minimal, therefore it is assumed that the variability of the climate can be captured by a single TRMM grid node. The number of TRMM grid locations covering the main island of Mauritius is shown in Figure A.43.

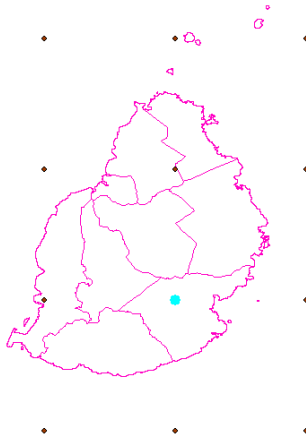


Figure A.43. TRMM grid points covering main islands of Mauritius. The highlighted point in cyan represents the selected TRMM grid cell.

A comparison between the historical TRMM precipitation for the country average and selected TRMM grid point during the time period of 1998 to 2013 is shown in Figure A.44. It is seen that the selected TRMM point closely represents the long-term climatology and rainfall characteristics of Mauritius with minimum error statistics across the period from 1998-2013. Stochastic generation of 10,000 years of daily precipitation is performed using WGEN for the selected TRMM grid cell location for Mauritius.

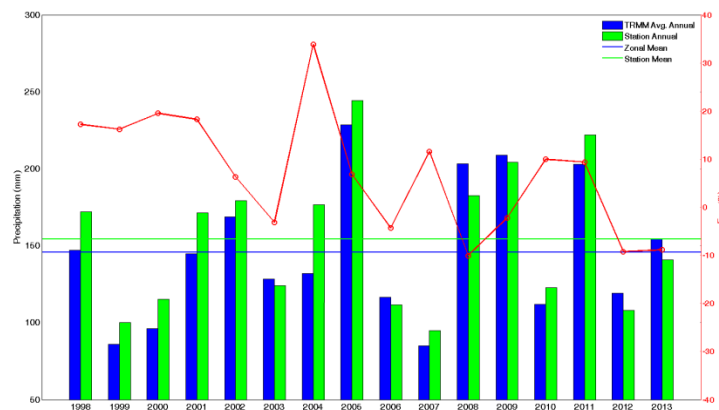


Figure A.44. Comparison of historical average annual TRMM precipitation with the selected TRMM grid point. Blue bars show the average annual precipitation of across all years (1998-2013) and green bars shows the selected TRMM station. Red line shows the error percentage for each year.

The statistical properties of daily precipitation, such as the mean, standard deviation, coefficient of variation of the historical (TRMM, 1998-2013) and stochastically generated (10,000 years) are compared in Figure A.45. The results reveal that the modeled precipitation preserves the statistical properties of the historical daily precipitation and seasonality of precipitation in Mauritius. Daily mean precipitation amounts are well preserved (Figure A.45a) and, the dispersion of daily precipitation amounts from the mean daily standard deviation is relatively preserved (Figure A.45b).

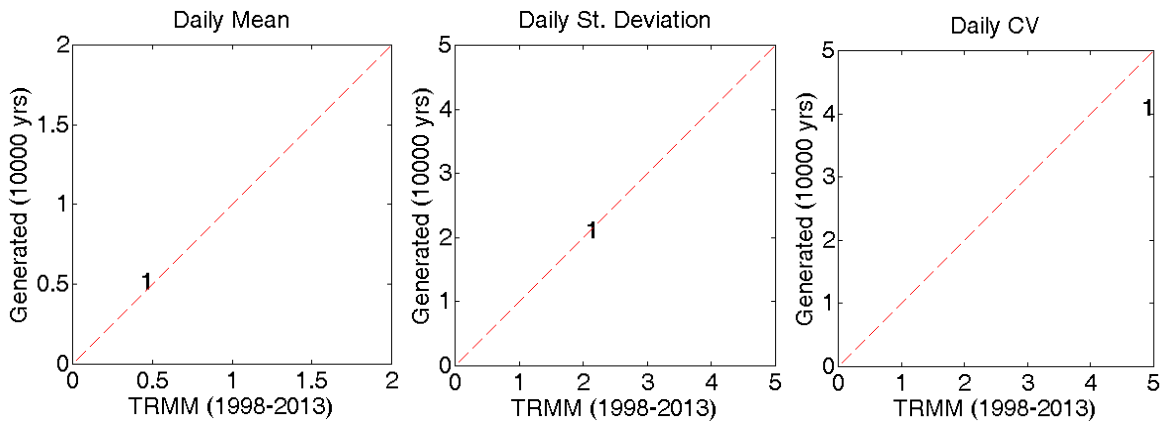


Figure A.45. Comparison of daily statistical properties from historical TRMM precipitation and 10,000 years of stochastic simulations for the selected TRMM point.

WGEN-generated 10,000-year stochastic daily precipitation catalog is compared with the observed areal precipitation for Mauritius in Figure A.46 and Table A.5. It is noted that the areal maximum precipitation from the stochastic simulation of 10,000 years are different compared to the TRMM historical period. This difference is primarily due to precipitation event occurrence and amount distributions of 10,000 years stochastic simulations at the selected TRMM point.

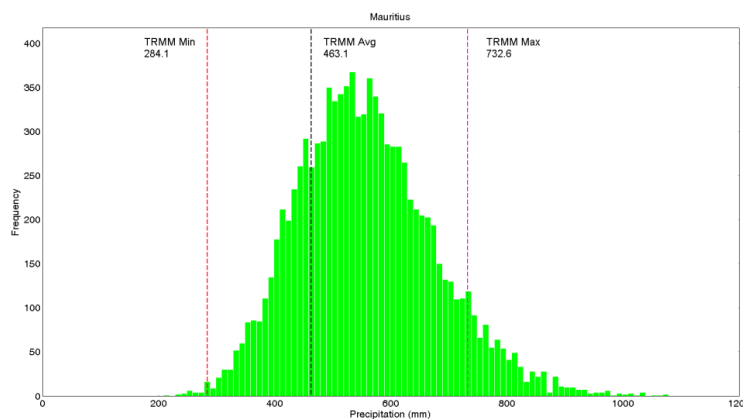


Figure A.46. Frequency distribution of stochastically generated and historical areal annual precipitation across Mauritius

Table A.5: Comparison of areal annual precipitation for 10,000 years across Mauritius compared to the historical time period

<i>Statistic</i>	<i>10,000 yrs Precipitation (mm)</i>	<i>TRMM (1998-2012) Precipitation (mm)</i>
Mean	557	463
Minimum	209	284
Maximum	1,078	733

The 7-5-days clause is applied to both the NTC TRMM data and the stochastic catalog for Mauritius. To examine if the identified NTC flood events exhibit a realistic frequency of occurrence, the Consequence Database developed in Appendix B, which consists of a list of significant loss-causing historical events, is compared to the event definition applied to the historical (TRMM) rainfall catalog. Multiple filters (e.g., no named storms and no tropical cyclone related annotations) are first used to identify the reported NTC precipitation events in the Consequence Database, and the total number of such events is derived for each year from 1998 to 2013. The annual frequency of NTC precipitation events based on the Consequence Database is plotted against that derived from the NTC TRMM data in Figure A.47, which shows that the inter-annual variation of both data bears high resemblance.

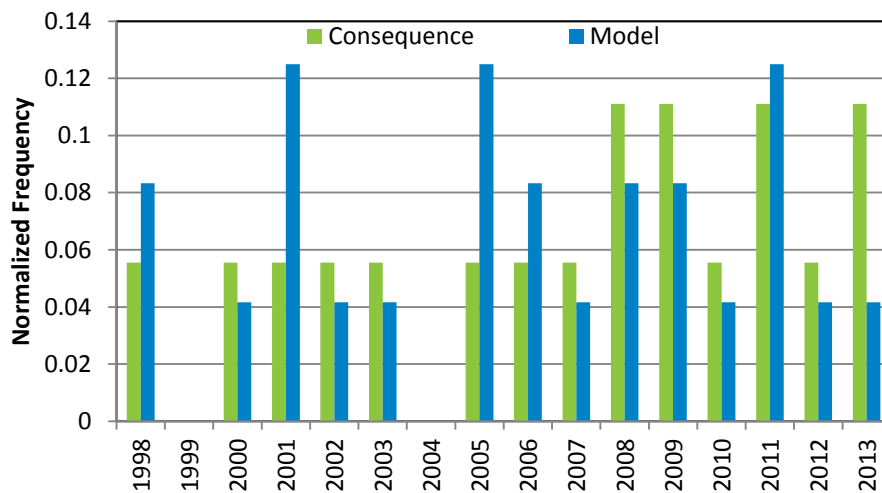


Figure A.47. Comparison between Consequence Database and TRMM-based NTC Precipitation Event Occurrence by Year for Mauritius

4.2.4.4 Seychelles

Similar to other island countries in the SWIO region, the climatic variability across the inner islands of Seychelles is minimal. Therefore, it is assumed that the variability of the climate can be captured by a single TRMM grid node, which represents the rainfall pattern and characteristics across the main islands. The number of TRMM grid locations covering Seychelles is shown in Figure A.48.

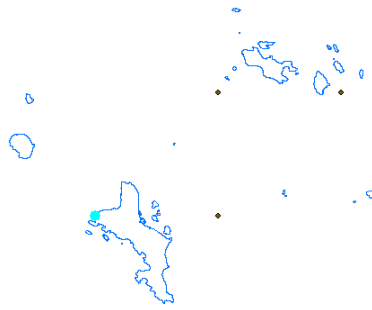


Figure A.48. TRMM grid points covering the inner islands of Seychelles. The highlighted point in cyan represents the selected TRMM grid cell.

Historical validation of precipitation modeling for the TRMM historical time period between 1998 and 2013 is shown in Figure A.49. It is seen that the selected TRMM point represent long-term climatology and rainfall characteristics of Seychelles with minimum error statistics across the period from 1998-2013. Stochastic generation of 10,000 years of daily precipitation is performed using WGEN for the selected TRMM grid cell location for Seychelles.

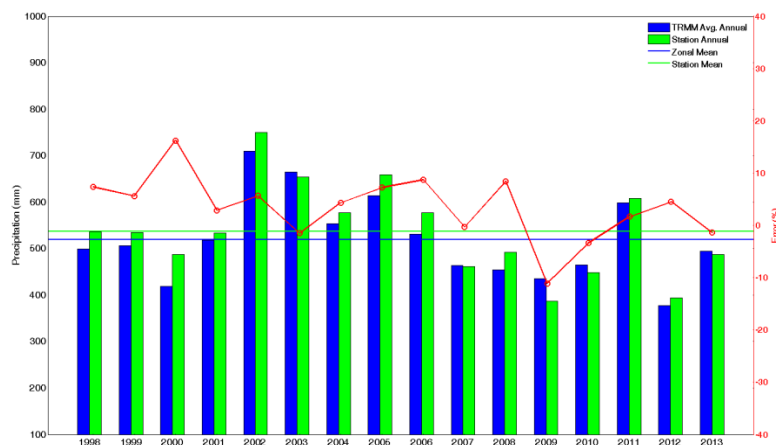


Figure A.49. Comparison of historical average annual TRMM precipitation with the selected TRMM grid point. Blue bars show the average annual precipitation of across all years (1998-2013) and green bars shows the selected TRMM station. Red line shows the error percentage for each year.

The statistical properties of daily precipitation, such as the mean, standard deviation, coefficient of variation of the historical (TRMM, 1998-2013) and stochastically generated (10,000 years) are compared in Figure A.50. The results reveal that the precipitation modeling preserves the statistical properties of the daily precipitation and seasonality of precipitation in Seychelles. Daily mean precipitation amounts are well preserved (Figure A.50a) and, the dispersion of daily precipitation amounts from the mean daily standard deviation is relatively preserved (Figure A.50b).

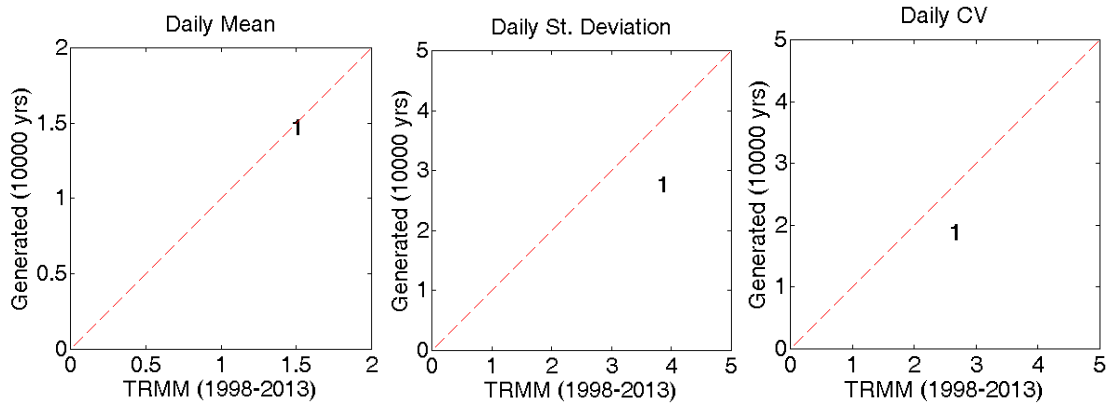


Figure A.50. Comparison of daily statistical properties from historical TRMM precipitation and 10,000 years of stochastic simulations for the selected TRMM point.

WGEN-generated 10,000-year stochastic daily precipitation catalog is compared with the observed areal precipitation for Seychelles in Figure A.51 and Table A.6. It is noted that the areal minimum, mean and maximum precipitation from the stochastic simulation of 10,000 years are similar compared to the TRMM historical period. This similarity is primarily due to capturing of precipitation event occurrence and amount distributions of 10,000 years stochastic simulations at the selected TRMM point.

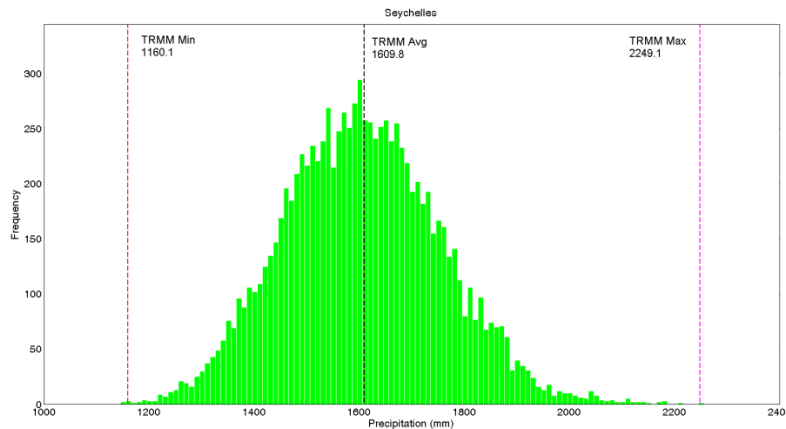


Figure A.51. Frequency distribution of stochastically generated and historical areal annual precipitation across Seychelles

Table A.6: Comparison of areal annual precipitation for 10,000 years across Seychelles compared to the historical time period

<i>Statistic</i>	<i>10,000 yrs Precipitation (mm)</i>	<i>TRMM (1998-2012) Precipitation (mm)</i>
Mean	1,606	1,610
Minimum	1,147	1,160
Maximum	2,249	2,249

The 7-5-days clause is applied to both the NTC TRMM data and the stochastic catalog for Seychelles. To examine if the identified NTC flood events exhibit a realistic frequency of occurrence, the Consequence Database developed in Component 1, which consists of a list of significant loss-causing historical events, is compared to the event definition applied to the historical (TRMM) rainfall catalog. Multiple filters (e.g., no named storms and no tropical cyclone related annotations) are first used to identify the reported NTC precipitation events in the Consequence Database, and the total number of such events is derived for each year from 1998 to 2013. The annual frequency of NTC precipitation events based on the Consequence Database is plotted against that derived from the NTC TRMM data in Figure A.51, which shows that the inter-annual variation of both data bears high resemblance.

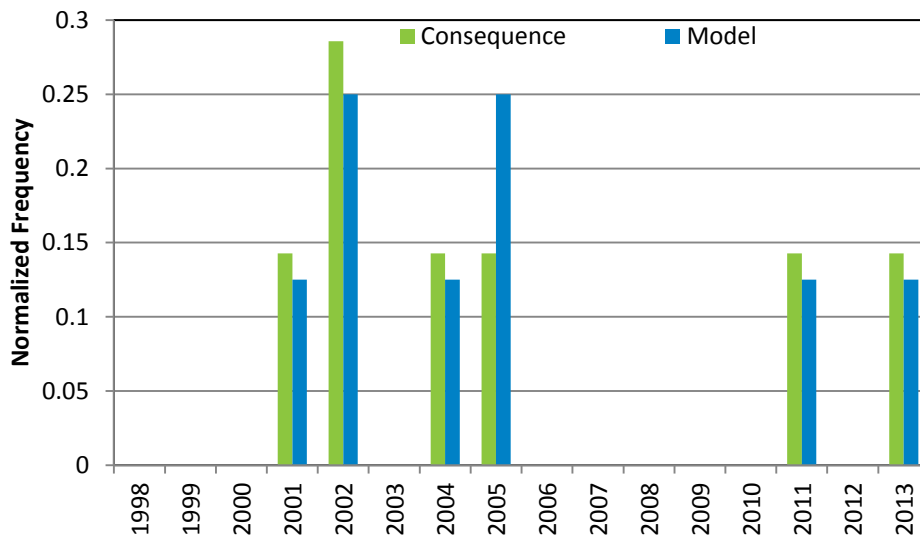


Figure A.52. Comparison between Consequence Database and TRMM-based NTC Precipitation Event Occurrence by Year for Seychelles

4.2.4.5 Zanzibar

Given the size of the country and the climatic variability of the SWIO region, the climatic variability across Zanzibar is minimal. Therefore, one can safely assume that the variability of the climate can be captured by a single TRMM grid node to represent the rainfall pattern and characteristics across the main islands. The number of TRMM grid locations covering the two main islands of Zanzibar is shown in Figure A.53.

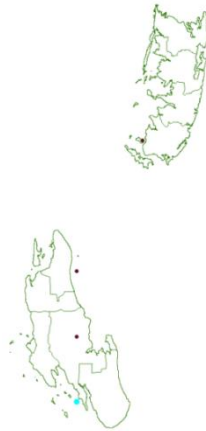


Figure A.53. TRMM grid points covering main islands of Zanzibar. The highlighted point in cyan represents the selected TRMM grid cell.

Historical validation of precipitation modeling for the TRMM historical time period between 1998 and 2013 is shown in Figure A.54. It is seen that the selected TRMM point represent long-term climatology and rainfall characteristics of Zanzibar with minimum error statistics across the period from 1998-2013. Stochastic generation of 10,000 years of daily precipitation is performed using WGEN for the selected TRMM grid cell location for Zanzibar.

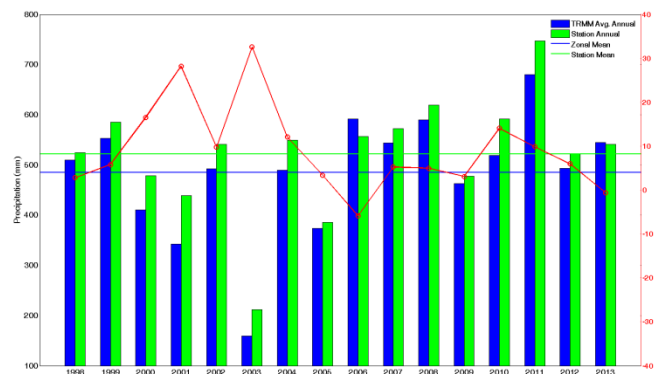


Figure A.54. Comparison of historical average annual TRMM precipitation with the selected TRMM grid point. Blue bars show the average annual precipitation of across all years (1998-2013) and green bars shows the selected TRMM station. Red line shows the error percentage for each year.

The statistical properties of daily precipitation, such as the mean, standard deviation, coefficient of variation of the historical (TRMM, 1998-2013) and stochastically generated (10,000 years) are compared in Figure A.55. The results reveal that the precipitation modeling preserves the statistical properties of the daily precipitation and seasonality of precipitation in Zanzibar. Daily mean precipitation amounts are well preserved (Figure 21a) and, the dispersion of daily precipitation amounts from the mean daily standard deviation is relatively preserved (Figure 21b).

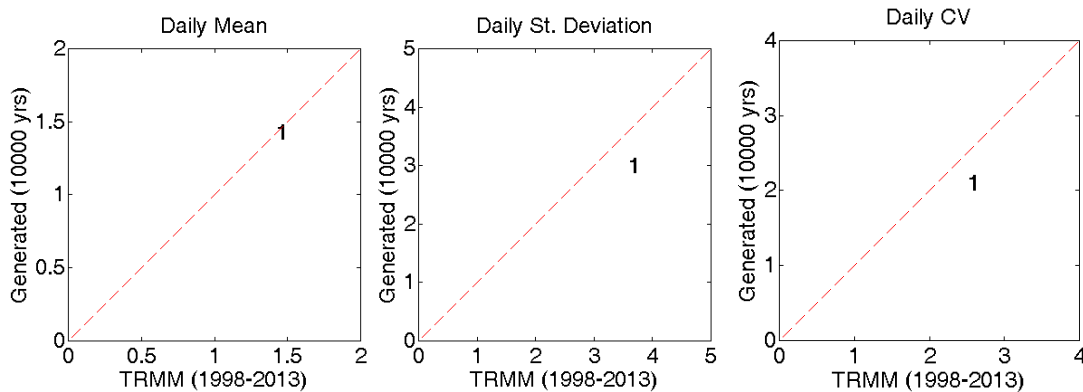


Figure A.55. Comparison of daily statistical properties from historical TRMM precipitation and 10,000 years of stochastic simulations for the selected TRMM point.

WGEN-generated 10,000-year stochastic daily precipitation catalog is compared with the observed areal precipitation for Zanzibar in Figure A.56 and Table A.7. It is noted that the areal mean and maximum precipitation from the stochastic simulation of 10,000 years are similar compared to the TRMM historical period. This similarity is primarily due to capturing of precipitation event occurrence and amount distributions of 10,000 years stochastic simulations at the selected TRMM point.

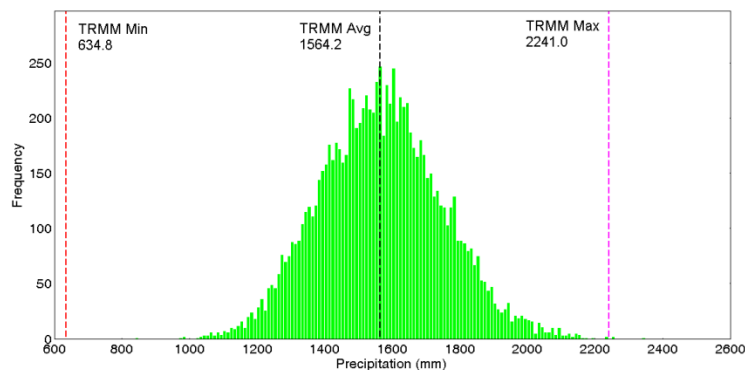


Figure A.56. Frequency distribution of stochastically generated and historical areal annual precipitation across Zanzibar

Table A.7: Comparison of areal annual precipitation for 10,000 years across Zanzibar compared to the historical time period

<i>Statistic</i>	<i>10,000 yrs Precipitation (mm)</i>	<i>TRMM (1998-2012) Precipitation (mm)</i>
Mean	1,567	1,564
Minimum	839	635
Maximum	2,343	2,241

The 7-5-days clause is applied to both the NTC TRMM data and the stochastic catalog for Zanzibar. To examine if the identified NTC flood events exhibit a realistic frequency of occurrence, the Consequence Database developed in Component 1, which consists of a list of significant loss-causing historical events, is compared to the event definition applied to the historical (TRMM) rainfall catalog. Multiple filters (e.g., no named storms and no tropical cyclone related annotations) are first used to identify the reported NTC precipitation events in the Consequence Database, and the total number of such events is derived for each year from 1998 to 2013. The annual frequency of NTC precipitation events based on the Consequence Database is plotted against that derived from the NTC TRMM data in Figure A.57, which shows that the inter-annual variation of both data bears high resemblance.

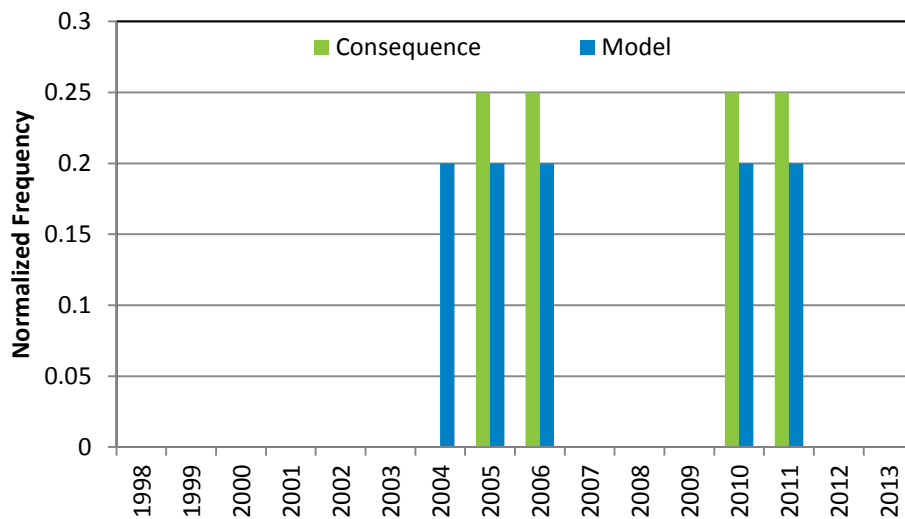


Figure A.57. Comparison between Consequence Database and TRMM-based NTC Precipitation Event Occurrence by Year for Zanzibar

4.2.5 References

- Adler, R.F., et. al (2000) "Tropical Rainfall Distributions Determined using TRMM Combined with Other Satellite and Rain Gauge Information," *Journal of Applied Meteorology*, Vol. 39, 2007-2023.
- Aldegheri, M. (1972). Rivers and streams on Madagascar. (In R. Battistini and G. Richard-Vindard (Eds.), *Biogeography and ecology in Madagascar*, Dr. W. Junk, B.V. Publishers the Hague, 1972.
- Chavas, D. R., and K. A. Emanuel (2010), A QuikSCAT climatology of tropical cyclone size, *Geophys. Res. Lett.*, 37, L18816.
- Huffman, G.J., et. al (2007) "The TRMM Multi-satellite Precipitation Analysis (TMPA): Quasi-Global, Multiyear, Combined-Sensor Precipitation Estimates at Fine Scales," *Journal of Hydrometeorology*, Vol. 8, 38-55.
- Jiang, H. and E.J. Zipser (2009) "Contribution of Tropical Cyclones to the Global Precipitation from Eight Seasons of TRMM Data: Regional, Seasonal, and Interannual Variations," *Journal of Climate*, Vol. 23, 1526-1543.
- National Oceanic and Atmospheric Administration (NOAA), (2015). Central Pacific Hurricane Center, (Accessed, 2015: <http://www.prh.noaa.gov/cphc/pages/FAQ/Forecasting.php>)
- Richardson, C. W. (1982). A comparison of three distributions for the generation of daily rainfall amounts. In V.P. Singh (Ed.), *Statistical Analysis of Rainfall and Runoff*. Paper presented at the International Symposium on Rainfall-Runoff Modeling (pp. 67-78), Water Resources Publications, 700 pp.
- Smith, R. E., and H. A. Schreiber (1973). Point processes of seasonal thunderstorm rainfall: 1. Distribution of rainfall events. *Water Resources Research*, Vol. 9(4), pp. 871-884
- Smith, R. E. and H. A. Schreiber (1974). Point processes of seasonal thunderstorm rainfall: 2. Rainfall depth probabilities. *Water Resource Research*, Vol. 10(3), pp. 418-423
- Woolhiser, D. A., and J. Roldán (1982), Stochastic daily precipitation models: 2. A comparison of distributions of amounts, *Water Resources Research*, 18(5), 1461-1468

4.3 Earthquake

An earthquake hazard model, consisting of a historical catalog, stochastic catalog, and intensity module, was developed for the SWIO region. This earthquake model is a part of a larger model of the Sub-Sahara region of Africa. Technical documentation for the earthquake model, with a focus on the SWIO region, is provided in this chapter. The chapter is structured in three major parts: (1) description of earthquakes and seismicity in the Southwest Indian Ocean, (2) the stochastic event generation process, and (3) the local intensity calculation module.

4.3.1 Earthquakes in the Southwest Indian Ocean

This section provides an overview of earthquakes and introduces several important concepts in earthquake modeling.

Earthquakes: An Overview

An earthquake results from a sudden displacement of rock along a fault. It accompanies a rapid release of energy in the form of seismic waves, which propagate outward from a focus.

The process begins when rocks situated along a fault experience a buildup in stress, and consequently start to deform. When the stress exceeds the strength of the rock and overcomes the friction that resists the relative movement of opposite sides of the fault, the fault ruptures and releases energy. Some of the energy released dissipates as friction along the fault; the rest is transferred as seismic waves that radiate outward from the initial point of rupture and cause ground motion at the Earth's surface.

Faults are rarely found in isolation; instead, they tend to form fault zones comprised of numerous faults of different sizes and orientations. Long faults may be segmented, with each segment having an individual rupture history and mechanism. Ruptures associated with a weak to moderate earthquake are generally contained within one segment of a fault, whereas more powerful earthquakes often manifest themselves along multiple segments. Fault zones vary in depth, width, and orientation.

A fault plane can be vertical or sloping in relation to the earth's surface. In sloping faults, the rock volume above the fault plane is known as the hanging wall, and the rock volume below the fault plane is the footwall. One type of earthquake faulting mechanism is dip-slip, which can be sub-classified as either normal or reverse faulting. Normal faulting occurs when the hanging wall slips down relative to the footwall, resulting in an extension of crustal matter. Reverse faulting occurs when the hanging wall lifts relative to the footwall, which causes a shortening of the crustal material. Strike-slip faults have a nearly vertical surface; their movement is horizontal, parallel to the strike of the fault surface. Oblique-slip faulting is a combination of strike-slip and normal or reverse faulting.

While faults may form a visible trace on the Earth's surface, some remain buried. These blind faults represent a significant seismic hazard, as they are often difficult to detect prior to rupture. Hazard assessment of blind faults is challenging and often plagued with uncertainty.

Generally, active faults are those that have demonstrated activity during the last 10,000 years, or during the Holocene period. Potentially active faults are those that have demonstrated activity during the last 1.65 million years, or during the Quaternary period.

Plate Tectonics

The theory of plate tectonics was developed to explain the evidence for large-scale motion of the Earth's continents. The crust and upper mantle form the rigid, strong lithosphere, which is divided into large plates that move relative to one another. The largest plates are the Pacific, North American, South American, Eurasian, African, and Australian plates.

These lithospheric plates move over the asthenosphere, a hot, viscous layer of weak rock that is continuously moving and transferring heat from the Earth's interior to the surface. The boundaries between plates are where most earthquake and volcanic activity occurs.

There are several types of boundaries between neighboring plates. Convergent boundaries occur where two plates move towards one another. When an oceanic plate collides with a continental plate, the denser oceanic plate sinks, or subducts, under the edge of the lighter continental plate; this is called a subduction zone (Figure A.58). Seismic activity is especially high in subduction zones.

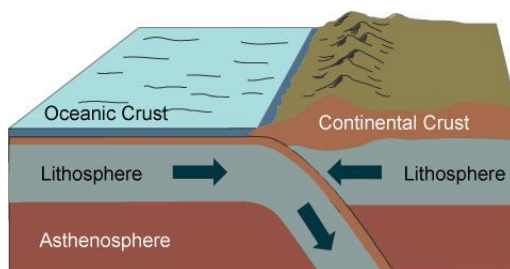


Figure A.58. The Earth's Layers at a Subduction Zone

Continental-collision boundaries occur where two low-density plate edges move towards one another. This process results in crustal rock being thrust upward, which is one way linear mountain systems can form. Divergent boundaries occur where plates move away from one another; this allows for the formation of new crustal material.

Transform boundaries occur where one plate moves past another. Due to massive amounts of friction, however, the plates do not simply glide past each other. Rather, stress builds up in the rocks along the fault until the strain is too great. At that point, the potential energy is released in the form of an earthquake.

While the majority of earthquakes occur at plate boundaries, intraplate earthquakes can occur along fault zones in the interior of a plate. A large intraplate earthquake usually has a long recurrence time, which makes it difficult to estimate the associated risk.

Seismic Waves

Seismic waves transmit tectonic energy through the earth at speeds approaching several miles per second. Seismic waves produce ground motion on the Earth's surface that may damage buildings, trees, cars, roads, and other structures. Soil properties, local geological features, and other factors play a role in attenuating or amplifying seismic waves at a given location.

There are several types of seismic waves. Body waves travel through the earth, while surface waves travel along its surface. Earthquakes generate two types of body waves: primary, or P, waves, and secondary, or S, waves. P waves travel faster and are capable of traveling through both solids and liquids. These waves exhibit an alternating compression-dilatation motion in the direction of wave propagation. S waves are slower and travel only through solid material. These waves produce a sideways-shearing motion perpendicular to the direction of wave propagation.

Surface waves, which are responsible for the majority of earthquake damage, include Love waves and Rayleigh waves. Love waves move horizontally, perpendicular to the direction of wave propagation. Rayleigh waves move slowly in an elliptical, or rolling, motion. Note that seismic wave amplitude, which is the height of an individual wave cycle, or the maximum displacement, decreases with increasing depth in the earth for these surface waves. The amplitude of a seismic wave is one measure of its destructive potential.

In addition to amplitude, there are several ways to mathematically describe wave activity. The wave frequency is the number of wave cycles per second that pass a reference point. A wave's period is the elapsed time, in seconds, between peaks, or the time it takes one complete cycle of the wave to pass a reference point. The wavelength is the distance between repeating units of a propagating wave of a given frequency at some instant in time.

Measuring Earthquake Magnitude and Intensity

The severity of an earthquake can be measured by the damage it inflicts on structures at the Earth's surface or by the energy released at its focus, which is where the rupture originates. Earthquake magnitude characterizes the total energy released by an earthquake, while earthquake intensity refers to the resulting level of ground shaking at a particular location and the observed effects of an earthquake on people, buildings, and other features. While the magnitude of an earthquake is a characteristic of the earthquake as a whole, intensity varies from place to place within an affected region.

An earthquake's intensity at different locations can be described semi-quantitatively using the Modified Mercalli Intensity (MMI) scale⁶, which was developed in its original form in 1902 and is based on observations of shaking severity and its effects at different locations. The MMI at a particular location is based on human judgment and the observed post-event damage. Today, ground-motion intensity can be directly measured using strong-motion seismographs. The characteristics of ground-motion intensity can be quantified by physical parameters, such as peak ground acceleration (PGA) and spectral acceleration (Sa). Shaking intensity at a particular location depends not only on earthquake magnitude, but also on the local surface geology and the proximity of the location to the earthquake source.

Magnitude is a measure of an earthquake's size. There are several types of earthquake magnitude, including moment magnitude (M_w), Richter magnitude (M_L), body-wave magnitude (M_b), and surface-wave magnitude (M_s). Magnitude scales are generally logarithmic in nature; that is, an increase of one point on a magnitude scale represents an approximately ten-fold increase in wave amplitude and thirty-fold increase in the amount of energy released during the earthquake. AIR models utilize the moment magnitude scale, which is based on seismic moment. The seismic moment of an earthquake is defined as:

$$M_0 = \mu AD, \text{ where}$$

μ = the shear modulus of elasticity

A = the rupture area

D = the average slip over the rupture area

The moment magnitude is related to the seismic moment as shown below:

$$M_w = (2/3) \log M_0 - 6.0,$$

where M_0 is in Newton meters (Nm).

The moment magnitude is considered superior to other magnitude scales because it is based on earthquake source parameters. This is in contrast to scales based on a particular type of seismic wave, like the surface-wave or body-wave magnitude scales, or scales founded on a particular type of instrument, such as the Richter magnitude scale.

The type and amplitude of the seismic waves that are recorded by an instrument depend on earthquake magnitude, the radiation pattern of seismic waves due to different rupture mechanisms, and the complex structures along the propagation path of the seismic waves that are between the source and seismic stations. The type of seismic waves generated by an earthquake is dependent on the event size. Small earthquakes

⁶ Please see <http://earthquake.usgs.gov/learn/topics/mercalli.php> for a more detailed description of this intensity scale.

generate seismic waves with short periods while larger earthquakes can generate seismic waves with longer periods.

Most seismic waves will saturate beyond a certain magnitude; that is, wave amplitude will not increase beyond that magnitude. Therefore magnitude scales based on the amplitude of a particular type of seismic wave will also experience saturation. Moment magnitude does not have such a limitation.

Paleoseismic and Geodetic Data

The modeling of earthquakes requires historical data. For large earthquakes, the catalog is complete further back in time compared to smaller events, because such events are more likely to have been observed and documented. However, improvements in instrument sensitivity and coverage have led to increased recordings of smaller events. The completeness of a historical catalog is therefore a function of time and magnitude.

Paleoseismology and geodetic data are often used to augment instrumentally recorded earthquake catalogs in order to estimate current seismic hazard. Paleoseismology is the study of the location, timing, and size of prehistorical earthquakes. Prehistorical earthquakes are evidenced by offsets in geologic formations found in exhumed fault zones, signs of rapid uplift or subsidence near coastal areas, laterally offset stream valleys, and liquefaction artifacts, such as sand boils.

The geodetic measurement of fault slip rate is another source of information that is used to supplement historical data. The Global Positioning System (GPS) is now the most widely used technology to measure fault slip rates of crustal deformations in a region. The observed crustal deformation represents elastic strain accumulation in the crust. By calculating the rate at which elastic strain accumulates along a fault or seismic zone, estimates can be made as to how often large earthquakes may occur.

Paleoseismic and geodetic data assist in estimating the frequency of large-magnitude earthquakes; for small events, the historical earthquake data is generally sufficient to estimate the recurrence rate because they occur much more frequently than large earthquakes. For earthquakes above some magnitude, which is region-dependent, geodetic and paleoseismic data become more reliable compared to historical earthquake data, as Figure A.59 illustrates.

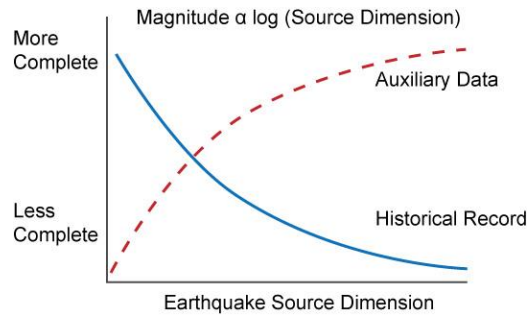


Figure A.59. Completeness of Auxiliary and Historical Record Data, Based on Earthquake Source Dimension

The Gutenberg-Richter Relationship

The Gutenberg-Richter relationship expresses the association between the magnitude and earthquake occurrence rate on a fault or in a given area, at or above each magnitude. The relationship can be used to provide a more complete picture of seismicity in regions where historical data is lacking, as it holds over a wide variety of magnitudes and locations.

The Gutenberg-Richter relationship is parameterized by the a-value, which is the logarithm of the earthquake occurrence rate above some reference magnitude, and the b-value, which is the rate that the logarithm of the cumulative annual frequency decreases as the magnitude increases. Scientists usually truncate this relationship at a limiting magnitude above which the probability of an earthquake's occurrence is zero (Figure A.60).

Note that the a-value is the logarithm of the y-intercept, and the b-value represents the slope of the line. The presence of large-magnitude characteristic earthquakes causes the shape of the frequency-magnitude distribution to be a nonlinear curve.

Historical seismicity data and geodetic-determined strain-rate model are used to estimate the upper-bound magnitude of the Gutenberg-Richter distribution.

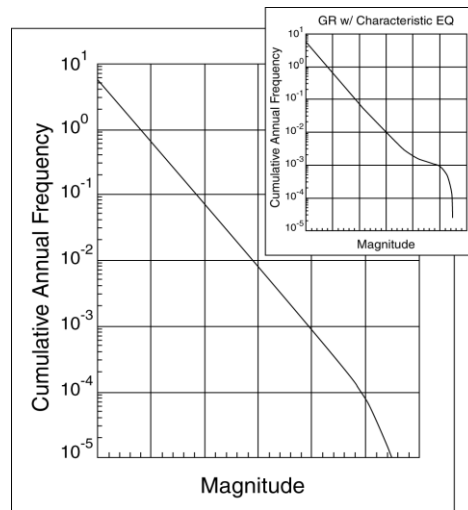


Figure A.60. Sample Gutenberg-Richter Distribution

Characteristic Earthquakes

The characteristic-earthquake theory states that active faults tend to generate earthquakes of about the same magnitude at regular time intervals. This concept is used to simulate seismic activity along active faults. In order to model seismicity using the characteristic-earthquake method, the earthquake magnitude and return period must be specified. Magnitude can be estimated from historical data, paleo-seismological data, and fault length. The return period is estimated from paleo-seismological data, fault slip rates, or seismic-moment rates as estimated from fault slip rates.

4.3.1.1 Earthquake Risk in Southwest Indian Ocean

The Hazard

The Southwest Indian Ocean (SWIO) earthquake model has been studied as part of a larger scope, i.e., the Sub-Saharan earthquake model. The SWIO region is part of the African Plate and is bounded at the West by the Central Indian Ridge, at the East by the Nubian Plate through the East-African Ridge, the North by the Arabian Plate, and at the South by the Antarctic Plate, via the Southwest Indian Ridge. The five island-countries that are the main focus of this project, which include Comoros, Madagascar, Mauritius, Seychelles and Zanzibar, are located within this area, and are mostly subjected to the seismic hazard from the remote boundaries of this region. Figure A.61 shows the tectonic setting of the entire Sub-Saharan region.

The Western part of the SWIO region is prone to a significant level of seismicity due to the East African rift system, which is an approximately 5,000-km long divergent boundary between the Nubian (West African) and Somalian (East African) plates. It is comprised of a series of fault-bounded basins and volcanic centers

stretching through East Africa in a roughly North-South direction, with seismicity, active faulting, and volcanism generally localized along narrow belts separating largely aseismic domains (Saria et al., 2014). The stretching between Nubian and Somalian plates extends between the Red Sea/Gulf of Aden to Malawi and continues southwards to the Southwest Indian Ridge. The East African Rift is seismically active featuring two main rift branches: the Eastern rift, located between the Gulf of Aden and central Kenya, characterized by many volcanoes, and the Western rift that extends between the Eastern edge of Kenya to Malawi, characterized by deep lakes and fewer volcanoes (Midzi et al., 1999; Chu and Gordon, 1999; Chorowicz, 2005, Saemundsson, 2010, Mulwa, 2013).

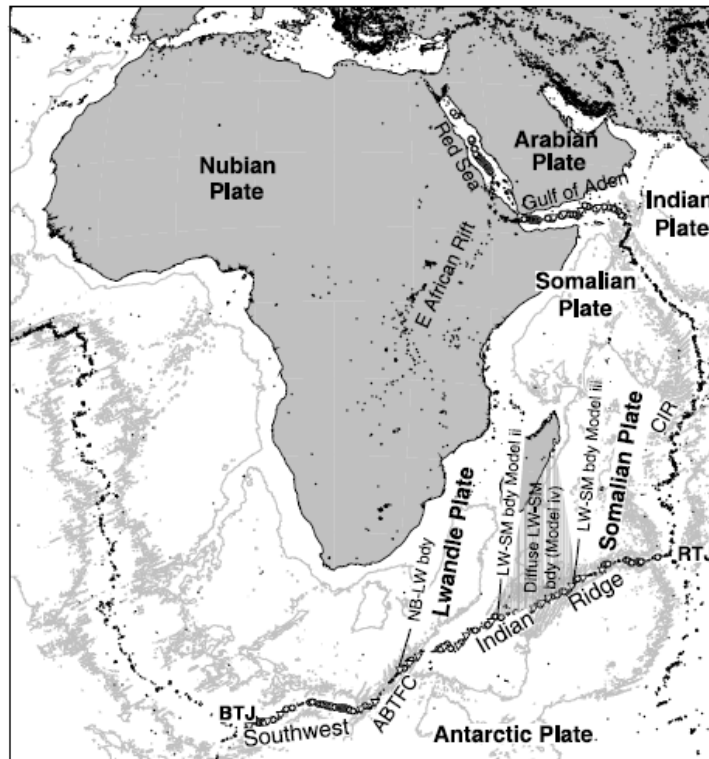


Figure A.61. Tectonic plates in the Sub-Saharan and Southwest Indian Ocean Regions (source: Horner-Johnson et al., 2007)

The region of African lithosphere along the Southwest Indian Ridge can be interpreted as a micro-plate in the African composite plate. This plate, the Lwandle micro-plate lies between the Nubian and Somalian plates along the Southwest Indian Ridge. Most earthquakes in the East Africa Ridge have extensional focal mechanisms, with a few exceptions, such as strike-slip events at the southern end of the western branch, and a cluster of reverse faulting events at the southern end of the Madagascar Ridge. These events, together with extensional events well documented in Madagascar, imply a counter clockwise rotation of the Lwandle plate with respect to Somalia (Saria et al., 2014).

Madagascar has an extensional tectonic regime. Multiple indications for this east-west extension can be observed on the central highlands of the island: the separation of Madagascar from Africa with the subsequent opening of the Mozambique Channel and the development of the Mahajunga and Morondava basin; the northward motion of separation of India from Madagascar, which resulted in a very straight and steep coast on the Eastern margin of the island; the presence of a deep fracture zone or a zone of crustal weakness and recent study signaled the presence of active faults in the Itasy area. The tectonic patterns of Southern Madagascar can be characterized by thrusts and folds at upper crustal levels, while at deeper levels by shear zones with a strong strike-slip component and folded domains (Lardeaux *et al.*, 1999; Andrianaivo and Ramasiarino, 2015).

Along the Eastern boundary of the SWIO region, the Central Indian Ridge, the Carlsberg Ridge and Owen Fracture zone discretely separate the Indian plate from the Somalian and Arabian plates through a series of spreading centers and transform faults. The Indian plate is separated from Somalian plate along the mid-ocean ridge, which is in the south of the Owen Fracture Zone. This boundary is completely submarine and is defined by the discrete seismicity of the Carlsberg Ridge and the Central Indian Ridge. The Arabian, Indian, and Somalian plate meet at a junction called Aden-Owen-Carlsberg triple junction. As a whole, the motion of the Indian plate and the Somalian plate interact in three classes: (1) oceanic spreading, (2) oceanic transform and (3) oceanic convergent (DeMets *et al.*, 2010; Pasupuleti and Ramancharla, 2014).

4.3.1.2 Significant Historical Earthquakes in Southwest Indian Ocean

Historical earthquakes losses are rare in the SWIO region and no earthquakes events have caused reported losses for any of the five nation islands in SWIO region Three of the most significant historical earthquakes, of magnitude 5 or greater, with epicenters in the vicinity of the five nations considered in the SWIO region are represented in Figure A.62. These three events have been selected by the United States Geological Survey (USGS), which reported non-zero shaking intensity in Comoros and Madagascar. The details of these three events are summarized in Table A.8.

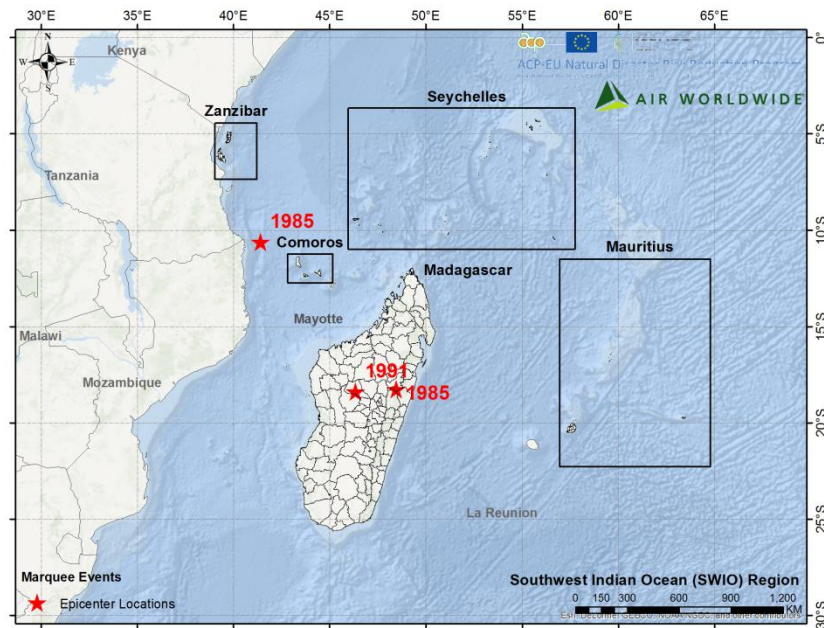


Figure A.62. Marquee earthquake events in the Southwest Indian Ocean region

Table A.8. Marquee earthquakes events

Country	Date	Magnitude	Depth (km)	Location
Comoros	May 14, 1985	6.3	30	Near the coast of Mozambique and Tanzania
Madagascar	October 4, 1985	5.5	26	West of the country's chief seaport Toamasina and approximately 100 km North-East of the capital Antananarivo
Madagascar	April 21, 1991	5.5	19	Approximately 150 km North-West of the capital Antananarivo, in the Bongolava region

Event Generation

The AIR Earthquake Model for Sub-Sahara captures the effect of shake damage on properties in 33 countries, including the five nation islands in the Southwest Indian Ocean region. AIR's seismicity model is based on historical seismicity, geological and geodetic data, and plate tectonics. The geographical domain of the Sub-Sahara Earthquake model is illustrated in Figure A.63.

In the AIR model, the foundation of earthquake hazard and loss analysis for Southwest Indian Ocean is a stochastic earthquake catalog. This stochastic catalog contains 100,000 simulated years of regional seismicity⁷.

⁷ An optimized 10,000-year stochastic catalog is then generated from the original 100,000-year catalog.

The core of the stochastic catalog is a seismicity model that represents the long term regional and local earthquake hazard in the Southwest Indian Ocean region. To reduce the epistemic uncertainty associated with this seismicity model, AIR collects earthquake information from multiple sources, including historical earthquake data from various local and regional historical earthquake catalogs, as well as slip rates and geometries of known faults in the region.

Specifically, a historical earthquake catalog is constructed by reviewing and integrating various local and regional catalogs, and converting earthquake magnitudes in the final historical catalog to unified moment magnitudes. Data on known faults and major fault systems, including fault geometries, direction of motion, and fault slip rates, if reliable, are obtained, largely from recent publications.

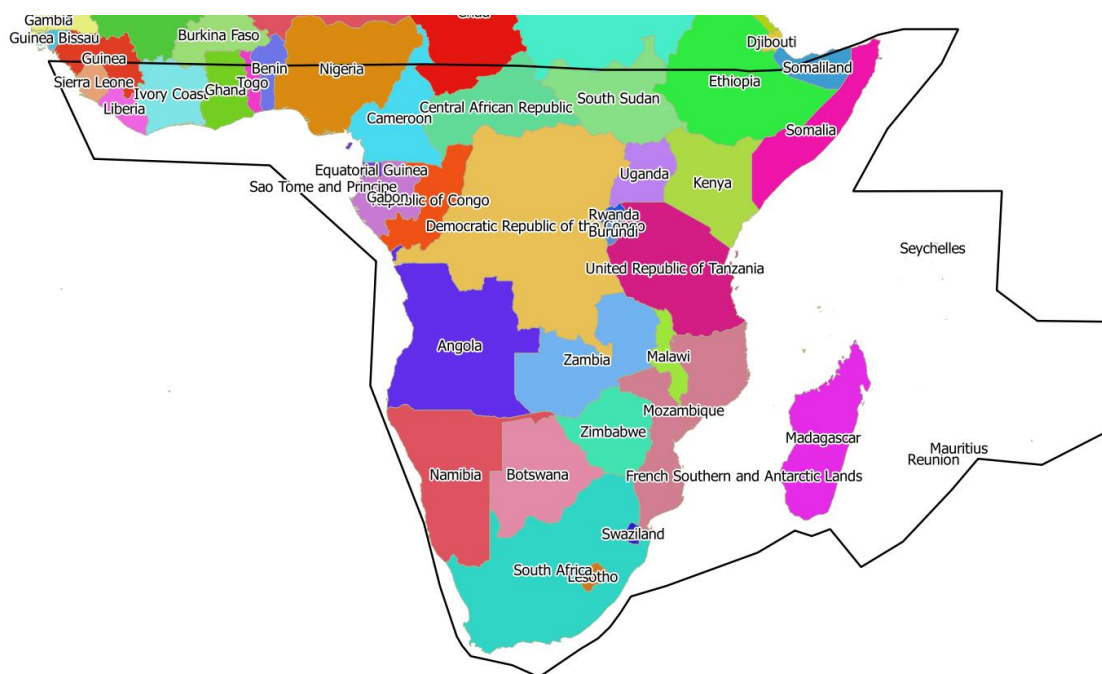


Figure A.63. Model Domain for the AIR Earthquake Model for Sub Sahara and Southwest Indian Ocean

4.3.1.3 Data Sources

AIR relies on a variety of information, including GPS data, geological fault data, and historical earthquake recordings to develop the model’s historical earthquake catalog. The primary sources for the SWIO historical earthquake catalog include:

- Global Earthquake Magnitude (GEM) Historical Earthquake Catalogue
- International Seismic Centre (ISC) EHB Bulletin

- ISC-GEM Global Instrumental Earthquake Catalogue
- Global Centroid Moment Tensor Catalog
- United States Geological Survey (USGS) Centennial Earthquake Catalog
- USGS Advanced National Seismic System (ANSS) Earthquake Catalog
- Incorporated Research Institutions for Seismology (IRIS) Earthquake Catalog
- National Oceanic and Atmospheric Administration (NOAA) Earthquake Catalog
- Global Seismic Hazard Assessment Program (GSHAP) Earthquake Catalog

Information from each of these sources was reviewed and merged, taking into consideration overall quality and completeness of the records. Additional information on the locations and magnitudes of significant historical earthquakes in the region obtained from published literature and reports was also incorporated into the final catalog. Figure A.64 shows the historical seismicity in and around the Southwest Indian Ocean region, by magnitude.

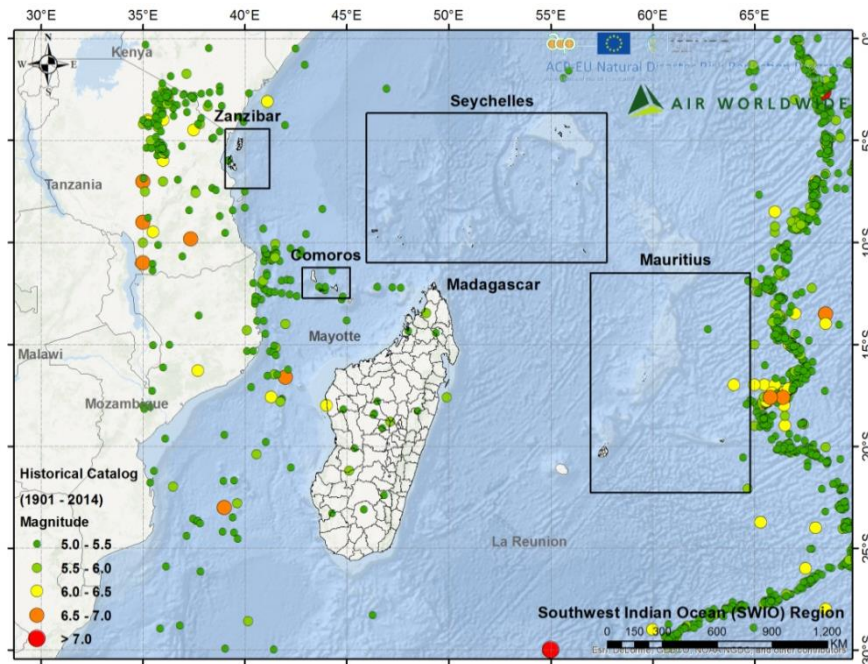


Figure A.64. Historical Seismicity by Magnitude

Geological Faults and Subduction Zone Segments

The model accounts for earthquakes on active crustal faults. For crustal faults, the fault geometry – including the fault length, depth, azimuth, and dip angle – rupture mechanism, slip rate, and characteristic magnitude were obtained from published research. The faults described in these documents were digitized, and the slip rates and recurrence times were applied in the model. Figure A.65 shows the main known faults in the Sub-Saharan region. A closer attention to the active faults in the region is given at each seismic source zone. For

example, Figure A.67 shows the active faults in two of the zones included in the Southwest Indian Ocean region.

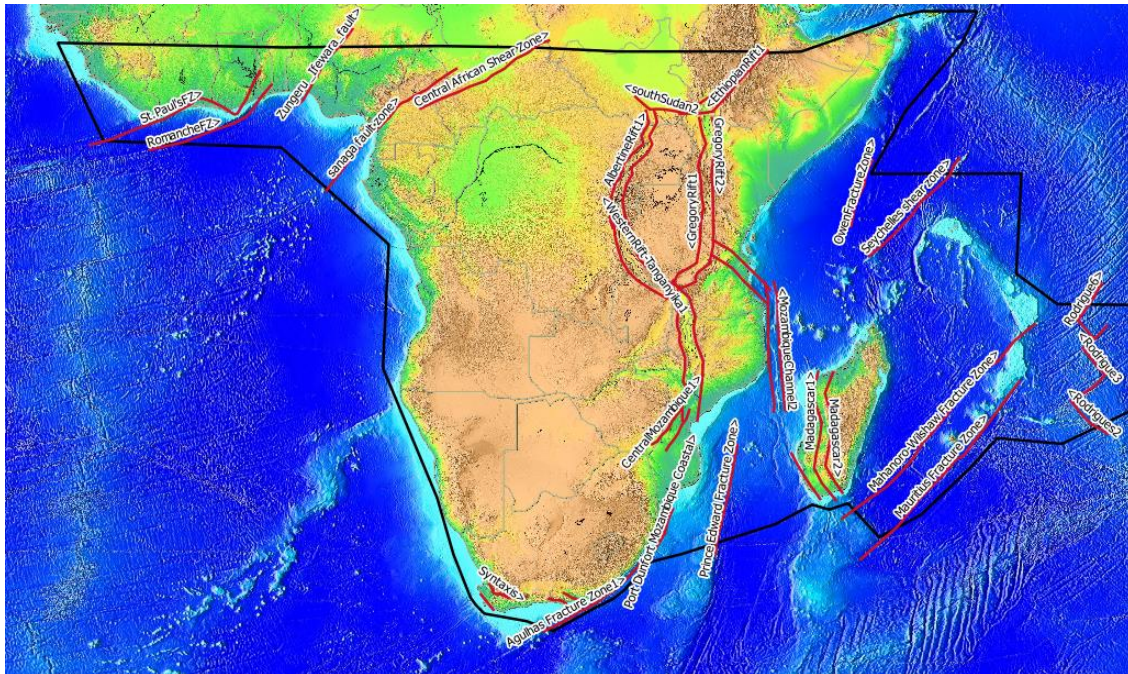


Figure A.65. Faults in the Sub-Sahara and Southwest Indian Ocean regions

The model uses detailed fault parameters, such as dip angle, the seismic coupling factor, slip rate, and upper-bound of characteristic-earthquake magnitude for all subduction zones and active faults. These parameters are based on an extensive review of published literature and Global Positioning System (GPS) studies. The geodetic data incorporated in the model is based on GPS measurement results collected from local and regional geodetic studies. Figure A.69 (left) shows the distribution of GPS data available in the Southwest Indian Ocean region (Stamps et al., 2015).

4.3.1.4 Modeling Regional Seismicity

Modeling regional seismicity involves using all available earthquake hazard data, including historical earthquake catalogs, geological fault information (e.g. fault location, geometry, and slip rates), paleoseismic and geodetic data to formulate the regional earthquake potential.

The modeled region is divided into a number of zones based on various pieces of seismotectonic data, including historic earthquake data, active faults, fault segmentation, and crustal deformation field. GPS data, fault slip rates, and plate motion velocities are used to compute the long-term seismic moment accumulation rate in each zone by means of a kinematic model. The long-term seismic moment accumulation rate determines the amount of seismic energy available within a seismic source zone. The total seismic energy constrains the

seismic moments released by earthquakes from all types of seismic sources in a zone, including active faults, subduction zones, and background seismicity.

A combination of the characteristic earthquake model and the Gutenberg – Richter magnitude frequency relationship (GR-relationship) is used to estimate the earthquake frequencies of various magnitudes. The parameters for the GR-relationship are determined from the historic seismicity data. For active faults and subduction zones with either paleoseismological data or fault slip rates, the return periods of earthquakes are estimated based on the characteristic earthquake model. Earthquakes are spatially distributed within each zone based on the three-dimensional distribution of historical events, the distribution and geometry of crustal faults, and the geometry of subduction zones. More details regarding this process are provided below.

Large earthquakes associated with active crustal faults are modeled as characteristic events. Moderate to small earthquakes occurring in subduction zones and along crustal faults, as well as the seismicity of regions not captured by these sources, are represented by background seismicity. A smoothed distribution is implemented on a three-dimensional grid and used to capture the background seismicity.

In the AIR Earthquake Model for Southwest Indian Ocean, the model domain is divided into multiple depth layers based on the depth distribution of historical events. The uppermost depth layer is called the top layer, which consists of the seismogenic crust, and the subsequent layers are referred to as deep layers. The top layer extends from the ground surface to a depth that ranges from 15-35 km for seismogenic crust. Seismicity below the top layer is modeled using a gridded-seismicity approach.

Seismic Source Zones

The Sub-Sahara and Southwest Indian Ocean regions are divided into source zones, based on historical earthquake data, seismotectonics, the distribution of mapped active faults, and geodetic estimates of crustal deformation rates.

The entire region is divided into 35 seismic source zones based on the geometry of major faults and the distribution of historical earthquake ruptures. Figure A.66 shows these source zones. The blue lines indicate zone boundaries and the green markers represent historical events. In particular, Figure A.67 shows Zone 23 (left) and Zone 8 (right), corresponding to the regions around Madagascar and Central Mozambique, respectively. The black lines represent its boundaries, the red lines show the active faults in that region, and the blue segments show strain rate vectors calculated from GPS data. A short description of each seismic source zone in the Southwest Indian Ocean region is given in Table A.9.

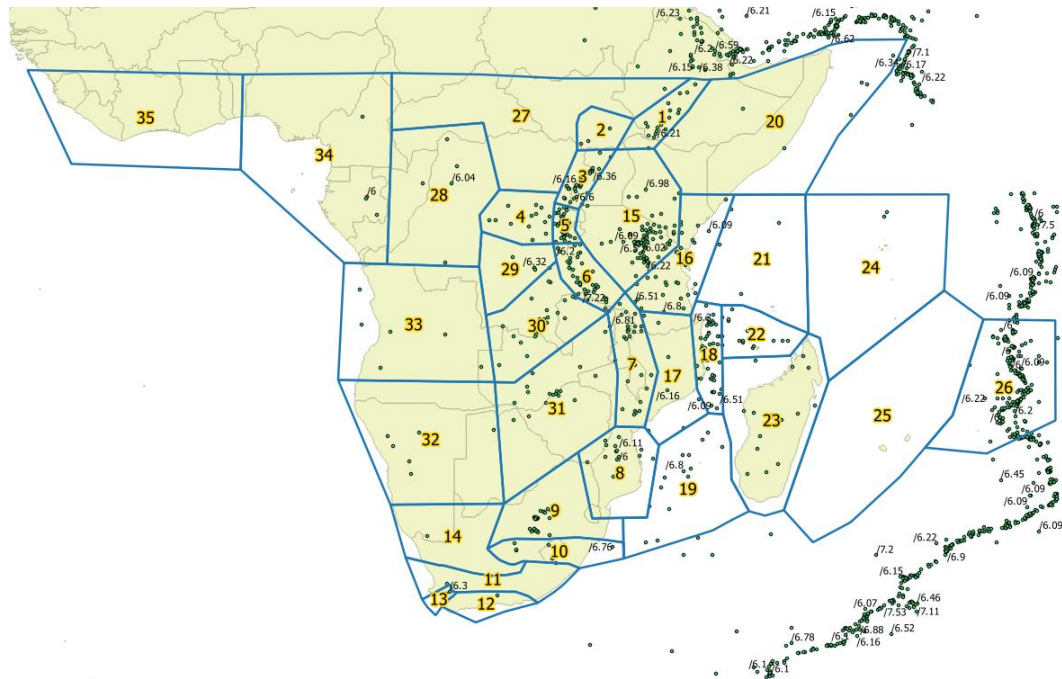


Figure A.66. Modeled Seismic Source Zones in the Sub-Sahara and Southwest Indian Ocean regions

For each seismic source zone, all available earthquake hazard data are transformed into a seismic moment rate, providing a seismic moment budget for that zone. Then, the total seismic moment budget in each source zone is accounted for through stochastic event generation using a combination of the characteristic earthquake approach (for earthquakes on known faults) and the distributed earthquake method (for earthquakes on unknown or unconstrained faults and major fault systems). In the AIR model, distributed earthquakes and background seismicity are modeled using the Gutenberg-Richter magnitude-rate relationship, which assumes time independence.

Table A.9. Modeled Seismic Source Zones in the Southwest Indian Ocean region

<i>Seismic Source Zone</i>	<i>Seismic Source Zone Description</i>
8	Central Mozambique
16	North Tanzanian Divergence
17	Mozambique Coast Plain
18	Mozambique Channel
19	Mozambique Basin
21	Somali Basin
22	Comoros island
23	Madagascar
24	Seychelles, Mascarene Bains and Plateau
25	Reunion Mauritius, Madagascar Basin
26	Rodrigues island, Central Indian ridge

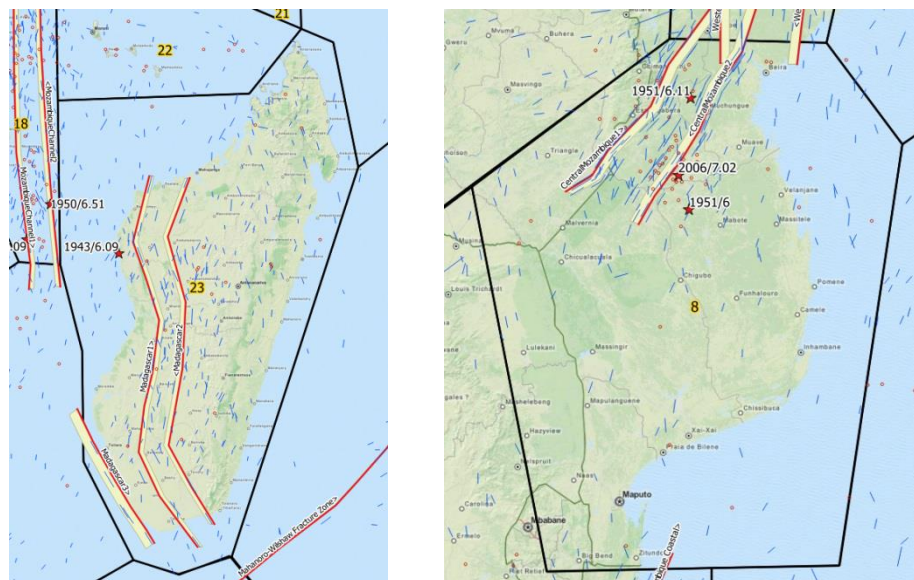


Figure A.67. Seismic Source Zones 8 (right) and 23 (left) in the Southwest Indian Ocean region

Modeling Regional Seismic Moment Rates

Historical earthquake and paleoseismic data are widely used for seismic-hazard analysis, but both types have limitations. Paleoseismic data is usually limited and historical catalogs can be too short to accurately constrain the recurrence times of large earthquakes. Plate motion rates and geodetic data, especially GPS data, can fill these data gaps and provide the long-term strain rates for a region. These rates provide a constraint on the seismic moment accumulation rate, which, in turn, provides a constraint on the rate of large earthquakes when the upper-bound earthquake magnitude can be determined.

AIR employs a kinematic model based on published GPS data and fault slip rates to obtain the seismic moment rate for each source zone. Plate motion velocities, GPS data, and fault slip rates are used to determine the regional strain rate field. The seismogenic thickness is determined for each seismic source zone using historical data on depth distribution. The strain rates are then converted to the tectonic moment rate for each seismic source zone. The tectonic moment rate determines the upper-bound energy budget for all earthquakes in each source zone. If there is no evidence of aseismic fault creeping, it is generally assumed that earthquakes will release the total energy available. If fault creep data is available, the energy released by this creep is accounted for, and a seismic coupling factor of less than one is assigned to the source zone.

The product of the tectonic moment rate and the seismic coupling coefficient is the total seismic moment rate budget for each source zone. This budget is consumed by characteristic earthquakes on faults and subduction zones and by earthquakes modeled according to a GR distribution. A characteristic model is applied to

estimate the rate of characteristic earthquakes on crustal faults and subduction zone segments, and a gridded-seismicity model is used to model GR earthquakes. Figure A.68 illustrates this process.

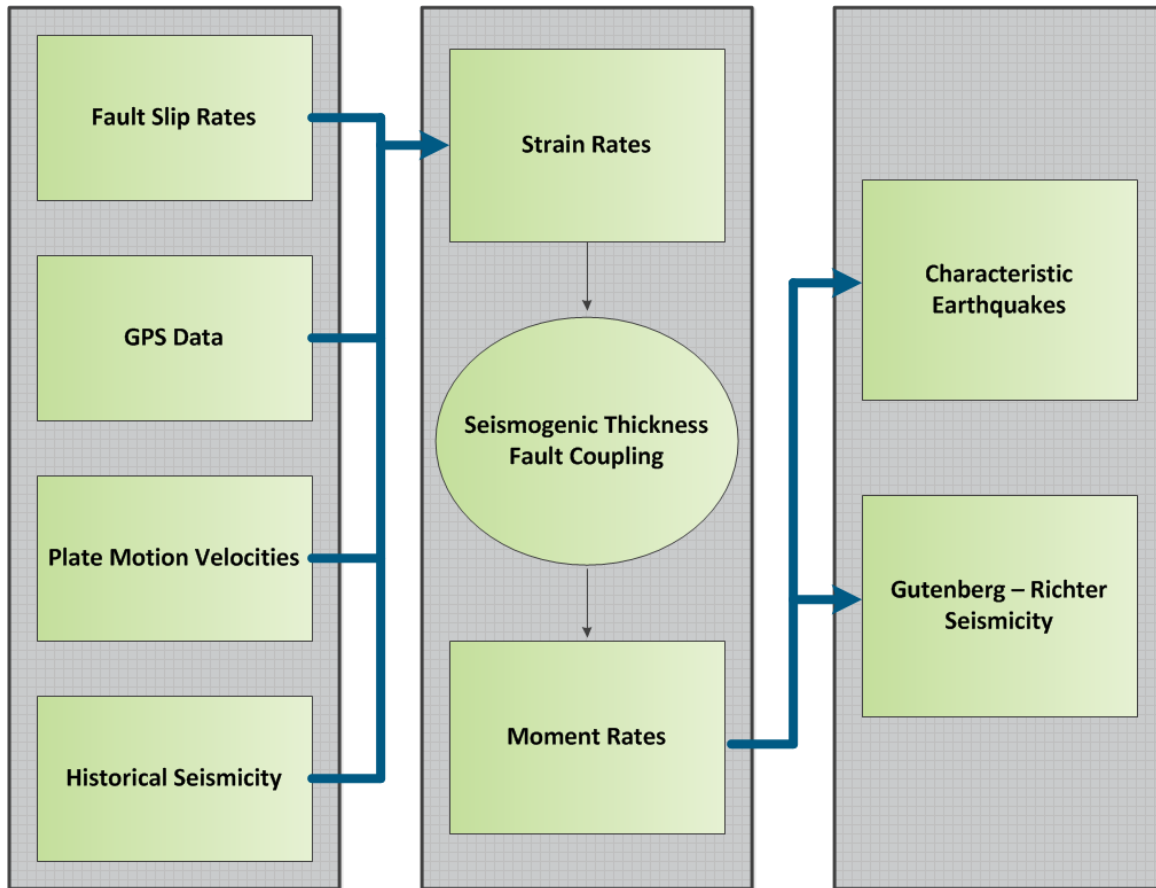


Figure A.68. Schematic of the Procedure Utilized to Model Seismic Moment Rate

Figure A.69 shows the recent GPS data (left panel) and associated modelled strain rate data (right panel) for the Sub-Saharan region developed by GEM (*Stamps et al, 2015*). In the left panel, each GPS station is marked by a point, and the arrow starting from the point shows the relative horizontal velocity in mm/yr. The circle or ellipse around the arrowhead shows uncertainty in measurement. In the right panel, the modelled annual moment rate is shown in log₁₀ scale in Newton*Meter/year.

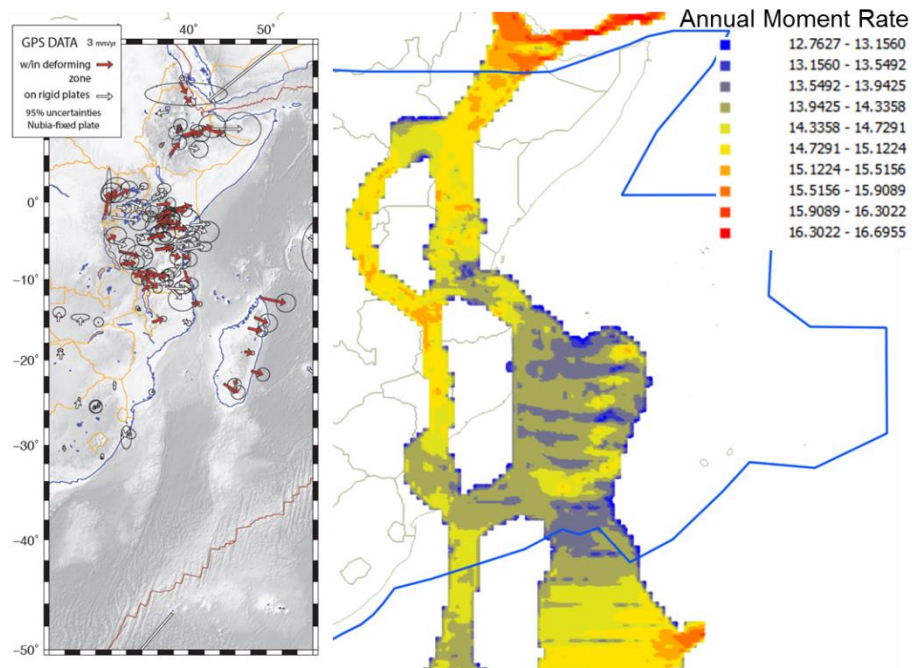


Figure A.69. GPS Velocity Observations from Sub-Saharan Africa Geodetic Strain Rate Model 1.0 (Stamps et al, 2015) and Calculated Annual Moment Rates in the Southwest Indian Ocean region

Gridded Background Seismicity

Background seismicity captures earthquake activity that is not explicitly modeled on known faults or subduction zones. In the AIR model, background seismicity is based upon the seismicity pattern evident in the historical data, in addition to having a certain degree of randomness imposed. This allows simulated earthquakes to occur anywhere within a source zone with the annual probability appropriate to each location. Thus, simulated earthquakes are not limited to the locations of previous earthquakes. The magnitude and rate of gridded background seismicity in the AIR Earthquake Model for Southwest Indian Ocean is based on Gutenberg-Richter distributions for each seismic source zone.

Historical data is used to quantify the frequency-magnitude and spatial distributions of the background seismicity. For each seismic zone in the model, the frequency-magnitude distribution based on a GR formulation is determined from the historical and instrumental data for the zone.

To parameterize the spatial distribution of earthquakes, 3-dimensional regional density functions for earthquake locations are constructed using the magnitude, epicenter, and depth of historical earthquakes. The contribution of each earthquake to these density functions is calculated using a Gaussian-type spatial probability distribution, with parameters defined by the magnitude, epicenter, and focal depth of the

earthquake, as well as the completeness of the catalog. The 3-dimensional density function for each zone is constructed on a 10-km wide grid with a correlation distance of 30 km for the Southwest Indian Ocean region.

The density function is sampled to obtain the location and depth of simulated earthquakes based on the GR frequency-magnitude distribution for each region. The result is a smoothed, but non-uniform, regional background seismicity that is compatible with the regional distribution and rates of historical earthquakes.

The AIR Earthquake Model for Southwest Indian Ocean simulates earthquakes of magnitude 5.0 and greater, as significant damage is unlikely to result from smaller events. However, events of moment magnitude 4.0 and greater are used to develop the model because they provide more complete information from which to estimate earthquake parameters. Regional seismotectonics and the magnitudes of the largest historical earthquakes in each zone were used to estimate the upper-bound magnitude for each seismic zone.

Studies show that different earthquakes generate different types of ground motion due to variations in the earth's physical properties at the earthquake origin. In regions dominated by plate subduction tectonics, most large earthquakes are associated with the subduction of an oceanic plate. Subduction may also impact the crust of the overriding plate, creating active faults and generating catastrophic, shallow crustal earthquakes.

In subduction zones, large, shallow interplate earthquakes generally occur at the plate interface, where the two converging plates slip against one another. These interface earthquakes are relatively shallow and include the largest events in subduction zones.

Modeling Time Independent Seismicity

The AIR Earthquake Model for Southwest Indian Ocean simulates earthquakes by source zone, with earthquake occurrence determined by a stationary Poisson (time independent) process for most of the model domain. Background seismicity is used to address earthquake hazard in regions that do not exhibit known faults.

For each source zone, the minimum set of parameters that must be determined include the upper bound earthquake magnitude, the occurrence rates of earthquakes above the minimum magnitude ($M \geq 5.0$), and the a-value and the b-value of the Gutenberg-Richter magnitude-frequency empirical relationship (the GR relationship). The method used to estimate each parameter is dependent on the available data in the zone.

According to the time-independent method, earthquake magnitude and frequency distribution are determined by the Gutenberg-Richter law. Specifically, historical earthquake data, including magnitude and catalog completeness time, is translated into seismic moment rate, and the fault slip rates and other fault data are used to estimate fault-specific moment rates within each zone. The results of kinematic modeling using geodetic data are converted into the strain and seismic moment rates of each zone. These estimates are integrated into a

single seismic moment budget for each zone, which is translated into the seismic rate using the seismic moment balance.

In cases where the seismic moment budget is lower than the moment requirements of a seismic source zone given the assumed model parameters, the upper bound magnitude of the GR distribution is reduced to balance the moment. However, a lower threshold for GR magnitude is enforced. In cases where the moment budget exceeds the moment requirements for the zone, the extra moment rate is released by characteristic earthquakes on faults defined as zone faults to characterize the locations of the potentially active faults.

Simulated earthquakes are spatially distributed within each zone based on the three-dimensional distribution of historical events, the distribution and geometry of crustal faults, and the geometry of subduction zones.

Distribution of Background Seismicity

Smoothed background seismicity – which allows the AIR model to capture seismicity in the model domain along as-yet-unknown or unmapped faults – is implemented in the model by smoothing the historical earthquake data to ensure full regional spatial coverage in the stochastic catalog. This procedure is shown schematically in Figure A.70.

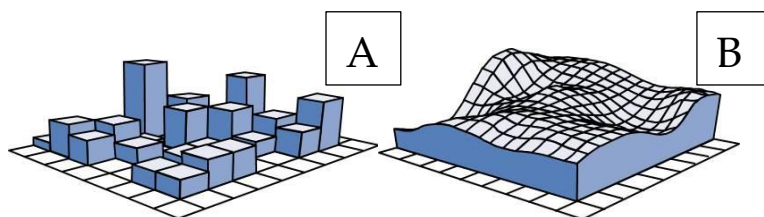


Figure A.70. Schematic representation of A) the spatial distribution of historical earthquakes in the model domain; and B) the spatial distribution of smoothed gridded seismicity

That is, in each source zone, some proportion of background seismicity is allowed to be uniformly distributed, so that areas devoid of historical events also have some potential seismicity to account for uncertainty in future event distribution. This process yields a realistic model of background seismicity that is consistent with the historical catalog, but allows earthquakes to occur where none have been recorded in the past.

However, the locations of larger magnitude background seismicity events are not randomly distributed. Rather, these events are distributed along source zone faults, which are defined to characterize the locations of larger known tectonic structures.

Depth Distribution of Earthquakes in the Stochastic Catalog

The depth distribution of earthquakes in the stochastic catalog follows a smoothed three-dimensional density function developed from the focal distribution of historical seismicity, as well as knowledge of regional

tectonics and the depth and geometry of the subducting plate. Characteristic earthquakes are constrained to shallow depths that are consistent with modeled fault geometries, and Benioff zone contour lines are used to define the depth distribution of large intra-slab and subduction interface earthquakes. Note that, in each seismic source zone, modeled maximum focal depth is consistent with historical observations.

A common problem among many historical catalogs is that depth information are frequently missed or constrained by limited default values (e.g. 0, 10, 30, 33 km). In order to minimize the impact of default depth values in the simulated catalog, we redistributed depths for related events using the EHB catalog (*Engdahl et al., 1998*), which is a global earthquake catalog with relatively high accuracy in depth. Events from the EHB catalog within the model domain are used to form reference depth density functions that account of inland and offshore earthquakes. For each group, abnormal depths are identified by comparing the depth density function given by the joint catalog and the EHB catalog. A randomly selected portion of events with abnormal depths are then assigned a new depth that is sampled from the depth density function in the EHB catalog (Figure A.71).

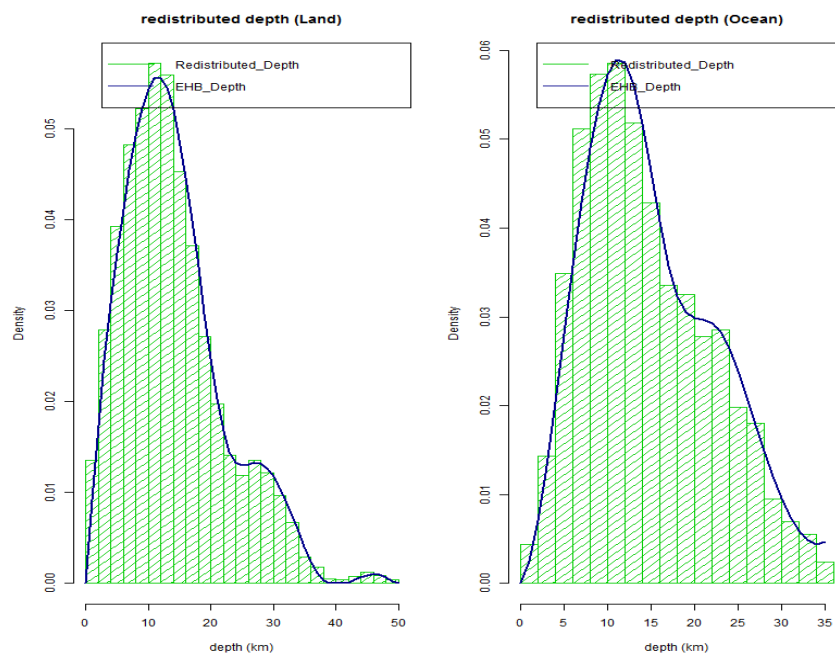


Figure A.71. Depths redistribution in the Southwest Indian Ocean for in-land (left) and ocean (right) earthquakes using the EHB (1998) catalog.

Following the aforementioned procedures, a stochastic catalog for the SWIO region is generated. The full stochastic catalog consists of 100,000 independent realizations of a given year. For the present investigation, a 10,000 year subset, which contains approximately 90,000 events of M5 and larger, that closely matches the statistics of the full catalog is extracted for computational efficiency and used to generate probabilistic

earthquake hazard maps for the region. Figure A.72 illustrates the distribution of earthquake events in the selected 10,000 year time-independent stochastic catalog, by magnitude, in the SWIO region.

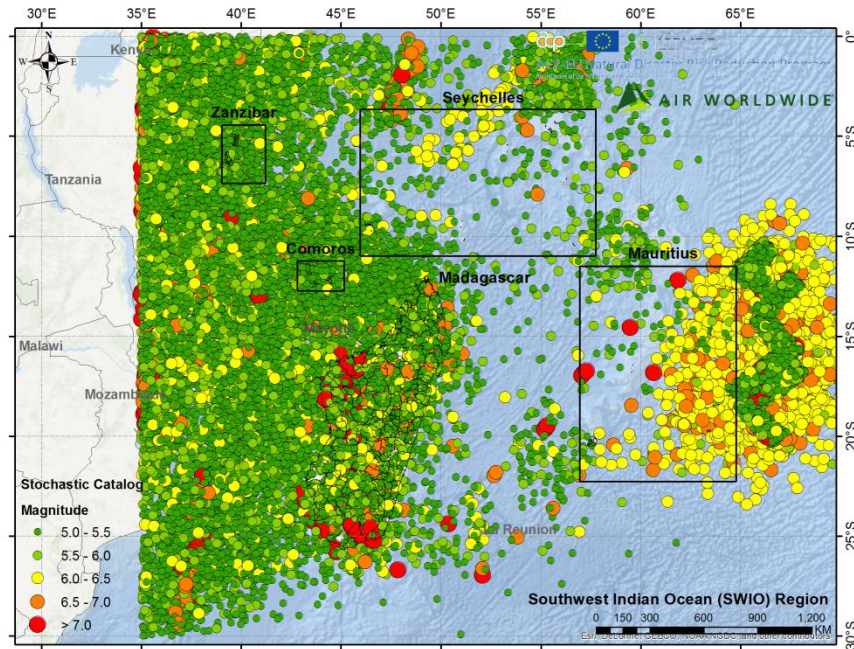


Figure A.72. 10,000 year time-independent stochastic catalog in the Southwest Indian Ocean region

4.3.1.5 Model Earthquake Variables

Epicenter

The epicenter of an earthquake is the location on the Earth’s surface directly above the point of initial rupture. For modern earthquakes, epicenters can be determined by gathering information from a network of local, regional, or global seismometers. For pre-instrumental earthquakes, the determination of earthquake-epicenter locations is greatly facilitated when the faults are visible on the surface. In the case of blind faults, epicenter locations must be inferred from the seismic activity of the area or by subsurface sounding techniques. Many faults remain undiscovered, however.

Magnitude

Magnitude, a measure of the energy released during an earthquake, provides a useful way to compare seismic events. As described previously, a variety of magnitude scales have been used to describe earthquakes. The AIR Earthquake Model for Southwest Indian Ocean utilizes the moment magnitude scale (M_w), which is considered to be superior to other magnitude scales because it is based on the physical properties of the

earthquake source and is more accurate for large earthquakes. Moment magnitude is applicable over a wider range of rupture sizes than other magnitude scales such as the Richter magnitude or body wave magnitude scales.

Focal Depth

The focal depth is the vertical distance between the point where the fault rupture originates and the Earth's surface (Figure A.73). Most earthquakes that take place outside of subduction zones occur within the top 20 km of the crust, whereas earthquakes that occur deeper than 30 km are usually subduction zone related. However, the focal depth of earthquakes in subduction zones can range from a few kilometers to 700 km. Focal depth is an important parameter because seismic waves are attenuated as they travel through the earth, away from their source, and deeper earthquakes of a given magnitude typically cause less damage than those at shallower depths. Therefore crustal events, in general, may cause more damage than deeper events not only because they often occur within land areas, but also because they are shallower and thus closer to the Earth's surface.

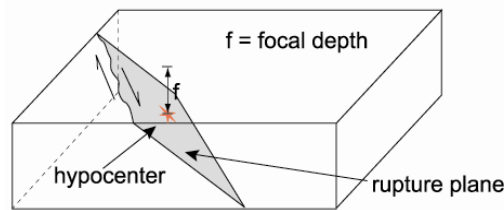


Figure A.73. Focal Depth

Focal depth is modeled both by a statistical approach based on historical earthquakes and by a physical approach using tectonic characteristics.

Rupture Length

Rupture length is the span of the fault that ruptures during an earthquake. In the AIR Earthquake Model for Southwest Indian Ocean, rupture length is modeled as a function of the magnitude of the event, with the relationships between rupture length and magnitude determined through empirical regression analysis. The rupture lengths of different types of earthquakes are determined using different magnitude-rupture length relationships appropriate for a particular type of earthquake.

Rupture Azimuth and Dip Angle

The rupture azimuth and dip angle are parameters that define the orientation of a fault. The rupture azimuth is the angle between true North and the line of intersection between the rupture plane and the surface of the Earth, measured clockwise from North as viewed from above. In the AIR Earthquake Model for Southwest Indian Ocean, the rupture plane is aligned with the principal faulting orientations for the region. For simulated

earthquakes based on the characteristic earthquake model, azimuths are aligned with fault orientations based on geological fault maps and recent earthquake fault plane solutions.

The dip azimuth is the angle between true North and the direction in which the rupture plane dips. By convention, the dip azimuth is 90 degrees clockwise from the rupture azimuth. The dip angle is the angle between the horizontal and the rupture plane. In the model, dip angles are estimated based on seismotectonic data, the rupture parameters of historical earthquakes, and published research. Since energy is distributed across the rupture plane, a fault's spatial orientation is important for estimating damage.

Fault Rupture Mechanism

See Section 4.3.1 for a description of the rupture mechanisms of faults. In this model, the fault rupture mechanisms for earthquakes are based on historical earthquake ruptures, geological fault data, and deformation styles predicted from kinematic modeling of GPS data.

4.3.1.6 Stochastic Catalog Summary Statistics

The AIR Earthquake Model for the Southwest Indian Ocean incorporates a 10,000-year stochastic catalog of 99,090 simulated events in the model domain. Stochastic events included in the model are of magnitude 5.0 and greater. The distribution of the events by magnitude is shown in Figure A.72. Note that not all these events are loss-generating events and that one event alone could generate losses in multiple countries.

4.3.1.7 Validating Stochastic Event Generation

AIR catastrophe models are extensively validated; each component of the model is carefully verified against historical data. This section provides a few exhibits that validate the stochastic event generation procedure.

Validating the Frequency of Simulated Earthquakes

Due to the low seismicity in the region and low number of events recorded in the past approximately 100 years, the validation of the stochastic catalog against the historical catalog is done for the entire region, rather than for individual countries.

Figure A.74 compares the historical and modeled frequency-magnitude distribution for the Southwest Indian Ocean region, irrespective of depth. Note that the frequency-magnitude distribution of historical earthquakes is not always smooth. This is because the historical earthquakes with high magnitudes are fairly rare in the region and uncertainty is higher in that part of the distribution. Figure A.75 compares the historical and stochastic probability distributions of magnitudes in the region, which further highlights the rarity of earthquakes $\geq M6.0$ in the region.

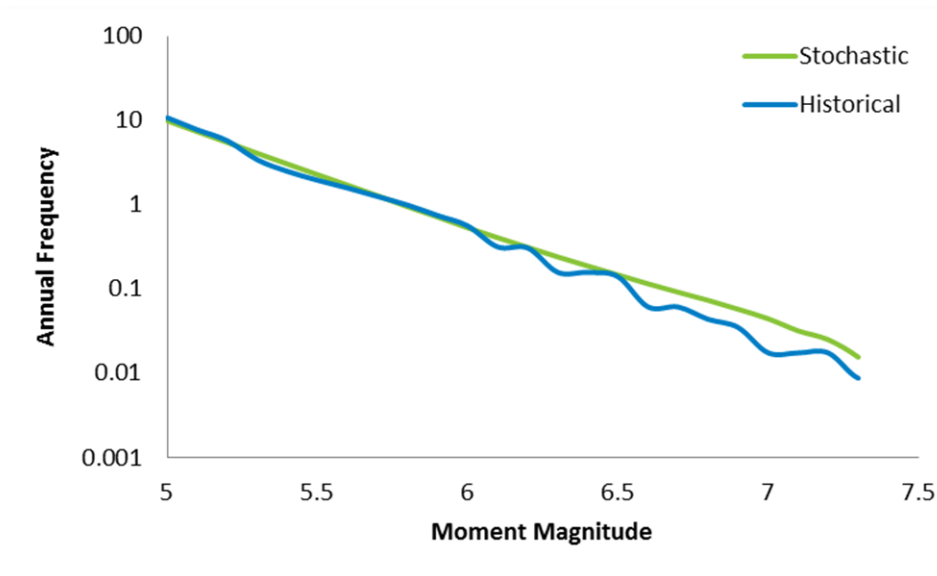


Figure A.74. Modeled vs. Historical Frequency-Magnitude Distributions in the Southwest Indian Ocean

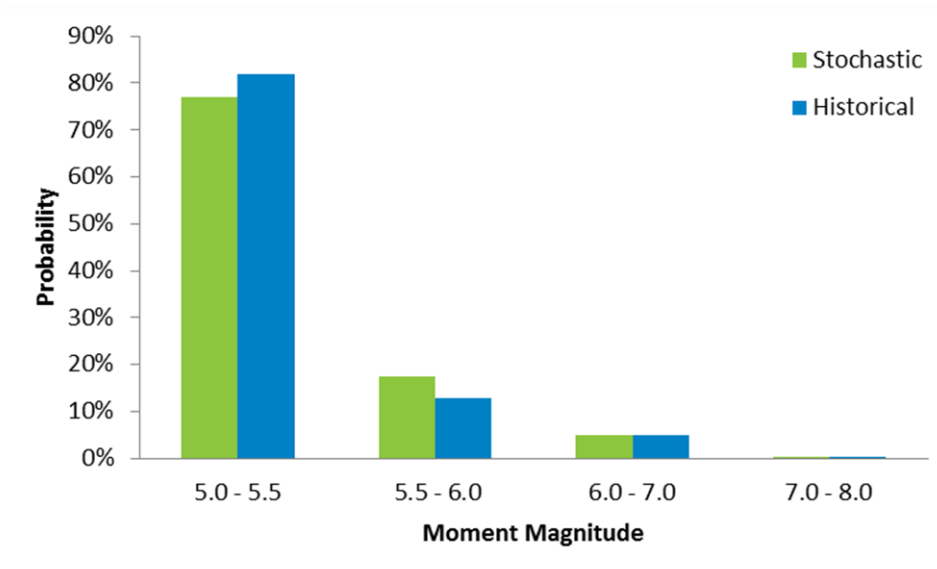


Figure A.75. Modeled vs. Historical Magnitude Distributions in the Southwest Indian Ocean

Validating the Location of Simulated Earthquakes

Figure A.76 shows a comparison between the 114 years of historical recorded events versus a randomly selected 114 year period extracted from the stochastic catalog, distributed by magnitude in the Southwest Indian Ocean Region. As expected, the stochastic events do not mirror the historical record, but instead

provide a realistic distribution of events in both regions of high seismicity (i.e., characteristic events) and low seismicity (i.e., background or GR-events).

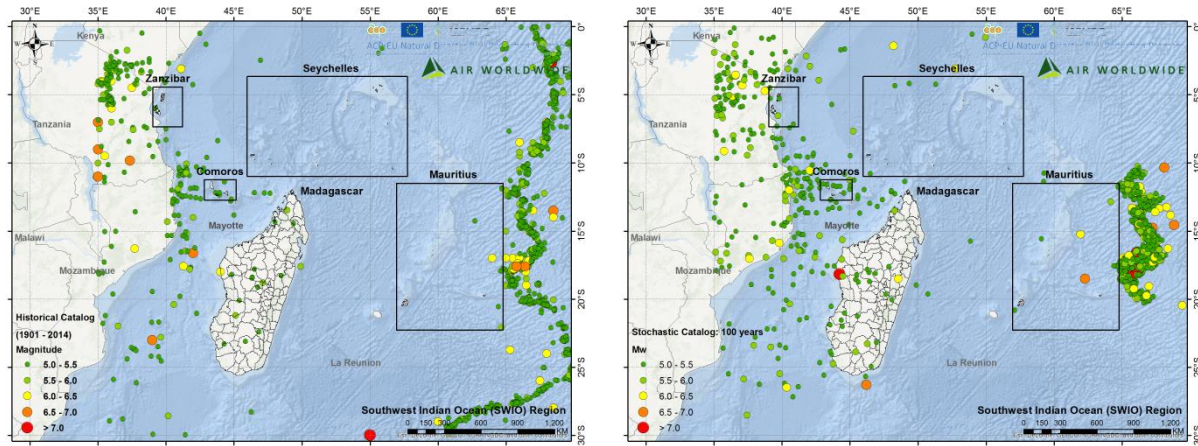


Figure A.76. Historical (left) vs. Stochastic (right) 114 year Catalogs of Earthquake Events (Note: The Mid-Indian ridge is only partially modeled (e.g., Zone 26) due to its remoteness relative to populated islands, resulting in the discrepancy between the historical and simulated event distributions on the right-hand side of each image)

Figure A.77 compares the cumulative percentages of historical and modeled events as functions of depth in the Southwest Indian Ocean region. Note that the depth distribution of historical earthquakes is not always smooth. This is because the depths of many historical earthquakes are not well constrained and, thus, these earthquakes are assigned default depth values, as discussed previously in Section 4.3.1.4. Figure A.78 shows the probability distributions of depths in the region.

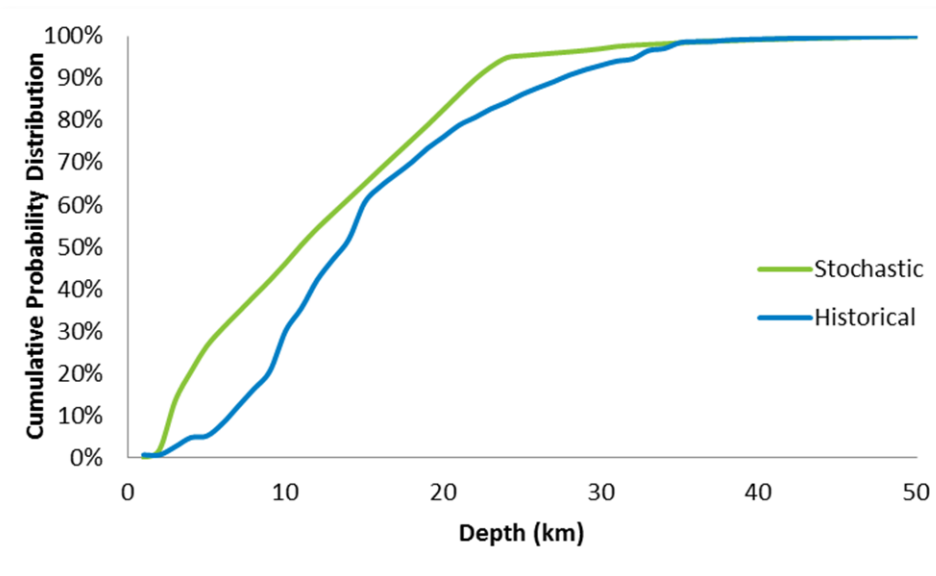


Figure A.77. Modeled vs. Historical Cumulative Depth Probability Distributions

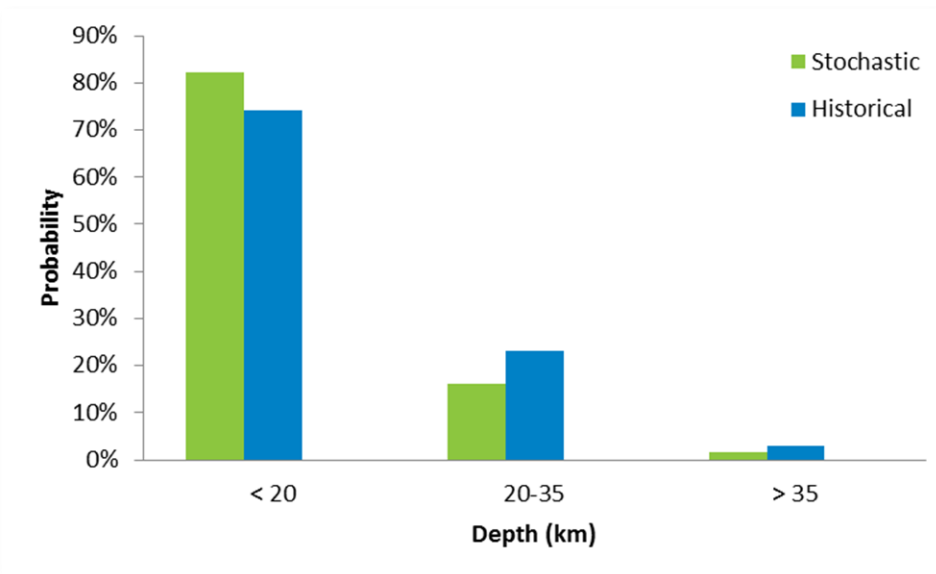


Figure A.78. Modeled vs. Historical Depth Distributions in the Southwest Indian Ocean

4.3.2 Local Intensity Calculation

After stochastic events have been generated, the intensity of ground shaking at a particular location must be calculated. Surface geology, attenuation, soil type, and other site amplification factors are considered in this component of the model.

The effects of an earthquake at a given site are often the result of multiple earthquake-related perils. While the initial shock affects the generation and many of the characteristics of these perils, their intensity at a site often depends on factors that are unrelated to the magnitude of the earthquake. If the event generates a tsunami, then coastal bathymetry and local topography are also taken into consideration to determine the effective tsunami inundation depth.

Ground-Shaking Intensity

In order to analyze damage and loss for each simulated earthquake, the ground-motion intensity at each affected surface location must be calculated. This ground motion can range from barely perceptible trembling to violent shaking, depending not only on the magnitude of the event, but also on the distance from the rupture to the affected site, the geological characteristics of the region, and local site conditions.

Ground-shaking intensity is commonly measured in terms of peak ground acceleration (PGA) and spectral acceleration (S_a). The peak ground acceleration is the maximum value of the ground acceleration and is typically referred to as motion in the horizontal direction. Spectral acceleration is the maximum response of a simple building, with a single natural frequency of vibration, to earthquake ground motions. S_a approximates the shaking intensity a building experiences during an earthquake.

Ground Motion Prediction Equations

Empirical ground motion prediction equations, or GMPEs, are practical tools used to estimate ground-shaking intensity as a function of the magnitude, location, and rupture mechanism of an earthquake. These equations, which were more commonly called attenuation relationships in the past, describe the rate at which certain ground-motion parameters evolve as the seismic waves propagate outward from the rupture source. Typically, ground motion decreases due to geometric spreading and the absorption and scattering of energy as the waves travel through the earth. However, depending on the soil type present at a specific location, the ground motion may experience amplification as well.

The general form of the GMPEs used in the AIR Earthquake Model for Southwest Indian Ocean model is as follows:

$$S_a = f(M, D, d, C, F, T)$$

where:

S_a = spectral acceleration or peak ground acceleration (m/s^2)

M = earthquake magnitude

D = distance from rupture plane (km)



d = focal depth (km)

C = site condition

F = faulting mechanism

T = period (inverse of frequency) (s)

The Southwest Indian Ocean region has minimal strong motion data resulting from the low seismicity and scarcity of instrumentation in the region. This deficit of data provides a challenge to validating the model's ground motion prediction equations (GMPEs). Fortunately, the Southwest Indian Ocean countries have similar tectonic characteristic as countries in the Southeast Asia, for which GMPEs have been validated for the AIR earthquake model in that region. As a result, the AIR Earthquake Model for the Southwest Indian Ocean region uses GMPEs similar to those applied for AIR's Earthquake model in Southeast Asia.

For crustal events, a combination of the attenuation relationships of Abrahamson et al. (2014), Boore et al. (2014), Campbell and Borzorgnia (2014), Chiou and Youngs (2014) and Idriss (2014) are used with appropriate weighting factors.

For deep interface events, a combination of the attenuation relationships of Addo et al. (2012), Atkinson and Boore (2003), Zhao et al. (2006), and Atkinson and Macias (2009) are used, with appropriate weighting factors dependent on magnitude.

For deep, intraslab events, a combination the relationships of Addo et al. (2012), Zhao et al. (2006) and Atkinson and Boore (2003, Global and Cascadia) are used.

Site Classifications and Ground-Motion Amplification

As seismic waves travel through the earth from the rupture source to the Earth's surface, earthquake ground-motion intensity may be amplified, or de-amplified, due to site conditions. The degree of amplification depends on the level of ground motion, the material properties of the site, and the frequency or period composition of the arriving waves. If the arriving seismic waves are of low-to-moderate intensity, a site with a soft surface geology may experience significantly higher levels of ground motion than a rock site. This is especially true for low-frequency seismic waves, which are the most damaging to mid- and high-rise buildings. On the other hand, if the incoming ground motion is very high (e.g. close to 1 g), a site with soft soils can experience lower ground motion than a site consisting of firm soil or rock.

Site conditions may be classified based on the physical properties of surficial geological materials. In the AIR Earthquake Model for Southwest Indian Ocean, local geological maps at various scales are used to develop site condition maps. Geological units are grouped into nine categories according to their similarities in physical properties, such as shear-wave velocities. These nine categories consist of the five original National Earthquake

Hazards Reduction Program (NEHRP) site classes (A – hard rock, B – rock, C – firm soil, D – soft soil, E – very soft soil) plus four intermediate classes between these five classes. The mean shear-wave velocity for each of the nine site classes is used to calculate ground-motion amplification factors. Table A.10 shows these classifications and their associated average shear wave velocity in meters per second. Maps detailing the average shear-wave velocity in the upper 30 meters of soil (the 30 meters immediately below the surface of the earth) are used to estimate site amplification. These are known as Vs30 maps and are constructed for the SWIO region using 400m topographic data and applying a topographic slope-based Vs30 calculation methodology proposed by Wald and Allen (2007). Figure A.79 shows the resulting soil map in the SWIO region with the NEHRP soil classification defined in Table A.10.

Table A.10. NEHRP Soil Classifications and average shear-wave velocities

Soil Classes	Description	Average Shear Wave Velocity (m/s)
A	Very hard rock	1620
AB	Hard rock	1150
B	Firm to hard rock	1050
BC	Firm rock	760
C	Soft to firm rock (gravelly soil and soft rock)	540
CD	Soft rock (gravelly and stiff soil)	370
D	Stiff clay and sandy soil	330
DE	Soft soil to firm soil (silty clay and sand)	280
E	Soft soil (includes mud)	160

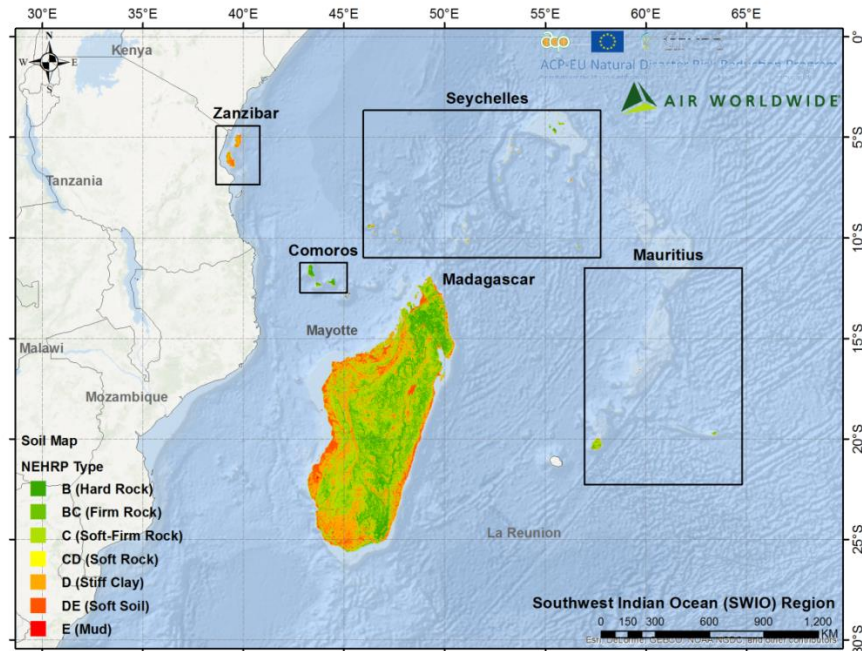


Figure A.79. NEHRP Classification Soil Map in the Southwest Indian Ocean Region

Stochastic and Correlated Ground Motion Fields

It is necessary to reconstruct the ground motion fields for selected historical events to make the modeled ground motion field as consistent with the observed intensity data as possible. This is a challenge, as the actual ground motion data for these events are often limited to: (1) a handful of recordings at different sites and; (2) a regional MMI intensity map. In every case in the SWIO region, insufficient information exists to construct unique regional ground motion fields for the selected historical earthquakes.

To address this challenge, a series of stochastic ground motion fields are simulated using GMPEs and available ground motion information for each event. These simulations consider site-to-site ground motion correlated effects (Mahdyiar et al. 2010) as described below.

The calculation of ground motion intensity has traditionally been described as a function of event magnitude, the source-to-site distance, and the local soil conditions. These calculations also account for variability in the ground motion, based on observed deviations during historical earthquakes. The variable ground motion intensities are included in the equations by means of a lognormally-distributed error term, also known as a "residual."

Recent studies of these ground motion residuals show that, rather than being randomly distributed through an area during an earthquake, there is a distinct correlation between residuals at one site and residuals at nearby sites. That is, observations have shown that if the ground motion is higher than expected at a particular site, it is more likely that a nearby site will also experience higher-than-expected ground motion.

For hazard and risk analysis, it is common practice to estimate the ground motion at sites using regional GMPEs. GMPEs provide estimates of the *median ground motion* as a function of magnitude, distance, and source mechanisms, and provide an estimate of uncertainty in ground motion due to source radiation, path, and local site effects. A typical GMPE often is formulated as:

$$\ln(Y) = \ln(\bar{Y}) + \varepsilon_{Inter} + \varepsilon_{Intra}$$

where Y is the logarithm of the point estimate of the ground motion (GM), \bar{Y} is the median of the logarithm of the point estimate of GM, and ε_{Inter} and ε_{Intra} are the inter- and intra-event random errors that reflect the source and path and site related uncertainties, respectively. ε_{Inter} and ε_{Intra} are assumed to be independent. The inter-event component leads to an overall regional spatial correlation for any two sites:

$$\rho_{GM} = \frac{\sigma_{Inter}^2}{\sigma_{Inter}^2 + \sigma_{Intra}^2}$$

where ρ_{GM} is the ground motion correlation. However, studies on the similarities in ground motion for different events, after removing the estimated median of the ground motion values, indicate that the ground motion correlation for sites close to one another is statistically larger than that predicted by the equation above.

This intra-site correlation, which is distance dependent, can have a large impact on the regional loss distribution, making the damage from some earthquakes very costly (Bazzurro and Park 2007). The overall ground motion correlation, including intra-site correlation, can be formulated as:

$$\rho_I = \frac{\sigma_{Inter}^2 + \rho(d)\sigma_{Intra}^2}{\sigma_{Inter}^2 + \sigma_{Intra}^2}$$

where ρ_I is the intra-site correlation and $\rho(d)$ represents the distance between stations (Boore et al. 2003, Park et al. 2007).

Estimating the expected losses for each calibrating earthquake requires simulating sets of stochastic ground motion fields that reflect the inter-event and intra-site spatial correlation constrained by observed ground motion data, when available. That is, when ground motion recordings are available, the information can be used to constrain the simulation at sites near the recording stations. For earthquakes with only MMI data or contour maps, the intensity information can be translated into ground motion values that are again used to constrain the simulation, while taking into consideration uncertainty in the intensity-to-ground-motion conversion. Thus the approach taken by AIR explicitly takes into account the quality of the available data.

In summary, it is important to formulate a stochastic ground motion simulation procedure that is: (1) based on the regional attenuation equations; (2) captures the stochastic nature of the ground motion and the intra-site correlation effects, and; (3) incorporates the constraints imposed by different kinds of observations.

A practical approach is to simulate a set of stochastic ground motion residuals, with respect to the median ground motion, at sites of interest that conforms to the imposed ground motion constraints. The many sets of residual fields capture the regional inter-event, intra-event, and intra-site correlation effects. Given that the residuals are simulated for the reference site conditions, the regional footprint can be constructed using information about the shallow soil site conditions.

By adding stochastically simulated residuals to the median ground motion and applying the shallow site response, different realizations of the ground motion footprint for an earthquake are created.

Hazard Maps in the Southwest Indian Ocean Region

Following the procedure described above, ground motion intensities, in terms of peak ground acceleration expressed in acceleration of gravity (g) units, have been calculated for each event in the stochastic catalog at a 1-km grid resolution. Figure A.80, Figure A.81, and Figure A.82 show the levels of ground shaking in Comoros, Madagascar, Mauritius, Seychelles and Zanzibar, respectively, due to earthquakes that have a 100 year mean return period, which is approximately equivalent to a 40% chance of being exceeded at least once in the next 50 years.. Peak ground accelerations greater than about 0.05 g are capable of generating damage to buildings with consequent economic losses.

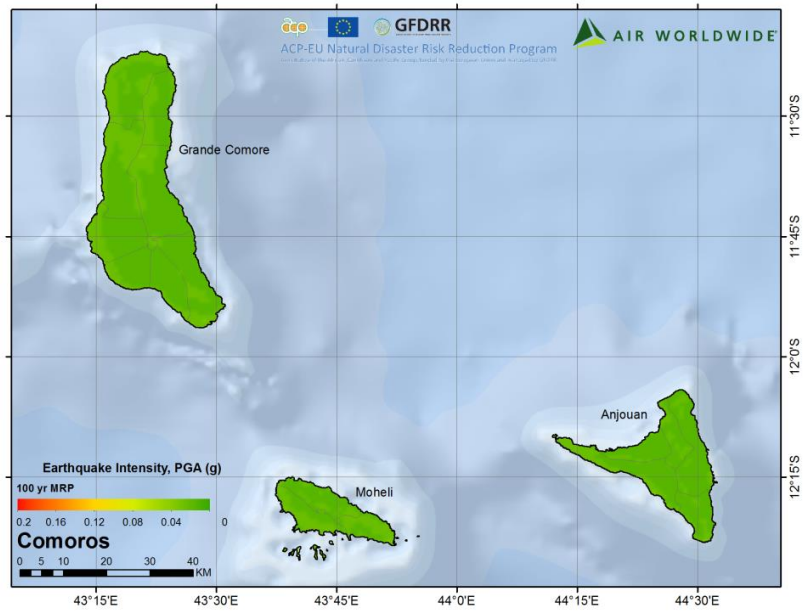


Figure A.80. Comoros: peak horizontal ground acceleration at the 100-year mean return period.

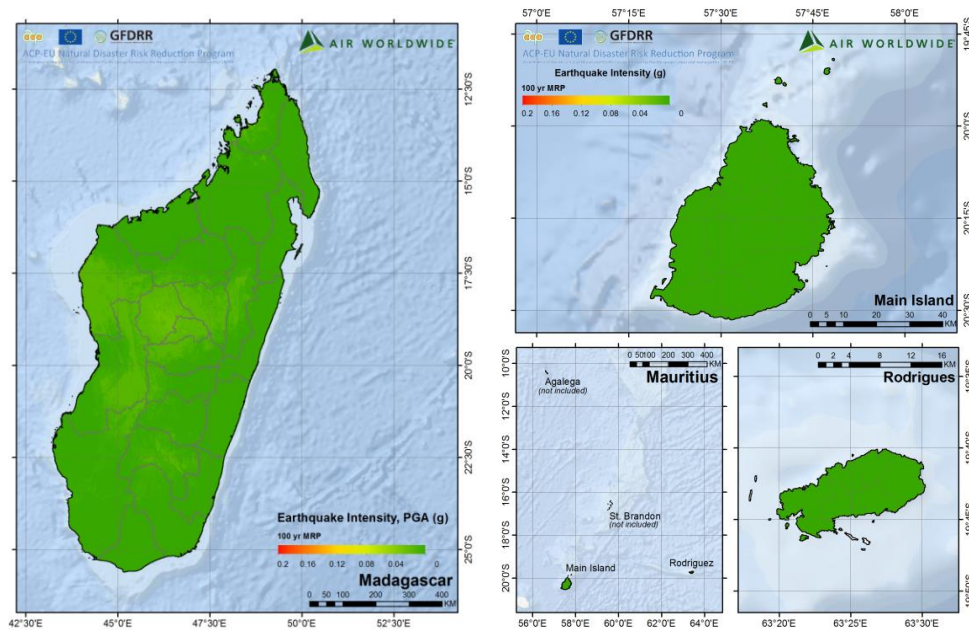


Figure A.81. Madagascar (left) and Mauritius (right) peak horizontal ground acceleration at the 100-year mean return period.

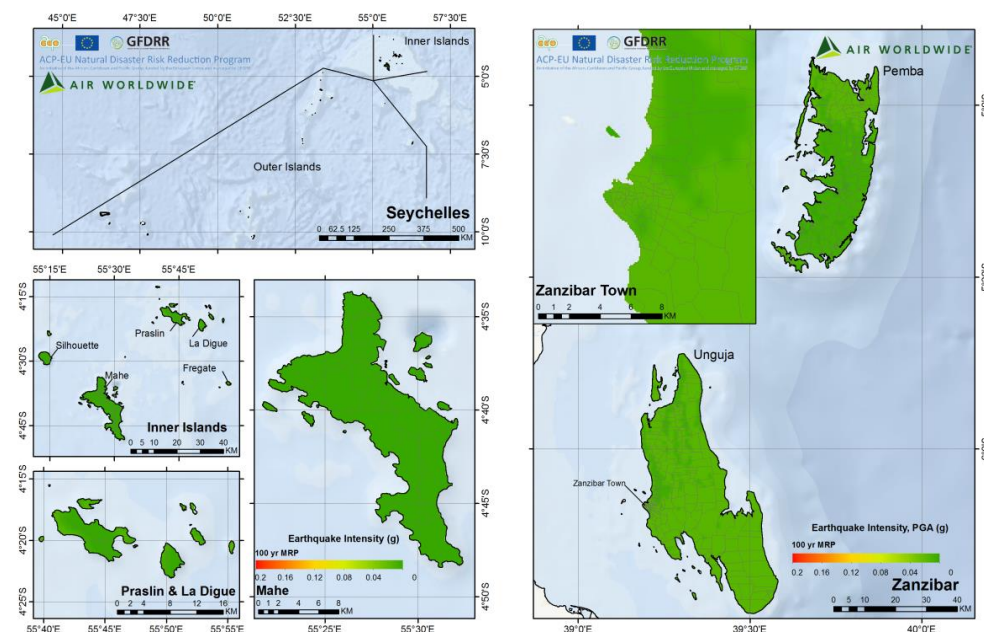


Figure A.82. Seychelles (left) and Zanzibar (right) peak horizontal ground acceleration at the 100-year mean return period.

Validating Local Intensity

The SWIO region has minimal strong motion data resulting from the low seismicity and scarcity of instrumentation in the region, therefore the validation of the ground motion intensity calculation is performed by comparing to other agency's modeled intensities in the region, such as those reported by the United States Geological Survey (USGS). Due to the low historical seismicity in the SWIO region, there are similarly few modeled intensities, which further complicates model validation. Thus, intensity validation is performed for the few significant events for which the USGS has also modeled regional intensities. This comparison is illustrated for two events in Figure A.83 and Figure A.84, which contrast the modeled ground motion intensity calculated by the AIR (left) and the USGS (right) models for the 1985 and 1991 earthquakes in Madagascar, respectively. The ground-motion intensities shown are expressed in terms of PGA (g) and validate well in terms of intensity and spatial distribution.

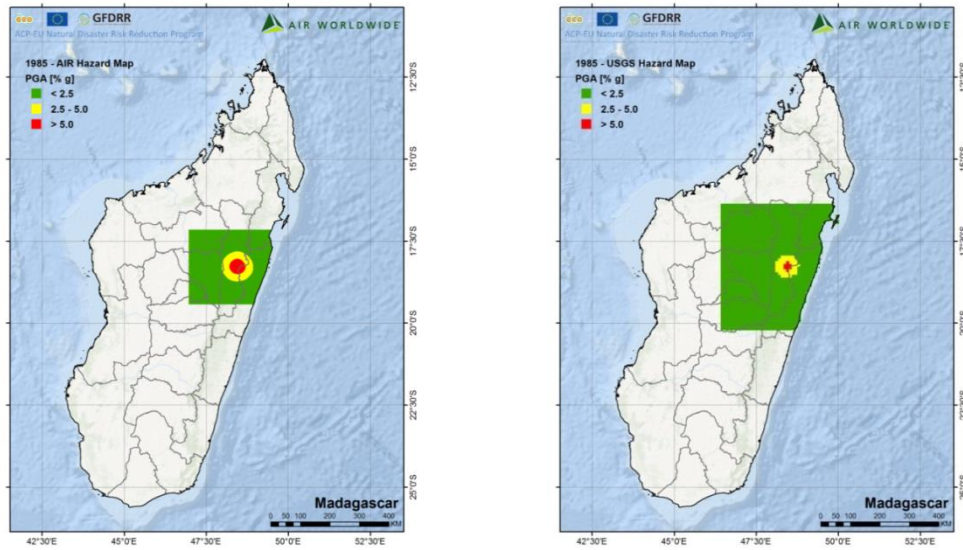


Figure A.83. AIR (left) vs. USGS (right) Modeled Ground Motion, the 1985 Madagascar Earthquake

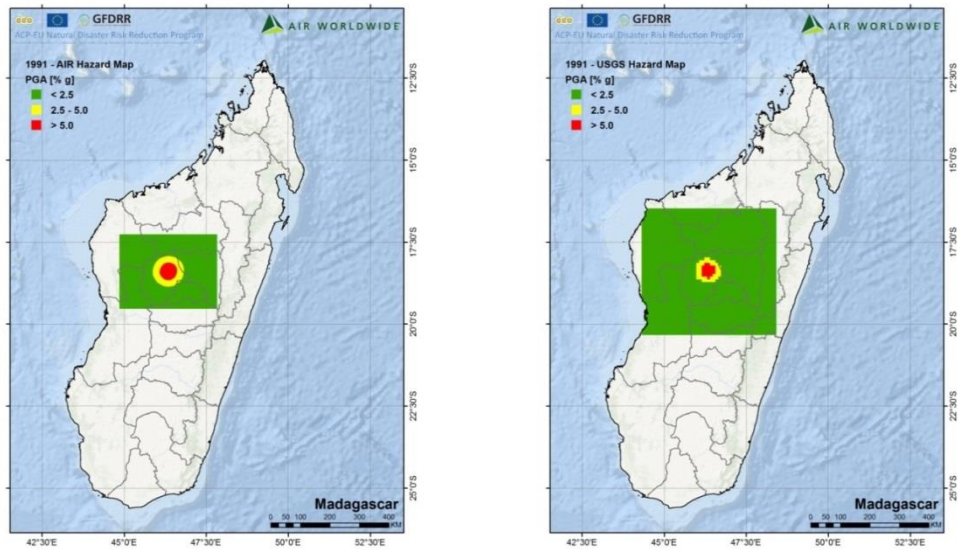


Figure A.84. AIR (left) vs. USGS (right) Modeled Ground Motion, the 1991 Madagascar Earthquake

4.3.3 Tsunamis in the Southwest Indian Ocean

Maps identifying tsunami risk zones have been developed for each major island in all of the SWIO countries. These maps characterize the “worst-case” tsunami risk zones of the SWIO islands and incorporate a set of modeled tele-tsunamis generated by earthquakes occurring elsewhere in the Indian Ocean. The rupture characteristics of the modeled earthquakes are used in conjunction with local bathymetry and elevation data to calculate tsunami propagation and run-up using the MOST modeling framework and the ComMIT platform, developed by NOAA. The resulting maps represent a maximum inundation footprint, which are constructed by superimposing the tsunami inundation footprints from each modeled event.

Overview

Due to the relatively low intensity of earthquakes in the SWIO region, the risk of tsunamis induced by local earthquakes is minor. However, the region is at risk of experiencing significant tele-tsunamis generated by subduction faults elsewhere in the Indian Ocean, as observed in the 2004 Indian Ocean Tsunami. Tsunamis are generated when offshore earthquake events result in an abrupt deformation of the sea floor, which displaces the water above the deformed area resulting in the movement of water, as illustrated in Figure A.85. The largest tsunamis are generated by earthquakes on megathrust subduction faults, which can cause significant vertical seafloor deformation.

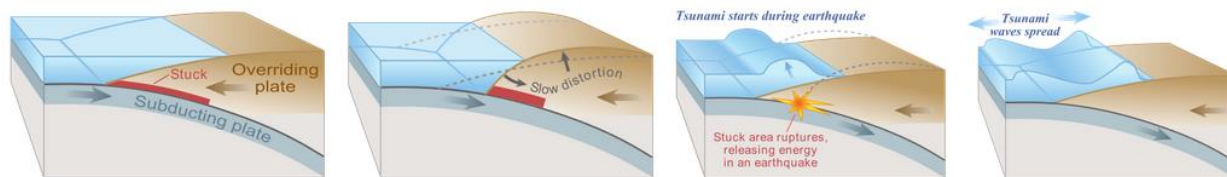


Figure A.85. An illustration of the mechanism of tsunami genesis at subduction zones (source: Wikipedia)

Although there are no major subduction zones in the SWIO region, tsunamis generated by subduction zones elsewhere, known as tele-tsunamis, are capable of traveling long distances in deep ocean water. These waves can be amplified and re-directed by bathymetric features on the seafloor, such as oceanic ridges, troughs, and basins, which can complicate the prediction of their regional distribution and local intensity.

Propagation and Inundation Model

The ComMIT (Community Model Interface for Tsunami) software tool, developed by the National Oceanic and Atmospheric Administration (NOAA) was used to compute the propagation of tele-tsunamis over the Indian Ocean, as well as the run-up and inundation along the SWIO island coastlines. ComMIT leverages the widely-used Method of Splitting Tsunamis (MOST) approach developed by Titov and Synolakis (1996) and was developed at the behest of the Intergovernmental Coordination Group for the Indian Ocean Tsunami Warning

and Mitigation System (ICG/IOTWS) in order to provide a user-friendly platform for constructing tsunami inundation maps.

In ComMIT, trans-oceanic wave propagation is precomputed for a number of major fault segments around the globe. The wave amplitudes resulting from single or multi-segment subduction earthquake events are scaled and combined to simulate the initial condition of tsunami event, as shown in Figure A.86. In order to more accurately calculate wave propagation and inundation near coastlines, the model additionally considers detailed elevation and bathymetry data.

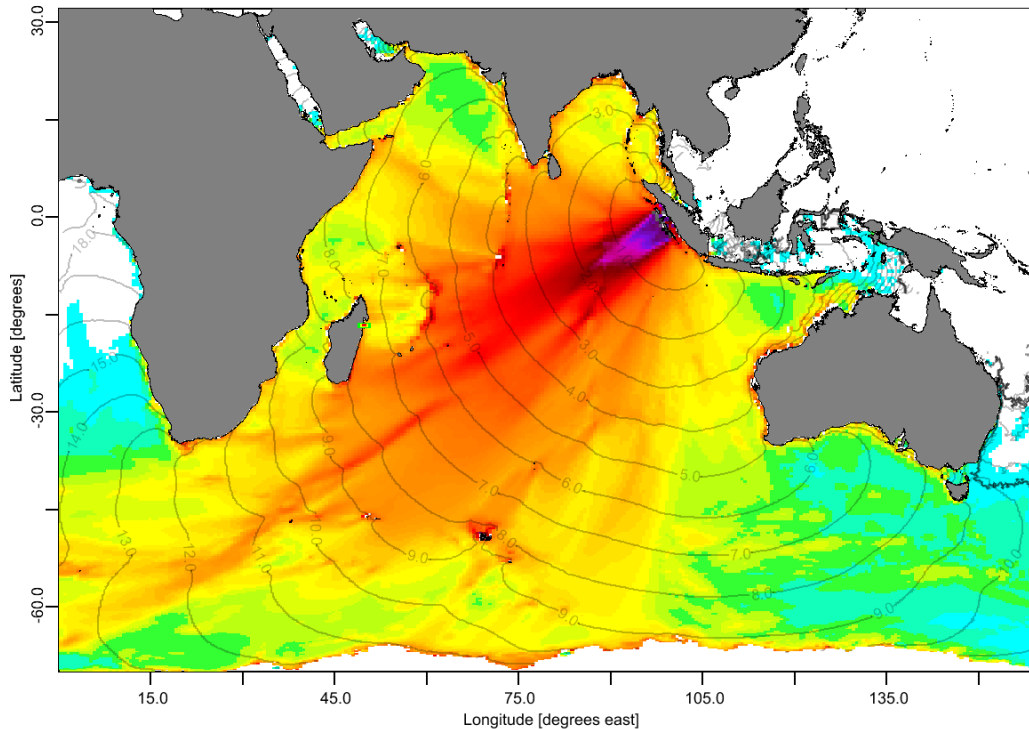


Figure A.86. An example of a pre-computed tsunami simulated on the Sunda fault in the ComMIT interface

Digital Elevation and Bathymetry Models

The digital elevation model (DEM) implemented in ComMIT and used to calculate tsunami propagation and run-up draws from a number of data sources, including elevation maps provided by the local governments, the Shuttle Radar Topography Mission 90-meter dataset (SRTM 90m), the Advanced Spaceborne Thermal Emission and Reflection Radiometer 30-meter dataset (ASTER), and the General Bathymetric Chart of the Oceans 30 arc-second dataset (GEBCO). In general, the GEBCO data is interpolated to 3 arc-seconds (approximately 90 meters) and merged with SRTM 90m. The provided local agency elevation datasets and the ASTER dataset are then used to refine areas of interest with finer topographic features. This refinement is

particularly important for small island nations, such as Seychelles, where the resolution of most global datasets is too coarse to accurately capture the coastline. The resulting tsunami risk maps show inundation areas at a resolution of 3 arc-seconds.

Tsunamigenic Event Selection

The major fault zones in the Indian Ocean are illustrated in Figure A.87. Among these regions, the highest risk of tele-tsunamis comes from the Makran Subduction Zone, located to the North of the SWIO islands, and the Sunda megathrust fault, located to the Northeast of the SWIO islands near Indonesia. Both of these subduction zones are shown in yellow. Other locations of interest include the Davie ridge, located in the Western portion of the SWIO domain, and the Mid-Indian Ridge, located to the East of the SWIO islands. Both of these divergent boundaries are shown in red below. Although these divergent boundaries have not produced a significant tsunami in recorded history, they are capable of producing tsunamis, albeit infrequently, neither of these seismic zones has produced a significant tsunami in recorded history. Additionally, no events in the AIR Southwest Indian Ocean Stochastic Earthquake Catalog are large enough to produce a significant tsunami, indicating that it is unlikely for the local tectonic conditions of the Southwest Indian Ocean region to produce earthquakes capable of generating large tsunamis.

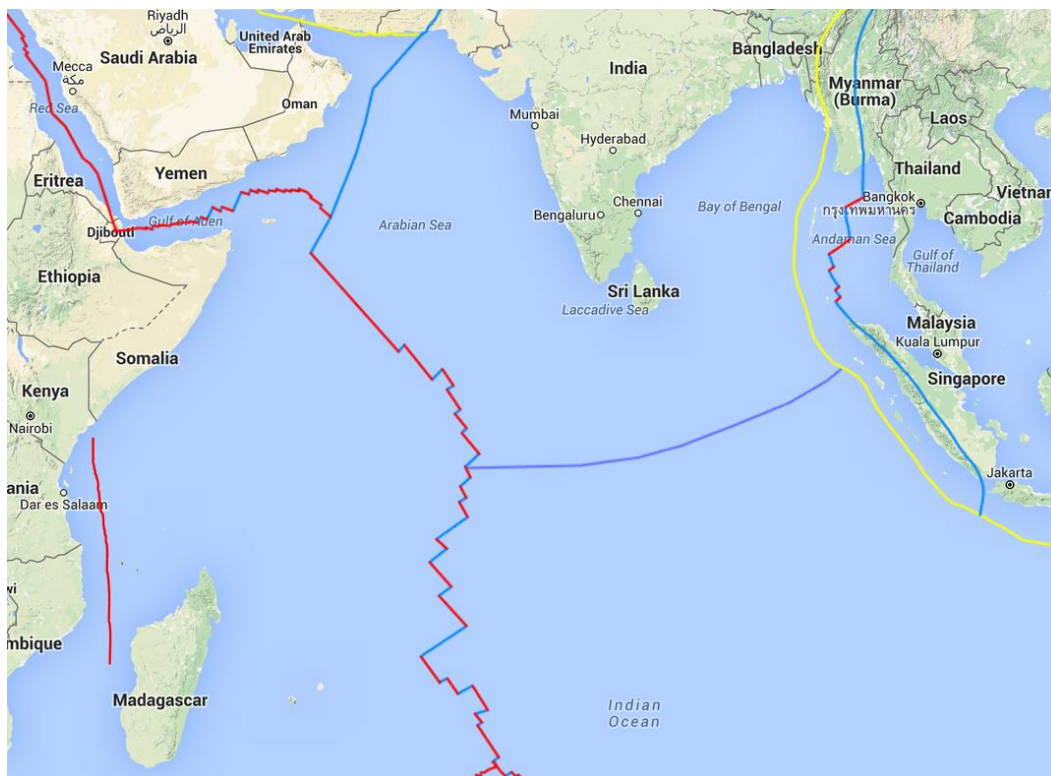


Figure A.87. Tectonic setting of the SWIO Region (source: IRIS, Google)

Thus, the primary tsunami risk that was considered for the SWIO islands is the effect of far-field tele-tsunamis generated by the Makran subduction zone, to the South of Iran and Pakistan, and the Sunda megathrust fault, which runs along the Southwestern and Southern coasts of the Indonesian Archipelago. Large tsunamigenic events that are characteristic of each major section of the Sunda fault were selected from the AIR Southeast Asia Earthquake Catalog and modeled in ComMIT. While there is no recorded history of earthquakes at the Makran fault producing tele-tsunamis that have reached the SWIO region, the largest earthquake theoretically possible in this region was modeled along this fault as well. The effects of all the modeled events on each of the islands were superimposed to produce the final tsunami inundation risk maps.

Results and Analysis

The tsunami risk zones identify high-risk areas derived from modeled events and historical observations. Low-lying coastal regions, areas with high offshore wave amplitudes in the model, and regions with significant historical inundation were used to identify these areas. Including historical inundation areas allows the identification of tsunami-susceptible areas that were not inundated in the modeled events due to the limitations of the MOST method, the available data, or the limited number of events selected. The resulting risk zones are distributed as expected, based on observations from the 2004 event. Coastlines in the direction of the tsunami source, low-lying coasts, and bays are at elevated risk, although some of the results can be counterintuitive. For example, the tsunami risk zones for Zanzibar, shown below in Figure A.88 appear to indicate widespread tsunami inundation on all coasts of both Pemba and Unguja islands. However, the map should be seen as a superposition of several severe tsunami events, with inundation footprints that reach far inland in some areas, due to flat terrain. Additionally, tsunamis can “wrap around” islands, affecting coasts that are not in the direct path of the tsunami wave.

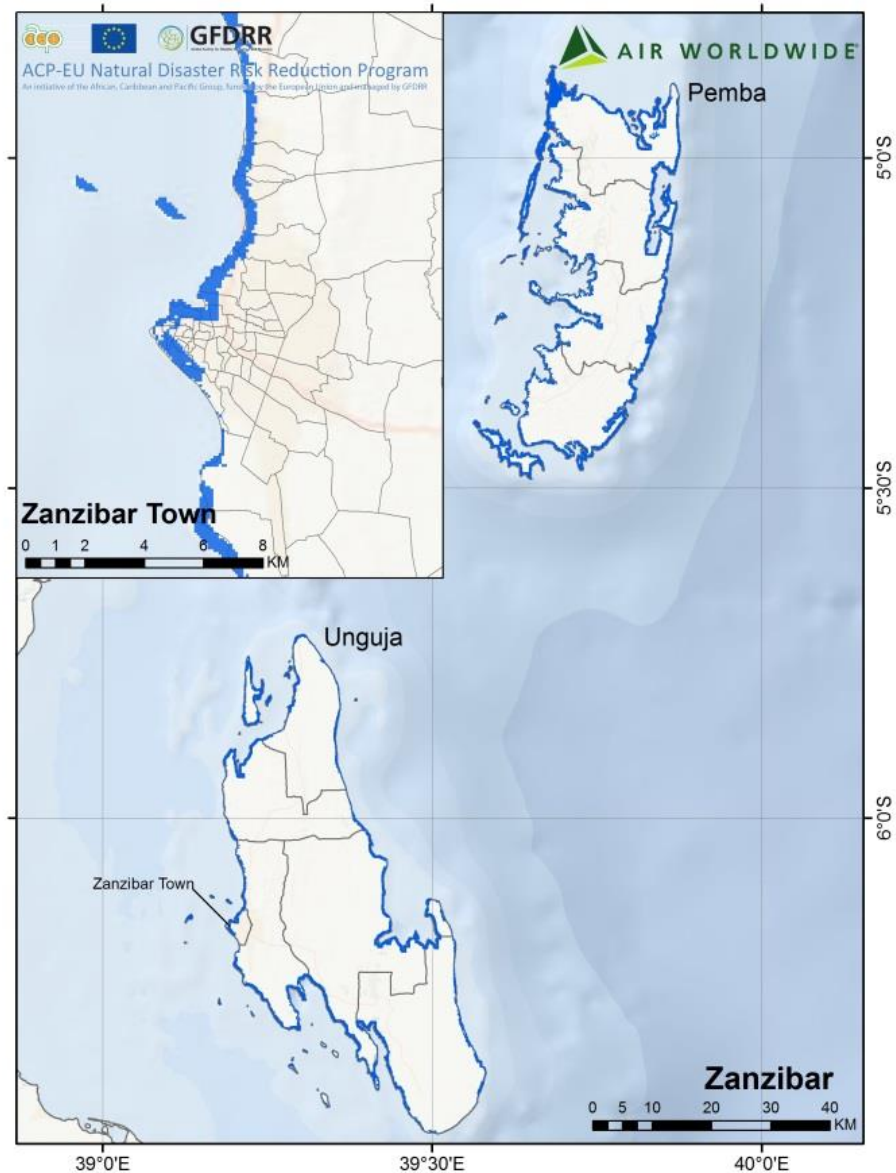


Figure A.88. Tsunami risk zones for Zanzibar

There is tsunami risk on every coast of Madagascar as well, but it is more localized than it is in Zanzibar. Risk areas align closely to expectations; a majority of them are along low-lying areas of Madagascar's Southeastern coast near Mananjary and Manakara, highlighted below in Figure A.89. Areas in and around the coastal lagoons and marshes along this coast are particularly vulnerable to tsunami inundation. Similar regions along

the coastline were inundated by the 2004 Indian Ocean tsunami, as reported by the International Tsunami Survey Team (Okal et al. 2006).

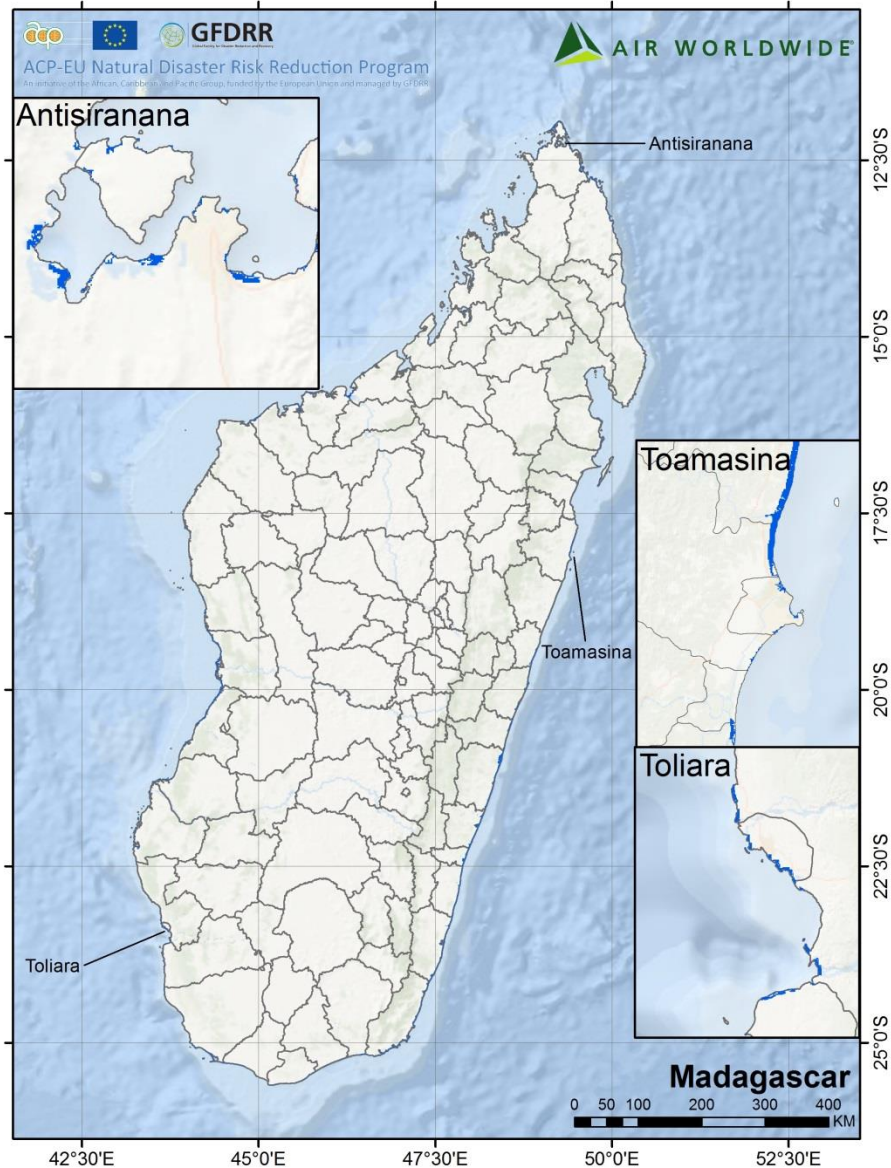


Figure A.89. Selected tsunami risk zones for Madagascar

The tsunami risk zones of Seychelles also correspond to previously recorded inundation measurements. A comparison between the Mahé tsunami risk map and the observed inundation resulting from the 2004 Indian Ocean tsunami from a report by the United Nations Development Project (UNDP) is presented below in Figure

A.90. As expected, the relatively flat areas of reclaimed land near the coast of Victoria are highly susceptible to tsunami inundation, as well as low-lying areas near shallow bays on all sides of the island. Note that areas not previously inundated by the 2004 event are still considered, such as the islands of Sainte Anne Marine National Park, reflecting the additional hazard imposed by the considered earthquake scenarios.

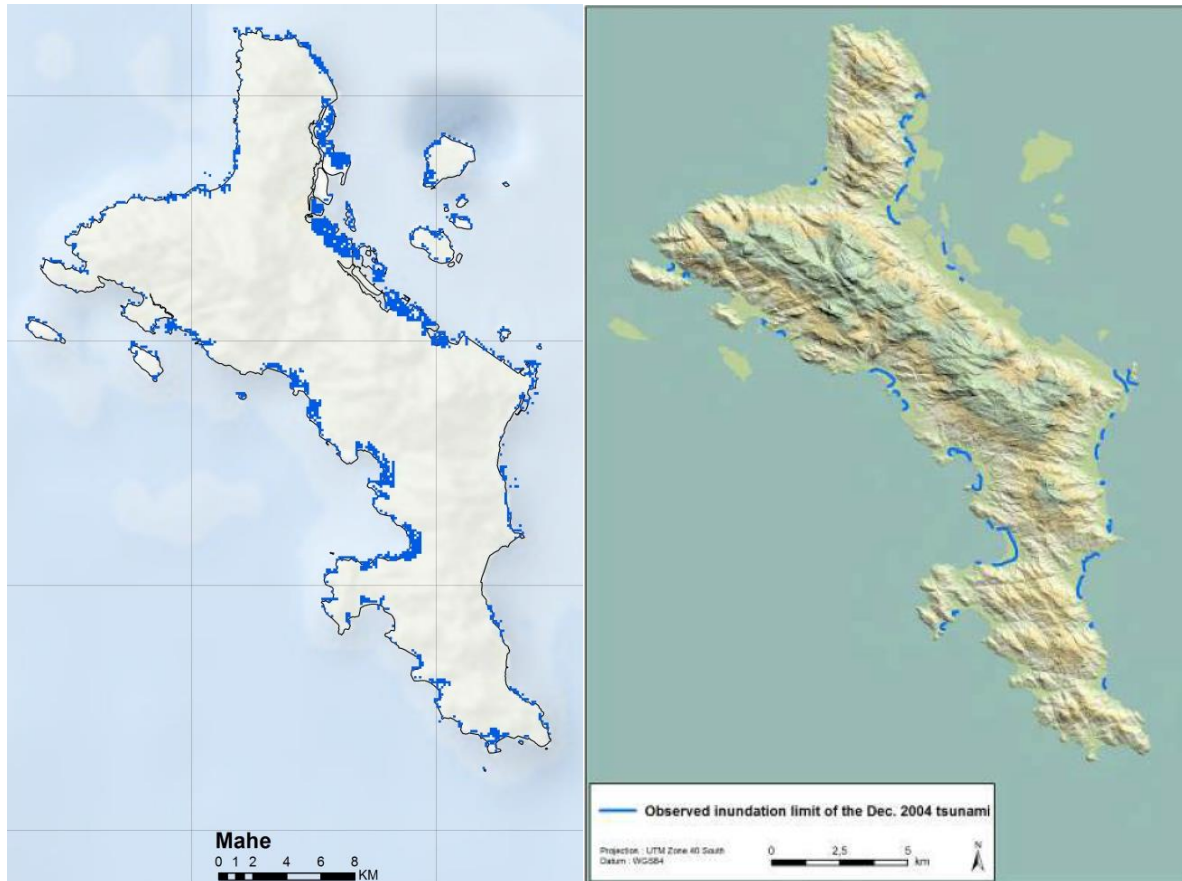


Figure A.90. Comparison between the modeled Seychelles tsunami map (left) and 2004 tsunami inundation by UNDP (right) for the island of Mahé

Limitations

The tsunami risk zones presented in this report are intended to provide a simplified understanding of tsunami hazard in the SWIO region. These zones are deterministic and are associated with various scenario events that have different occurrence probabilities and inundation depths. Although it is true that events of the magnitude and scale of those used in this analysis are infrequent, these maps should not be used for any forecasting or predictive purposes. The inundation zones primarily indicate areas that are geographically susceptible to significant tsunami run-up.

The tsunami risk zones were developed using publically available, third-party software and data. Accurate, high-resolution bathymetry and elevation data can be leveraged to produce more reliable results. The quality of the maps can further be improved by incorporating more inundation and amplitude data from historical tsunamis, as well as information on tidal effects, which are not currently considered.

4.3.4 References

- Abrahamson, N. and W. Silva, 1997, "Empirical Response Spectral Attenuation Relations for Shallow Crustal Earthquakes," *Seismological Research Letters*, 68, 94-127.
- Abrahamson, N. A., Silva, W. J., and Kamai, R., 2014, "Summary of the ASK14 ground motion relation for active crustal regions", *Earthquake Spectra* 30, 1025–1055.
- Andrianaivo L and Ramasiarinoro V.J., 2015, Proceedings of the World Geothermal Congress 2015, Melbourne, Australia, Structural Model of the Itsay Geothermal Prospect in Central Madagascar: Preliminary Review.
- Applied Technology Council, 1985, *ATC-13 Earthquake Damage Evaluation Data for California*. Redwood City, California: Applied Technology Council.
- Atkinson, G. and D. Boore, 2003, "Empirical Ground Motion Relations for Subduction-Zone Earthquakes and Their Application to Cascadia and Other Regions," *Bulletin of the Seismological Society of America*, 93, 4, 1703-1729.
- Atkinson, G. M., and Boore, D. M., 2011, "Modifications to existing ground-motion prediction equations in light of new data", *Bull. Seismol. Soc. Am.* 101, 1121–1135.
- Boore, D. M., Stewart, J. P., Seyhan, E., and Atkinson, G. M., 2014, "NGA-West2 equations for predicting PGA, PGV, and 5% damped PSA for shallow crustal earthquakes", *Earthquake Spectra*, 30, 1057–1085.
- Campbell, K. W., and Bozorgnia, Y., 2014, "NGA-West2 ground motion model for the average horizontal components of PGA, PGV, and 5% damped linear acceleration response spectra", *Earthquake Spectra*, 30, 1087–1115.
- Chiou, B. S.-J., and Youngs, R. R., 2014, "Update of the Chiou and Youngs NGA model for the average horizontal component of peak ground motion and response spectra", *Earthquake Spectra* 30, 1117–1153.
- Chorowicz J., 2005, "The East African rift system", *Journal of African Earth Sciences*, Vol. 43.
- Chu D. and Gordon R.G., 1999, "Evidence for motion between Nubia and Somalia along the Southwest Indian ridge", *Nature*, Vol. 398(4).
- DeMets, C., R. G. Gordon, D. F. Argus, and S. Stein, 1994, "Effect of Recent Revisions to the Geomagnetic Reversal Time Scale on Estimates of Current Plate Motions," *Geophysical Research Letters*, 21, 2191-2194.
- DeMets C., Gordon R.G. and Argus D.F., 2010, "Geologically current plate motions", *Geophysical Journal International*, Vol. 181.
- Engdahl, E.R., R. van der Hilst, and R. Buland, 1998, "Global teleseismic earthquake relocation with improved travel times and procedures for depth determination", *Bull. Seism. Soc. Am.* 88, 722-743.

- Horner-Johnson B.C., Gordon R.G. and Argus D.F., 2007, "Plate kinematic evidence for the existence of a distinct plate between Nubian and Somalian plates along the Southwest Indian Ridge", *Journal of Geophysical Research*, Vol. 112.
- Idriss, I. M., 2014, "An NGA-West2 empirical model for estimating the horizontal spectral values generated by shallow crustal earthquakes", *Earthquake Spectra* 30, 1155–1177.
- Lardeaux J.M., Martelat J.E., Nicollet C., Pili E., Rakotondrazafy R. and Gardon, H., 1999, "Metamorphism and tectonics in Southern Madagascar: An Overview", *Gondwana Research*, Vol. 2(3).
- Midzi A., Hlatywayo D.J., Chapol L.S., Kebede F., Atakan K., Lombe D.K., Turyomurugyendo G. and Tugume F.A., 1999, "Seismic hazard assessment in Eastern and Southern Africa", *Annali di Geofisica*, Vol. 42(6).
- Mulwa J.K., Kimata F. and Duong N.A., 2013, "Chapter 19: Seismic Hazard", *Developments in Earth Surface Processes*, Vol 16.
- Okal E.A., Fritz H.M., Raveloson R., Joelson G., Pančošková P., and Rambolamanana G., 2006, "Madagascar Field Survey after the December 2004 Indian Ocean Tsunami", *Earthquake Spectra*, Vol. 22(S3), S263-S283.
- Pasupuleti V.D.K. and Ramancharla P.K., 2014, "Interactions and seismicity of Indian tectonic plate with its neighboring plates: an overview", *International Journal of Advanced Earth Science and Engineering*, Vol 3(1).<http://www.globalquakemodel.org/what/seismic-hazard/strain-rate-model/>
- Sadigh, K., C. Y. Chang, J. A. Egan, F. Makdisi, and R. R. Youngs, 1997, "Attenuation Relationships for Shallow Crustal Earthquakes based on California Strong Motion Data," *Seismological Research Letter*, 68, 180-189.
- Saemundsson K., 2010, "East African rift system – an overview ", *Short Course on Exploration of Geothermal Resources organized by the United Nations University*.
- Saria E., Calais E., Stamps D.S., Delvaux D. and Hartnady C.J.H., 2014, "Present-day kinematics of the East African Rift", *Journal of Geophysical Research: Solid Earth*.
- Stamps, D.S., E. Saria, C. Kreemer, 2015, "Sub-Saharan Africa Geodetic Strain Rate Model" 1.0, August 2015, Strain Rate Model / Sub-Saharan Africa, available from <http://www.globalquakemodel.org/what/seismic-hazard/strain-rate-model/>.
- Wald, D. J., and T. I. Allen, 2007, "Topographic slope as a proxy for seismic site conditions and amplification", *Bull., Seism. Soc. Am*, Vol. 97, No. 5, 1379-1395.
- Youngs R. R., S. J. Chiou, W. J. Silva, and J. R. Humphrey, 1997, "Strong Ground Motion Attenuation Relationships for Subduction Zone Earthquakes," *Seismologic Research Letter*, 68, 58-73.

4.4 Landslide

Landslide susceptibility zonation maps have been generated for the three islands of Comoros and indicate areas of high, medium, and low susceptibility. The zonation maps represent the results of the most up-to-date research methods for determining landslide susceptibility for the currently available data for Comoros. Based on the available information, the frequency ratio method was selected as most suitable for the analysis to determine the qualitative landslide susceptibility. The results from the landslide susceptibility zonation maps categorize the area of the three islands as approximately 4% high susceptibility, 40% medium susceptibility, and 56% low susceptibility.

4.4.1 Introduction

The landslide susceptibility of a region is generally defined as the probability of a landslide occurrence, which may be based on empirical or modeled information (Lepore et al. 2011). When the conditions that promote slope instability are identified, it may be possible to give a qualitative or a semi-quantitative measure about the landslide susceptibility for the area under consideration (Varnes and IAEGC 1984). This approach to landslide susceptibility zonation implicitly assumes that future slope failures will occur with similar probability and under the same conditions that led to past and present soil instabilities. However, the geomorphological factors which generate landslides for a particular area may vary over time, and the resulting zonation maps should be interpreted with care.

The country of Comoros consists of the islands of Grand Comore, Anjouan, and Moheli, which are volcanic in origin but at different evolutionary stages in geological development. The youngest is Grand Comore, with two shield volcanoes of La Grille and Mount Karthala. Geochemical dating of the island gives the initiation of volcanism as far back as 0.13 Ma (mega-annum), and it is still emerging through geologically frequent volcanic eruptions from Mount Karthala. For Anjouan, the geochemical dating of post-erosional soil layers gives the initiation of volcanism between the ages of 1.5 and 0.4 Ma. And for Moheli island, the initiation of volcanism on the island has been dated to 2.8 to 0.62 Ma. (Charmoille 2013; Esson et al. 1970; Flower 1972; Späth et al. 1996)

The morphology of the islands is similar to those formed by other shield volcanoes, such as the Hawaiian volcanoes, in different stages of growth and erosion (Okal et al. 2009). The soil characteristics vary from one island to another, which is a consequence of their geological formation and weathering over time. Both Anjouan and Moheli have portions of cementitious soil marked by erosion, while Grand Comore has less variation in marked relief with Mount Karthala rising to 2,361 meters. (Abdoulkarim and Soule 2011)

4.4.2 Landslide Susceptibility

Landslide susceptibility zonation is based on methods to identify and obtain the correlations between landslide-inducing factors and areas where landslides have been recorded. In general, the basic causes of slope

instability are well known from case-studies of specific failures. These landslide-inducing factors include geomorphological, hydraulic, hydrological, and anthropogenic characteristics.

4.4.3 Brief Summary of Methodologies

Methods for assessing the landslide susceptibility of a given area have evolved over time. The applicability of each method varies according to the quality and quantity of available information. The first two methods discussed in this section, engineering analysis and the qualitative method, are presented for reference and were not ultimately used for the landslide susceptibility zonation analysis of Comoros. Instead, the third presented approach, the frequency ratio method, was selected as the most suitable method for the landslide susceptibility zonation analysis as based on the available data sources and information for Comoros.

Engineering Analysis

If detailed geotechnical information (i.e. soil boring profile) is available, then conventional engineering analysis may be used to determine the susceptibility of a region to landslides. A widely used numerical method for assessing slope instability for a specific site is the use of engineering analysis, which calculates a factor of safety against mass movement sliding by using the site's soil characteristics, profiles, and relevant hydrologic information. The data required to perform a detailed engineering analysis was not available for Comoros at the time of writing, therefore this method is not used for the present investigation.

Qualitative Method

If a site lacks detailed site specific soil data, then the landslide susceptibility may alternatively be estimated using qualitative methods that consider contributing factors (e.g., slope of the ground surface, land use, etc.) that correlate to areas where past landslides have been recorded. An example of a qualitative method is one that assigns a numerical rating system to different contributory factors that are subsequently weighted and combined to assess landslide potential (Varnes and IAEGC 1984). While the qualitative method considers typical landslide inducing factors, it does not explicitly consider historical landslide frequency and is ultimately not used for the present investigation.

Frequency Ratio Method

The landslide susceptibility analysis method selected for the present investigation is the frequency ratio approach (Lepore et al. 2011). This method is preconditioned on historical landslide information, such as their location, slope, and total landslide area. Each landslide-inducing factor in a historical landslide area is considered and is evaluated individually. Each factor is then reclassified into a series of bins (e.g., slope of ground surface into increments of 5° bins) as determined by engineering judgement. For a given region, if the

total area is A , and the portion where past landslides have occurred is A_L , then the frequency ratio is calculated for each bin of each factor as F_{fi} :

$$F_{fi} = \frac{\frac{A_{L|fi}}{A_L}}{\frac{A_{fi}}{A}}$$

where $A_{L|fi}$ and A_{fi} are the portions of landslides and total area (A_L and A) with characteristic factor f having a factor value within a bin range i .

Values for F_{fi} are interpreted relative to 1. $F_{fi} < 1$ signifies that there is proportionally less landslide area with characteristic f in bin i than there is total area with characteristic f in bin i , which indicates that the characteristic factor f is less likely to contribute to slope instability. When $F_{fi} \sim 1$, then the percent of landslide area with characteristic f in bin i is roughly equal to the proportion of the total area with characteristic f in bin i . If $F_{fi} > 1$, then there is a greater percentage of landslide area with characteristic f in bin i than in the total area with characteristic f in bin i , which indicates a propensity of the characteristic factor f to lead to slope instability and soil failure.

After obtaining F_{fi} for each characteristic factor f in each bin i , the summation over all landslide-inducing factors f and all bins i , is made to obtain the Susceptibility Index (SI) for landslide susceptibility zonation.

$$SI = \sum_{f=f_i}^{f_k} \sum_{i=1}^{n_f} F_{fi}$$

Higher values of SI indicate a higher propensity of an area to soil failure. This methodology is well suited for application in regions with variable resolution gridded data, such as Comoros.

4.4.4 Data Sources

In order to develop landslide susceptibility zonation for the islands of Comoros, a spatial database of various contributory factors for the three islands was constructed from publically available information and from data provided by the client. The spatial database includes elevation, slope, aspect, distances to roads, land cover, land use, historical landslide inventory, and soil descriptions from existing soil maps, and soil classification. Not all data were suitable for use in the analysis, but are listed here to indicate their consideration. The sources of data include:

1. Route locations from topographic maps from a project by UNDP Comoros 2014 (National Geographic Institute 1993, images from Google Earth, and GPS surveys). By use of GIS software, a raster containing the Euclidean distance to the nearest route was calculated for each raster cell (90 m resolution).

2. Land use map of the Comoros archipelago (Island of Grand Comore, Anjouan, and Moheli) developed under the project for Community Involvement Sustainable Development (ECDD) from high resolution satellite images by UNDP Comoros 2014 (Figure A.91). The land use information was processed by GIS software from shape files to 90 meter resolution.
3. The USGS Land Cover Institute (LCI) for 0.5 km MODIS-based Global Land Cover Climatology from http://landcover.usgs.gov/global_climatology.php (Broxton et al. 2014) (Figure A.92). Through analysis, it was found that this land cover information gave more consistent results than the land use information from UNDP Comoros 2014, and therefore land cover information was selected as a factor for the frequency ratio method.
4. SRTM 90 meter data [Shuttle Radar Topography Mission (SRTM GL3 Global 90m SRTM_GL3); Farr et al. 2000; Far et al. 2007; Kobrick 2006; Rosen et al. 2000] (Figure A.93)
5. Soil descriptions from soil maps digitized by UNDP Comoros (2014) for Grand Comore (1:50,000, Latrille 1977) and Anjouan (1:100,000, Scientific Research Institute of Madagascar – Service Soil 1951) islands (Figure A.94 and Figure A.95). The soil description shapefiles for Grand Comore and Anjouan islands were processed by GIS software to 90 m resolution rasters. No information was provided for Moheli island. This data was not used for the frequency ratio analysis in order to yield consistent zonation results across the three islands.
6. Data from the Harmonized World Soil Database at 1km x 1km resolution (FAO et al. 2012) (Figure A.96). Although this global database contains data for Comoros, its coarse soil classification resolution renders it unsuitable for the selected analysis method (i.e. Grand Comore is listed with only one soil classification).
7. Previous landslide events were digitized from figures in the report: “Etude de Vulnerabilite aux Aleas Climatiques et Geologique en Union des Comores”, by Ahmed Abdoukarim and Hamidi Soule, Centre des Operations de Secours et de la Protection Civile, Union des Comores, Projet COSEP / PNUD #00069668. The estimated landslide areas and locations were digitized through GIS software and converted to 90 m resolution rasters. Information on the locations and areas of historical landslides is necessary in this analysis to determine landslide susceptibility zonation through the frequency ratio method. (Figure A.97)

Within the literature, it is known that landslides may also be induced by earthquakes, heavy rainfall, for flooding. Information for these landslide-inducing factors is based on hazard data at 1 km resolution generated by this project, as publically available information did not have sufficient data quality or resolution to be considered for the frequency ratio method. The 500 year return period peak ground acceleration for earthquake hazard, the 100 year return period accumulated rainfall for tropical cyclone precipitation, and the 100 year return period flood depth from non-tropical cyclone precipitation were evaluated with the frequency ratio

method and the results were inspected. Based on the currently available data from the three hazards, the landslide-inducing factor based on earthquake ground shaking increased the efficacy of the Susceptibility Index (SI), while the landslide-inducing factors from tropical cyclone precipitation and non-tropical cyclone flooding had a smaller effect. Note that flows from volcanic eruptions are not considered in the analysis.

Datasets obtained directly as raster images are used at their native resolutions for the landslide susceptibility zonation. Datasets that were not in the form of raster images are resampled to 90 m resolution square cell sizes through GIS software. Due to the different resolutions and different information sources, not all datasets overlap consistently. Therefore, care should be taken in interpreting the resulting landslide susceptibility zonation map, especially near the islands' boundaries where datasets may be inconsistent due to poorer quality resolution.

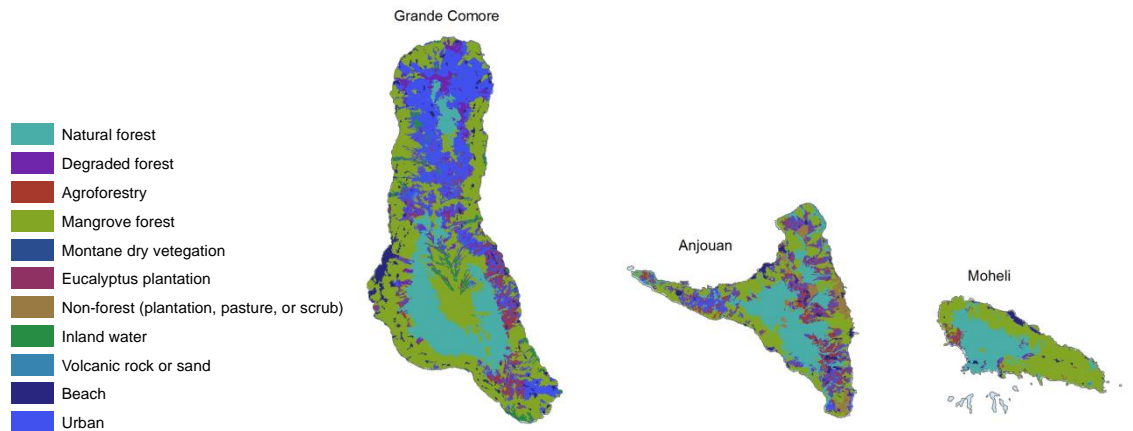


Figure A.91 Land use map of the Comoros archipelago (Island of Grand Comore, Anjouan, and Moheli) developed under the project for Community Involvement Sustainable Development (ECDD) from high resolution satellite images (UNDP Comoros 2014)

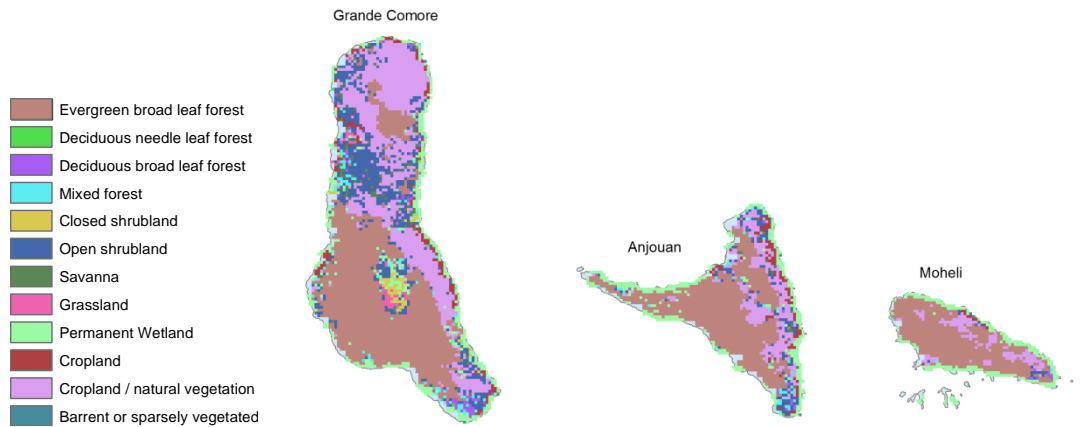


Figure A.92 Map of 0.5 km MODIS-based Global Land Cover Climatology from the USGS Land Cover Institute

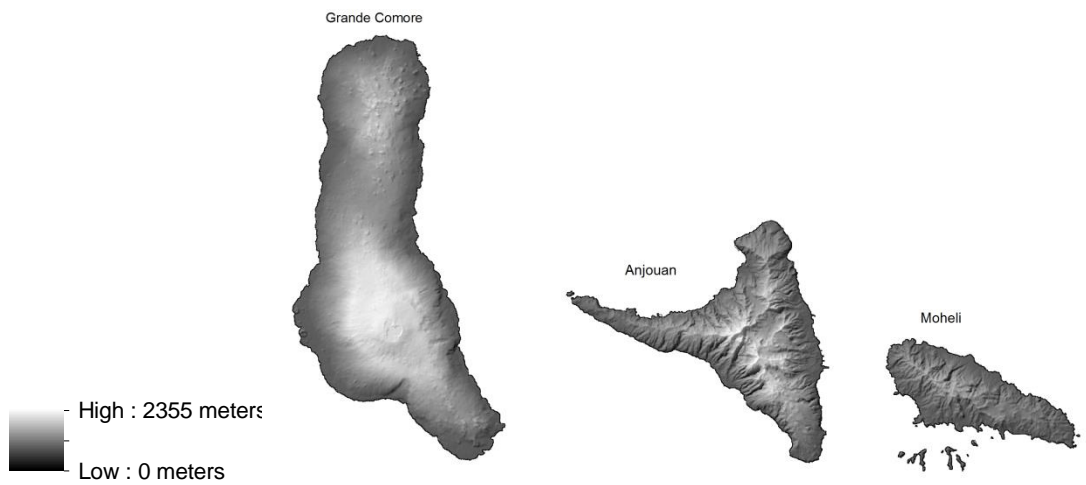


Figure A.93 SRTM 90 meter resolution data (Shuttle Radar Topography Mission, SRTM GL)

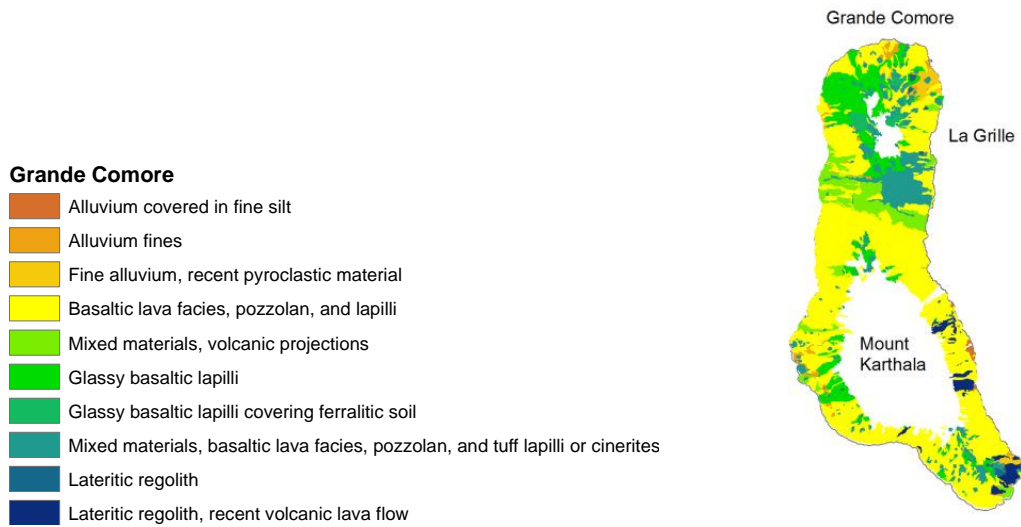


Figure A.94 Grand Comore island soil descriptions. White spaces denote areas of no listed information and coincide with the locations of the two shield volcanoes of La Grille and Mount Karthala. (UNDP Comoros 2014)

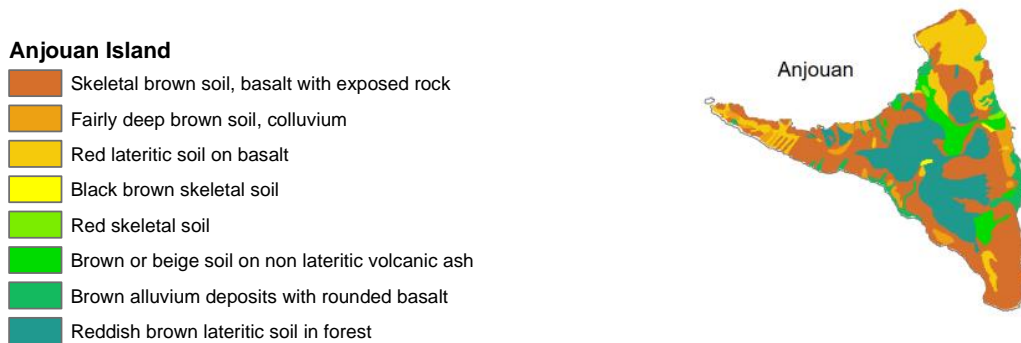


Figure A.95 Anjouan island soil descriptions (UNDP Comoros 2014)

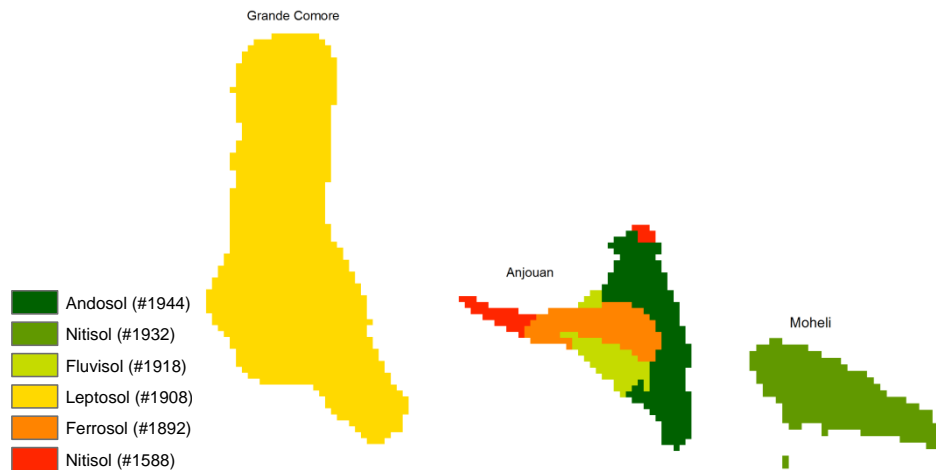


Figure A.96 Data from the Harmonized World Soil Database (FAO et al. 2012).

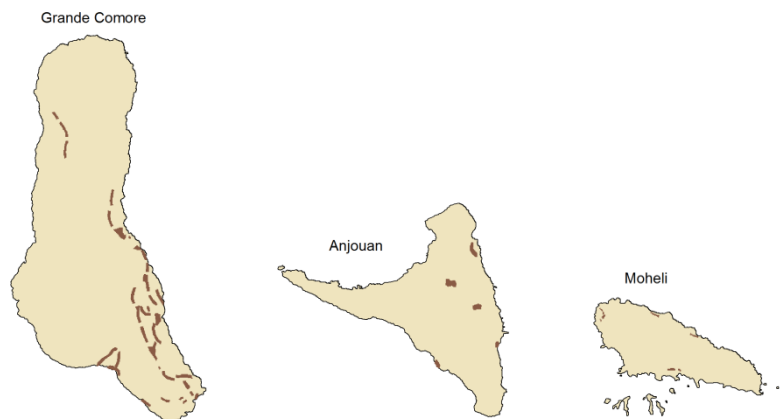


Figure A.97 Locations of previous landslides for the Union of Comoros are indicated in brown (Abdoulkarim and Soule 2011)

4.4.5 Assumptions and Limitations of Methodology and Data

The assumptions and limitations are briefly discussed in this section and are intended to inform the user about selectively improving future landslide analyses by using higher quality input data. In this case, as based on the available data sources, the frequency ratio method provides the most suitable method for performing a landslide susceptibility risk assessment.

Frequency Ratio Method

The frequency ratio method is a bivariate model that involves the analysis of two variables to determine their empirical relation to calculate the landslide susceptibility per unit area. Strictly speaking, the bivariate model

assumes the conditional independence of its variables, and the frequency ratio method is also based on this assumption of conditional independence, with respect to the probability of landslide occurrence. Although certain variables may be correlated, there is insufficient information available to confirm correlation and independence of each considered variable is assumed.

Although the limitations of the data sources are mentioned previously, it should be reiterated that the landslide susceptibility zonation analysis is heavily dependent on the quality of the data sources and available historical landslide information. The available landslide inventory for Comoros is necessarily a subset of previous landslides and subject to the vagaries of human observation and funding. Methods described by Malamud et al. (2004) for studying landslide inventories and their statistical properties were applied to the historical landslide inventory for Comoros. Through inspection of their areas and frequencies, it was concluded that, although the size of some of these landslides may be larger than those studied in Malamud et al. (2004), the available landslide inventory for Comoros still provides a reasonable representation of the islands' historical landslides. Results from the frequency ratio method support this conclusion.

4.4.6 Discussion and Results

The parameters used in the analysis were the 1) slope aspect, 2) slope, 3) curvature, 4) elevation, 5) distance to roads, 6) land cover, 7) 500 year return period peak ground acceleration, 8) 100 year return period accumulated rainfall from tropical cyclone precipitation, and 9) 100 year return period flood depth from non-tropical cyclone precipitation. Each individual parameter was separated into different classification bins, each unit area (by raster pixel) was then further classified as a landslide zone or a no-landslide zone based on the historical inventory of landslides on the three islands. For example, the slope parameter was divided into 10 different bins of $0^\circ < x \leq 5^\circ$, $5^\circ < x \leq 10^\circ$, etc., with the 10th bin of $45^\circ < x$, where x is the value of the slope at that pixel. In this manner, the frequency ratio F_{fi} was calculated for all parameters and each of their bins.

The Susceptibility Index SI was then calculated from the frequency ratios for each individual unit area for each island and the results divided into categories of high, medium, and low landslide susceptibility. The categories of high, medium, and low are based on the mean \bar{x} and the standard deviation σ of the SI values. SI values less than the mean \bar{x} are categorized as "low" susceptibility, SI values between the mean \bar{x} and $\bar{x} + 2\sigma$ are categorized as "medium," and SI values above $\bar{x} + 2\sigma$ are categorized as "high" susceptibility. A further step was taken to filter as low susceptibility the unit areas which were less than 3° slope angle, as this is the minimum slope where landslides are expected (Solomon et al. 2004).

The proportion of the total area of Comoros and the area of historical landslides that lie within each susceptibility category is presented in Table A.11. The second column indicates that Comoros has 4% of its area within the high susceptibility zone, 40% within the medium susceptibility category, and 56% within the low susceptibility zone. The third column indicates that 27% of historical landslides have occurred in high susceptibility zones, 52% have occurred in in medium susceptibility zones, and 18% have occurred in low

susceptibility zones. While the high and medium landslide susceptibility zones constitute only 41% of the total area of Comoros, they capture approximately 82% of the historical landslide areas, providing good validation of the frequency ratio method. See Figure A.98 for the landslide susceptibility zonation map overlaid with the historical landslides.

Table A.11 Comparison of proportions of areas within high, medium, and low landslide susceptibility for islands and landslides

Category	Comoros Area (%)	Historical Landslide Area (%)
High	4	27
Medium	40	55
Low	56	18

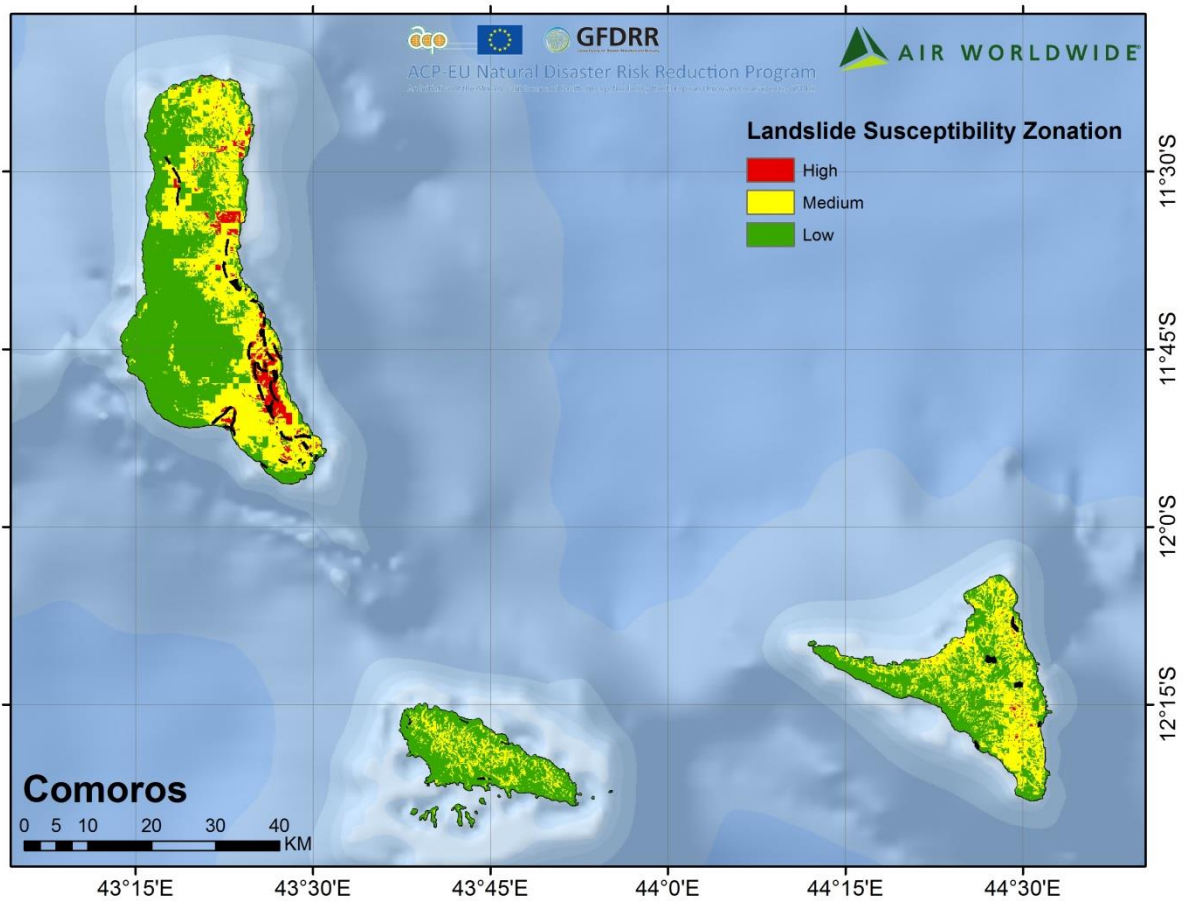


Figure A.98 Landslide susceptibility zonation for Comoros by island with historical landslides shown in black (90 m x 90 m resolution)

As expected, the landslide susceptibility zonation map is dependent on specific characteristics of the local soil topography. Abdoukarim and Soule (2011) have reported that landslides on Anjouan and Moheli have affected particular roads where the terrain has very steep slopes. However, some existing landslides on Moheli have also been observed in lower landslide risk areas near the coast.

As an example, a recent landslide on Moheli in March 2014 near a length of national highway that was recently constructed was induced by a local moderate earthquake (Mansourou 2015). The road is built near a section of steeply sloped soils which is approximately 2 kilometers from the town of Ouallah located in the southwest region of Moheli (Figure A.99) and is located in a zone of low landslide susceptibility, according to the frequency ratio method.

It is possible that some landslides have been caused by anthropogenic actions where the topography has been altered, which are not necessarily captured by the frequency ratio method. The frequency ratio method in this analysis takes into account the slope aspect, slope, curvature, elevation, distance to roads, and land cover and is dependent on the data source vintage, but does not account for recent alterations in topography.



Figure A.99 Affected site ~2 kilometers from the town of Ouallah 1 in Moheli (Source: Mansourou, 2014)

4.4.7 Conclusion

In this investigation, a frequency ratio method was implemented for developing landslide susceptibility zonation maps for the Union of Comoros. The resulting maps demonstrate the relative landslide potential for the three islands of Grand Comore, Anjouan, and Moheli. The results from the landslide susceptibility zonation

map should be interpreted with care, as the Susceptibility Index is dependent on the vintage and quality of the input data sources. However, the zonation map may be used for identifying higher risk regions, and further field surveys for analysis may be conducted to note where and how mitigation efforts may be applied.

Mitigation of landslide risk may be approached by considering the impact of urbanization and the inherent susceptibility of the topography. Informal settlements may inadvertently be built on at-risk areas, and their inhabitants may exacerbate the situation by disturbing sloped soils for housing foundations or crops. These mitigation measures may then include building retaining walls, relocating inhabitants to lower risk locations, or changing agricultural methods.

4.4.8 References

- Abdoulkarim, A. and Soule, H. (2011). *Etude de vulnérabilité aux aléas climatiques et géologique en Union des Comores, Centre des Operations de Secours et de la Protection Civile*. Projet COSEP / PNUD No. 00069668, Développement des Capacités de Gestion des Risques de Catastrophes naturelles et Climatiques, en Union des Comores (in French)
- Bommer, J.J., Rolo, R., Mitroulia, A., and Berdousis, P. (2002). *Geotechnical properties and seismic slope stability of volcanic soils*, Proceedings from the 12th European Conference on Earthquake Engineering, Paper Reference 695, Barbican Centre, London, UK, from 9th-13th September
- Broxton, P.D., Zeng, X., Sulla-Menashe, D., and Troch, P.A. (2014). *A global land cover climatology using MODIS data*. *Journal of Applied Meteorology and Climatology*, 53, 1593–1605
- Charmoille, A. (2013). *Ebauche du fonctionnement hydrogéologique de l'île d'Anjouan (Comores): Typologie des ressources en eau disponibles et discussion sur l'impact de la déforestation*. Bristol Conservation and Science Foundation, Engagement Communautaire pour le Développement Durable, (in French)
- Diko, M.L., Ekosse, G.E., Ayonghe, S.N., and Ntasin, E.B. (2012). *Physical and geotechnical characterization of unconsolidated sediments associated with the 2005 Mbonjo landslide, Limbe, Cameroon*. *International Journal of Physical Sciences*, 7(20), 2784-2790
- Diko, M. L., Banyini, S.C., and Monareng, B.F. (2014). *Landslide susceptibility on selected slopes in Dizanani, Limpopo Province, South Africa*. *Jambá: Journal of Disaster Risk Studies*, 6(1), Article #101
- Esson, J., Flower, M.F.J., Strong, D.F., Upton, B.G.J. and Wadworth W.J. (1970). *The geology of the Comores Archipelago*. *Geological Magazine*, 547-549
- FAO/IIASA/ISRIC/ISS-CAS/JRC, 2012. *Harmonized World Soil Database (version 1.2)*. FAO, Rome, Italy and IIASA, Laxenburg, Austria. Retrieved on March 18, 2015 from <http://webarchive.iiasa.ac.at/Research/LUC/External-World-soil-database/HTML/index.html?sb=1>
- Farr, T. G., and Kobrick, M. (2000). *Shuttle radar topography mission produces a wealth of data*. *Eos, Transactions American Geophysical Union*, 81(48), 583-585
- Farr, T. G. et al., 2007. *The shuttle radar topography mission*. *Review of Geophysics*, 45(2), RG2004
- Fawcett, T., 2006. *An introduction to ROC analysis*. *Pattern Recognition Letters*, 27, 861-874
- Flower, M.F.J. (1972). *Petrology of volcanic rocks from Anjouan, Comores Archipelago*. *Bulletin of Volcanology*, 36, 238-250
- Hong, Y., Adler, R., and Huffman, G. (2007). *Use of satellite remote sensing data in the mapping of global landslide susceptibility*, *Natural Hazards*, 43(2), 245-256

- Hürlimann, M., Ledesma, A., and Martí, J. (2001). *Characterization of a volcanic residual soil and its implications for large landslide phenomena: application to Tenerife, Canary Islands*. *Engineering Geology*, 59, 115-132
- Hürlimann, M., Martí, J., and Ledesma, A. (2004). *Morphological and geological aspects related to large slope failures on oceanic islands, the huge La Orotava landslides on Tenerife, Canary Islands*, *Geomorphology*, 62, 143-158
- Hürlimann, M., 1999. *Geotechnical analysis of large volcanic landslides: The La Orotava events on Tenerife, Canary Islands*, A dissertation submitted to the Technical University of Catalonia, Barcelona, 228 pp.
- Kitutu, M.G., Muwanga, A., Poesen, J., and Deckers, J.A. (2009). *Influence of soil properties on landslide occurrences in Bududa district, Eastern Uganda*. *African Journal of Agricultural Research*, 4(7), 611-620
- Kobrick, M., 2006, *On the toes of giants--How SRTM was born*, *Photogrammetric Engineering and Remote Sensing*, 72, 206-210
- Larsen, M.C., and Torres-Sánchez, A.J. (1998). *The frequency and distribution of recent landslides in three montane tropical regions of Puerto Rico*. *Geomorphology*, 24, 309-331
- Lepore, C., Kamal, S.A., Shanahan, P., and Bras, R.L. (2011). *Rainfall-induced landslide susceptibility zonation of Puerto Rico*. *Environmental Earth Sciences, Special Issue* (25 February 2011)
- Malamud, B.D., Turcotte, D.L., Guzzetti, F., and Reichenbach, P. (2004). *Landslide inventories and their statistical properties*. *Earth Surface Processes and Landforms*, 29, 687-711
- Mansourou, A. 2015. *L'évaluation des risques de tremblement de terre et glissement de terrain sur l'île autonome de Mohéli en Union des Comoros, Croissant-Rouge Comorien*, 55 pp.
- Nadim, F., Kjekstad, O., Peduzzi, P., Herold, C. and Jaedicke, C. (2006). *Global landslide and avalanche hotspots*. *Landslides*, 3, 159-173
- Okal, E.A., Fritz, H.M., and Sladen, A. (2009). *2004 Sumatra-Andaman Tsunami Surveys in the Comoro Islands and Tanzania and Regional Tsunami Hazard from Future Sumatra Events*. *South African Journal of Geology*, 112, 343-358
- Rosen, P. A., Hensley, S., Joughin, I.R., Fuk, K.L., Madsen, S.N., Rodriguez, E., and R.M. Goldstein, 2000. *Synthetic aperture radar interferometry*, *Proceedings of the IEEE*, Vol. 88, Issue 3, pp. 333-382
- Solomon, B.J., Storey, N., Wong I., Silva, W., Gregor, N., Wright, D., and McDonald, G. (2004). *Earthquake-hazards scenario for a M7 Earthquake on the Salt Lake City segment of the Wasatch Fault Zone, Utah*. *Utah Geological Survey, Special Study 111DM*
- Späth, A. Le Roex, A.P., and Duncan, R.A. (1996). *The geochemistry of lavas from the Comores Archipelago, Western Indian Ocean: Petrogenesis and mantle source region characteristics*. *Journal of Petrology*, 37(4), 961-991

Takahashi, T., and Shoji, S. (2002). *Distribution and classification of volcanic ash soils*. Global Environmental Research, 6, 83-97

Uriás, H.Q., Garcia, H. and Mendoza, J.S.P. (2007). *Determination of the relationship between precipitation and return periods to assess flood risks in the city of Juarez, Mexico*, Session 5 of the Proceedings of the UCOWR Conference on July 24, 2007, Paper 47

UNDP Comoros. (2014). *Rapport: modélisation de la base de données GDB-COMOROS, Projet: Intégration de la réduction des risques de catastrophes dans les politiques en vue de réduire la pauvreté en Union des Comores*

Varnes, D.J. and IAEGC (the International Association of Engineering Geology Commission). (1984). *Landslide hazard zonation: A review of principles and practice*. United National Educational, Scientific, and Cultural Organization.

Wahlstrand, A., 2015. *Physical and chemical topsoil changes and landslide susceptibility assessment under tropical conditions*, Institutionen for Naturgeografi, Stockholms Universitet, Licentiatavhandling, Naturgeografi

5 Appendix B – Consequence Database

The consequence database is a collection of all reported impacts from natural catastrophes in the Southwest Indian Ocean for the island nations of Comoros, Madagascar, Mauritius, Seychelles, and Zanzibar. In the context of the consequence data, considered “impacts” include causalities, affected people, and financial losses. The database is split into two primary sections, (1) meteorological hazards of tropical cyclones and flooding, and (2) geological hazards of earthquakes and landslides (Comoros only).

5.1 Consequence Database for Tropical Cyclones and Flooding

5.1.1 Data Sources

The consequence data from natural hazards that have occurred in the South West Indian Ocean (SWIO) for Comoros, Madagascar, Mauritius, Seychelles, and Zanzibar have been collected from a variety of sources. The SWIO region is prone to multiple hazards, although not all at the same level of severity. The natural events considered in the consequence database include tropical cyclones and other related events, such as severe storms and floods. The consequence database presents the findings of a thorough data collection effort and the database is considered a comprehensive inventory of recorded events that had a significant impact on the population in the SWIO region. Much of the data collected for the database was aggregated from a number of major disaster databases, which are publically available. These major databases include:

1. The Emergency Events Database (EMDAT, 2016) maintained by the Centre for Research on the Epidemiology of Disasters (CRED) at the School of Public Health of the Université Catholique de Louvain located in Brussels, Belgium.
2. The Global Active Archive of Large Flood Events maintained by the Dartmouth Flood Observatory (DFO, 2016), which covers the period 1985 – 2015.
3. The GLIDE (2016) initiative (Global Identifier Number), originally proposed by The Asian Disaster Reduction Center (ADRC).
4. “ReliefWeb,” an online service (ReliefWeb, 2016) provided by OCHA (United National Office of Humanitarian Affairs) that monitors the websites of international and non-governmental organizations, governments, research institutions and the media for news, reports, press releases, appeals, policy documents, analysis and maps related to humanitarian emergencies worldwide (e.g., UN reports, IFRC updates, OCHA reports etc.).

5. The Disaster Information Archive developed and maintained by the Asian Disaster Reduction Center (2016). ADRC was established in 1998 in Kobe, Hyogo prefecture, with the mission to enhance the disaster resilience of the 29 member countries.
6. The Hungarian National Association of Radio Distress-Signaling and Infocommunications (RSOE) operates the Emergency and Disaster Information Services (EDIS)
7. The Disaster Inventory System – DesInventar (2016)
8. The International Best Track Archive for Climate Stewardship (IBTrACS): Unifying tropical cyclone best track data.

5.1.2 Explanation of Database Data and Data Fields

Over 170 unique event entries from tropical cyclones, flooding, and secondary hazards have been collected and collated from the aforementioned sources. Each event has some recorded notable effect on the population or damage to the building inventory. Many entries, especially those from very damaging events, contain data from multiple sources, and, as expected, discrepancies exist for the quantitative data, particularly economic losses. By design, the discrepancies have been preserved and each relevant piece of data in the consequence database is appropriately referenced. Analysis of the information in the consequence database has not been undertaken and therefore events with unique identification numbers within a data source that are chronologically close or overlapping have not been eliminated. This consequence database represents a comprehensive collection of the significant reported historical events (e.g., tropical cyclones, floods, and secondary hazards) but is not a complete record of all occurrences within the history of these five countries.

The interrelated nature between tropical cyclones and flooding is undeniable. In addition to damage from wind, many tropical cyclones cause damage and loss from flooding. Tropical cyclones that do not make landfall may still pass close enough to land to produce significant precipitation events, in terms of the number of lives lost or economic damage to infrastructure and agriculture. To separate event types into two categories (e.g., tropical cyclone events and flood events), events that cite named tropical cyclones within their data sources (e.g. WMO) are categorized as tropical cyclones (“TC Flag”), although flooding may have also resulted. Exceptions to this subjective guideline are instances where the event is specifically listed as a flood event by the source information (e.g., the GLIDE initiative) despite overlapping with a named tropical cyclone. Events that are not categorized as a tropical cyclone event (“TC Flag”) are categorized as a flood event (“FL Flag”), and are either specifically listed or described as a flood event. This method is not a rigorous analysis and represents an approximate categorization based on the available data.

The referenced sources discussed in the previous section typically report a brief summary of the disaster consequence (e.g., number of people affected and/or number of lives lost), and some accounts are strictly qualitative (e.g., “crops were damaged”). For each entry in the consequence database, data from each field is

aggregated to account for the total consequence from a particular disaster event (including related secondary events or effects), and generally most or all of the damage occurs in the country listed. For tropical cyclone events, the losses are aggregated per event; specific details on the relative losses are noted for some events (e.g., damage to infrastructure). The main data fields of the consequence database are outlined below:

- **People Affected** – A measure of the estimated number of people affected by the event. People affected include those that became homeless, injured, displaced, evacuated, or disrupted (e.g., affected by loss of utilities) by the peril.
- **People Displaced** – A subset of the number of people affected, this indicates the number of people required to vacate their residence due to the peril, such as those evacuated or displaced.
- **Economic Damage** – The estimated total economic impact of the event consists of direct damage (e.g., damage to infrastructure, crops, housing). Estimated loss is typically reported in U.S. dollars (USD), corresponding to the monetary loss at the time of the event (e.g., current/nominal USD). Data reported in local currency are converted appropriately by using rates for the specific (time-of-event) dates based on information supplied by leading market data contributors [e.g., The World Bank (2015) Official exchange rate]. Losses are reported as the monetary cost at the time of the event. A break-down of losses (e.g., losses per sector, such as social sector, private sector, and infrastructure), crop losses, and locations for deaths and building damages may be available for those events where detailed assessment reports were issued [e.g., United Nations Office of Humanitarian Affairs (OCHA) Situation Report].
- **Deaths** – The total number of people reported dead, missing or presumed dead as a result of the event, including any resulting deaths from starvation, injury, or disease.
- **Buildings Destroyed** – The total number of buildings (typically listed as “houses”) reported to be destroyed as a result the event. Partially destroyed houses are also cataloged.
- **TC Flag** – An indicator that the event is cited as a tropical cyclone or a typhoon by the data sources, except where contraindicated by the data source (e.g., the GLIDE initiative).
- **FL Flag** – An indicator that includes events which are not flagged by the “TC Flag” and includes events that are cited or described as floods, flashfloods, or classified as flood by the data sources.
- **Effect** – A description such as flooding, flashflood, landslide, and/or storm surge to illustrate the effects of the event. These four categories are also separated out into columns for ease of identification. Each peril (e.g., flood, flash flood, storm surge, and landslide) has its own column header and may be filtered with the “yes” indicator for each event. Note that “flood” frequently but not always accompanies a tropical cyclone event. This absence may be an inadvertent omission of information from the data sources and may not necessarily be an indication of a lack of flooding.

5.1.3 Discussion of Significant Events

The South West Indian Ocean region frequently experiences flooding from tropical cyclones and monsoonal precipitation. The consequence database lists notable tropical cyclones and floods. Some recent and historically significant events are briefly discussed in this section

Tropical Cyclone Giovanna (2012)

Intense tropical cyclone Giovanna began as a tropical depression on February 9, 2012, as reported by RSMC La Reunion, Meteo-France. In the next few days, the storm quickly intensified and strengthened to a category 4 (SSHS) cyclone which made landfall on the eastern coast of Madagascar at Andovoranto on February 13, 2200 UTC. It then crossed westward with very strong winds (230 km/h to 180 km/h) and moved back to open waters on February 15 to circle Madagascar southward and eastward to then dissipate east of Madagascar on February 21 (Figure B.1). Flooding and strong winds caused significant damage in the eastern and central parts of Madagascar; approximately 44,129 homes were destroyed and almost 250,000 people were affected by the tropical cyclone. The cyclone killed at least 35 people and injured 284. Economic damage to infrastructure and agriculture was estimated at 100 million USD (untrended).

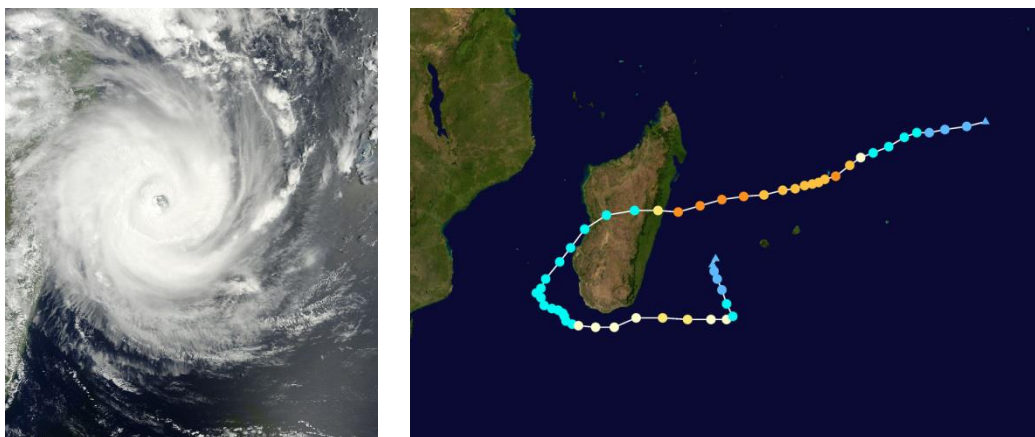


Figure B.1 Tropical cyclone Giovanna (2012) and storm track on the right. [Source: (left) Giovanna Feb 13 2012 0630Z by NASA image by Jeff Schmaltz, LANCE/EOSDIS MODIS Rapid Response Team at NASA GSFC; (right) Giovanna 2012 track by Keith Edkins - Created using Wikipedia:WikiProject Tropical cyclones/Tracks]

Floods in Comoros (2012)

From April 20-25, 2012, Comoros experienced torrential precipitation (1,738 mm total) that caused heavy floods, landslides, and rockfalls. On the three islands of Grande Comore, Anjouan, and Moheli, the water supply, electricity, and telecommunications services were disrupted. The main regions affected are Bambao, Hambou, Mbadjini Est on Grande Comore; Sima and Domoni on Anjouan; and Nioumachioi and Hoani on

Moheli. By April 26th, the government of Comoros declared a State of Emergency and emergency humanitarian coordination meetings were held on the 27th. From the preliminary assessments in May 2012, 64,987 people (8-9% of the population) were directly affected by the floods. A total of 14,000 people (1,800 families) continue to be displaced and housed in relocation centers or dwellings of relatives. Economic damage was estimated at 20 million USD (untrended).⁸



Figure B.2 (left) Flooding of Vovouni Village, April 2012 and (right) Destroyed road and bridge at Hambou, Grande Comore, April 2012 (Source for both photos: DGSC)

Tropical Cyclone Ivan (2008)

Tropical cyclone Ivan was one of the most destructive cyclones to strike Madagascar. On February 17, 2008, the cyclone made landfall north of Fanoarivo and caused extensive damage to Sainte-Marie and in the northeast and northwest of the Madagascar mainland; rainfall continued for several days after the cyclone passed. Approximately 135,508 houses were destroyed and an estimated 300,000 to 500,000 people were affected. Major destruction to electricity, water, and communication networks was also reported. Initial reports of economic damage were as high as 60 million USD (untrended); however, a post-disaster needs assessment later that same year for cyclones Fame, Ivan, and Jokwe calculated a total estimate of damage and losses of 333 million USD (untrended) for all sectors⁹. The majority of the damage is attributed to tropical cyclone Ivan, as cyclones Fame and Jokwe proved less severe.

⁸ "Early Recovery Plan: Comoros Flooding 2012." By the Union of Comoros, Moroni, August 2012

⁹ "Damage, Loss, and Needs Assessment for Disaster Recovery and Reconstruction after the 2008 Cyclone Season in Madagascar: Cyclone Fame, Ivan, and Jokwe in Madagascar." A report prepared by the Government of Madagascar with the support of the United Nations and The World Bank. Antananarivo, May 2008.

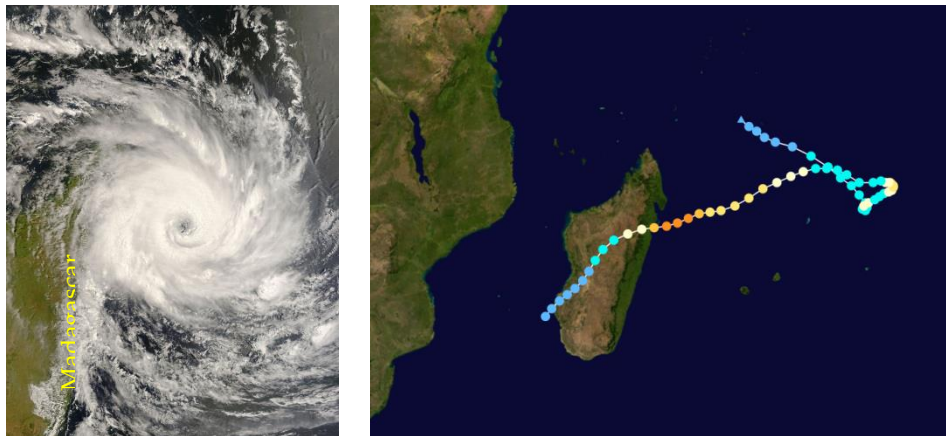


Figure B.3 Tropical cyclone Ivan (2008) and storm track on the right. [Source: (left) Ivan 16 Feb 2008 0645Z by NASA image courtesy, LANCE/EOSDIS MODIS Land Rapid Response Team, at NASA GSFC; (right) Ivan 2008 track – Created using Wikipedia:WikiProject Tropical cyclones/Tracks]

Tropical Cyclone Indlala (2007)

On March 15, 2007, tropical cyclone Indlala struck the north-eastern coast of Madagascar and left considerable damage on the northeast and northwest regions. Existing records cite that 150 people died, 126 people were injured, and possibly more than 200,000 people were directly affected by the cyclone. The cyclone reportedly caused a rockslide that collapsed an entire mountain, which buried two villages under many tons of rock and killed 20 people. Large areas were flooded in the cities of Sambava Antalaha and Maroantsetra in the north.

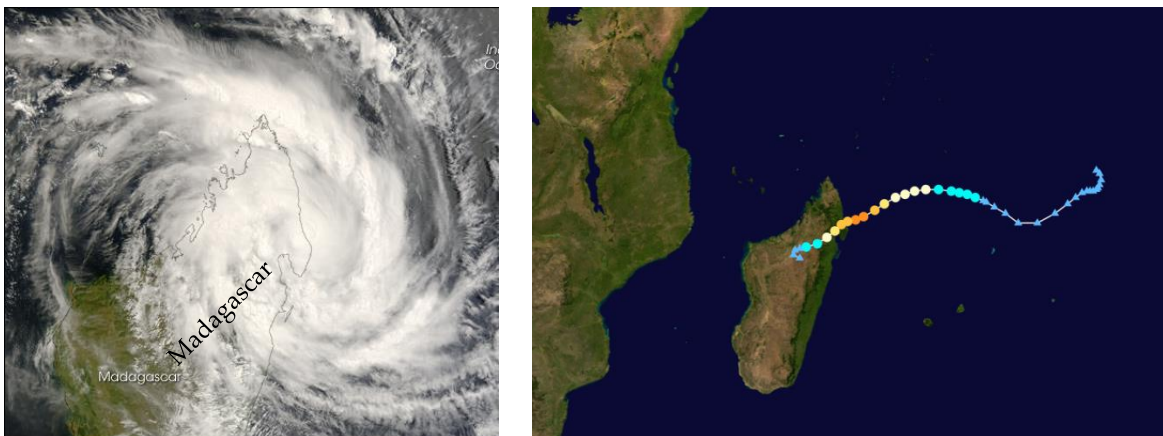


Figure B.4 Tropical cyclone Indlala (2007) [Source: (left) Indlala March 15 2007 by NASA image by Jeff Schmaltz, LANCE/EOSDIS MODIS Rapid Response Team at NASA GSFC; (right) Indlala 2007 track - Created using Wikipedia:WikiProject Tropical cyclones/Tracks]

Tropical Cyclone Gafilo (2004)

Tropical cyclone Gafilo was an unusually large and violent tropical cyclone recorded in the South West Indian Ocean during the 2003-2004 season. On March 7, Gafilo made landfall near the north-eastern part of Madagascar, near Atalaha with 225 km/h winds and then returned on March 8 as a tropical storm in the southwest before dissipating over the ocean on March 12. The number of people affected is estimated at 774,000 to almost 1,000,000 by some disaster databases. At least 216,581 people were displaced by flooding and strong winds, and an estimated 363 people were killed. 105,040 homes were destroyed, and the tropical cyclone inflicted 250 million USD (untrended) damage to Madagascar. The nearby island nations were not as affected by Gafilo. Comoros reported 1 death, and Seychelles had at least 9 houses partially destroyed.

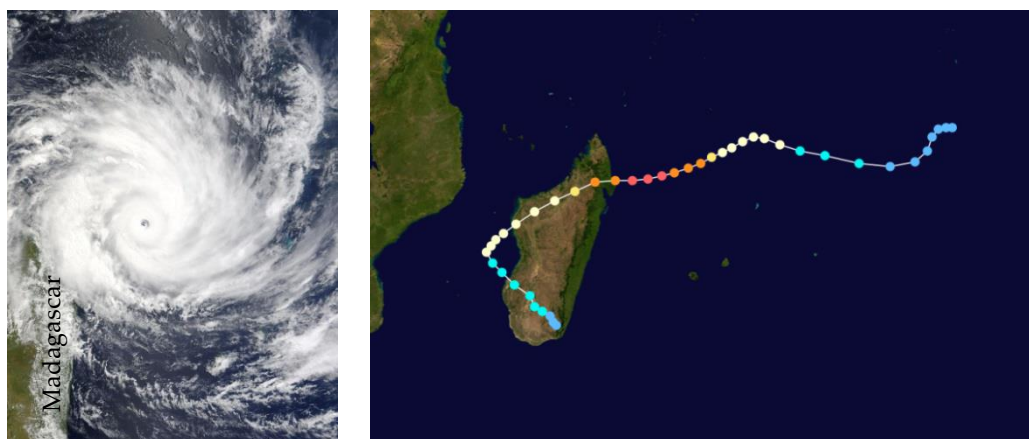


Figure B.5 Tropical cyclone Gafilo (2004) and storm track on the right. [Source: (left) Gafilo 2004-03-06 0655Z by NASA image courtesy, Jeff Schmaltz, LANCE/EOSDIS MODIS Land Rapid Response Team, at NASA GSFC; (right) Gafilo 2004 track - Created using Wikipedia:WikiProject Tropical cyclones/Tracks]

Floods in Madagascar (2003)

By January 24, 2003, heavy rains had fallen in Madagascar for at least two weeks and flooded the provinces of Antananarivo, Fianarantsoa, Antsiranana, Mahajanga, and Toamasina. The recorded rainfall was more than 550 mm, which is more than double the monthly average for month of January. More than 300 houses were entirely destroyed and 25,500 people were affected. Reports indicated that 3,388 hectares of agriculture were damaged. Three dykes and four bridges were destroyed, and three roads were cut off.



Figure B.6 Flooding in 2003, Madagascar. (Source: UNDP / Michel Matera)

5.1.4 Database Statistics

This section outlines key statistics of the consequence database, with the main intent of providing a summary of recorded disaster data and presenting a quantitative overview of consequences from the natural hazards considered (Table B.1). Over 170 entries for all five countries have been recorded; over 90 entries are defined as “catastrophic”, which is defined as being reported with either at least 10,000 people displaced or affected, at least 10 million (untrended) USD in losses, or at least 10 deaths. Approximately 80% of the catastrophic entries are related to tropical cyclones; the remaining percent have been categorized as flood category. Note that the number of entries refers to each country. When progressing through the SWIO region, a tropical cyclone may affect more than one country. For example, if a tropical cyclone causes loss of life or economic loss for both Comoros and Madagascar, then it is counted in the consequence database as two entries due to its unique impact per country.

While the data search for the consequence database was completed thoroughly, data for each entry may not be comprehensive, as some accounts of consequence may not have been recorded consistently or even reported. The quality of data is especially apparent for earlier decades, such as 1950-1959, where for example only 1 event is recorded for Comoros, with significant loss of life yet no economic damage reported. Within the consequence database, quantitative data for economic loss and loss of life is reported for only about 56% and 57% of the database entries, respectively. Nevertheless, the consequence database serves as a valuable tool for assessing the impact of significant events, which are used for model validation purposes.

For the five countries of Comoros, Madagascar, Mauritius, Seychelles, and Zanzibar, more than 12 million people have been affected by tropical cyclones, floods, and secondary hazards since 1950. Taken as a whole, this is a significant portion of the population for these five regions and is about 45% of the almost 27 million

people residing here¹⁰. Reported economic losses are also significant, totaling to more than 7 billion USD (untrended) since 1950.

When inspecting consequence information by country (Table B.2 to Table B.6) for tropical cyclones, floods, and secondary hazards, Madagascar has the greatest number of catastrophic events (57), the most loss of life recorded (3,067 deaths), and the largest economic loss reported (5,497 million USD, untrended) (Table B.3). Mauritius is the second most catastrophic, with 23 catastrophic events, 442 people killed, and 1,509 million USD (untrended) (Table B.4). Comoros has a total of 9 catastrophic events, a reported 671 lives lost, and 85 million USD in economic losses (untrended) (Table B.2). Seychelles and Zanzibar have comparatively few catastrophic events, despite Seychelles having 26 events total. Seychelles has 2 catastrophic events, 23 lives lost, and 13.5 million USD in economic losses (untrended) (Table B.5). Zanzibar has the fewest events, with 2 catastrophic events with no deaths and no recorded economic losses (despite a reported 20,000 houses destroyed). As noted previously, the total number of events in each country is a reflection of the hazard frequency and reporting consistency, thus the actual risk in each region may be understated in this list due to underreporting.

Table B.1 Summary for Comoros, Madagascar, Mauritius, Seychelles, and Zanzibar by decade of consequence database for tropical cyclones, floods, and related secondary hazards. Economic losses are not trended.

<i>Decade</i>	<i>Economic Loss (\$M USD)</i>	<i>Casualties</i>	<i>Events</i>	<i>Catastrophic Events</i>
1950-1959	0	524	1	1
1960-1969	64	284	8	5
1970-1979	795	281	11	9
1980-1989	1,024	475	25	18
1990-1999	265	783	22	13
2000-2009	4,518	1,308	74	29
2010-2015	437	476	29	18

¹⁰ 2014 census data from the World Bank for Comoros, Madagascar, Mauritius, and Seychelles and 2012 census data for Zanzibar (Office of Chief Government Statistician, Zanzibar)

Table B.2 Summary for Comoros by decade of consequence database for tropical cyclones, floods, and related secondary hazards. Economic losses are not trended.

<i>Decade</i>	<i>Economic Loss (\$M USD)</i>	<i>Casualties</i>	<i>Events</i>	<i>Catastrophic Events</i>
1950-1959	0	524	1	1
1960-1969	0	0	0	0
1970-1979	0	1	1	0
1980-1989	43	54	6	5
1990-1999	0	67	1	1
2000-2009	0	3	4	0
2010-2015	43	22	3	2

Table B.3 Summary for Madagascar by decade of consequence database for tropical cyclones, floods, and related secondary hazards. Economic losses are not trended.

<i>Decade</i>	<i>Economic Loss (\$M USD)</i>	<i>Casualties</i>	<i>Events</i>	<i>Catastrophic Events</i>
1950-1959	0	0	0	0
1960-1969	8	110	2	2
1970-1979	420	264	6	6
1980-1989	675	410	8	7
1990-1999	65	508	10	9
2000-2009	4,015	1,350	36	22
2010-2015	314	425	11	11

Table B.4 Summary for Mauritius by decade of consequence database for tropical cyclones, floods, and related secondary hazards. Economic losses are not trended.

<i>Decade</i>	<i>Economic Loss (\$M USD)</i>	<i>Casualties</i>	<i>Events</i>	<i>Catastrophic Events</i>
1950-1959	0	0	0	0
1960-1969	56	174	6	3
1970-1979	375	16	4	3
1980-1989	307	11	11	6
1990-1999	194	203	8	3
2000-2009	497	27	15	5
2010-2015	80	11	7	3

Table B.5 Summary for Seychelles by decade of consequence database for tropical cyclones, floods, and related secondary hazards. Economic losses are not trended.

<i>Decade</i>	<i>Economic Loss (\$M USD)</i>	<i>Casualties</i>	<i>Events</i>	<i>Catastrophic Events</i>
1950-1959	0	0	0	0
1960-1969	0	0	0	0
1970-1979	0	0	0	0
1980-1989	0	0	0	0
1990-1999	7	5	3	0
2000-2009	7	0	17	1
2010-2015	<1	18	6	1

Table B.6 Summary for Zanzibar by decade of consequence database for tropical cyclones, floods, and related secondary hazards. Economic losses are not trended.

<i>Decade</i>	<i>Economic Loss (\$M USD)</i>	<i>Casualties</i>	<i>Events</i>	<i>Catastrophic Events</i>
1950-1959	0	0	0	0
1960-1969	0	0	0	0
1970-1979	0	0	0	0
1980-1989	0	0	0	0
1990-1999	0	0	0	0
2000-2009	0	0	2	1
2010-2015	0	0	2	1

5.1.5 Database Statistics of Tropical Cyclones

As observed in Table B.7, tropical cyclones tend to have a greater effect in the SWIO region in terms of economic loss and loss of life as compared to the impact from non-cyclone precipitation and flooding. In the tropical cyclone consequence database, there are a total of 104 entries that have been gathered from the previously mentioned information sources. A total of 6,628 million USD of known economic losses are recorded from 1950-2015. Economic loss trends are not immediately apparent from the consequence database. For example, although economic losses are greatest in the 2000-2009 decade, the previous decade 1990-1999 has a much smaller economic loss compared to its two adjacent decades of 1980-1989 and 2000-2009. Additionally, although only comprising 6 years, the most recent partial decade of 2010-2015 shows an economic loss of 350 million USD (untrended), which is significantly smaller than its preceding decade of 2000-2009 (4,028 million USD, untrended). The ambiguous pattern in the economic losses may result from a number of factors, such as the quality of the historical records, urbanization, or construction compliance with disaster resistant techniques.

For Madagascar, 48 of its 59 entries are catastrophic events, with a reported 5,327 million USD in economic losses (untrended) and 2,943 lives lost (Table B.9). Mauritius has 19 catastrophic events, 419 people killed, and 1,120 million USD of economic losses (untrended) (Table B.10). Comoros has 7 catastrophic events, 645 people killed, and 65 million USD of economic losses (untrended) (Table B.8). And lastly, Seychelles has only 1 catastrophic event, with an economic loss of 5.7 million USD (untrended) and no people reported killed (Table B.11). Zanzibar does not have historical observations on the direct impact from tropical cyclones within the consequence database.

Table B.7 Summary for Comoros, Madagascar, Mauritius, Seychelles, and Zanzibar by decade of consequence database for tropical cyclones. Economic losses are not trended.

<i>Decade</i>	<i>Economic Loss (\$M USD)</i>	<i>Casualties</i>	<i>Events</i>	<i>Catastrophic Events</i>
1950-1959	0	524	1	1
1960-1969	64	284	8	5
1970-1979	795	280	10	9
1980-1989	1,024	457	23	16
1990-1999	256	778	16	12
2000-2009	4,028	1,292	34	21
2010-2015	350	392	11	11

Table B.8 Summary for Comoros by decade of consequence database for tropical cyclones. Economic losses are not trended.

<i>Decade</i>	<i>Economic Loss (\$M USD)</i>	<i>Casualties</i>	<i>Events</i>	<i>Catastrophic Events</i>
1950-1959	0	524	1	1
1960-1969	0	0	0	0
1970-1979	0	0	0	0
1980-1989	43	36	5	4
1990-1999	0	67	1	1
2000-2009	0	1	1	0
2010-2015	23	17	1	1

**Table B.9 Summary for Madagascar by decade of consequence database for tropical cyclones.
Economic losses are not trended.**

<i>Decade</i>	<i>Economic Loss (\$M USD)</i>	<i>Casualties</i>	<i>Events</i>	<i>Catastrophic Events</i>
1950-1959	0	0	0	0
1960-1969	8	110	2	2
1970-1979	420	264	6	6
1980-1989	675	410	7	6
1990-1999	65	508	9	8
2000-2009	3,865	1,276	26	17
2010-2015	294	375	9	9

Table B.10 Summary for Mauritius by decade of consequence database for tropical cyclones. Economic losses are not trended.

<i>Decade</i>	<i>Economic Loss (\$M USD)</i>	<i>Casualties</i>	<i>Events</i>	<i>Catastrophic Events</i>
1950-1959	0	0	0	0
1960-1969	56	174	6	3
1970-1979	375	16	4	3
1980-1989	307	11	11	6
1990-1999	191	203	5	3
2000-2009	158	15	4	3
2010-2015	34	0	1	1

**Table B.11 Summary for Seychelles by decade of consequence database for tropical cyclones.
Economic losses are not trended.**

<i>Decade</i>	<i>Economic Loss (\$M USD)</i>	<i>Casualties</i>	<i>Events</i>	<i>Catastrophic Events</i>
1950-1959	0	0	0	0
1960-1969	0	0	0	0
1970-1979	0	0	0	0
1980-1989	0	0	0	0
1990-1999	0	0	1	0
2000-2009	6	0	3	1
2010-2015	0	0	0	0

5.1.6 Database Statistics of Floods

The flood consequence database contains 67 entries which have been gathered from the previously mentioned information sources. Although the database consists of events recorded from 1977 and onwards, the first known economic loss is observed in 1995 from Mauritius. Altogether, the known economic losses are 586.7 million USD from 1990-2015 (untrended). Within the region, Mauritius is the country that has the largest recorded economic loss of 388.9 million USD (untrended), 23 deaths, and 4 catastrophic events (Table B.15). Madagascar comes second, with 9 catastrophic events, 170 million USD of economic losses (untrended), and 124 people killed (Table B.14). Comoros has 2 catastrophic events of 7 events, 26 lives lost, and economic loss of 20 million USD (untrended) (Table B.13). Seychelles has 1 catastrophic event from a total of 22 events and known economic loss of 7.8 million USD (untrended) (Table B.16). The last region, Zanzibar, indicates 2 catastrophic events with no deaths and no economic losses recorded, although an estimated 20,000 houses were destroyed in the decade 2000-2009 (Table B.17).

Table B.12 Summary for Comoros, Madagascar, Mauritius, Seychelles, and Zanzibar by decade of consequence database for non-cyclone precipitation and flooding. Economic losses are not trended.

<i>Decade</i>	<i>Economic Loss (\$M USD)</i>	<i>Casualties</i>	<i>Events</i>	<i>Catastrophic Events</i>
1950-1959	0	0	0	0
1960-1969	0	0	0	0
1970-1979	0	1	1	0
1980-1989	0	18	2	2
1990-1999	10	5	6	1
2000-2009	490	88	40	8
2010-2015	87	84	18	7

Table B.13 Summary for Comoros by decade of consequence database for non-cyclone precipitation and flooding. Economic losses are not trended.

<i>Decade</i>	<i>Economic Loss (\$M USD)</i>	<i>Casualties</i>	<i>Events</i>	<i>Catastrophic Events</i>
1950-1959	0	0	0	0
1960-1969	0	0	0	0
1970-1979	0	1	1	0
1980-1989	0	18	1	1
1990-1999	0	0	0	0
2000-2009	0	2	3	0
2010-2015	20	5	2	1

Table B.14 Summary for Madagascar by decade of consequence database for non-cyclone precipitation and flooding. Economic losses are not trended.

<i>Decade</i>	<i>Economic Loss (\$M USD)</i>	<i>Casualties</i>	<i>Events</i>	<i>Catastrophic Events</i>
1950-1959	0	0	0	0
1960-1969	0	0	0	0
1970-1979	0	0	0	0
1980-1989	0	0	1	1
1990-1999	0	0	1	1
2000-2009	150	74	10	5
2010-2015	20	50	2	2

Table B.15 Summary for Mauritius by decade of consequence database for non-cyclone precipitation and flooding. Economic losses are not trended.

<i>Decade</i>	<i>Economic Loss (\$M USD)</i>	<i>Casualties</i>	<i>Events</i>	<i>Catastrophic Events</i>
1950-1959	0	0	0	0
1960-1969	0	0	0	0
1970-1979	0	0	0	0
1980-1989	0	0	0	0
1990-1999	4	0	3	0
2000-2009	339	12	11	2
2010-2015	46	11	6	2

Table B.16 Summary for Seychelles by decade of consequence database for non-cyclone precipitation and flooding. Economic losses are not trended.

<i>Decade</i>	<i>Economic Loss (\$M USD)</i>	<i>Casualties</i>	<i>Events</i>	<i>Catastrophic Events</i>
1950-1959	0	0	0	0
1960-1969	0	0	0	0
1970-1979	0	0	0	0
1980-1989	0	0	0	0
1990-1999	6	5	2	0
2000-2009	1	0	14	0
2010-2015	<1	18	6	1

Table B.17 Summary for Zanzibar by decade of consequence database for non-cyclone precipitation and flooding. Economic losses are not trended.

<i>Decade</i>	<i>Economic Loss (\$M USD)</i>	<i>Casualties</i>	<i>Events</i>	<i>Catastrophic Events</i>
1950-1959	0	0	0	0
1960-1969	0	0	0	0
1970-1979	0	0	0	0
1980-1989	0	0	0	0
1990-1999	0	0	0	0
2000-2009	0	0	2	1
2010-2015	0	0	2	1

5.1.7 Database Statistics of Landslides

The secondary hazard of landslides has been recorded for 16 entries in the consequence database for both tropical cyclones and floods from 1986 to 2014. The data sources often do not specifically describe the secondary hazard landslides and do not include magnitude or exact locations of the landslide(s). Most of these land sliding events are associated with flooding and tropical cyclones, with the exception of a land sliding event in Comoros in 2014 that was triggered in combination by a moderate seismic event and then tropical cyclone Hellen. Economic loss, loss of life, and other consequence measures are not attributed solely to landslides and therefore a summary table is not generated for landslides induced by tropical cyclones or flooding.

5.2 Consequence Database for Earthquakes and Tsunami

5.2.1 Data Sources

The consequence data from natural hazards that have occurred in the South West Indian Ocean (SWIO) for Comoros, Madagascar, Mauritius, Seychelles, and Zanzibar have been collected from a variety of sources. Although earthquakes, tsunamis, and volcanic eruptions are not as frequent as tropical cyclones and flooding for these five countries, the SWIO region does have historical impacts from these events. The consequence database presents the findings of a thorough data collection effort and the database is considered a comprehensive inventory of recorded natural hazards that had a significant impact on the population in the SWIO region. The data collected was aggregated from a number of major disaster databases and from reports, which are publically available. These databases include:

1. The Emergency Events Database (EMDAT, 2016) maintained by the Centre for Research on the Epidemiology of Disasters (CRED) at the School of Public Health of the Université Catholique de Louvain located in Brussels, Belgium.

2. "ReliefWeb," is an online service (ReliefWeb, 2016) provided by OCHA (United National Office of Humanitarian Affairs) that scans the websites of international and non-governmental organizations, governments, research institutions and the media for news, reports, press releases, appeals, policy documents, analysis and maps related to humanitarian emergencies worldwide (e.g., UN reports, IFRC updates, OCHA reports etc.).
3. The Disaster Inventory System – DesInventar (2016)
4. National Oceanic and Atmospheric Administration (National Centers for Environmental Information) (NOAA, 2016)

5.2.2 Explanation of Database Data and Data Fields

122 consequence entries from 22 unique earthquakes and volcanic eruptions have been collated from the previously mentioned sources for the consequence database. Each entry has recorded a notable effect on the population or damage to the building inventory or surroundings. An event may have multiple entries due to different locations with reported notable effects (e.g., 87 locations for measured tsunami wave heights in the SWIO region from the 2004 M_w 9.1 Sumatra Indonesia earthquake). Some entries may contain data from multiple sources, and, as expected, discrepancies exist for the quantitative data, such as number of buildings destroyed. By design, the discrepancies have been preserved and each piece of information has been appropriately referenced. Analysis of the information in the consequence database has not been undertaken and therefore events with unique identification numbers within a data source that are chronologically close or overlapping have not been eliminated. This consequence database represents a comprehensive collection of the significant historical events (e.g., earthquakes, tsunami, volcanic eruptions and secondary hazards) but is not a complete record of all occurrences within the history of these five countries.

Earthquakes, volcanic eruptions, and tsunami are interrelated; for example, a tsunami may be caused by an earthquake which is many kilometers away rather than by a nearby local source. To separate entries into two categories, a "Local Source" flag has been designated with a "Y" to indicate if the earthquake or volcanic eruption occurs within the region of Comoros, Madagascar, Mauritius, Seychelles, or Zanzibar. If the earthquake or volcanic eruption occurs outside of this region, then the "Local Source" flag is designated with an "N." Additionally, when an entry is specifically described or identified as having caused a tsunami event, then it is recorded as a tsunami entry ("Y") in the consequence database even if a wave run-up height has not been recorded. Entries that are not specifically listed or described as causing a tsunami are not indicated as tsunami entries. This method is not a rigorous analysis and represents an approximate categorization based on the available data.

The referenced sources discussed in the previous section typically report a brief summary of the disaster consequence (e.g., number of people affected and/or number of lives lost), and some accounts are strictly qualitative (e.g., "crops were damaged"). For each entry in the consequence database, data from each field is

aggregated to account for the total consequence from a particular disaster event (including related secondary events/effects such as landslide), and generally most or all of the damage occurs in the country listed. For seismic events, the losses are aggregated per event; specific details on the relative losses are noted for some events (e.g., damage to infrastructure). The main data fields of the consequence database are outlined below:

- **People Affected** – A measure of the estimated number of people affected by the event. People affected include those that became homeless, injured, displaced, evacuated, or disrupted (e.g., affected by loss of utilities) by the peril.
- **People Displaced** – A subset of the number of people affected, this indicates the number of people required to vacate their residence due to the peril, such as those evacuated or displaced.
- **Economic Damage** – The estimated total economic impact of the event consists of direct damage (e.g., damage to infrastructure, crops, housing). Estimated loss is typically reported in U.S. dollars (USD), corresponding to the monetary loss at the time of the event (e.g., current/nominal USD). Data reported in local currency are converted appropriately by using rates for the specific (time-of-event) dates based on information supplied by leading market data contributors [e.g., The World Bank (2015) Official exchange rate]. Losses are reported as the monetary cost at the time of the event. A break-down of losses (e.g., losses per sector, such as social sector, private sector, infrastructure), crop losses, and locations for deaths and building damages) may be available for those events where detailed assessment reports were issued [e.g., United Nations Office of Humanitarian Affairs (OCHA) Situation Report].
- **Deaths** – The total number of people reported dead, missing or presumed dead as a result of the event, including any resulting deaths from starvation, injury, or disease.
- **Buildings Destroyed** – The total number of buildings (typically listed as “houses”) reported to be destroyed as a result the event. Partially destroyed houses are also cataloged.
- **Local Source Flag** – An indicator that the event is cited as a nearby local event by the data sources.
- **Tsunami Flag** – An indicator that the event is cited as causing a tsunami by the data sources, (e.g., the National Oceanic and Atmospheric Administration).
- **Effect** – A description, such as tsunami or landslide, to illustrate the effects of the event. These two categories are also separated out into columns for ease of identification. Each peril (e.g., tsunami or landslide) has its own column header and may be filtered with the “Y” indicator for each event. Note that “tsunami” may sometimes but not always accompany a significant earthquake event. This absence may be an inadvertent omission of information from the data sources and may not necessarily be an indication of a lack of tsunami wave run-up.

5.2.3 Discussion of Significant Events

The South West Indian Ocean region occasionally experiences earthquakes, tsunamis, and volcanic eruptions. The consequences database lists notable events. Some recent and historically significant events are briefly discussed in this section.

Karthala Volcano (2005)

In 2005, two large eruptions of Mount Karthala on Grande Comore affected 39,000 people in April and 245,000 people in November. The first eruption, on April 16, pushed clouds of smoke and ash into the sky which affected villages in the Dimani and Pidjani regions on the eastern side of the island. By the next day, as many as 10,000 people fled from their homes to seek refuge on other parts of the island in case of gas and lava flow. At least 720 water tanks in 36 villages were contaminated by volcanic debris and were deemed not potable. Later the same year, the second eruption again projected ash and smoke, which covered extensive areas of Grande Comore Island with volcanic debris, namely the south eastern and south western areas of the island and the capital, Moroni. Of the 245,000 people affected by smoke and ashes in 76 villages, 175,000 people did not have access to potable water due to contaminated water tanks. The inhalation of volcanic dust has also affected many people by making it difficult to breathe freely.



Figure B.7 (left) Phreatic eruption of Mount Karthala on the afternoon of April 17, 2005 (Source: Daniel Hoffschir, Global Volcanism Program), and (right) Lava lake formed in Chahalé crater of Mount Karthala (Source: Hamid Soulé, Karthala Volcano Observatory)

Indian Ocean Earthquake and Tsunami (2004)

On December 26, 2004, a megathrust earthquake with an epicenter off the west coast of Sumatra, Indonesia, triggered a series of deadly tsunami along the coasts of neighboring countries with waves as high as 30 meters. More than 4,000 kilometers away from the epicenter, the country of Seychelles experienced 2 deaths, 105 destroyed houses, a possible 500 damaged buildings, and 4,830 affected people from the resulting tsunami.

Several hotels and buildings were flooded, and the observed flood height was 1.9 meters at 50 meters inland distance at the international airport at Pointe Larue in Mahe and 3 meters at 250 meter inland distance in Baie Ste Anne, Praslin. Although no deaths from the tsunami were recorded for Mauritius and Madagascar, post event observations recorded that a maximum height of the water of 3.8 meters at 24 meters inland for a beach in Mauritius, and of 5.4 meters at 28 meters inland for Madagascar. In Madagascar, an estimated 1,000 people were displaced, and in Mauritius, an entire village with an unrecorded number of people was submerged by large waves. It is cited that a “significant economic loss in millions of dollars” was suffered by Mauritius and that “considerable” economic damage was suffered by the Madagascar’s tourism, fishing, and infrastructure sectors. No casualties were recorded for Comoros and Zanzibar, although some livestock and five canoes were washed away. Post event field surveys were conducted to established locations and amplitude of runup (Jackson et al. 2005; Okal et al. 2006a; Okal et al. 2006b; Okal et al. 2009).



**Figure B.8 The remains of a road swept away by the tsunami (photo taken from repaired section).
 (Source: M. de Vries, UNEP)**

Moderate Earthquake and Landslides in Comoros (2014)

On March 12, 2014, a moderate magnitude 4.8 earthquake struck the island of Anjouan in Comoros. This event was followed by heavy rains from tropical cyclone Hellen. Although the earthquake cause limited damage and no deaths, the combined effects from the two events caused land subsidence and cracks in the soil, which led to the evacuation of 3,030 people from the village of Mahale, Anjouan, on March 31. By early April, deep fissures in the soil and resulting landslides damaged building, roads, and water supplies. One of the roads past Mahale village cracked and eroded, cutting off access to the capital city for four villages of Harembo, Hajoho, Handrouva, and Jimlime (approximate population of 10,000 people). (UNICEF Comoros 2014) (Figure B.9)

The same seismic event and heavy rains from tropical cyclone Hellen also induced landsliding approximately 2 miles from the town of Ouallah in the southwest region of Moheli, Comoros. Cracks in the soil induced from

the seismic event and water saturation of the clayey soils at the site from heavy rainfall caused blockage of the recently constructed highway for reportedly 100 meters. (Figure B.10)



Figure B.9 Landslide on Anjouan, Comoros, induced by moderate earthquake and tropical cyclone Hellen (Source: Walter D. Mooney, USGS)



Figure B.10 Landslide on Moheli, Comoros, induced by moderate earthquake and tropical cyclone Hellen (Source: Mansourou, 2014)

5.2.4 Database Statistics

This section outlines key statistics of the consequence database, with the main intent of providing a summary of recorded disaster data and presenting a quantitative overview of consequences from natural hazards (Table B.1). 22 unique earthquakes, tsunami, and volcanic eruptions have been recorded for the countries of Comoros, Madagascar, Mauritius, Seychelles, and Zanzibar; six of these have been defined as “catastrophic”, which is defined as being reported with either at least 10,000 people displaced or affected, at least 10 million USD in

losses (untrended), or at least 10 deaths. Of these catastrophic events, 4 events are caused by volcanic eruptions from Comoros, 1 event is from a seismic event also on Comoros, and the remaining event is from a non-local earthquake originating from Indonesia, Sumatra. Note that the number of events refers to each unique event that may cause multiple entries in the consequence database. If an earthquake (or other event) affects more than one country or location, then it is listed in the consequence database with multiple entries.

While the data search for the consequence database was completed thoroughly, data for each entry may not be comprehensive, as some accounts of consequence may not have been recorded consistently or even reported. For example, no known consequence events are reported from 1910 to 1939, but it is not clear if no notable events occurred or if the impact of events was not recorded; and thus, no available information is generated from databases sources. This region also has many locally generated earthquakes of small magnitude, which may not cause damage or have a consequence recorded. The scarcity of consequence data endemic to this region denotes the lesser significance of earthquakes and volcanic eruptions as compared to tropical cyclones and floods. Within the consequence database, quantitative data for economic damage is reported for 1 event (4.5% of events); for loss of life, it is reported for 4 events (18% of events). Nevertheless, the consequence database serves as a valuable tool for assessing the impact of significant events, which are used for model validation purposes.

For the five countries of Comoros, Madagascar, Mauritius, Seychelles, and Zanzibar, an estimated 324,030 people have been affected by earthquakes, volcanic eruptions, tsunamis, and secondary hazards since 1883. This is approximately 1% of the combined countries' population of almost 27 million people¹¹. The reported economic losses are 30 million USD (untrended), which represents 0.1% of the combined countries' estimated gross domestic product at current prices in USD¹². However, it is surmised that not all economic damage has been comprehensively tallied and cataloged, nor reported. Although the reported number of people affected and damage sustained are relatively small, there still exist severe consequences for those people impacted by these events.

¹¹ 2014 census data from the World Bank for Comoros, Madagascar, Mauritius, and Seychelles and 2012 census data for Zanzibar (Office of Chief Government Statistician, Zanzibar)

¹² Derived from 2013 and 2012 Gross Domestic Product per capita at current prices in USD (United Nations Statistics Division), 2013 census data (The World Bank), and 2012 census data (Office of Chief Government Statistician, Zanzibar)

Table B.18 Summary for Comoros, Madagascar, Mauritius, Seychelles, and Zanzibar by decade of consequence database for earthquakes, tsunami, and volcanic eruptions. Economic losses are not trended.

<i>Timespan</i>	<i>Economic Loss (\$M USD)</i>	<i>Casualties</i>	<i>Total Reports</i>	<i>Total Events</i>	<i>Severe Events</i>
Pre-1900	-	-	6	2	-
1900-1909	-	17	2	2	1
1910-1919	-	-	-	-	-
1920-1929	-	-	-	-	-
1930-1939	-	-	-	-	-
1940-1949	-	-	1	1	-
1950-1959	-	-	-	-	-
1960-1969	-	-	1	1	-
1970-1979	-	1	1	1	1
1980-1989	-	-	1	1	-
1991-1999	-	-	4	4	-
2000-2009	30	5	152	7	3
2010-2015	-	-	7	3	-

When inspected on a per country basis, certain patterns appear in the data. Comoros and Mauritius are the two countries where earthquakes from nearby local sources have generated sufficient ground shaking to be observed, albeit with no recorded economic damage. Comoros is the only country affected by volcanic eruption within its own boundaries, with a total of 309,200 people affected since 1977. For volcanic eruption outside of the immediate SWIO region, such as from Mt. Puyehue in Chile or Mt. Krakatau in Indonesia, only Mauritius and Seychelles have observations noted in historical documents. Madagascar has only 1 event with multiple entries indicating 55 locations of measured tsunami wave run-up heights and 1 resulting death from the 2004 Indonesia, Sumatra earthquake (M_w 9.1). Consequence data for Madagascar concerning earthquakes, volcanoes, tsunami, or secondary hazards is either not recorded consistently in historical documents or is naturally scarce. Likewise, Zanzibar records 7 locations of measured tsunami wave run-up height from the same 2004 Indonesia, Sumatra earthquake but has no other events with associated consequences. Mauritius has 12 unique events and no reported loss of life or economic damage reported for both local and nonlocal event sources. Seychelles has been affected by tsunami run-up generated by earthquakes from outside of its borders, namely from Indonesia, Chagos Archipelago Region, or Pakistan.

5.2.5 Database Statistics of Landslides

The secondary hazard of landslides has been recorded for 1 entry for the country of Comoros in the consequence database for earthquakes, tsunami, volcanic eruptions and other secondary hazards. Volcanic eruptions were not considered as landslides for this study. This singular entry for landslides in Comoros was induced by both a moderate earthquake on Anjouan and from the heavy rainfall of tropical cyclone Hellen in 2014. For more details on the event, refer to the Section 3 describing the significant events.

5.3 References

- Asian Disaster Reduction Center (2015). Disaster Information Archive, accessed in January and February 2015 from http://www.adrc.asia/latest_disaster.php
- DesInventar (2016). Disaster Information Management System, UNISDR (The United Nations Office for Disaster Risk Reduction), retrieved in May 2015 from <http://www.desinventar.net/country-list.html>
- DFO (2016). G.R.Brakenridge, "Global Active Archive of Large Flood Events", Dartmouth Flood Observatory, University of Colorado, retrieved in March 2015 from <http://floodobservatory.colorado.edu/Archives/index.html>
- EMDAT (2016). The International Disaster Database, retrieved May 28, 2015, and February 10, 2016, from <http://www.emdat.be/database>
- GLIDE (2016). GLObal IDentifier number, accessed in February and March 2015, from <http://www.glidenummer.net/>
- Hungarian National Association of Radio Distress-Signaling and Infocommunications (RSOE) and the Emergency and Disaster Information Services (EDIS) (2016), accessed in May 2015 from <http://hisz.rsoe.hu/alertmap/index2.php>
- Jackson, L.E., Jr., Barrie, J.V., Forbes, D.L., Shaw, J., Manson, G.K., and M. Schmidt (2005). "Effects of the 26 December 2004 Indian Ocean Tsunami in the Republic of Seychelles," Report of the Canada-UNESCO Indian Ocean Tsunami Expedition 19 January – 5 February 2005, Geological Survey of Canada, Open File #4539, 73 pp.
- Knapp, K. R., M. C. Kruk, D. H. Levinson, H. J. Diamond, and C. J. Neumann, 2010: The International Best Track Archive for Climate Stewardship (IBTrACS): Unifying tropical cyclone best track data. *Bulletin of the American Meteor. Society*, 91, 363-376, retrieved on April 17, 2015
- Mansourou, A. (2015). "L'évaluation des Risques de tremblement de terre et Glissement de terrain sur l'île autonome de Mohéli en Union des Comores," *Croissant-Rouge Comorien*, 55 pp. (in French)
- NOAA (2016). National Centers for Environmental Information, accessed October 2015, from <https://www.ngdc.noaa.gov/hazard/hazards.shtml>
- Okal, E.A., Fritz, H.M., Raveloson, R., Joelson, G., Pančošková, P., and G. Rambolamanana (2006). "Madagascar Field Survey after the December 2004 Indian Ocean Tsunami," *Earthquake Spectra*, 22(S3), S263-S283.
- Okal, E.A., Sladen, A., and E.A.S. Okal, (2006). "Rodrigues, Mauritius, and Réunion Islands Field Survey after the December 2004 Indian Ocean Tsunami," *Earthquake Spectra*, 22(S3), S241-S261.

Okal, E.A., Fritz, H.M., and A. Sladen (2009). "2004 Sumatra-Andaman Tsunami Surveys in the Comoro Islands and Tanzania and Regional Tsunami Hazard from Future Sumatra Events," *South African Journal of Geology*, 112, 343-358.

ReliefWeb, a specialized digital service of the United Nations Office for the Coordination of Humanitarian Affairs (2016), accessed in February, March, and April 2015 and March 2016 from <http://www.reliefweb.int>

UNICEF Comoros (2014). "Emergency Response to the Earthquake Disaster in Comoros," Final Report SM140220, 19 pp.

About AIR Worldwide Corporation

AIR Worldwide Corporation (AIR) is the scientific leader and most respected provider of risk modeling software and consulting services. AIR founded the catastrophe modeling industry in 1987 and today models the risk from natural catastrophes and terrorism in more than 50 countries. More than 400 insurance, reinsurance, financial, corporate and government clients rely on AIR software and services for catastrophe risk management, insurance-linked securities, detailed site-specific wind and seismic engineering analyses, agricultural risk management, and property replacement cost valuation. AIR is a member of the ISO family of companies and is headquartered in Boston with additional offices in North America, Europe and Asia. For more information, please visit www.air-worldwide.com.

